Filtration of NaCl and WOx Nanoparticles using Wire Screens and Nanofibrous Filters

by

Raheleh Givehchi

A thesis
presented to the University of Waterloo
in fulfillment of the
thesis requirement for the degree of
Doctor of Philosophy
in
Mechanical and Mechatronics Engineering

Waterloo, Ontario, Canada, 2016

AUTHOR'S DECLARATION

I hereby declare that I am the sole author of this thesis. This is a true copy of the thesis, including any required final revisions, as accepted by my examiners.

I understand that my thesis may be made electronically available to the public.

Abstract

Airborne nanoparticle filtration is essential for the protection of public health and the environment. The principles and fundamentals of air filtration have been validated with respect to micron particles; however, the mechanisms for airborne nanoparticle filtration are still uncertain. Conventional filtration theory states that diffusion dominates the behavior of submicron particles and that filtration efficiency increases inversely with the size of fine particles. This theory implies that nanoparticles can be effectively captured by properly designed air filters. However, some researchers have pointed out that single-digit nanosized airborne particles may behave like gas molecules upon impacting the filter media, if the kinetic energy is greater than the adhesion energy. As a result, such small nanoparticles may rebound from the filter media upon collision, in what is called thermal rebound. However, this phenomenon has not yet been observed in experimental studies, so uncertainties are still associated with the concept of thermal rebound, which itself has yet to be either proven or disproven.

Despite the large amount of work done on nanoparticle filtration, there is still a gap between theory and experiments. This research aims to understand the interaction between nanoparticles and various filter media. The following tasks were done to achieve this goal:

1) Determining the performance of a scanning mobility particle sizer coupled with a Faraday cup electrometer (SMPS+E) for sizing airborne nanoparticles,
2) Implementing the nanoparticle filtration tests using wire screens for various particle number concentration distributions,
3) Developing a new thermal rebound model to determine the particle size at which thermal rebound occurs,
4) Characterizing PVA nanofibrous filters for nanoparticle removal,
5) Evaluating the effects of particle concentration on the filtration of PVA nanofibrous filters.

Before conducting any filtration efficiency measurement, the performance of the scanning mobility particle sizer coupled with a Faraday cup electrometer (SMPS+E, GRIMM 7.860) was analyzed for NaCl and WOx particles at various particle number concentration distributions. The effects of instrument parameters, including the sheath air flow rate and sample air flow rate on particle number concentration distribution and on the lower and upper particle size detection limits were investigated theoretically and experimentally. For both types of nanoaerosol particles, the measurement of particle number concentration distribution depended on the selection of sheath air and sample air flow rate ratio,

which depended on the initial particle concentrations and aerosol flow rate. Due to the high resolution of GRIMM SMPS+E for particle classification, no mobility shift was observed.

The filtration efficiencies of nanoparticles with a broad size range and concentrations were then determined for uncharged micron-sized stainless-steel wire screens. Results showed that the filtration efficiency of WOx nanoparticles depends on particle number concentration distribution. For particles smaller than the mode size, the filtration efficiency followed the conventional theoretical model; however, the filtration efficiency deviated from that conventional model for larger particles. This result is likely due to the different morphology of WOx particles, which affects both particle charging and measurement performance.

The next step was to develop a new filtration model by considering the possibility of thermal rebound effect. Theoretical analysis showed that, when nanoparticles collide on a solid filter media, it is more likely for plastic deformation to occur than elastic deformation does. Therefore, the nanoparticle filtration model was developed based on the assumption of plastic deformation of nanoparticles upon impaction to the surface of the filter media. Furthermore, results showed that the probability of thermal rebound increases inversely with relative humidity, which attenuates capillary force.

The interactions between nanoparticles and various filter media are characterized by surface loading. Electrospun PVA nanofibrous filters were thus fabricated, then characterized in terms of fiber size distribution by SEM analysis using an automated tool, and their filtration performances were evaluated using NaCl nanoparticles. The higher the applied voltage and tip-to-collector distance and the shorter the deposition time, the higher the quality factors of the nanofibrous filters. Furthermore, the filter quality factor can be greatly improved by stacking up single layer filters made in a short deposition time.

The electrospun PVA nanofibrous filters were then tested for sub-4 nm WOx particles with triple modal particle number concentration distributions at a low relative humidity (RH=2.9%). The upstream particle concentration affected the performance of nanofibrous filters, as it was higher at the lower particle concentration. The filtration efficiency for sub-2 nm particles showed that the particle critical diameter, below which thermal rebound may happen, is in the range of 1.07-1.17 nm. An analytical model was developed to predict the effects of particle concentration. Comparison between the developed model and experiments showed qualitative agreement; but more research is needed to further improve the model.

Acknowledgements

I would like to thank my supervisor, Prof. Zhongchao Tan, for his patient guidance, incredible support and encouragement. His positive outlook and confidence in my research inspired me and changed the way I look at life. I would like to thank him for his ongoing and excellent advices. I would like to thank my PhD committee members, Prof. Jeffrey Siegel from the University of Toronto, Prof. William Anderson, Prof. Fue-Sang Lien and Prof. John Wen from the University of Waterloo.

I would also like to thank Jason Benninger, Greg Friday, Andy Barber, James Merli and Gil Cossette for their technical support. My warm gratitude goes to all the current members and alumni of APRIL lab during the years of my PhD, especially Hesheng Yu, Fang Liu, Chen-ping Ni, Jorge Ahne and Wala Bkari. It was also a great pleasure to work with fantastic coop students and undergraduate research assistants including Patrick Bardo, Simon Liu, Sion Chung and Osemudiamen Omon-Anolu. I would also like to express my thanks to Ms. Mary McPherson for her valuable editorial insights of this thesis. Financial support from NSERC, CFI, Ontario government and O_2 Canada are also acknowledged.

I wish to thank my parents, Ali and Asieh, and my brothers Reza and Ramin. Thanks for your constant unconditional love and encouragements. Words cannot express my gratitude for everything you have done.

Above all, I would like to thank my beloved friend, schoolmate and husband, Mohammad, for his understanding and love during the past few years. I owe you everything.

Dedication

To

My Parents & My Husband

Table of Contents

List of Figures

List of Tables

List of Symbols

Symbol	Term	Unit
a	contact radius between particle and another surface	m
A	Area	m^2
A_H	Hamaker constant	J
C	concentration of nanoparticles	$1/cm^3$
C_c	Cunningham coefficient	-
C_{down}	downstream particle concentration	$1/cm^3$
C_i	mean thermal speed of ions	m/s
C_{up}	upstream particle concentration	$1/cm^3$
d_f	fiber diameter	m
d_g	gas molecule diameter	m
d_p	particle diameter	m
D	diffusion coefficient of particles	m^2/s
D_n	diffusion coefficient of neutral nanoparticles	m^2/s
e	electron charge	C
e	coefficient of restitution	-
E	total efficiency of a single fiber	-
E	electric field	V/m
E	elastic Young's modulus	N/m^2
E^*	reduced Young's modulus	N/m^2
E_{ad}	adhesion energy	J
E_C	single fiber efficiency based on concentration	-
E_D	single fiber efficiency by diffusion	-
E_{DR}	single fiber efficiency by interception of diffused particles	-
E_{eff}	effective single fiber efficiency	-
E_{ni}	potential energy of an impact particle	J
E_{nr}	potential energy of a rebound particle	J
E_R	single fiber efficiency by interception	-
F	external force	N
F_e	electrostatic force	N

F_c	capillary force	N
g	gravitational acceleration	m/s^2
H	hardness of the deformed solid	N/m^2
K^*	composite Young's modulus	N/m^2
K_b	Boltzmann's constant	J/K
K_e	proportionality constant	Nm^2/C^2
K_P	mechanical constant of particle	m^2/N
K_S	mechanical constant of filter	m^2/N
KE_{ni}	kinetic energy of an impact particle	J
KE_{nr}	kinetic energy of a rebound particle	J
Kn	Knudsen number	-
Kn_p	particle Knudsen number	-
Ku	Kuwabara constant	-
L	thickness of filter	m
m	mass of the gas molecules	Kg
n	number of charges on the particle	-
N	number concentration of gas molecules	$1/m^3$
N_i	ion concentration	$1/m^3$
P	Pressure	Pa
Pe	Peclet number	-
q	charge carried by particle	C
Q_a	sample air flow arte	lpm
Q_F	quality factor	Pa^{-1}
Q_{sh}	sheath air flow rate	lpm
R	interception parameter	-
R^*	characteristic radius of two bodies	m
Re	Reynolds number	-
Re_P	particle Reynolds number	-
RH	relative humidity	-
Stk	Stokes number	-

t	Time	s
T	Temperature	k
TR	thermal rebound coefficient	-
U	aerosol flow velocity	m/s
U_0	face velocity	m/s
$\bar{v}_{im}$	mean impact velocity in thermal rebound	m/s
v_{im}	impact velocity in thermal rebound	m/s
V_r	root mean square velocity of the gas	m/s
v_{ni}	particle impact velocity	m/s
v_{nr}	particle rebound velocity	m/s
v_y	elastic yield velocity	m/s
w	basis weight of the filter	kg/m^2
Y	elastic limit	N/m^2
Z_0	equilibrium distance between bodies	m
Z_p	electrical mobility of a particles	$m^2/(V.s)$
Greek letters		
α	solidity of filter	-
δ	deformation height	m
ΔP	pressure drop across the filter	Pa
$\Delta\gamma$	specific adhesive energy	J/m^2
ΔZ	electrical mobility bandwidth	$m^2/(V.s)$
ε	particle adhesion efficiency	-
ε_0	permittivity of a vacuum	$C^2/(N.m^2)$
η	total filtration efficiency	-
λ	gas mean free pass	m
λ	elasticity parameter	-
μ	kinetic viscosity	Kg/(m.s)
μ	Tabor coefficient	-
v	Poisson ratio	-

ρ	Density	Kg/m^3
ρ_p	particle density	Kg/m^3
σ	surface tension of water	N/m
σ_g	geometric standard deviation	-

Chapter 1
Introduction

1.1 Problem Statement

Air pollution constitutes gases, liquid droplets, particulate matter or biological materials in excessive amounts. Major air pollutants include carbon monoxide (CO), sulfur dioxide (SO_2), nitrogen oxide (NOx), volatile organic compounds (VOCs), ground-level ozone (O_3), and particulate matter (PM). Particulate matter refers to a complex mixture of small airborne particles generated from a variety of sources: dust, volcanic emissions, combustion, heating, cleaning, transportation, industry, urban activities, land use, etc. Particle size is an important property of particulate matter that determines their behavior. Particle sizes range from nanosized to micron-sized. The focus of this study is on airborne nanoparticles. Unlike micron particles, nanoparticles exhibit unique and unusual properties that may affect their dynamics in the air.

Airborne nanoparticles are produced from many sources such as combustion and nanotechnology applications (Donaldson et al. 2005; Mädler and Friedlander 2007). With the advent of nanotechnology over the last few decades, concerns have arisen over the potential adverse impact of nanoparticles on human health (Ferreira et al. 2013), and the removal and control of nanoparticles are critical to the protection of public health (Oberdörster et al. 2005). One of the most common methods to remove airborne nanoparticles is air filtration.

The fundamentals of air filtration have been validated with respect to micron particles; however, the mechanisms associated with the application of filters for airborne nanoparticles are still uncertain. It has been shown that small nanoparticles may behave like gas molecules upon their impaction on the surface of the filter media. Small nanoparticles may not attach to the filter media when their mean thermal impact velocities are higher than the required capture velocity (Dahneke 1971; Wang and Kasper 1991). This phenomenon is known as thermal rebound. In this case, small nanoparticles may rebound from the surface upon collision due to their high impact velocities, leading to a decrease in filtration efficiency. Although a variety of studies, both analytical and experimental, are related to nanoparticle filtration, researchers remain uncertain about the size of nanoparticles below which thermal rebound occurs, and whether the effect of thermal rebound prevents small nanoparticles from being captured by conventional filters.

One of the missing factors in the thermal rebound theory is the effect of capillary force between the nanoparticle and the surface of the filter media. Studies have shown the increase of the adhesion energy between a particle and a solid surface at high relative humidity (Bateman et al. 2014; Chen et al. 2011; Stein et al. 1994; Vasiliou et al. 1999). It was also reported that the filtration efficiency for micron particles increases with the level of relative humidity (Brown 1993; Miguel 2003; Mullins et al. 2003; Xu et al. 2014); however, it is not clear whether this applies to nanosized particles and affects the thermal rebound.

Filtration testing of nanoparticles is a process that involves the generation of nanoparticles and accurate sizing and quantification of such particles. Among various commercial instruments used for sizing and quantifying nanoparticles, scanning mobility particle sizer (SMPS) is widely used. A typical SMPS usually consists of a differential mobility analyzer (DMA) that classifies nanoparticles based on their electrical mobility, and a condensation particle counter (CPC) or a Faraday cup electrometer (FCE) for measuring nanoparticle concentration. Studies have shown that instrumental errors due to the mobility shift of nanoparticles in particle size classification devices may lead to the artifacts of thermal rebound (Alonso et al. 1997; Heim et al. 2006). Thus, prior to any filtration test, a state-of-the-art instrument is required to minimize errors in the measurement of nanoparticle number concentration distribution.

Various methods have been used to produce nanoscale test aerosol particles; however, few can generate nanoparticles down to 1 nm with sufficient numbers. Only a few researchers have utilized sub-2 nm particles along with larger ones (Alonso et al. 1997; Heim et al. 2010; Ichitsubo et al. 1996; Kim et al. 2006; Otani et al. 1995), of which three studies showed the possibility of thermal rebound for sub-2 nm particles (Ichitsubo et al. 1996; Kim et al. 2006; Otani et al. 1995). Thus, generating a stable, repeatable and reproducible nanoparticle concentrations for particles down to 1 nm in diameter is important for determining the interaction between these nanoparticles and filter media.

The characteristics of filters also affect the interaction between nanoparticles and filters. Thermal rebound has not been observed in commercial fibrous filters (Golanski et al. 2009; Huang et al. 2007; Japuntich et al. 2007; Kim et al. 2007; Van Osdell et al. 1990); however, it may happen on wire screen filters for sub-2 nm particles (Ichitsubo et al. 1996; Otani et al. 1995). Due to the sizes of openings in wire screens, nanoparticles may pass through the screen. Employing thin nanofibrous filters with

randomly deposited fibers, whereby filtration is characterized by surface loading instead of depth loading (Yoon et al. 2008) may eliminate the artifacts associated with commercial filters and wire screens.

Filters with micron-sized fibers are widely used for nanoparticle filtration. These filters are effective for particles greater than 300 nm, but inefficient for smaller particles (Barhate and Ramakrishna 2007). Compared to conventional filters made of micron-sized fibers, the nanofibrous filters reveal superior performance, with higher removal efficiencies than conventional filters, due to slip flow and a large surface-area-to-volume ratio. Although earlier studies have been done to determine the filtration efficiencies of these filters for micron particles and the most penetration particle size (MPPS), studies on the effects of nanofibrous filters on sub-100 nm particles are limited.

In the current study, both wire screens and nanofibrous filters were employed as the filter media. Electrospun PVA nanofibrous filters were fabricated by electrospinning and characterized using an automated tool. The filtration efficiencies of these filters were evaluated for WOx and NaCl nanoparticles. A brand-new scanning mobility particle sizer coupled with a Faraday cup electrometer (SMPS+E, GRIMM 7.860) was employed to measure nanoparticle number concentration distribution. Few researchers have reported the performance of GRIMM SMPS in conjunction with a Faraday cup electrometer. Gaining deeper insights into the instrument mechanisms, factors that affect its performance, possible issues which deserve more attention will minimize artifacts associated with the process and ensure that the instrument to accurately measure particle number concentration distributions.

1.2 Research Objectives

The major objective of this research is to understand the interaction between nanoparticles and the filter media. To achieve this goal, the following tasks were done.

1) Determined the performance of SMPS for sizing and quantifying nanoparticles,
2) Implemented the nanoparticle filtration testing of wire screens for various particle number concentration distributions,
3) Developed a new thermal rebound model to determine the particle size at which thermal rebound occurs,

4) Characterized PVA nanofibrous filters for nanoparticle removal
5) Evaluated the effects of particle concentration on the filtration efficiency of PVA nanofibrous filters.

1.3 Research Approach

The overall structure of this thesis is shown in Figure 1-1.

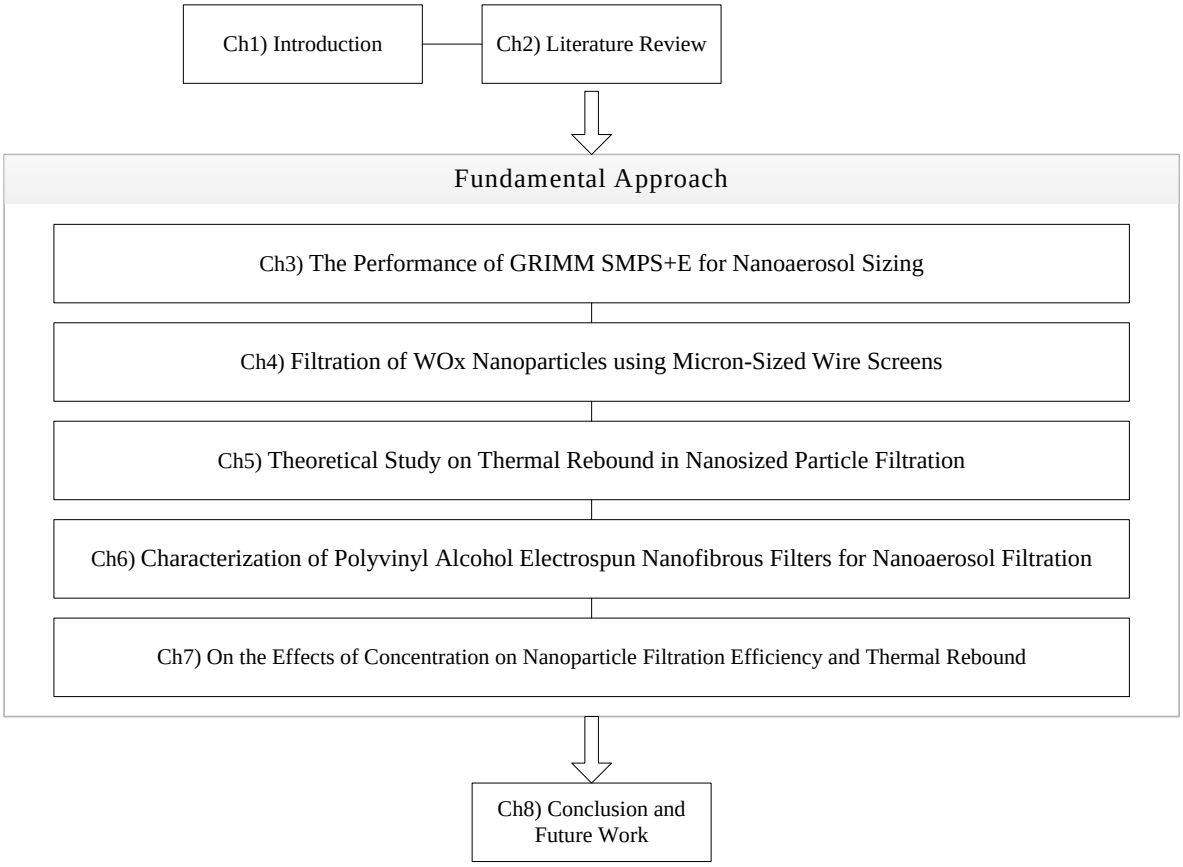

Figure 1-1. Thesis structure

The thesis is organized into eight chapters. Chapter 1, the current chapter, provides an overview of the research problem and describes the motivation, opportunities, and objectives of the research. These factors form the basis of a comprehensive review of the relevant literature on the filtration of airborne nanoparticles in Chapter 2. The review covers background knowledge about the properties of nanoparticles, filtration and thermal rebound theory. Chapter 3 evaluates the performance of a scanning

mobility particle sizer coupling with a Faraday cup electrometer (GRIMM SMPS+E) for measurement nanoparticle number concentration distribution. By the end of this chapter, the effects of parameters such as particle concentration, aerosol flow rate, sheath air flow rate and sample air flow rate on the accuracy of particle number concentration distribution measurement are determined. For high-resolution measurement with minimum diffusion loss, the FCE has to be attached to the exit of the DMA. Moreover, due to the fast response time of GRIMM FCE (1/4 s), purging between measurements is not necessary. The differences between the geometry of the GRIMM DMA and that of TSI allow the former device to measure nanoparticle number concentration distributions at the low sheath air to sample air flow rate ratio of 5:1. The GRIMM SMPS+E measurement device are employed in the following filtration tests.

Chapter 4 describes the experimental method used to determine the nanoparticle filtration efficiency. Methods to minimize errors in filtration efficiency measurements are first determined. The filtration performance of uniform wire screens for WOx and NaCl nanoparticles. It is shown that the filtration efficiencies for both monodispersed and polydispersed particle measurements agree well with each other, thus eliminating the need to employ monodispersed particles in the rest of the filtration tests. Furthermore, the filtration efficiency measurements show the same results for sheath air to sample air flow rate ratios of both 5:1 and 10:1. The efficiencies of wire screens for both NaCl and WOx particles show that these particles behave differently during filtration. In contrast to NaCl particles, the filtration efficiency of WOx particles larger than the size of peak concentration depends on upstream particle concentration. This surprising behavior may be due to WOx's different morphology, which affects particle charging and as a result both filtration efficiency and measurement performance. For particles smaller than the mode size, the filtration efficiencies of WOx particles increase as the size of nanoparticles decrease down to 2.35 nm without showing thermal rebound.

Chapter 5 explains the theoretical study on thermal rebound of nanoparticles and determines the critical diameter below which thermal rebound may occur. The effects of gas properties and material properties on thermal rebound theory are investigated. When nanoparticles collide on the surface of solid filter media, it is more likely for plastic deformation to occur than elastic deformation. Therefore, nanoparticle filtration model should be based on the assumption of plastic deformation. A more accurate thermal rebound theory is developed by consideration of the effects of capillary and

electrostatic forces. Results show that the capillary force between a particle and the filter surface increases with the relative humidity level, leading to a reduction in the rebound of nanoparticles from the filter media. Thermal rebound of nanoparticles may only occur at extremely low relative humidity conditions (RH<5%).

Chapter 6 determines the performance of nanofibrous filters for nanoparticle removal. It introduces a method for characterizing nanofibrous filters and employing them for high quality filtration. The applied voltage, tip-to-collector distance, and deposition time of electrospinning process are all found to affect fiber size, solidity and thickness, and ultimately the quality factors of nanofibrous filters. Single layer filters made with a higher applied voltage, longer tip to collector distance and shorter deposition time correspond to greater filter quality factors. Employing multiple layers of thin nanofibrous filters greatly increases the filter quality factors of the PVA nanofibrous filters. After fabricating and testing for typical NaCl particles, PVA nanofibrous filters are employed to remove sub-3.3 WOx particle number concentration distributions in Chapter 7. The filtration behavior of nanoparticles through nanofibrous filters is investigated. Results show that the filtration efficiencies of sub-1.8 nm particles are strongly affected by their concentrations. The lower the particle concentration, the higher the filtration efficiency is. Moreover, the possibility of thermal rebound is shown to increase at lower particle concentrations. Finally, major findings and future directions are discussed in Chapter 8.

Chapter 2
Literature Review[1]

2.1 Summary

This chapter provides an overview of recent studies on the filtration of airborne nanoparticles. Theoretical methods for the calculation of single fiber efficiency are well described. The physical properties of nanoparticles and filters affect the performance of air filters; a better understanding of these parameters may help in the design of a high-performance filter for the effective separation of nanoparticles.

Classical filtration theory assumes that the efficiency of nanoparticle adhesion is at unity when nanoparticles strike a filter; however, it has been pointed out that small nanoparticles have a sufficiently high impact velocity to rebound from the surface upon collision, a mechanism called thermal rebound. Thus, according to the thermal rebound theory, the adhesion efficiency of nanoparticles decreases if their size is reduced. However, this phenomenon has not yet been observed in experiments and uncertainties still remain in thermal rebound.

Existing conventional filters are effective for particles larger than 300 nm; however, their performance is not sufficient for smaller particles. Nanofibrous filters which are conventionally produced by electrospinning may effectively be employed for nanoparticle removal. This chapter describes recent studies in which nanofibrous filters are used for nanofiltration.

2.2 Nanoparticle

Nanoparticles are particles with at least one dimension less than 100 nm. Airborne nanoparticles are sometimes referred to as nanoaerosols or ultrafine particulate matter. Nanoaerosols comprise over 95% of particulate matter when the particle number concentration is considered (Whitby 1978). This fact

[1] A similar version of this chapter was published as:

Givehchi, R., and Tan, Z. (2014). An Overview of Airborne Nanoparticle Filtration and Thermal Rebound Theory. *Aerosol and Air Quality Research*, 14:45-63.

emphasises the importance of measuring nanoparticle number concentration rather than their mass concentration. Nanoparticles have a large surface area to volume ratio, which leads to a higher surface reactivity and other unique properties (Paur et al. 2011). Surface area is a widely accepted property in studies of the toxicity of nanoparticles (Oberdörster et al. 2005).

Airborne nanoparticles can be generated from diverse sources but are produced primarily in combustion (Donaldson et al. 2005) and nanotechnology applications. The examples of nanoparticle combustion sources are transportation (Buseck and Adachi 2008; Lim et al. 2009; Lim et al. 2008; Yin et al. 2012), indoor fumes, smoking (Hofmann et al. 2009; Van Dijk et al. 2011), cooking (Torkmahalleh et al. 2012; Wallace et al. 2004), heating (Jung et al. 2006), biomass burning (Weimer et al. 2009), etc. Nanoparticles are produced from other sources as well such as from polymers (Motzkus et al. 2012; Tsai et al. 2008), cleaning, laser printers (Wang et al. 2011b), photocopiers, agriculture (Buseck and Adachi 2008) and welding. Nanoparticles are also generated from the applications of nanotechnology, in which their small size is essential, such as drug delivery, injections, inhalable medicines and tracers (Allen and Cullis 2004; Jawahar and Reddy 2012; Tiwari et al. 2012).

As the concentrations of nanoparticles increase with the development of nanotechnology, concerns have arisen with respect to the potential negative impact on human health. Nanoparticles can cause adverse health effects due to the direct action of the particles or acting as carriers of toxic elements (Elsaesser and Howard 2012; McKenna et al. 2008; Oberdörster et al. 2005; Wang and Pui 2011). Because nanoparticles are not removed by the upper respiratory tract, they are inhaled into the deeper areas. Their rather high deposition (more than 90%) in the alveolar region or other respiratory tract regions leads to their subsequent entry into the blood stream (Castellano et al. 2009; Marra et al. 2010; Oberdorster et al. 1995; Tsai et al. 2012). The small size and large surface area of nanoparticles enable significant interaction with biological systems (Kreyling et al. 2006b; Oberdorster et al. 1995; Oberdörster et al. 2007; Roduner 2006). As a result, exposure to nanoparticles may cause numerous adverse health effects, such as ischemic heart disease, cardiovascular diseases, stroke, chronic bronchitis, asthma, and respiratory tract infections (Lin et al. 2009; Mengersen et al. 2011).

Filtration is the most common and simplest method of removing particulate matter from the air. Particles are deposited and captured upon collision with the surface of the filter media, due to the

adhesion between particles and the surface. Various types of filters are used in different applications for air cleaning, with the ones most commonly used being membrane and fibrous filters.

The fundamental mechanisms of air filtration have been validated using micron particles; however, the mechanisms associated with airborne nanoparticles remain uncertain. For decades, nanoparticles have been considered to be captured by a filter surface by Brownian motion. However, recent studies have pointed out that those small nanoparticles striking a filter surface could rebound if the amount of initial kinetic energy of the approaching particle surpasses that of the adhesion energy between the particle and the surface (Dahneke 1971; Wang and Kasper 1991). Nanoparticles are so small that they approach the size of molecules and may behave like a gas molecule upon impaction. Wang and Kasper (1991) assumed that a nanoparticle strikes a surface with an impact velocity following the Maxwell-Boltzmann distribution, according to which the critical velocity of a nanoparticle is defined as that below which a particle can rebound from the surface. Consequently, filtration efficiency was thought to decrease for such small particles due to the thermal rebound. Uncertainties are still associated with the occurrence of thermal rebound in experimental and theoretical studies. A number of assumptions underline in thermal rebound theory: consideration of neutral particles, a Maxwell-Boltzmann distribution of the particle velocity, no energy loss, elastic impaction, normal impaction, and smooth surfaces. A question arises here if the consideration of these assumptions is applicable for airborne nanoparticles.

In the last few decades, there have been a great amount of publications that focused on nanoparticle filtration and thermal rebound. Advances in this area of research deserve a systematic overview. This chapter provides an overview of nanoparticle filtration theory and the corresponding parameters that affect nanoparticle filtration efficiency; the analytical methods of developing thermal rebound theory for airborne nanoparticles, including a description of the effect of thermal rebound on filtration efficiency; and an in-depth discussion of the knowledge gaps related to nanoparticle filtration and thermal rebound. The conclusion to be derived from this analysis is that a great deal of uncertainty remains with respect to nanoparticle filtration.

2.3 Nanoparticle Filtration

The properties of nanoparticles and filter media could affect the performance of an air filter. Particle filtration efficiency is calculated based on the efficiency of a single fiber. Several attempts in laboratory settings have been made to calculate the single fiber efficiency associated with a variety of particle deposition mechanisms of particles. Of the developed models, only a few can be used as a means of calculating single fiber efficiency for nanoparticle removal. The following discussion is divided into two sections. Theoretical methods of calculating single fiber efficiency for nanoparticles are first presented, followed by an examination of the effects of numerous parameters, such as humidity and particle shape on nanoparticle filtration efficiency.

2.3.1 Calculation of nanoparticle filtration efficiency

The filtration efficiency (η) is expressed as a function of single fiber efficiency (E) (Hinds 1999):

$$\eta = 1 - \exp\left[\frac{-4\alpha EL}{\pi d_f(1-\alpha)}\right] \tag{2-1}$$

where α is the solidity of the filter, L is the thickness of the filter, and d_f is the fiber diameter. This equation was obtained theoretically by correlation between single fiber efficiency and total efficiency of a filter. Single fiber efficiency is the fraction of particles deposited on a unit length of fiber which is normal to the air flow direction. Single fiber efficiency is based on the consideration of all the individual deposition mechanisms and overestimates the overall efficiency, because particles captured may be counted more than once. It is assumed that a particle is collected by a fiber upon collision. For nanoparticles, diffusion and interception are the most important.

Diffusion is the primary mechanism of nanoparticle deposition on surfaces. The single fiber efficiency based on diffusion mechanism is a function of Peclet number (Pe), which is defined as

$$Pe = \frac{d_f U}{D} \tag{2-2}$$

where U is the aerosol flow velocity, and D is the diffusion coefficient.The diffusion coefficient of particles with a low Reynolds number in air is the function of the particle diameter (d_p) (Hinds 1999)

$$D = \frac{K_b T C_c}{3\pi\mu d_p} \tag{2-3}$$

where K_b is Boltzmann's constant $1.38 \times 10^{-23} J/K$, T is temperature, μ is air viscosity, and C_c is the Cunningham coefficient, which indicates the non-continuum interaction between the particles and the carrier gas. Nanoparticles are small enough to approach the mean free path of a gas under normal conditions; the Cunningham coefficient is thus used as a means of including consideration of the slip condition in the gas flow (Allen and Raabe 1985):

$$C_C = 1 + Kn_P \left[1.257 + 0.4 \exp\left(-\frac{1.1}{Kn_P}\right)\right] \tag{2-4}$$

where Kn_P is the particle Knudsen number, which is calculated as the ratio of the mean free path of the gas (λ) and the particle radius as follows:

$$Kn_P = \frac{2\lambda}{d_p} \tag{2-5}$$

The Knudsen number is used for determining the validation of the flow continuity assumption in the Navier-Stokes equation. For nanoparticles, the continuum flow assumption fails and the flow becomes a free molecular, which means that the mean free path of molecules is much larger than the nanoparticle diameter. In this case, each molecule travels a number of times at many length scales of the nanoparticle before collision with other molecules (Przekop and Gradoń 2008).

The diffusion coefficient of a neutral nanoparticle in the range of 0.5 nm to 2 nm is (Leob 1961)

$$D_n = \frac{0.815 V_r}{12\pi N \left(d_g + d_p\right)^2} \sqrt{1 + \frac{m}{M}} \tag{2-6}$$

where V_r is the root mean square velocity of the gas (502 m/s at STP), d_g is the gas molecule diameter (0.37 nm), N is the number concentration of gas molecules ($2.45 \times 10^{-25} /m^3$ at STP), m is the molecular weight of the carrier gas (28.96 for air at STP), and M is the molecular weight of the nanoparticles. The molecular weight of the particles is much larger than that of the air molecules, so the square root term can be neglected (Ichitsubo et al. 1996). For singly charged nanoparticles, Eq.(2-6) will be changed to (Ichitsubo et al. 1996)

$$D = \frac{D_n}{1 + \frac{0.402e^2\left(d_g\right)^3}{8K_b\,T\left(d_g + d_p\right)^4}} \tag{2-7}$$

The interception mechanism is more effective when particles approach a fiber within a one-particle radius distance (Hinds 1999). The efficiency is a function of interception parameter (R), which is defined as

$$R = \frac{d_P}{d_f} \tag{2-8}$$

Single fiber efficiencies based on consideration of Brownian diffusion, interception and interception of diffused particles are given in Table 2-1.

Table 2-1. Single fiber efficiency due to Brownian diffusion and interception

Single fiber efficiency due to Brownian diffusion		
Pich 1965	$E_D = 2.27\,Ku^{-1/3}Pe^{-2/3}(1 + 0.62Kn_f Pe^{1/3}Ku^{-1/3})$	$Ku = -0.5ln\alpha - 0.75 - 0.25\alpha^2 + \alpha$ $Kn_f = \frac{2\lambda}{d_f}$
Stechkina 1966	$E_D = 2.9\,Ku^{-1/3}Pe^{-2/3} + 0.624Pe^{-1}$	boundary layer analysis
Krish and Stechkina 1978	$E_D = 3.2\,(Ku + \tau Kn_P)^{-1/2}(\tau Kn_P)^{1/2}Pe^{-1/2}$	Gas slip if $\delta_1 = \left(\frac{2(\mathrm{Ku} + \tau\mathrm{Kn})}{\mathrm{Pe}}\right)^{1/3} < \mathrm{Kn}$ δ_1 is the boundary layer length charectrstics τ is a coefficient that is dependent on a gas-fiber interaction and it is assumed to be unity
Kirsch and Fuchs 1968	$E_D = 2.7Pe^{-2/3}$	No gas slip $0.01<\alpha<0.15$
Lee and Liu 1982b	$E_D = 2.6\left(\frac{1-\alpha}{Ku}\right)^{1/3} Pe^{-2/3}$	No gas slip
Lee and Liu 1982b	$E_D = 1.6\left(\frac{1-\alpha}{Ku}\right)^{1/3} Pe^{-2/3}$	Fibers are not prependicular to the flow direction and are not uniform distributed
Liu and Rubow 1990	$E_D = 1.6\left(\frac{1-\alpha}{Ku}\right)^{1/3} Pe^{-2/3}C_d$	Gas slip

		$C_d = 1 + 0.388Kn_f\left[\frac{(1-\alpha)Pe}{Ku}\right]^{1/3}$
Payet et al. 1992	$E_D = 1.6\left(\frac{1-\alpha}{Ku}\right)^{1/3} Pe^{-2/3} C_d C_{d'}$	Gas slip $C_{d'} = \left[1 + 1.6\left[\frac{1-\alpha}{Ku}\right]^{1/3} Pe^{-\frac{2}{3}} C_d\right]^{-1}$
Hinds 1999	$E_D = 2Pe^{-2/3}$	No gas slip
Wang et al. 2007b	$E_D = 0.84Pe^{-0.43}$	Gas slip
Single fiber efficiency due to interception		
Krish and Stechkina 1978	$E_R = \frac{1+R}{2Ku}[2\ln(1+R) - 1 + \alpha + \left(\frac{1}{1+R}\right)^2\left(1-\frac{\alpha}{2}\right) - \frac{\alpha}{2}(1+R)^2]$	No gas slip
Lee and Gieseke 1980	$E_R = \left(\frac{1-\alpha}{Ku}\right)R^2(1+R)^{\frac{-2}{3(1-\alpha)}}$	No gas slip
Pich 1966a	$E_R = \frac{(1+R)^{-1} - (1+R) + 2(1+1.996Kn_f)(1+R)\ln(1+R)}{2(-0.75 - 0.5ln\alpha) + 1.996Kn_f(-0.5 - ln\alpha)}$	No gas slip
Lee and Liu 1982b	$E_R = \left(\frac{1-\alpha}{Ku}\right)\frac{R^2}{1+R}$	No gas slip $R < 0.2, \alpha < 0.5$
Lee and Liu 1982b	$E_R = 0.6\left(\frac{1-\alpha}{Ku}\right)\frac{R^2}{1+R}$	Fibers are not prependicular to the flow direction and are not uniform distributed
Liu and Rubow 1990; Payet et al. 1992	$E_R = 0.6\left(\frac{1-\alpha}{Ku}\right)\frac{R^2}{1+R}C_r$	Gas slip $C_r = 1 + \frac{1.996Kn_f}{R}$
Single fiber efficiency due to interception of diffused particles		
Stechkina and Fuchs 1966	$E_{DR} = \frac{1.24R^{2/3}}{(ku.Pe)^{1/2}}$	$Ku/Pe < 0.024$

A number of studies have been conducted in order to validate the models developed for calculating nanoparticle filtration efficiency as listed in Table 2-1. For example, Lee and Liu (1982) developed theoretical equations to express single fiber efficiency, based on consideration of Brownian diffusion ($E_D = 2.6\left(\frac{1-\alpha}{Ku}\right)^{1/3} Pe^{-2/3}$) and interception ($E_R = (\frac{1-\alpha}{Ku})\frac{R^2}{1+R}$); however, these equations do not account the effect of gas slip. The experimental validation of the equations was based on a real filter with irregularities in fiber direction and non-uniformly distributed fibers, which showed that the

numerical coefficients for diffusion and interception should be replaced by 1.6 and 0.6, respectively. Liu and Rubow (1990) later modified Lee and Liu's (1982) corrected equation by including the gas slip effect and correction factors of C_d and C_r for Brownian diffusion and interception, respectively. It was observed that the filtration efficiency of nanoparticles with a low Peclet number is greater than unity. In 1992, Payet *et al*. modified Liu and Rubow's (1990) diffusion efficiency equation by adding an additional correction factor ($C_{d'}$) to lower the efficiency value to less than unity. An experimental study was also employed as a means of validating the previous correction in particle size range from 80 nm to 400 nm (Payet et al. 1992).

An experimental study by Podgórski *et al*. (2006), who employed sebacic acid-bis ester particles ranging from 10 nm to 500 nm, showed that if the mean diameter of the fiber is considered, the theoretical equations predicted by Payet *et al*. (1992) for both diffusion and interception slightly overestimate the measured filtration efficiency data; however, the theoretical equations are in good agreement with experimental studies if a resistance-equivalent fiber diameter is considered (Podgórski et al. 2006). Steffens and Coury (2007) employed a high-porosity filter to collect NaCl particles in the range of 8.5 nm to 94.8 nm at aerosol flow velocities of 0.03 m/s to 0.25 m/s. The measured filtration efficiency showed that the equation predicted by Lee and Liu (1982) for both diffusion and interception mechanisms underestimated the experimental data, and that those predicted by Liu and Rubow (1990) overestimated the experimental data (Steffens and Coury 2007a). Wang *et al*. (2007) calculated filtration efficiency based on a Brownian diffusion of HF-type and HE-type filters with effective fiber diameters of 1.9 µm, 2.9 µm, 3.3 µm, and 4.9 µm and packing densities of 0.039-0.047, 0.049, and 0.05, using silver particles in the range of 3 nm to 20 nm and NaCl particles in the range of 15 nm to 400 nm at aerosol flow velocities of 5.3 cm/s, 10 cm/s, and 15 cm/s. The results showed that the filtration efficiency measured experimentally is in good agreement with the equation predicted by Stechkina (1966) if the Peclet number is larger than 100 and in good agreement with Krish and Stechkina's (1978) equation for a Peclet number in the order of unity. The authors developed an additional equation that is a function of a Peclet number ($E_D = 0.84Pe^{-0.43}$) and that is in good agreement for all Peclet numbers values.

Wang *et al*. (2008) employed four filters, with solidities of 0.134, 0.104, 0.059, and 0.034, and tested the penetration of silver particles in the range of 3 nm to 20 nm and of NaCl particles in the range of

20 nm to 300 nm at face velocities of up to 40 cm/s. The experimental data agreed well with the data calculated based on Brownian diffusion and interception predicted by Pich (1966) for particles larger than 20 nm (Wang et al. 2008). Another experimental study, which employed neutral NaCl nanoparticles with diameters down to 10 nm at filtration velocities of 0.03 m/s to 0.5 m/s, demonstrated that the single fiber efficiency predicted by Kirsch and Fuchs (1968) is in good agreement for wire screens, and that the efficiency predicted by Wang *et al*. (2007) is in good agreement for a real filter (Yamada et al. 2011). Gomez *et al*. (2012) employed a mixed screen diffusion battery containing two aluminum screens surrounding a gold screen. The penetration of a sub-10 nm NaCl particle through the diffusion battery was measured, and the results showed that the single fiber efficiency predicted by Kirsch and Fuchs (1968) agrees well with that measured in the experiment, which was based on consideration of the equivalent fiber diameter of the diffusion battery (Gómez et al. 2012).

Validation of filtration models has been done for nanoparticle filtration efficiency in laboratory settings and studies of real filters using in situ test methods are lacking (e.g., Rim et al. 2010; Stephens and Siegel 2013). In conclusion, each theoretical study is best used in a specific situation related to the particular characteristics of the filter and particle, but none developed thus far is accurate enough for use with a wide range of particle and filter parameters.

Another factor that influences filtration performance is the charge states of the particles (Chen and Huang 1998). Most particles and filters may carry ions. It has been shown that filtration efficiency has been found to be much lower for uncharged particles than for highly charged ones; for smaller particle size, because of the lower charging efficiency the discrepancy between the removal of charged and uncharged particles decreases (Kim et al. 2006) and the electrostatic forces may not play an important role to remove nanoparticles (Wang and Otani 2013). Thus, the effective mechanisms for removing nanoparticles with low charged level are Brownian diffusion and interception that were completely discussed.

Another approach to the calculation of single fiber deposition efficiency is tracing the trajectory of a particle and determining the collision of the particle to the surface of a fiber. The Langevin equation is employed to describe the motion of nanoparticles, and Brownian dynamics algorithm is used to integrate the Langevin equation in order to calculate the single fiber efficiency. A detailed description of this algorithm is available in a number of earlier publications (Bałazy and Podgórski 2007).

A filter quality factor (Q_F) is used as a measure of the performance level of filters; pressure drop (ΔP) and particle collection efficiency (η) are the key parameters that determine the value of this factor. The best filter has the highest removal efficiency and lowest pressure drop. The quality factor is calculated as (Hinds 1999)

$$Q_F = \frac{-\ln(1-\eta)}{\Delta P} \tag{2-9}$$

The pressure drop occurs because of the resistance of the fiber to the flow. The relationship between the pressure drops and the face velocity is linear (Davies 1950):

$$\Delta P = \frac{64\mu U_0 L}{d_f^2}\alpha^{\frac{3}{2}}(1+56\alpha^3) \tag{2-10}$$

where α is the solidity of the filter, L is the thickness of the filter, d_f is the fiber diameter, U_0 is the face velocity, and μ is the gas viscosity. Eq.(2-10) was originally developed for a fiber diameter in the range of 1.6 μm to 80 μm and a filter solidity in the range of 0.006 to 0.3 (Davies 1950). The equation was later validated for smaller filter diameters in the range of 98 nm to 1.54 μm and filter solidities in the range of 0.039 to 0.084 (Hung and Leung 2011; Werner and Clarenburg 1965). The pressure drop is proportional to the thicknesses of the filter and its face velocity and is inversely proportional to the square of the diameter of the fiber. Considering the aerodynamic slip in the gas, the pressure drop is (Pich 1966b):

$$\Delta P = \frac{16\mu U_0 L\alpha(1+1.996Kn_f)}{d_f^2[Ku+1.996Kn_f(-0.5ln\alpha-0.25+0.25\alpha^2)]} \tag{2-11}$$

Based on classical filtration theory and Brownian diffusion, the removal efficiency for nanoparticles is significantly high and decreases with increased particle size due to lower levels of Brownian diffusion.

However, studies indicate that small nanoparticles may rebound from the surface upon collision due to their high impact velocities, which causes a decrease in filtration efficiency. Thus, it is likely that another mechanism is associated with particle deposition, one that has adverse effects on small nanoparticles with respect to thermal rebound. This mechanism must be considered in any investigation of filtration efficiency.

2.3.2 Advances in nanoparticle filtration efficiency

It has been shown that nanoparticle shape and material could affect its filtration efficiency. Particle shape affects volume, surface area, and motion, with a consequent impact on the rate of filter cake formation, and filtration efficiency. Most particles are non-spherical, and their shape affects the drag force, settling velocity, and electrical mobility (Intra and Tippayawong 2011). Studies show that cubic particles provide lower particle removal efficiency than do aerodynamically similar spheres. The contact areas following collisions between the filter surface and spherical particles travelling in divergent directions are the same; however, this area may be different for other particle shapes, which alter particle collection efficiency (Boskovic et al. 2005). Spherical particles may either slide or roll upon collision; however, cubic particles could either slide or tumble, increasing the probability of detachment from the surface (Boskovic et al. 2005). An experimental study has determined the effect of particle shape on filtration efficiency. At a filtration velocity of 5 cm/s to 20 cm/s, three particle shapes in the range of 50 nm to 300 nm in diameter were considered: spherical PSL, perfect MgO cubes, and transitional NaCl cubes with rounded corners. The finding showed that spherical particles result in greater removal efficiency, followed by NaCl and MgO. The rounded corners or sharp edge of the NaCl particles cause them to roll or tumble, respectively, upon contact with the surface (Boskovic et al. 2008). Particle shape is thus a significant factor that affects dust cake formation and filtration efficiency (Nazarboland et al. 2007).

The particle material could affect the efficiency of the filter because of differences in shape, densities, hardness, electrostatic forces, and chemical reactions. Numerous studies have been conducted with respect to the effect of different kinds of particle materials: sodium chloride (Bałazy et al. 2004; Heim et al. 2005), diethylhexyl phthalate (DEHP) (Bałazy et al. 2004; Japuntich et al. 2007), silver (Kim et al. 2007), graphite (Golanski et al. 2010), and titanium dioxide (Golanski et al. 2010). However, these studies have revealed no obvious linked between the type of aerosol and filtration efficiency, and the removal efficiency discrepancy attributes to the difference in particle shape.

It is observed that increasing a level of humidity increases removal efficiency of the filter for micron size particles (Brown 1993; Miguel 2003); however, this application for nanosized particles is still in doubt. Kim *et al*. 2006 tested the filtration efficiency for sub-100 nm neutralized NaCl particles at a face velocity of 2.5 cm/s and at different humidity conditions: 0.04 %, 1.22 %, and 92 %. The results

showed for sub-100 nm particles, that filtration efficiency is independent of relative humidity, because capillary force has no effect on nanoparticles adhesion (Kim et al. 2006). Montgomery *et al*. 2015 showed that the filtration efficiency of NaCl nanoparticles is independent of relative humidity for clean filters; however, it is not the case for loaded filters. Relative humidity has adverse effects on the filtration efficiency of NaCl nanoparticles for loaded filters (Montgomery et al. 2015).

2.4 Thermal Rebound

In the past, it was considered that airborne nanoparticles were captured by a surface due to Brownian diffusion; however, Wang and Kasper (1991) suggested the possibility of thermal rebound for particles smaller than 10 nm. When a particle impacts with the surface, its initial kinetic energy is transformed to elastic deformation, plastic deformation or heat. If all of the initial kinetic energy is consumed, the particle stops and sticks to the surface; otherwise, if the energy stored as elastic deformation is high enough to overcome the adhesion energy, the particle rebounds from the surface. The adhesion of a particle to a surface is thus related to its impact velocity. For impact velocities lower than a critical velocity, particles stick to the surface, and at impact velocities higher than the critical level, they rebound from the surface (Figure 2-1). The following section is divided into analytical work and experimental work regarding thermal rebound of nanoparticles.

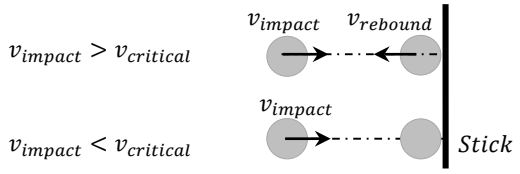

Figure 2-1. Particle impaction with a frictionless surface

2.4.1 Analytical work

Wang and Kasper (1991) developed a thermal rebound theory by consideration of impact velocity and critical velocity of nanoparticles. The particle impact velocity was characterized by thermal velocity, which is based on the Maxwell-Boltzmann distribution in a Brownian motion (Brown 1993). A Maxwell-Boltzmann distribution describes the speed of molecules in an ideal gas flow characterized by thermal velocity. The molecules move randomly, rapidly, and freely without any interaction with

other molecules; however, brief elastic collisions may occur (Mandl 1988). The probability density function of molecule speed in a gas is expressed according to a Maxwell-Boltzmann distribution as

$$f(v_{im}) = 4\pi {v_{im}}^2 \left(\frac{m}{2\pi K_b T}\right)^{3/2} exp\left(-\frac{m{v_{im}}^2}{2K_b T}\right) \quad (2\text{-}12)$$

where $f(v_{im})$ is the probability density function, v_{im} is the impact velocity of the molecule, K_b is Boltzmann constant ($1.38 \times 10^{-23}\ J/K$), T is the temperature, and m is the mass of the gas molecule. The mean impact velocity of the molecule ($\bar{v}_{im}$) is

$$\bar{v}_{im} = \sqrt{\frac{8K_b T}{\pi m}} \quad (2\text{-}13)$$

replacing the molecular mass with the particle mass based on consideration of particle density (ρ_P) and diameter (d_P), the mean impact velocity of a particle is defined as follows:

$$\bar{v}_{im} = \left(\frac{48K_b T}{\pi^2 \rho_P d_P^3}\right)^{1/2} \quad (2\text{-}14)$$

A Maxwell-Boltzmann distribution determines the speed of gas molecules that are moving freely in the flow; however, particles may not move freely without interaction with other particles. In reality, the particle resistance in a gas flow and the viscosity of the flow cause decreases in particle speed that have not been considered in literatures. Nanoparticles could agglomerate and changes in particle size and particle number concentration that may alter their speed distribution. Thus, a Maxwell-Boltzmann distribution might not be the best approach for the calculation of the thermal impact velocity of nanoparticles, and it is one of the analytical sources of error for thermal rebound theory.

The particle critical velocity is defined based on the conservation of energy, in which, the summation of the kinetic and potential energy of a particle prior to and after a collision remains the same (Dahneke 1971):

$$KE_{nr} + E_{nr} = (KE_{ni} + E_{ni}).\, e^2 \quad (2\text{-}15)$$

where KE and E indicate the kinetic energy and the potential energy of a particle, respectively. nr and ni refer to the rebound particle and the impact particle, respectively, and e is the coefficient of restitution. When the particle mass and velocity are considered, the equation changes to

$$\frac{v_{nr}}{v_{ni}} = \left(e^2 - \frac{E_{nr} - E_{ni}.e^2}{mv_{ni}^2/2}\right)^{1/2} \quad (2\text{-}16)$$

If v_{nr} approaches zero, the particle will be captured, and the critical velocity (v_{cr}) is thus defined as

$$v_{cr} = \left[\frac{2}{me^2}\left(E_{nr} - E_{ni}.e^2\right)\right]^{1/2} \quad (2\text{-}17)$$

Two situations of the equation above may exist:

$$E_{nr} = E_{ni} = E \rightarrow v_{cr} = \left[\frac{2E(1-e^2)}{me^2}\right]^{1/2} \quad (2\text{-}18)$$

$$E_{nr} \gg E_{ni} \rightarrow v_{cr} = \left(\frac{2E_{nr}}{me^2}\right)^{1/2} \quad (2\text{-}19)$$

Wang and Kasper (1991) employed Eq.(2-19) to calculate the critical velocity, above which thermal rebound occurs. It was assumed that the potential energy of the particle after impaction is significantly greater than the potential energy before impaction and that it is equal to the particle-surface adhesion energy. However, nanoparticles may have negligible potential energy before and after impaction because of their small size and the assumption might be invalid.

Particle impaction is characterized by a coefficient of restitution that is the ratio of the rebound velocity to the impact velocity. Models have been developed for predicting the coefficient of restitution (Stevens and Hrenya 2005; Tabor 1948; Wu et al. 2003), based on which the amount of the energy loss can be estimated. Energy loss could occur during plastic deformation, adhesion, friction and vibration.

A number of researchers have predicted the energy loss to elastic deformation when a particle strikes a surface and have shown that a small fraction of the kinetic energy is lost (Hunter 1957; Hutchings 2001). The coefficient of restitution for impaction of different type of micron particles to a hard smooth surface was in the range of 0.73 to 0.84 (Wall et al. 1990). In previous theoretical studies of thermal rebound, the coefficient of restitution was assumed to be near unity for small particles (Dahneke 1971; Wang and Kasper 1991). However, for nanometer-sized particles the coefficient of restitution may not be unity and the absolute value is unknown (Ayesh et al. 2010). Earlier studies show that the coefficient of restitution is dependent on the impact velocity as well as the material and surface of a nanoparticle (Ayesh et al. 2010; Jung et al. 2010; Rennecke and Weber 2013a; Sato et al. 2007). The coefficient of

restitution is small for impact velocities close to the critical velocity, which leads to small rebound velocities (Rennecke and Weber 2013a). The coefficient of restitution is also dependent on the mechanical properties and hardness of nanoparticles and surface. The coefficient of restitution is smaller for impaction between a harder particle and a softer surface, as stored energy transfers to lost energy due to the difference between the mechanical properties of the nanoparticle and the surface (Sato et al. 2007). The molecular dynamic simulation for collision of nanoparticles at room temperature showed that nanoparticles in the range of 0.5 to 2 nm did not rebound from the surface due to their significant energy loss (Sato et al. 2007). The molecular dynamic simulation used by Ayesh et al. (2010) confirmed the small coefficient of restitution for nanoparticles, which is less than 0.6 for solid nanoparticles. Therefore, the coefficient of restitution for a nanoparticle has a small value that should be taken into account in thermal rebound studies.

A variety of theories have been developed for calculating the adhesion energy between a particle and a surface based on elastic or plastic impaction. Common elastic adhesion energy models are the Bradley-Hamaker (BH), Hertz, Johnson-Kendall-Roberts (JKR), and Derjaguin-Muller-Toporov (DMT), and plastic adhesion energy models are represented by the Maugis-Pollock (MP), and Weir-McGavin (WM), as described in the following subsections.

2.4.1.1 BH elastic adhesion energy

The BH theory is used to consider van der Waals interactions between two rigid spheres (Bradley 1932). The BH model assumes a point of contact between bodies due to Van der Waals forces and fails to consider the adhesion force resulting from the impaction. The interaction energy between spherical particles with a diameter of d_p and a flat surface is given by

$$E_{ad} = \frac{A_H}{12}\left[\frac{d_p}{Z_0} + \frac{d_p}{d_p + Z_0} + 2\ln\left(\frac{Z_0}{d_p + Z_0}\right)\right] \tag{2-20}$$

where A_H is the Hamaker constant between a particle and a surface, which are available in literatures (Tsai et al. 1991), and Z_0 is the equilibrium distance between bodies (0.4 nm). The Hamaker constant is typically in the order of 10^{-19} to 10^{-20} joules. As the particle approaches the surface, the adhesion energy is given as

$$E_{ad} = \frac{A_H d_p}{12 Z_0} \qquad Z_0 \to 0 \tag{2-21}$$

Eq.(2-21) is valid only for large particles and it does not apply to nanoparticles. The Hamaker constant between the particle and the surface is given as

$$A_H = \sqrt{A_{H1} A_{H2}} \tag{2-22}$$

where A_{H1} and A_{H2} are the Hamaker constants of a particle and a surface, respectively.

Because the BH model ignored the specific adhesion energy between bodies, which plays an important role in nanoparticle adhesion, it is not suitable for calculating the adhesion efficiency of nanoscale materials.

2.4.1.2 Hertz elastic adhesion energy

Another model of the non-adhesive contact of a sphere on a plane with no surface forces was described by Hertz (1882), whose theory is based on a frictionless interface between the bodies, a flat surface, small strains in the elastic limit, a hemispherical pressure distribution in the contact area of the bodies, no pressure outside the contact area, and consideration of an elastic half-space solid. The adhesion energy (E_{ad}), the contact radius between bodies (a), and the deformation height (δ) in the Hertz model are given by

$$E_{ad} = \Delta\gamma \pi a^2 \tag{2-23}$$

$$a^3 = \frac{F R^*}{K^*} \tag{2-24}$$

$$\delta = \frac{a^2}{R^*} \tag{2-25}$$

where F is the external force, K^* is the composite Young's modulus, $\Delta\gamma$ is the specific adhesive energy, and R^* is the characteristic radius of two bodies with diameters of d_p and d_s:

$$K^* = \frac{4}{3\pi}(K_P + K_S)^{-1} \tag{2-26}$$

$$K_i = \frac{1 - v_i^2}{\pi E_i} \tag{2-27}$$

$$R^* = \left(\frac{2}{d_p} + \frac{2}{d_s}\right)^{-1} \tag{2-28}$$

where E_i is the elastic Young's modulus, v_i is the Poisson ratio of the material, and K_i is the mechanical constant of material.

$\Delta\gamma$ is the surface adhesive energy per unit contact area that accounts for the surface energy of both materials per contact area:

$$\Delta\gamma = \gamma_1 + \gamma_2 - \gamma_{12} \tag{2-29}$$

where $\gamma_1$and γ_2 are the adhesion components of surfaces that are equal for identical materials, and γ_{12} is the interaction adhesion energy between bodies, which is zero for smooth surfaces. Considering that the surface adhesive energy per unit area results from van der Waals forces, the adhesion energy can be presented as a Hamaker constant, as follows (Derjaguin et al. 1975; Xu and Willeke 1993):

$$\Delta\gamma = \frac{A_H}{12\pi Z_0^2} \tag{2-30}$$

According to Hertz theory, any surface interactions such as Van der Waals forces and adhesive interactions between bodies are not considered, and the application is restricted to small amounts of deformation and linear elasticity. The presence of an adhesion force causes the contact radius to be larger than that predicted by the Hertz model, and in the absence of a load, the contact radius is not zero, so a pull off force is required in order to separate the particle from the surface.

2.4.1.3 JKR elastic adhesion energy

Based on the Hertz theory (1896), Johnson, Kendall, and Roberts (1971) developed the JKR model for considering the surface adhesion energy between elastic solids inside the contact area (Johnson et al. 1971). The contact area between solids is significantly larger than that predicted by the Hertz model even at lower loads and is likely to be a constant contact diameter when the load approaches zero; however, the contact radius is smaller than that in plastic deformation models. The JKR model

considers the effect of adhesion energy and contact pressure inside the contact area. The contact radius between bodies is therefore given by the following equation:

$$a^3 = \frac{R^*}{K^*}\left[F + 3\Delta\gamma\pi R^* + \sqrt{6\Delta\gamma\pi R^* F + (3\Delta\gamma\pi R^*)^2}\right] \tag{2-31}$$

and the contact radius at zero applied force is changed to

$$a = \left(\frac{6\Delta\gamma\pi {R^*}^2}{K^*}\right)^{1/3} \tag{2-32}$$

It has been shown that the pull-off force is independent of the elastic and Young's modulus and is given as

$$F_{pull-off} = \frac{3}{2}\,\Delta\gamma\pi R^* \tag{2-33}$$

The contact radius in the JKR adhesion model can be changed to that of the Hertz model ($a^3 = \frac{FR^*}{K}$) if the surface adhesive energy is neglected ($\Delta\gamma = 0$).

2.4.1.4 DMT elastic adhesion energy

Derjaguin, Muller, and Toporov (1975) developed another adhesion model known as the DMT model, which included the consideration of the van der Waals contact interactions between solids inside the contact area. They found that the repulsive interaction forces between bodies cause deformation of the particles (Derjaguin et al. 1975). The effectiveness of the model has been proven for smaller and stiffer contact solids (Rahmat et al. 2012). The DMT model has been validated for micron particles; however, the impact mechanisms of nanoparticles might differ from those of micron particles because of the molecular interactions (Teodorescu and Rahnejat 2007). The main defect in this theory is that it neglects deformations outside the contact area (Maugis 2000). The contact radius (a), deformation depth (δ), and pull-off force are respectively given by

$$a^3 = \frac{R^*}{K^*}(F + 2\Delta\gamma\pi R^*) \tag{2-34}$$

$$\delta = \frac{a^2}{R^*} \tag{2-35}$$

$$F_{pull-off} = 2\Delta\gamma\pi R^* \tag{2-36}$$

In Eq.(2-34), at zero applied force, the contact radius changes to

$$a^3 = \left(\frac{2\Delta\gamma\pi R^{*2}}{K^*}\right)^{1/3} \tag{2-37}$$

Table 2-2 summarizes the BH, JKR, and DMT elastic models and their assumptions. As can be observed, the pull-off force in the JKR model differs from that according to the DMT or BH models because these models are used on two different sides of a Tabor parameter spectrum (Tabor 1977).

Table 2-2. Contact mechanical models

Model	Explanation	Pull-off force
JKR	Fully elastic, adhesion force	$P = 3/2\ \Delta\gamma\pi R^*$
BH	Fully elastic, van der Waals	$P = 2\ \Delta\gamma\pi R^*$
DMT	Fully elastic, adhesion force and van der Waals	$P = 2\ \Delta\gamma\pi R^*$

2.4.1.5 Tabor coefficient

The Tabor coefficient (μ) provides an explanation of the contradictions among the JKR, DMT, and BH elastic models (Tabor 1977). The Tabor coefficient is the ratio of the elastic displacement of surfaces to the effective range of surface forces at the pull-off point, and it indicates which model is applicable:

$$\mu = \frac{(R^*)^{\frac{1}{3}}(\Delta\gamma)^{\frac{2}{3}}}{Z_0(E^*)^{\frac{2}{3}}} \tag{2-38}$$

where E^* is reduced Young's modulus for a particle and a surface:

$$E^* = \frac{3}{4}K^* = \frac{1}{\pi(K_P + K_S)} \tag{2-39}$$

Accordingly, for small value of Tabor parameter, BH and DMT models, and for large Tabor parameter, JKR model is more applicable. As shown in Figure 2-2, the normalized pressure load ($\bar{P} = P/\pi wR$, where P is pull off force) varies continuously from 2, in the DMT model ($for\ \lambda < 0.1$, where λ is the elasticity parameter defined as $\lambda = 1.16\mu$), to 3/2, in the JKR model ($for\ \lambda > 5$) (Greenwood 1997; Johnson and Greenwood 1997; Muller et al. 1980; Tsai et al. 1991). The DMT theory is used for

hard materials, small radii, and low adhesion energies, and JKR model is applied for soft material, large radii, compliant spheres, and large adhesion energy (Maugis 2000).

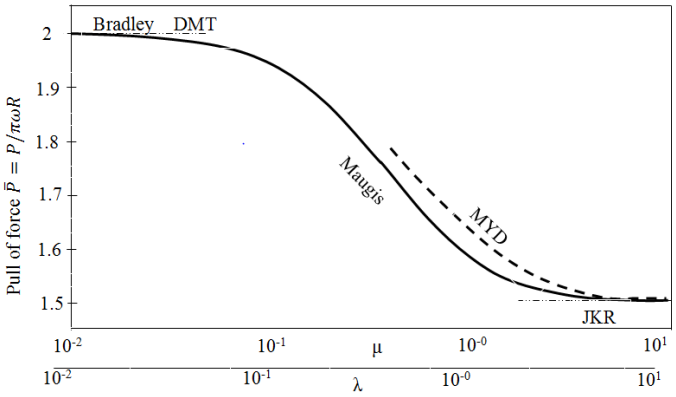

Figure 2-2. Variations in the normalized pressure load by elasticity parameter (λ) or the Tabor parameter (μ); courtesy of Johnson and Greenwood (1997)

Johnson and Greenwood presented the adhesion map and suitable model by dividing $\bar{P} - \lambda$ diagram into regimes based on elasticity parameter that correspond to different elastic models as shown in Figure 2-3 (Johnson and Greenwood 1997). This figure shows that the BH and DMT models are employed at low elasticity parameters; whereas, the JKR model is employed at higher elasticity numbers. The Maugis-Daugdale (M-D) equations are used for the transition between DMT and JKR adhesion energy models.

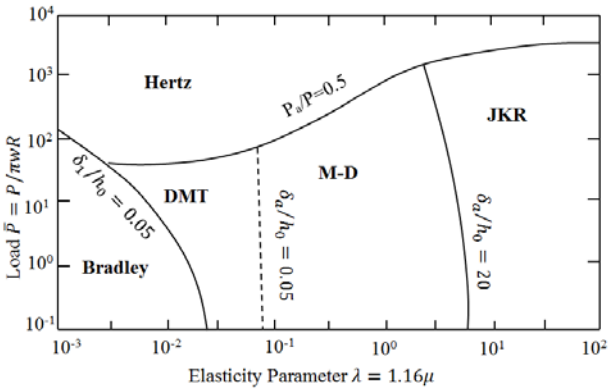

Figure 2-3. Adhesion map; courtesy of Johnson and Greenwood (1997)

2.4.1.6 MP plastic adhesion energy

The previous models considered elastic contact between materials; however, Krupp (1967) suggested that plastic deformation could occur in the inner circular region, and elastic deformation could occur in the outer one (Krupp 1967). The Maugis-Pollock (MP) plastic adhesion model is used for calculating the the adhesion energy between bodies upon plastic collision (Maugis and Pollock 1984). The contact area between bodies is determined through consideration of the hardness of the deformed material (H) and the specific adhesion energy ($\Delta\gamma$). The relation between the contact radius and the external force is given as

$$F = \pi a^2 H - 2\pi\Delta\gamma R^* \tag{2-40}$$

where F is the external load, and H is the hardness of the deformed solid. After complete plastic deformation, the mean pressure becomes constant, and the hardness can be calculated as $H = 3Y$, where Y is the elastic limit, or yield stress. When the external force is zero, the contact radius and pull-off force are respectively given by

$$a = \left(\frac{2\Delta\gamma R^*}{H}\right)^{1/2} \tag{2-41}$$

$$F_{pull-off} = 2\Delta\gamma\pi R^* \tag{2-42}$$

The particle critical velocity in a plastic regime can thus be calculated and compared with the impact velocity of particles with a wide range of diameters in order to determine the probability of the occurrence of thermal rebound.

2.4.1.7 WM plastic adhesion energy

A recent approach for calculating the critical velocity of nanoparticles in a plastic deformation regime is the Weir and McGavin (WM) method. Fully plastic deformation is assumed when spherical nanoparticles impact a much harder plane surface, which is justified for impact velocities greater than 10 m/s, and fully elastic impaction (JKR) is assumed during particle rebound. In this model, the yield stress is assumed to be constant for nanoscale materials. Based on this model, the critical velocity of the nanoparticles and pull-off force, respectively, are given as (Weir and McGavin 2008)

$$v_{Cr} = \left(\frac{4\Delta\gamma^2}{5.3^{\frac{1}{3}}\rho_P Y R^{*2}} \right)^{1/2} \tag{2-43}$$

$$F_{pull-off} = \frac{3}{2}\,\Delta\gamma\pi R^* \tag{2-44}$$

2.4.1.8 Elastic yield velocity

When a particle collides with the filter, the particle is compressed elastically until the yield pressure is reached; compression beyond this point leads to plastic deformation (John 1995). It has been shown that, once they begin to yield, the rate of plastic deformation of nanoparticles is greater than that of bulk bodies. This is due to the great hardness of the nanosized particles (Ayesh et al. 2010). Plastic deformation cannot be recovered as energy required for particle rebound; however, as the energy lost in plastic deformation increases, greater energy will be stored in a secondary elastic deformation that enables the particles to rebound (Xu et al. 1993).

The elastic yield velocity is used to define the plastic and elastic regimes of particle deformation upon collision, and the impaction changes continuously from elastic to plastic deformation because of the increases of the impaction velocity. For small nanoparticles with impact velocities greater than the elastic yield velocity, plastic deformation occurs, and for larger particles with impact velocities smaller than the elastic yield velocity, primary elastic deformation occurs. The elastic yield velocity can be described as follows (Xu and Willeke 1993):

$$v_y = \left(\frac{2\pi}{3K^*}\right)^2 \left(\frac{2}{5\rho_P}\right)^{1/2} Y^{5/2} \tag{2-45}$$

The elastic limiting velocity is dependent on the density, elastic strain limit and mechanical constant of the particle as well as the surface material with different mechanical constant. For different particles and filters, the elastic and plastic impaction regimes also differ. And this should be taken into consideration in the studies of thermal rebound theory.

Wang and Kasper (1991) employed BH (Eq.(2-21)) and JKR models (Eqs.(2-23),(2-32)) for calculating the adhesion energy between a spherical particle and a surface. The BH theory considers the van der Waals interactions and the point of contact between the particle and the surface; however,

the JKR theory takes into account the adhesion energy and the contact area between the particle and the surface. Due to the relatively minor differences between these theories, the JKR theory, which includes consideration of the finite contact area, was employed in Wang and Kasper's research for the calculation of the adhesion energy of the particle and the surface. As a result, the respective calculation of adhesion energy and critical velocity based on JKR theory are as follows:

$$E_{ad} = \Delta\gamma\pi a^2 = \left[\frac{81}{64}\pi^7 d_P^4 \Delta\gamma^5 \left(K_p + K_s\right)^2\right]^{1/3} \tag{2-46}$$

$$v_{cr} = \left[\frac{3^7\pi^4\left(K_p + K_s\right)^2\Delta\gamma^5}{\rho_p^3 d_p^5}\right]^{1/6} \tag{2-47}$$

A comparison of the impact velocity and the critical velocity as a function of particle diameter for steel particles approaching polystyrene filter led to the conclusion that thermal rebound occurs for sub-10 nm particles because of excessive impact velocity. The rebound is dependent on the mechanical constant and the specific adhesion energy. For particles greater than 10 nm, the impaction velocities are less than the critical velocity, so that the particles attach to the surface.

2.4.1.9 Adhesion efficiency

The effective single fiber efficiency (E_{eff}) based on consideration of the thermal rebound, calculated as

$$E_{eff} = E.\varepsilon \tag{2-48}$$

where E is the total single fiber efficiency and ε is the adhesion efficiency. In the conventional filtration theory, adhesion efficiency is considered to be a unity value; however, the value is actually less than one if thermal rebound occurs. The adhesion efficiency due to the thermal rebound (ε) is defined as follows (Wang and Kasper 1991):

$$\varepsilon = \int_0^{v_{cr}} f(v_{im})dv_{im} \Big/ \int_0^{\infty} f(v_{im})dv_{im} \tag{2-49}$$

With a Boltzmann distribution for the particle impact velocity the equation becomes

$$\varepsilon = \int_0^{1/TR} \left(\frac{32}{\pi^2}\right) x^2 \exp\left(-\frac{4x^2}{\pi}\right) dx \qquad (2\text{-}50)$$

where TR is the thermal rebound coefficient that is the ratio of the mean impact velocity and the critical velocity ($TR = \bar{v}_{im}/v_{cr}$). Calculating single fiber efficiency based on consideration of Brownian diffusion and interception and using the Lee and Liu (1982) equation, which does not consider gas slip for nanoparticles, results in an efficiency value greater than 1 for nanoparticles with diameters of approximately sub-10 nm.

Recently, Mouret *et al*. (2011) employed a Tabor parameter to demonstrate that the BH and JKR models used by Wang and Kasper are associated with the extremes of the Tabor spectrum. They concluded that for sub-100 nm particles, the Tabor value is less than 0.1, and the BH theory should be used for calculating the adhesion energy (Johnson 1997; Mouret et al. 2011). The researchers also pointed out that the approximation of BH adhesion energy equation used by Wang and Kasper was inaccurate for sub-20 nm particles. Thus, they have employed Eq.(2-21) and showed that no thermal rebound occurs with steel nanoparticles down to 1 nm approaching copper filter, and they also demonstrated that the thermal rebound effect increases as the temperature rises; however, the temperature must be as high as 1000 K for thermal rebound to be observed (Mouret et al. 2011). The modification theory of Mouret *et al*. is a reasonable conclusion in light of the reasons why most researchers are unable to verify thermal rebound.

As discussed earlier, adhesion energy models were employed in the calculation of particle critical velocity; however, the adhesion energy is dependent on material properties (Tsai et al. 1991) such as Hamaker constant, mechanical constant of materials, surface adhesive energy per unit contact area and elastic yield stress. Some of these parameters are not available for nanosized particles depending on the type of materials (Hartland 2004); this affects the calculations of adhesion energy and nanoparticle critical velocity.

The Mouret *et al*. (2011) theory had the same problem that Wang and Kasper (1991) encountered in the calculation of single fiber efficiency. They employed Lee and Liu (1982) and Stechkina and Fuchs (1968) equations that fail to consider gas slip and results the nanoparticle removal efficiency of greater than one. As a result, additional theoretical studies are needed for the determination of the critical particle diameter below which thermal rebound may occur.

2.4.2 Experimental work

A large and growing body of literature includes respects related to whether or not thermal rebound leads to the reduction of filtration efficiency. Table 2-3 summarizes the experimental studies related to the thermal rebound theory and their results.

Table 2-3. Experimental studies in thermal rebound theory

References	Particle characteristics	Media type	Operating conditions and filter characteristics	Instrument	Results
Scheibel and Porstendörfer 1984	silver particles: 3.5 nm < dp <130 nm	tube and screen-type diffusion batteries	df = 0.005 cm α = 0.2798 U = 2.4 cm/s	EC[1] DMA[2] TEM[3]	No thermal rebound
Van Osdell et al. 1990	silver particles: 4 nm < dp < 10 nm DOP particles: 32 nm < dp < 420 nm	glass fiber filter, composite fiber filter, and membrane filter	df < 1 μm α = 0.069-0.078 U = 0.5-20 cm/s L = 0.035-0.470 mm	CNC[4] EC	No thermal rebound
Otani et al. 1995	silver particles 1nm < dp < 10 nm	stainless steel wire screens, and circular aluminum tubes	wire screens: df = 52, 300 μm α = 0.293, 0.310 U = 1.2-3.6 cm/s ds = 4.2 cm circular tube: d = 6 mm L = 0.5, 1, 2 m	DMA FCE[5]	Thermal rebound for dp < 2 nm in circular tubes
Skaptsov et al. 1996	WO_3, and MoO_3 3.1 nm < dp < 15.4 nm	stainless steel, and wire screen	Q = 2 lpm U = 2.92 cm/s T=295, 316, 337 K	EC UCPC	No thermal rebound
Ichitsubo et al. 1996	silver, and NaCl particles: 1 nm < dp < 7 nm	single stage wire screen (stainless steel type 316)	df =75 μm α = 0.289 Q = 6 lpm ds =32 mm	DMA FCE	Thermal rebound for dp < 2 nm
Alonso et al. 1997	silver, and NaCl particles: 1 nm < dp < 7 nm	single stage wire screens, and tubes	df = 75 μm α = 0.289 Q = 1,3,6 lpm ds = 11, 32 mm	Tandem DMA CNC	No thermal rebound
Heim et al. 2005	NaCl (charged, uncharged) particles: 2.5 nm < dp < 20 nm	stainless steel, nickel mesh, and polypropylene	df = 4.2 μm, α = 0.0022 df = 54.6 μm, α = 0.34 df = 110 μm, α = 0.387	DMA CPC	No thermal rebound
Kim et al. 2006	NaCl (singly charged, uncharged, neutralized) particles: 1 nm < dp < 100 nm	glass fibrous filters	df = 9.1, 11.8 μm Q = 4.4 lpm df = 4.15 cm U = 2.5 cm/s	Nano DMA PSM[6]-CNC	Thermal rebound for dp < 2 nm
Huang et al. 2007	NaCl particles: 4.5 nm < dp < 10 μm	fibrous filter for respiratory masks	df = 13 μm α = 0.035 Q = 30, 60, and 85 lpm	Long DMA Nano DMA CPC	No thermal rebound

Japuntich et al. 2007	NaCl, dioctyl phthalate (DOP) particles: 10 nm < dp < 400 nm	Hollingsworth and Vose (H &V) fiber glass filter	df = 1.9 to 4.9 μm α = 0.039 to 0.050	DMA SMPS[7]	No thermal rebound
Kim et al. 2007	silver particles: 3 nm < dp < 20 nm	Hollingsworth and Vose (H &V) fiber glass fibrous filter	df = 1.9 to 4.9 μm α = 0.039 to 0.050 U = 5.3,10, 0.15 m/s	UCPC DMA	No thermal rebound
Steffens and Coury 2007b	NaCl particles: 8.5 nm < dp < 94.8 nm	polyester filter fiber filter of cellulose (HEPA)	α = 0.920 h = 0.4 mm df = 0.45 μm		No thermal rebound
Wang et al. 2007b	silver particles: 3 nm < dp < 20 nm NaCl particles: 15 nm < dp < 400 nm	Hollingsworth and Vose (H &V) fiber glass filters: HE1073, HE1021, HF0031, HF0012	α = 0.05, 0.049, 0.047, and 0.039	Nano DMA CPC	No thermal rebound
Rengasamy et al. 2008	silver particles: 4 nm < dp < 30 nm NaCl: 20 nm < dp < 400 nm	N95 and P100 filter	Q = 85 lpm	Nano DMA UCPC	No thermal rebound
Shin et al. 2008b	silver particles: 3 nm < dp < 20 nm	stainless steel wire screen	df = 90 μm T<500K	UCPC Nano DMA	No thermal rebound
Golanski et al. 2009	graphite particles: 10 nm < dp <100 nm	fiber glass, HEPA, and Electret	basis weight 150, 85, and 75 g/m2	SMPS	No thermal rebound
Van Gulijk et al. 2009	NaCl, $CaCl_2$, $(NH_4)_2SO_2$, $NiSO_4$ electrically neutral 7 nm < dp < 20 nm	stainless steel grid, and wire screen	df = 40 μm	EC CPC-SMPS	Possibility of thermal rebound for NaCl, $NiSO_4$
Heim et al. 2010	singly charged WOx 1.2 nm < dp < 8 nm	eclectically grounded metal wire grid	df = 54.4, 50.1, 101.2 μm α = 0.335, 0.313, 0.297	DMA FCE	No thermal rebound
Brochot et al. 2011	carbon, NaCl, copper particles: 5 nm < dp < 400 nm	fiber glass	df =3.19 μm, 5.14 μm α = 0.05, 0.064 L = 552, 427μm	Nano DMA UCPC CNC	No thermal rebound
Yamada et al. 2011	NaCl particles: 10 nm <dp < 60 nm	wire screen	df = 30, 60, 2.1, 9.5 μm α = 0.215, 0.276, 0.088, 0.172 L = 0.06, 0.12, 0.38, 0.28 mm	DMA CPC	No thermal rebound
Chen et al. 2013	NaCl, Ag particles: 20 nm <dp < 500 nm	nuclepore filter	pore size: 1 and 3 μm U = 2-15 cm/s	DMA CPC	No thermal rebound

[1] Electrostatic Classification, [2] Differential Mobility Analyzer, [3] Transmission Electron Microscope,
[4] Condensation Nuclei Counter, [5] Faraday Cup Electrometer, [6] Particle Size Magnifier, [7] Scanning Mobility Particle Sizer.

In all of the experimental work listed above, only three groups of researchers reported the thermal rebound of particles smaller than 2 nm, but they were likely artifacts because of instrument error. In 1984, researchers tested the filtering of silver nanoparticles down to 3.5 nm through tube and screen-type diffusion batteries and showed that the nanoparticle penetration curves followed those of classical filtration theory (Scheibel and Porstendörfer 1984). One criticism of this study is related to the material of the particles tested. Silver is a soft material that may not exhibit elastic behavior upon impact with a filter surface, so the plastic impaction that decreases the rebound velocity of the particle may lead to higher capturing efficiency. Another experimental study filtered polydispersed silver particles as small as 4 nm and monodispersed dioctylphthalate (DOP) particles as small as 32 nm through fibrous and membrane filters, but the researchers observed no thermal rebound effect in their results (Van Osdell et al. 1990). Multilayer filters may therefore not be an efficient device for determining the existence of thermal rebound, because rebounded particles from the upper layers may be captured by the other layers of the filter. Thus, although thermal rebound could be associated with nanoparticles, it appears to have no significant consequences in multilayer filters.

Otani *et al*. (1995) employed silver nanoparticles in the range of 1 nm to 10 nm, which were passed through wire screens and circular tubes. Their results show that nanoparticle penetration increases for nanoparticles with diameters less than 2 nm in circular tubes; however, thermal rebound did not affect particle penetration in wire screens (Otani et al. 1995). The discrepancy between the particle penetration of wire screens and that in circular tubes appeared to be due to the capture of nanoparticles in the multilayers comprising wire screen filters. Also problematic is the fact that the results of the study relied too heavily on the accuracy of the DMA and FCE, which was in doubt at that time. In another filtration efficiency study, eight stages of wire screens were used to filter out tested tungsten oxide and molybdenum oxide particles, and the thermal rebound was not observed (Skaptsov et al. 1996). In this case, rebounded particles may also be captured by successive stages.

Ichitsubo *et al*. (1996) carried out a study involving the penetration of NaCl and silver particles up to 7 nm in diameter through a single-stage wire screen and showed the probability of thermal rebound for particles with sizes smaller than 2 nm. Their results also showed that the particle penetration trend is a function of the particle material for sub-2 nm particles, due to the differences in hardness of the materials: the greater the hardness, the higher the probability of particle rebound. One of the limitations

of this study is that the size range of the particles may not be accurate because of the inaccuracy of the DMA and FCE available at that time. Alonso *et al*. (1997) employed a single-stage wire screen similar to the one used by Ichitsubo *et al*. (1996). Their experimental measurements obtained with the use of tandem DMA did not show particle rebound. They also concluded that using a single DMA for nanoparticle measurement had caused errors in previous studies so that earlier results were unreliable. In 2005, Heim *et al*. tested the filtration efficiency of charged and uncharged NaCl particles down to 2.5 nm in diameter through a metal and plastic filter and did not observe thermal rebound for small nanoparticles (Heim et al. 2005). Kim *et al*. (2006) later employed monodispersed NaCl particles down to 1 nm to test the filtration efficiency of glass fibrous filters. A particle size magnifier was used prior to a condensation nucleus counter in order to increase the nanoparticle counting efficiency, especially for sub-10 nm particles. Their results showed that filtration efficiency decreases for charged and uncharged sub-2 nm particles due to the effect of thermal rebound. The method used to measure particle concentrations thus strongly affects conclusions with respect to thermal rebound for small nanoparticles. The question that needs to be answered is which equipment is associated with the greatest efficiency and is the most reliable for measuring nanoparticle concentrations.

In 2007 and 2008, a number of studies examined the validation of thermal rebound theory using a variety of particles (NaCl, DOP, and silver) and filters (fibrous filter, fiber glass, H&V, N95, P100, and stainless steel wire screen), employing SMPS with long and nano DMA. No thermal rebound was observed for tests involving NaCl particles with diameters down to 4.5 nm, silver particles with diameters down to 3 nm, or DOP particles with diameters down to 10 nm. Particles below these sizes were not tested for (Huang et al. 2007; Japuntich et al. 2007; Kim et al. 2007; Rengasamy et al. 2008; Shin et al. 2008b; Steffens and Coury 2007a; Wang et al. 2007b).

In 2009, Golanski *et al*. (2009) filtered out graphite particles in the range of 10 nm to 100 nm through a fibrous and electret filter, with the filtration efficiency measured by SMPS showing no thermal rebound effect (Golanski et al. 2009). In the same year, Van Gulijk *et al* (2009) measured the nanoparticle removal efficiency of a variety of electrically neutral polydispersed particles (NaCl, $CaCl_2$, $(NH_4)_2SO_2$, and $NiSO_4$) with diameters ranging from 7 nm to 20 nm passed through a stainless steel screen. Their results indicated the possibility of thermal rebound occurrence for NaCl and $NiSO_4$ nanoparticles. Based on which they postulated that the lower sticking efficiency was due to salt particles

having a lower Hamaker constant than metal particles, which increases the effect of thermal rebound. Neutral nanoparticles have a lower sticking probability than charged particles due to the weaker image forces between the nanoparticles and a surface (Van Gulijk et al. 2009).

In another study by Heim *et al*. (2010) DMA and FCE were used to measure the penetration of singly charged tungsten nanoparticles ranges from 1.2 nm to 8 nm through three different wire grids. In that study, no thermal rebound was observed for tungsten particles, and the lower penetration measured for sub-3 nm particles was attributed to the smaller image forces. In the same year Brochot *et al*. (2011) employed a variety of nanoparticles (carbon, NaCl, and copper) ranging from 5 nm to 400 nm passed through fiber glass filters. The particle concentration measurements using nano DMA, CNC, and UCPC did not reveal thermal rebound effect. However, the discrepancies among the penetration levels of NaCl, carbon, and copper nanoparticles indicated that the morphology of the nanoparticles affects the efficiency of particle removal (Brochot et al. 2011).

Yamada et el. (2010) passed NaCl particles in the size range of 10 nm to 60 nm through different wire screens in order to determine the effect of a non-uniformly packed filter on particle-removal efficiency. Their results showed that the efficiency measured aligned with classical filtration theory with no thermal rebound being observed (Yamada et al. 2011).

Most researchers considered the STP conditions and did not take into account the effect of gas pressure on the thermal rebound theory. Recently, Rennecke and Weber (2013a) conducted a numerical analysis and experiments in order to understand whether thermal rebound is pressure dependent for nanoparticles; they found that the collection efficiency of a low-pressure impactor and impact velocity decreased with the increase of the chamber pressure. Furthermore, in another study (Rennecke and Weber 2013a) they showed that dense NaCl nanoparticles had a higher chance to rebound in the low pressure impactor than porous NaCl and dense spherical silver nanoparticles did. This result is in contradiction to other experimental studies, which did not show the possibility of thermal rebound for NaCl nanoparticles. The disagreement is likely because the drag force at ambient pressure leads to the nanoparticle energy loss prior to nanoparticle rebound; consequently, a nanoparticle is likely to be captured by a surface.

In summary, researchers have employed a variety of methodologies for experimental measurement as a means of minimizing uncertainties based on the sampling method, filter holder design, electrostatic

effect, morphology effect, particle type, and measurement method. Most of the experimental studies led to the conclusion that particle removal efficiency increases with decreased particle size, and no thermal rebound was observed. The key finding of these studies is that thermal rebound may not present a significant problem with multilayer filters because rebounded particles may be captured by the other layers. Only a few of the studies dealt with single fiber efficiency; however, in those studies, the reliability of the measurement equipment was inadequate. Improved studies are needed with respect to examining the filtration efficiency of monodispersed nanoparticles through a single-stage wire screen with more reliable equipment. The filtration efficiencies of a single-stage wire screen in a uniform structure are more similar to the theoretical simulations due to the elimination of the effect of inhomogeneity of the filter on nanoparticle filtration efficiency. Employing monodispersed nanoparticles instead of polydispersed ones could minimize the nanoparticle concentration measurement errors as well. In conclusion, no convincing results have been produced that either prove or disprove the thermal rebound theory. A need exists for an investigation of the effects of thermal rebound and a determination of whether those effects prevent the capture of nanoparticles by conventional filters.

2.5 Nanofibrous Filters

Nanofibrous filters appear to be a cost-effective option for nanoparticle filtration (Bahk and Wang 2014; Barhate and Ramakrishna 2007; Podgórski et al. 2006). Nanofibers have several advantages over microfibers in nanoparticle filtration: nanofibrous filters have higher removal efficiencies than conventional filters, due to slip flow, and nanofibers have a large surface-area-to-volume ratio, which increases the particle deposition rate and, consequently, filtration efficiency. Nanofibrous media are characterized as having a long lifetime, high loading capacity, low air resistance, low basis weight, and high permeability (Graham et al. 2002). In the last few decades, nanofibers have been playing important roles in filtration applications, and the related market size is expected to reach US$700 billion by 2020 (Alivisatos et al. 1998; Suthar and Chase 2001; Xia et al. 2003).

In traditional filtration theory, it is assumed that air flow around the fibers is continuous without a slipping effect, where the air velocity at the fiber surface is zero (Hinds 1999). However, this assumption is no longer valid at the nanoscale; and, slip flow must be considered for fibers with a Knudsen number greater than 0.1, i.e., those with a diameter smaller than 500 nm (Graham et al. 2002).

Slip flow conditions greatly benefit the filtration of nanoparticles: more particles approach the fiber surfaces, increasing the capture of nanoparticles by Brownian diffusion, interception, and impaction (Grafe and Graham 2003; Stechkina et al. 1969). Slip flow also lowers air flow resistance, due to decreased drag force on the nanoparticles (Hung and Leung 2011; Yoon et al. 2008). Moreover, the interception efficiency increases as the size of fiber approaches that of aerosol particles. Nanofibrous filters are promising alternatives for the removal of nanoparticles with higher efficiency at low pressure drops (Grafe and Graham 2003).

Various technologies have been developed for the manufacturing of nanofibers, including phase separation, drawing, self-assembly, template synthesis and electrospinning. Electrospinning is widely utilized in many industries to produce high-quality nanofibrous filters for wastewater treatment or air filtration.

Electrospinning is the process of creating nanofibers from a liquid polymer solution in an electric field. It was first patented in 1902 (Morton 1902), but not widely utilized until the 1990s (Ramakrishna et al. 2006). In electrospinning, the polymer solution is injected through a capillary needle charged to a high voltage, typically 10 kV to 30 kV. The applied voltage induces a charge on the surface of the liquid droplet, and when this is sufficiently high, the hemispherical surface of the fluid elongates and a Taylor cone is established. Polymer jets are able to form when the applied repulsive electric force overcomes the surface tension of the deformed drop of the suspended polymer solution formed on the tip of the syringe. The polymer jet is emitted from the Taylor cone and drawn toward the grounded collector. As a jet travels through the air, the solvent evaporates, leaving behind polymer fibers to be collected on an electrically grounded target positioned at a fixed distance from the needle. Thus, the electrospinning jet can be thought of as a string of charge elements connected by a viscoelastic medium, with one end fixed at the point of origin and the other end free. The free end of the electrospinning jet follows a chaotic path as it travels towards the grounded collector and is randomly deposited onto the filter medium. This chaotic motion is the result of a complicated interaction of variables including viscosity, conductivity, surface tension, electrostatic force, air friction, gravity and ambient parameters.

Fibers produced by this method have a diameter in the range of a few nanometers to several hundred nanometers (Barhate and Ramakrishna 2007; Ward 2005). Electrospun nanofibers can be in the order

of hundreds of kilometers and, as a result, they are environmentally safe because they are unlikely to become airborne nanoparticles and enter the body (Yoon et al. 2008).

In recent years, a number of studies have been conducted with the goal of determining the filtration efficiency of nanofiber filters (Hung and Leung 2011; Podgórski et al. 2006; Qin and Wang 2006; Wang et al. 2008; Yun et al. 2007). For example, Podgórski *et al*. (2006) employed fibrous filters that were composed of microfibers and nanofibers, with the mean fiber diameter varying from 0.74 µm to 1.41 µm, and that were produced by means of a melt-blown method for removing nanoparticles with diameters in the range of 10 nm to 500 nm in diameter. The use of such nanofiber filters resulted in greater efficiency than did the use of microfiber filters. For the collection of polydispersed particles containing nanoparticles, the authors recommended a triple-layer design filter, with dense micrometer-size fibers for support, porous nanofibers for the middle layer, and intermediate-size fibers for the front layer. Ahn et al. (2006) investigated the performance of nylon 6 electrospun nanofibers for the filtration of 300 nm particles at a face velocity of 5 $cm \cdot s^{-1}$ (Ahn et al. 2006). The fibers were in the range of 80-200 nm and had a basis weight of 10.75 $g \cdot m^{-2}$. Results showed that the filtration efficiency of nanofibrous filters was higher than that of commercial HEPA filters. Zhou et al. (2006) reported that a polylactic acid (PLA) sub-micron fibrous filter performed better than a filter with 10-µm fibers for capturing sub-0.7 µm particles (Zhou et al. 2006).

Yun *et al*. (2007) carried out experiments with Polyacrylonitrile (PAN) nanofibers with a mean fiber diameter of 0.27 µm to 0.4 µm produced by electrospinning in order to collect NaCl nanoparticles in the range of 10 nm to 80 nm and observed a better performance with the electrospun fibers than commercial ones. They showed that nanoparticle penetration decreases with increased filter thickness; however, single fiber efficiency and the quality factor are independent of filter thicknesses (Yun et al. 2007).

Leung et al. (2010) tested polyethylene oxide (PEO) nanofibers with a mean fiber diameter of 208 nm on non-woven microfibers for sodium chloride (NaCl) nanoparticles in the size range of 50-480 nm (Leung et al. 2010). They concluded that nanofibrous filters with a high packing density could be used for highly efficient air filtration (Leung et al. 2010). Hung et al. (2011) investigated the filtration efficiency of nylon-6 electrospun filters using nanoparticles in the range of 50-500 nm and concluded

that a high filter quality could be achieved by employing multilayer filters with low basis weight (Hung and Leung 2011).

Overall, studies have shown that due to Brownian diffusion and interception, nanofibers improve the efficiency of nanoparticle removal; however, the smaller the fiber diameter, the higher the pressure drop, a consideration that has led some researchers to experiment with multilayer filters, consisting of differing fiber diameters and densities in each layer (Podgórski et al. 2006).

2.6 Knowledge Gap and Research Needed

Although there have been many advances in nanoparticle filtration; there is still a need to consider the effect of thermal rebound on filters. A number of assumptions underline in the theoretical and experimental studies. It was assumed that the impact velocity of particles follows a Maxwell-Boltzmann distribution; while this distribution is for ideal gas molecules, the validity of its use for nanoparticles is in doubt. In previous studies, JKR and BH models have been employed to calculate the adhesion energy between bodies. Both models assume elastic impaction between the bodies, but fail to consider the implications if nanoparticle impaction is completely plastic and energy loss is not neglected. Thus, the particle-surface adhesion energy based on plastic deformation should be considered for calculating the nanoparticle critical velocity.

JKR and BH models, which are employed in previous studies, are validated for micron particles; however, the impact mechanisms for microscale and nanoscale particles deviate because latter must include consideration of molecular interactions (Teodorescu and Rahnejat 2007). Thus, the selection of a contact model that accounts for both scales is always based on underlying assumptions. These models require the exact value of the mechanical constant, Hamaker constant, and the specific adhesion energy between bodies; however, such exact values are unavailable for most materials. Also, a further question arises here if these parameters are size-independent and they are the same for bulk materials and nanoparticles. Studies show that the material properties of nanoscale bodies differ from those of bulk materials. Nanomaterials also have higher yield stresses than bulk materials (Richter et al. 2009). Thus, incorporating the material properties of nanoparticles based on those bulk materials may lead to inaccuracies in the thermal rebound theory. Another study revealed that the nonlocal dielectric properties of materials affect the Hamaker constant for small nanoparticles (Esquivel-Sirvent and Schatz 2012), and Pinchuk later indicated that the Hamaker constant is greater for nanoparticles smaller

than the mean free path of electrons with diameters in the order of 2 nm (Pinchuk 2012). Thus, the size dependence of the dielectric properties of nanoparticles means that the Hamaker constant is also size dependent for the nanoparticles that will be considered in future studies. Furthermore, previous studies relied on a variety of ranges of specific adhesion energy requirements in contact adhesion models. Wang and Kasper (1991) based their work on $\Delta\gamma = 0.01\, J/m^2$; however, Mouret *et al*. (2011) later pointed out that the specific adhesion energy in the Wang and Kasper's research should be $\Delta\gamma = 0.005\, J/m^2$. Rennecke *et al*. (2013) used a value of 0.5 for NaCl particles (Mulheran 1994; Rennecke and Weber 2013b). A great deal of uncertainty is thus related to the determination of the amount of specific adhesion energy especially in the case of nanomaterials.

Theories of particle-surface adhesion energy apply to smooth surfaces; however, the surfaces of the nanoparticles and the filter are not smooth, so including consideration of surface roughness is essential. Rebound velocity has been reported to depend on material properties and surface topography (Chang and Ling 1991). Surface roughness can play an important role in the determination of the adhesion force between nanoparticles and a wavy surface (Delrio et al. 2005). It has been found that surface roughness affects the surface force, the interaction in terms of specific adhesion energy, the impact mechanisms, the energy exchange, and particle rebound (Broom 1979; Paw U 1983; Tabor 1977). Consideration of contact adhesion models for wavy surfaces should thus be included in the thermal rebound theory.

Although impaction velocity has 3 directions (x, y, z), only impaction along normal direction is considered in existing thermal rebound models and analysis. Particles may collide with the surface obliquely and the tangential component of the impact velocity may contribute to the probability of either adhesion or rebound. The effect of the impaction angle on thermal rebound theory is still uncertain. Oblique impaction could affect the coefficient of restitution and the critical velocity and, consequently, influence the probability of the occurrence of thermal rebound, a factor that has not been considered in previous thermal rebound theories. A normal impact velocity contributes to deformation, and a tangential velocity promotes particle rotation and enlarges the contact area. A tangential force causes shear stress which creates a horizontal shift from the contact area (Savkoor and Briggs 1977). As a result, including consideration of oblique particle impaction may change the thermal rebound theory because this factor was neglected in previous studies. It has been pointed out that the critical

velocity for a particle to be captured in oblique impaction is lower than that negotiated for perpendicular impaction (Aylor and Ferrandino 1985; Broom 1979). Studies have shown that the rebound velocity for smaller impact angles is higher than that for larger angles and that the coefficient of restitution decreases with increases in incident angle of the impact (Tabakoff and Malak 1987). Including consideration of oblique impaction in elastic and plastic impaction is therefore important. A number of studies have demonstrated the importance of the tangential forces with respect to the rebound angle in elastic impactions (Maw et al. 1976; Maw et al. 1981). It has also been reported that that plastic deformation can dispel the initial kinetic energy in oblique impactions and can affect rebound behavior, especially at high impaction angles (Wu et al. 2008).

In reality, drag force may also affect the rolling and detachment of particles on a filter's surface (Liu et al. 2011). However, this important factor is omitted in existing thermal rebound theory, even though it also helps to explain the discrepancy between thermal rebound models and experimental work.

The effect of capillary force was not considered in earlier studies of nanoaerosol filtration and thermal rebound. Studies have shown the increase of the adhesion energy between a particle and a solid surface at a high relative humidity (Bateman et al. 2014; Chen et al. 2011; Stein et al. 1994; Vasiliou et al. 1999). It has also been reported that the filtration efficiency for micron particles increases with the level of relative humidity (Brown 1993; Miguel 2003; Mullins et al. 2003; Xu et al. 2014); however, it is not clear whether this phenomenon applies to nanosized particles.

Earlier thermal rebound models were developed based on consideration of uncharged particles and filters; however, in reality, most aerosol particles and filters carry ions. A few studies have been done to determine the effect of the charge state of sub-100 nm particles on filtration (Kim et al. 2006; Yun et al. 2007). In Kim et al. (2006) the filtration efficiency of sub-100 nm sodium chloride particles was shown to be lower for uncharged particles than for charged particles at the face velocity of 2.5 cm/s, and this discrepancy decreases with a decrease in the particle size (Kim et al. 2006). Another study on an electrospun filter for sub-80 nm NaCl particles showed that nanoparticle removal efficiency is independent of the charge state of particles, indicating the negligible effect of columbic force compared to a strong diffusion force (Kousaka et al. 1990; Yun et al. 2007). However, no studies have been done to determine the effect of electrostatic charge on thermal rebound theory. Addressing all the current knowledge gaps may eliminate the need to consider thermal rebound in a certain way.

Various studies explored the filtration efficiency of nanofibrous filters for micron particles and the most penetrating-particle size (MPPS) of 300 nm, but studies on the effect of employing nanofibrous filters for sub-100 nm NaCl and WOx particles are limited. A missing factor in nanoparticle filtration studies is the effect of upstream particle concentration on filtration efficiency. Upstream particle concentration may affect the charge states and agglomeration rates of particles, which also contribute to filtration efficiency and the occurrence of thermal rebound.

2.7 Conclusions

This chapter has discussed nanoparticle filtration and the thermal rebound theory as related to nanoparticles. While methods have been developed for calculating the single fiber efficiency of micron particles, doubt still exists with respect to the calculation of the single fiber efficiency of nanoparticles. The theoretical analysis of single fiber efficiency with respect to nanoparticles is approximate because it has been based on validations for micron particles. A better understanding of the physical properties specific to nanoparticles could lead to the design of high-performance filters for collecting nanoparticles.

In spite of the investigation of the thermal rebound theory for airborne nanoparticles in numerous studies, since its development, no convincing results have clearly demonstrated the role of thermal rebound, if any, in nanoparticle filtration. Neither the JKR nor the BH adhesion energy model is suitable for calculating the adhesion energy between nanoparticles and a surface. More accurate theoretical analysis and experiments are thus required in order to prove or disprove the thermal rebound theory.

Nanofibrous filters reveal superior nanoparticle filtration due to both Brownian diffusion and interception. Such filters have higher removal efficiencies than conventional filters, due to slip flow and a large surface-area-to-volume ratio. In order to determine the complicated behavior of nanoparticles in filtration, more experimental study is needed at high particle concentrations of sub-100 nm particles.

Chapter 3
The Performance of GRIMM SMPS+E for Nanoparticle Sizing

3.1 Summary

This chapter aims to evaluate the performance of a scanning mobility particle sizer coupled with a Faraday cup electrometer (GRIMM SMPS+E 7.860) for particle number concentration distribution measurement. This task is important and critical for the topics covered in the following chapters, which are mainly for the nanoparticle removal efficiencies of various filters. In order to measure the filtration efficiency, the upstream and downstream particle concentrations have to be measured. Any errors in the measurements of airborne nanoparticle concentration distributions may lead to inaccurate filtration efficiency calculation. Thus, the GRIMM SMPS+E performance is evaluated to guarantee the reliability of further experiments of the thesis.

Experiments were done to determine the performances of the equipment for different particle types, particle sizes, and particle concentrations. NaCl and WOx nanoaerosol generators were used in this study. WOx particles were generated in the size range of 0.8 to 30 nm. NaCl particles were in the size range of 10 to 130 nm. The effects of instrumental parameters such as the sheath air flow rate, sample air flow rate and number of channels on the particle number concentration distribution measurement were investigated.

It was found that the GRIMM SMPS+E works accurately but operates differently than other SMPSs as follows:

- In order to minimize the diffusion losses of nanoparticles, the fast FCE has to be attached to the exit of the DMA to measure the concentrations of nanoparticles immediately after their classification in high resolutions.
- Due to the fast response time of GRIMM FCE (¼ s), purging between tests is not necessary.
- A sheath air to sample air flow rate ratio of 5:1 can be employed for nanoparticle classification for S-DMA.

3.2 Introduction

Various commercial instruments have been and are still used for sizing and quantifying airborne nanoparticles (e.g., the electrical low pressure impactor-ELPI, scanning mobility particle sizer-SMPS, fast mobility particle sizer-FMPS, particle size magnification-PSM, aerodynamic focusing and electrometer (Tan et al. 2015; Tan and Wexler 2007)). Among them, one of the most common methods for measuring the nanoparticle number concentration distribution is a scanning mobility particle sizer (SMPS). SMPS is used to measure the electrical mobility size distributions of submicron-particles continuously over several orders of magnitude for both particle size and concentration (Flagan 1998; McMurry and Woo 2002; Watson et al. 2002). A typical SMPS usually consists of a differential mobility analyzer (DMA) to classify nanoparticles based on their electrical mobilities and a condensation particle counter (CPC) or a Faraday cup electrometer (FCE) to measure nanoparticle concentration.

The SMPS employs a bipolar diffusion charger prior to the electrostatic classifier, so introduced nanoparticles get a well-defined equilibrium Boltzmann charge distribution. The common radioactive sources contain alpha radiates (^{241}Am and ^{210}PO) or beta radiates (^{85}Kr, ^{14}C, and ^{63}Ni). Particles with equilibrium charges are then introduced through a DMA and merged with sheath air to minimize particle diffusion loss. The DMA classifies polydispersed particles into monodispersed particles with known sizes based on their electrical mobility by varying the voltage (Liu and Pui 1974; Stolzenburg and McMurry 2008; Wang and Flagan 1990; Winklmayr et al. 1991). DMA contains two cylinders with an annual space between them. With this particular device, applying a positive voltage to the inner electrode of DMA causes the electric field between cylinders, which affects the trajectory of charged particles. Positively charged particles are repelled from the inner cylinder and deposited on the outer one. Negatively charged particles drift towards the inner electrode. The exact location of particles attracted to the outer cylinder depends on the electrical mobility of these particles, sheath air, aerosol flow rate and the DMA geometry. As the electrical mobility of particles decreases, they collect on the lower part of the cylinder. Thus, in a DMA, for specified operating conditions, particles with a narrow range of mobility will be classified as monodispersed particles.

The width of this narrow mobility is defined by the ratio of sheath air flow to the sample air flow rate. The probability of a particle with a given size that successfully passing through the classifier is

called the transfer function of DMA (Ω). The transfer function depends on particle mobility, voltage, flow rate and DMA geometry. For a matched aerosol flow rate and sample air flow rate, the transfer function is triangular (Knutson and Whitby 1975). It can be plotted as a function of electrical mobility (Figure 3-1) or as the corresponding particle diameter.

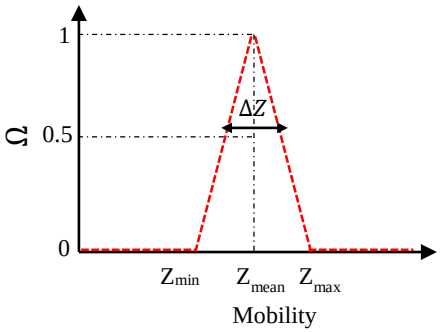

Figure 3-1. Transfer function of DMA

The mean electrical mobility of (Z_{mean}) classified particles is:

$$Z_{mean} = \frac{Q_{sh}}{2\pi vL}\ln(R_2/R_1) \tag{3-1}$$

where Q_{sh} is the sheath air flow rate (*lpm*), R_1 is the outer radius of the inner electrode (*cm*), R_2 is the inner radius of the outer electrode (c*m*), L is the electrode length (*cm*), and v is the potential difference between the inner and outer electrode (*volts*), which varies exponentially with constant time (Collins et al. 2004). This relation is independent of both the particle trajectory and air flow profile in the DMA. The electrical mobility of a charged particle (Z_p) is calculated by

$$Z_p = \frac{neC_c}{3\pi\mu d_p} \tag{3-2}$$

where n is the number of charges on the particle, e is the electron charge ($1.6\text{x}10^{-19}$ C), μ is the gas viscosity, and C_C stands for the Cunningham coefficient. Equate Eqs.(3-1) and (3-2), gets:

$$v = \frac{3\mu Q_{sh}}{2LneC_c}\ln(R_2/R_1)\, d_p \tag{3-3}$$

or

$$d_p = \frac{2LneC_c}{3\mu Q_{sh}} \frac{v}{\ln(R_2/R_1)} \quad (3\text{-}4)$$

Both n and C_c depend on particle diameter. An ideal DMA classifies only one size of aerosol at a constant voltage. In reality, particles in a narrow size range exit DMA, and the corresponding mobility bandwidth (ΔZ) is defined as

$$\Delta Z = \frac{Q_a}{Q_{sh}} Z_{mean} \quad (3\text{-}5)$$

where Q_a is the sample air flow rate. Eq.(3-5) shows that based on the sheath flow and aerosol flow, particles with electrical mobility in the range of $Z_{mean} \pm \Delta Z$ are classified. And, the higher the sheath air to sample air flow ratio causes a narrower size range of particles to exit the DMA with constant voltage.

One of the errors in particle number concentration distribution measurement of small nanoparticles is caused by diffusion broadening (Stolzenburg 1988). The broadening causes the triangular shape of transfer function to change to the Gaussian curve. The diffusion broadening depends on both the geometry (Inner diameter, outer diameter, length) and operating conditions (sheath air flow, aerosol flow, carrier gas properties) of the DMA. In order to minimize the diffusion broadening of nanoparticles, parameters involved in transfer function calculation should be taken into careful consideration.

Classified particles are then counted by a CPC or a FCE, each of which works with different principles. A CPC detects particles using an optical method, and a FCE detects them with an electrical method. In a CPC, nanoparticles are exposed to saturated alcohol or water vapor, and then transferred into a cold condenser to be cooled by thermal diffusion. These nanoparticles then grow by a heterogeneous condensation into droplets large enough to be detected by optical light scattering (>1 μm). The lower detection limit of the particle size (Kelvin diameter) is determined by the properties of working fluid, or the supersaturation ratio of the condensing vapor. At the lower detection limit (d_{50}), CPC is able to count half of the particles. One critical issue for CPC is that high diffusional loss causes low counting efficiency for nanosized particles. The lower particle size detection limit of a commercial CPC is approximately 2 nm (Ankilov et al. 2002). The problem with these devices is that even small fluctuations of operating conditions cause high measurement counting errors for small nanoparticles

(Sem 2002). FCE is an alternative device for detecting nanoparticles at higher detection limits for particle concentration than a CPC. FCE detects the electrical current of charged particles at a response time of less than 100 ms (Keck et al. 2009), and provides precise concentration measurement independent of particle composition (Ankilov et al. 2002). The lower detection limit of a FCE depends on the sensitivity of the specific FCE.

Two examples of commercial SMPS are from TSI Inc. (Shoreview, MN, USA) and GRIMM (Grimm Aerosol Technik GmbH & Co. KG, Ainring, Germany). TSI SMPS has been widely used in North America; however, less reported the performance of GRIMM SMPS employing a Faraday cup electrometer. The particle size range and concentrations measured with related instruments are summarized in Table 3-1.

Table 3-1. Specifications of various measurement devices

Model	**Particle Size**	**Single count mode particles/cm^3**	**Concentration Range (photometric mode) particles/cm^3**
TSI, CPC 3007	10 nm->1µ	-	0-10^5
TSI, CPC 3772	10 nm	$1x10^4$	-
TSI, CPC 3775	4 nm->3µm	$5x10^4$	10^7
TCI, CPC 3776	2.5-20 nm	$3x10^5$	-
TSI, CPC 3783	7 nm	$1x10^6$	-
TSI, CPC 3787	5 nm	$2.5x10^5$	-
TSI, CPC 3788	2.5 nm	$4x10^5$	-
TSI, CPC 3790A	23 nm->3µm	1-$1x10^4$	-
TSI Electrometer 3068 B	2 nm-5µ		
TSI Electrometer 3070A	10nm-1µ		
GRIMM, CPC 5.401	5 nm	$2x10^4$	10^7
GRIMM, CPC 5.402	5 nm	10^4	10^7
GRIMM, CPC 5.403	4.5 nm->3µm	$2x10^4$	10^7
GRIMM FCE 5.700	<0.8 nm-1100 nm	55-10^8	-

In the absence of an absolute standard method, intercomparison of the results of various measurement instruments becomes important as a way to check accuracy (Joshi et al. 2012). A number of studies have compared the particle number concentration distributions measured by various commercially available SMPS (Alofs et al. 1995; Joshi et al. 2012; Watson et al. 2011; Wiedensohler et al. 2012). Imhof et al. (2006) compared three different scanning mobility particle sizers of same type and model (DMA TSI 3071A, CPC TSI 3022A) for a road tunnel particles and observed about 30% discrepancies

for particles smaller than 50 nm, and 10% discrepancies for particles larger than 200 nm, for reasons that are unclear (Imhof et al. 2006). Helsper et al. (2008) compared five SMPSs (TSI-long SMPS, TSI-Nano SMPS, two GRIMM SMPS+C, custom-made IFT-TDMPS) for ambient air and showed that GRIMM SMPS+C measured 48% higher number concentration than TSI SMPS. The discrepancies may result from different charging algorithm by the different manufacturers (Helsper et al. 2008).

Asbach et al. (2009) compared four mobility particle sizers (TSI FMPS 3091, TSI SMPS 3936-CPC 3786, TSI SMPS 3936-CPC 3010, GRIMM SMPS+C-CPC 5.404) for NaCl and diesel soot particles in a wind tunnel, and observed the independency of results on particle material. Experiments at different instrument settings (e.g., aerosol and sheath flow), also showed that the measured particle number concentration distributions from SMPSs from the same manufacture deviated from each other because of the high sensitivity of SMPS to flow rate, or perhaps inaccurate flow rate calibration. They showed that the NaCl concentrations of GRIMM SMPS+C was about 42% higher with the count median diameter shifted slightly toward a smaller diameter than that of TSI SMPS (17% smaller than that for TSI); however, the mode diameters measured by GRIMM SMPS+C agreed well with those of the TSI SMPS. Results also showed that employing both M-DMA and L-DMA in GRIMM SMPS+C results in the same particle number concentration distribution measurement (Asbach et al. 2009). Later on, Watson et al. (2011) employed four commercial SMPS of TSI-nano (DMA 3085, UCPC 3025A), TSI-standard (L-DMA 3081, CPC 3010), GRIMM SMPS+C (M-DMA 5.500, CPC 5.403), and MSP (1000XP WPS) for ambient exposure studies. They reported that the greatest particle concentration was measured by GRIMM SMPS; however, both geometric mean diameter and geometric standard deviation measured by GRIMM SMPS were lower than those by MSP and TSI-standard SMPS. Results from GRIMM SMPS+C and TSI-nano SMPS agreed well for particles in the size range of 30 nm to 50 nm; however, GRIMM reported 23% and 40% more particles than TSI-nano SMPS in the particle size range of 10-30 nm and 5-10 nm, respectively (Watson et al. 2011).

Joshi et al. (2012) compared GRIMM SMPS+C (L-DMA, CPC 5.403) and TSI SMPS (DMA 3080, CPC 3775) for test particles (NaCl, $(NH_4)_2SO_4$) and ambient particles. Results showed that GRIMM SMPS counted higher particle concentrations with smaller geometric mean diameters than TSI SMPS. It was shown that the ratio between concentrations measured by GRIMM to TSI increased as the particle concentration increased; however, the effect of particle concentration on this ratio is not

significant for two TSI SMPSs. The difference is also greater for small particles than large ones. The discrepancy may be caused by differences in CPC counting efficiency, particle diffusion loss, or differences between transitions from single counter to photometric counter mode in CPC (Joshi et al. 2012).

Despite of the studies to compare the TSI SMPS and GRIMM SMPS+C, only one compared the performance of GRIMM SMPS+E with that of TSI electrometer. Since, the GRIMM electrometer is more accurate than CPC, it is usually employed as a reference for particle counter calibration (Wimmer et al. 2008). Comparing the GRIMM FCE 5.700, TSI FCE 3068B, Vienna FCE slow and Attoui FCE for molecular clusters in the range of 1 nm to 1.6 nm showed that some of the features of particle number concentration distributions lost in the measurement with the two slow FCEs (Vienna FCE slow and Attoui FCE). Moreover, an artificial shift toward small particles was observed for the TSI FCE measurement due to its internal delay time and counting of particles stepping down from larger voltages (Wimmer et al. 2008).

Overall, the discrepancy between the particle number concentration distributions of various measurement devices is associated with either possible sources of uncertainties or lack of knowledge about physical phenomena (Coquelin et al. 2013). Some examples of the uncertainties include bipolar charge distribution, DMA transfer function, DMA flow rate, CPC counting efficiency (Stolzenburg et al. 2005), and diffusional particle loss (Watson et al. 2011; Wiedensohler et al. 2012). Due to these uncertainties, the particle number concentration distributions measured using different instruments may vary.

Since few studies have employed GRIMM SMPS+E for particle number concentration distribution measurement, research is needed to determine the performance of GRIMM SMPS+E for the measurement of airborne nanoparticle number concentration distribution. The aim of this chapter is to gain insights about the effects of factors (such as number of channels, sheath to flow rate, particle type, particle concentration, particle polarity, and classifying order of particles from larger to smaller ones) on nanoparticle number concentration distribution measurement.

In this study, a brand new scanning mobility particle sizer coupled with a Faraday cup electrometer (SMPS+E, GRIMM 7.860) was employed to measure particle number concentration distribution. The SMPS+E consists of a differential mobility analyzer (DMA, GRIMM Model 5.706) for classifying

polydispersed particles into monodispersed particles categories based on their electrical mobility, and a Faraday cup electrometer (FCE, GRIMM Model 5.705), for measuring the number of charged nanoparticles. One of the claimed features of this device that distinguishes it from others is its high resolution and good accuracy for the specific sizes of particles, especially those smaller than 2 nm (Keck et al. 2009). According to the supplier manual, SMPS+E can detect particles in the size range of 0.8 nm to 1100 nm.

In this device, a radioactive neutralizer (GRIMM 5.521, $_{241}$AM, Intensity: 3.7 MBq for air flows up to 5 lpm; ~100µCi, $Nt \geq 10^7$, N is the number of ions per cm^3 and t is the residence time of particles in seconds) is employed prior to the DMA to evaluate nanoparticles to reach Boltzmann-charged equilibrium states before being introduced into the DMA. A DMA controller is used to control the applied voltage, sample flow rate and sheath flow rate. Polydispersed aerosol particles can be classified by a stepwise change in the applied voltage. During the measurement, the positive voltage starts at a high value (10 kV) and decreases stepwise; thus, particles with larger diameters are classified and detected first, followed by smaller ones. Excess air is used to remove any neutral and remaining particles. The sample flow rate is in the range of 1-5 lpm, and the sheath flow can be controlled in the range of 3-20 lpm. Coupling the sample flow rate with the sheath flow rate adjusts the size and size resolution of the detected particles. A minimum sheath to sample air flow ratio of 5:1 was recommended for more accurate size measurements (Giechaskiel et al. 2009). The higher the sheath air flow rate, the smaller the particle loss is, and it therefore enables the DMA to have a better resolution for monodispersed classification (Keck et al. 2009).

It is claimed by the supplier that a fast and high sensitive Faraday cup electrometer (FCE, GRIMM Model 5.705) is coupled with the SMPS to detect unipolar charged particles in the range of 0.8 to 1100 nm, with particle concentrations in the range of 10^3-10^8 P/cm^3 (GRIMM 2012). Charged nanoparticles enter the FCE at a flow rate of 1.5 lpm and deposit their charges on a filter. The electrical current of elementary charges on aerosol particles is then converted to a voltage by an amplifier with a resistor of 2.5 TΩ. Particle concentration is calculated based on sample air flow and the charges of the nanoparticles. In this device, a space between the FCE and outer case is wide enough for the rinse air to keep the annular section contaminant and electrical-charge free and to reduce noise. The rinse air

flow makes the FCE sensitive to particle concentration changes in about 200 ms and minimizes the response time. At last, the FCE is then discharged by applying a current through a 1 TΩ resistor.

The GRIMM SMPS+E and TSI SMPS work with different measurement techniques and principals. The differences include neutralizers, DMA controller settings, monodispersed measurements, time intervals, purge times, and lower detection limits. All of these are summarized in Table 3-2.

Table 3-2. Specifications and limitations of GRIMM SMPS and TSI SMPS devices

Model	**GRIMM SMPS+E 7.860**	**TSI SMPS 3936**	**TSI SMPS 3938**
Neutralizer	$_{241}$Am	Soft x-ray/$_{85}$Kr	Soft x-ray/$_{85}$Kr
Charging theory	ISO 15900	ISO 15900:2009	ISO 15900:2009
Default applied voltage	Positive	Negative	Negative
Scanning times (s)	24-144*	16	<10 - 300
Sample air flow rate (lpm)	1,1.2,1.5, 2 2.5,3,5	0.3, 0.6, 1, 1.5**	0.2-5
Sheath air flow rate (lpm)	3,4,5,6,8 10,12,15,20	3,6,10,15**	2-30
Sheath to aerosol flow	>5:1	>10:1	>10:1
Number of channels	12,23,45,89	Up to 167	Up to 167
CPC	-	Water/butanol	Water/butanol
FCE		-	-
Time interval (s)	0.1	1	1
Particle concentration	10^3-10^8	1-10^7	10^7
Particle size range	<0.8 nm-1100 nm	2.5-1000 nm**	2.5-1000 nm**

**depends on the CPC type.
*depends on number of channels, sample air, sheath air, wait time, and precision

Radioactive neutralizer: The particle concentration distribution depends strongly on the charge states of nanoparticles, especially for a SMPS employing an FCE. Thus, the role of a radioactive neutralizer prior to DMA is important. GRIMM employs a $_{241}$Am (5.6 MeV, 100 μCi) and TSI employs an $_{85}$Kr (0.695 MeV, 10 mCi) radioactive neutralizer. Particles get in touch directly with the $_{241}$Am foil inside the GRIMM neutralizer housing; however, they do not get in touch with the TSI $_{85}$Kr radioactive ionizer but rather only with the radiation that is emitted outside the stainless steel housing. Thus, neutralizing with $_{85}$Kr requires much stronger source concentrations (10 mci for $_{85}$Kr compared to 100 μCi for $_{241}$Am). Generation of one pair of ions required about 34 eV; thus, employing $_{241}$Am with an energy of 5.6 MeV is very efficient for the Boltzmann equilibrium charge distribution of particles. Employing $_{241}$AM material as the neutralizer has several advantages over $_{85}$Kr including its long half-

life (433 years), high energy (5.6 MeV), and durability. On the other hand, alpha particles from radioactive sources lose their energy in a short distance of 5 cm (Wiedensohler et al. 2012), which minimizes the distance between the neutralizer and the DMA.

DMA applied voltage: The applied voltage in GRIMM SMPS+E is from large voltage stepping down, which causes particles to be classified from large to smaller ones. It is reverse for TSI SMPS. Thus, for multiple samples of polydispersed particles without purging between samples, large particles from previous sample are counted as small ones in the next sample, resulting in artifacts especially for smaller particles (Japuntich et al. 2007). Since the GRIMM SMPS+E classifies particles from large to smaller, leftover smaller particles from previous samples maybe counted as large ones in the next sample.

Sheath air to sample air flow rate ratio: The GRIMM SMPS+E can be operated with a sheath air flow rates from 3 to 20 lpm. A minimum sheath air to sample air ratio of 5:1 was recommended by Giechaskiel et al. (2009). The TSI SMPS is usually operated with a sheath air flow rate of up to 15 lpm in single blower mode, and a minimum sheath air to sample air flow ratio of 10:1 is recommended.

Polarity of classified particles: The polarity of the applied voltages in DMAs for both TSI SMPS and GRIMM SMPS+E differs. TSI usually employs a negative voltage, which causes positively charged particles to exit the DMA; however, GRIMM applies a positive voltage, which means that negatively charged particles exit from the DMA. The electrical mobility of negatively charged particles is greater than that of positive one, which may lead to more diffusion loss and different calculations.

Stepping time interval /Purge time: The GRIMM FCE can be used with stepping intervals of down to ~0.1 s without producing artifacts, whereas the TSI FCE 3068B is limited to time intervals larger than 1 s. The greater time interval of TSI compared to GRIMM causes a mobility shift toward smaller particles (Wimmer et al. 2008). Fast measurement of size distributions at high resolutions employing the GRIMM FCE help reduce the errors for the measurement of polydispersed particles (Wimmer et al. 2008). In addition, due to the high sensitivity of the GRIMM FCE, purging between tests is not necessary. As will be shown in section 3.4.2.4, any changes in the particle number concentration distributions are applied to the measurement in less than 1 s; however, purging is essential for the TSI SMPS (Japuntich et al. 2007).

***Monodispersed/Polydispersed*:** Both DMA from TSI and GRIMM manufacture can produce monodispersed particles in one channel. However, because TSI usually employs CPC, and GRIMM employs FCE, the particle counting principals for these two devices are different. Particles exiting the DMA are singly charged monodispersed particles. Any changes in the charge states of particles when traveling the distance to the counting device does not affect the CPC's counting efficiency; however, it might affect the FCE's counting efficiency. CPC's counting efficiency is independent of particle's charge states; whereas, FCE's counting efficiency strongly depends on particle's charge states. For instance, multiple charged particles may increase the current detected by the FCE, which overestimate particle concentrations. In order to minimize the diffusion losses of nanoparticles, the fast FCE has to be located as close as possible to the exit of the DMA, and it features high input flow rate (Wimmer et al. 2008). The preferred approach is to have the GRIMM FCE attached to the exit of DMA to measure the concentrations of monodispersed particles immediately after their classification in high resolutions. In this case, particles with adequate charges pass through the FCE.

Concentration detection limit: TSI SMPS employing CPC has a higher particle concentration limit; while, the GRIMM FCE has a lower detection limit of particle concentration. The Faraday cup electrometer is able to detect 0.35 fA, which is equivalent to 65 charges/cm^3 at 2lpm, or to the noise level of 650 particles/cm^3 with about 10% uncertainty. Thus, measurement with the FCE is more reliable at high particle concentrations rather than low ones.

In this chapter, a performance of a brand new scanning mobility particle sizer coupled with a Faraday cup electrometer (SMPS+E, GRIMM 7.860) to measure particle number concentration distribution is investigated. Both NaCl and WOx nanoparticle number concentration distributions were tested. WOx particles were generated at various particle number concentration distributions in the range of 0.8 to 30 nm. NaCl particles were generated in two particle number concentration distributions in the range of 10 to 130 nm. The effects of instrumental parameters such as the sheath air flow rate, sample air flow rate and number of channels, on the particle number concentration distribution measurement were investigated.

3.3 Materials and Method

Figure 3-2 shows the schematic diagram of the experimental setup used for measuring the airborne nanoparticle number concentration distribution. This setup consisted of an aerosol generator, an

emission sampling system, and a measurement system. In order to minimize the particle losses in the setup, the shortest possible pipe lengths were selected.

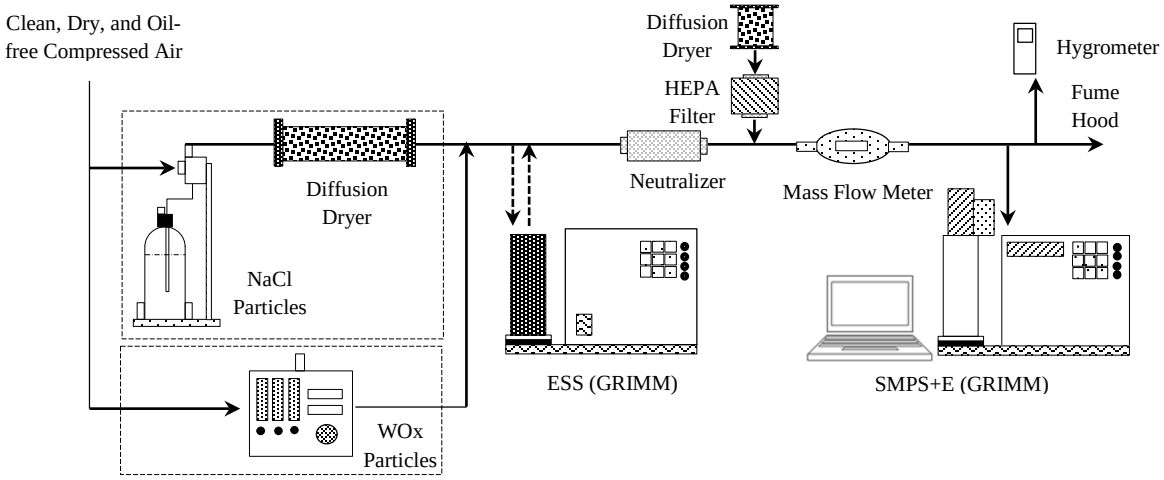

Figure 3-2. Schematic diagram of the experimental setup

In this study, two types of particles were used: NaCl and WOx. A constant output atomizer (TSI model 3076) was employed to generate polydispersed NaCl particles, typically greater than 10 nm. A filtered air supply (TSI, Model 3074) was employed to provide dry, filtered air at a regulated pressure. NaCl material (Sigma-Aldrich) was mixed with fresh distilled water at 0.01 g/liter and 0.1 g/l. The compressed air pressure applied to the atomizer was between 10 psi and 35 psi.

A tungsten oxide generator (GRIMM Aerosol techniK, Model 7.860) was used to generate nanoparticles in the range of 0.8 nm to about 30 nm. Using evaporation/condensation mechanisms, a piece of tungsten filament is evaporated by indirect heating in a small ceramic tube. The filament changes its color to white when it used up. The size and concentration of WOx nanoparticles can be controlled by adjusting three air flows: the tungsten air flow, carrier air flow, and diluting air flow. The hot WOx vapor then contacts the carrier air flow to induce homogeneous condensation. Diluting air flow is used to adjust the particle size range and concentration level and to avoid coagulation. The tungsten air flow is in the range of 1.6-16 $l.h^{-1}$; the carrier air in the range of 50-500 $l.h^{-1}$, and the diluting air in the range of 180-1800 $l.h^{-1}$. With this device, particles down to 0.8 nm can be generated and their size distribution remained steady during the experiment. The generated nanoparticles are highly

charged due to the effect of the thermoemission of electrons in the ceramic tube (Heim et al. 2010; Peineke and Schmidt-Ott 2008).

The generated aerosols (either NaCl or WOx) were passed through the diffusion dryer (TSI, Model 3062) to become dry. The generated nanoaerosols were highly charged, and they were passed through a radioactive neutralizer (Staticmaster Model P-2031) that employed a radioactive source $_{210}$PO of ~20 mCi activity, where Boltzmann charge equilibrium was expected. Similar to the approach of Kim et al. (2006), nitrogen gas was introduced into the bipolar charger continuously for a few hours to purge the device. The neutralized particles were then mixed and diluted with dried and clean air upstream from the filter in order to reach the desired flow rates at atmospheric pressure.

An air emission sampling system (ESS, GRIMM Aerosol techniK, Model 7.860) was employed to dilute the nanoaerosols concentration. ESS is usually used to sample nanoparticles directly from a hot exhaust gas with a temperature up to 500 ^{o}C. ESS contains one or two dilution stages that are employed to dilute the generated nanoparticles by re-circulating mass flow. Dilution air and sample air are mixed in a counter flow mixer in a sampling probe, before passing through the aerosol cooler to reach room temperature. The dilution system is mainly used to prevent condensation of nanoparticles and formation of new particles, to reduce the particle concentration at the detection limit of the measurement device, and to reduce the sample temperature to the range required by the measurement. In this study, the ESS was employed to dilute tested nanoaerosols prior to measurement device. At the sample flow rate of 1 lpm, the dilution ratios are 1:10 and 1:100 for the first and second dilution stages, respectively.

A hygrometer (Control Model 9020526) was employed to measure the relative humidity and temperature of the air stream. A pre-calibrated mass flow meter (TSI Model 4043) and an upstream valve were employed to regulate the aerosol flow rate to a desired rate. The mass flow meter measures the flow rate up to 200 STD lpm, along with the pressure and temperature of the flow. The volumetric flow rate (Q), as a function of the standard flow rate (Q_{STD}), temperature and pressure, is calculated using Eq.(3-6) following the manual instruction.

$$Q = \mathrm{Q}_{STD}\left[\frac{273.15 + T}{273.15 + 21.11}\right]\frac{101.3}{P_m} \tag{3-6}$$

where T (^{o}C) is the measured air temperature, and P_m (kPa) is the absolute pressure.

An isokinetic sampling probe downstream of the filter was used for aerosol sampling, and air samples were directed into the SMPS+E. For nanoparticles, the effect of isokinetic sampling was observed to be negligible on sampling efficiency (Appendix A). The SMPS+E (GRIMM Aerosol Technik, Model 7.80) was brand new and calibrated by the supplier right before the experiments. Two different DMA columns (S-DMA 55-100, M-DMA 55-340) were used in this study, in order to get the nanoparticle concentration data for a wider range of particle sizes. The recommended scan time of 300 s was used for scanning particle number concentration distributions for stable incoming aerosols (Erickson et al. 2007).

3.4 Results and Discussions

3.4.1 Feed nanoparticle characterization

The size distribution of nanoparticles has to be stable, repeatable, and reproducible (Giechaskiel et al. 2008). Thus, parameters affecting the generated particle number concentration distribution were investigated to ensure stable feed aerosols were used.

3.4.1.1 Constant output atomizer

Figure 3-3 shows the aerosol flow rate as a function of applied air pressure. It shows that aerosol flow linearly depends on the applied pressure, as its value increases at higher applied pressure. The aerosol flow rate was adjusted to 1 lpm, which is the air flow rate at the lowest applied pressure of 10 psi, for all the following experiments.

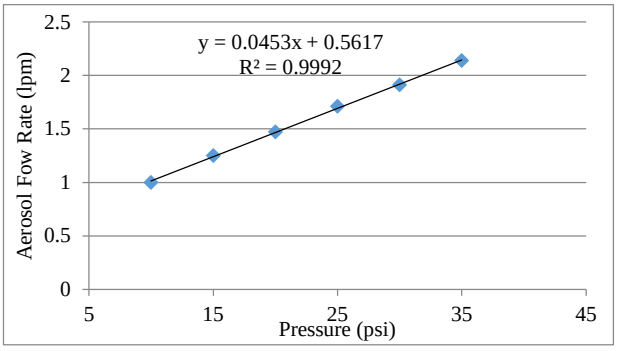

Figure 3-3. Aerosol flow rate as a function of applied pressure

Figure 3-4 and Figure 3-5 show the nanoparticle number concentration distributions versus particle diameter at applied voltages in the range of 10 psi and 35 psi at two different salt concentrations of 0.01 g/l and 0.1 g/l, respectively.

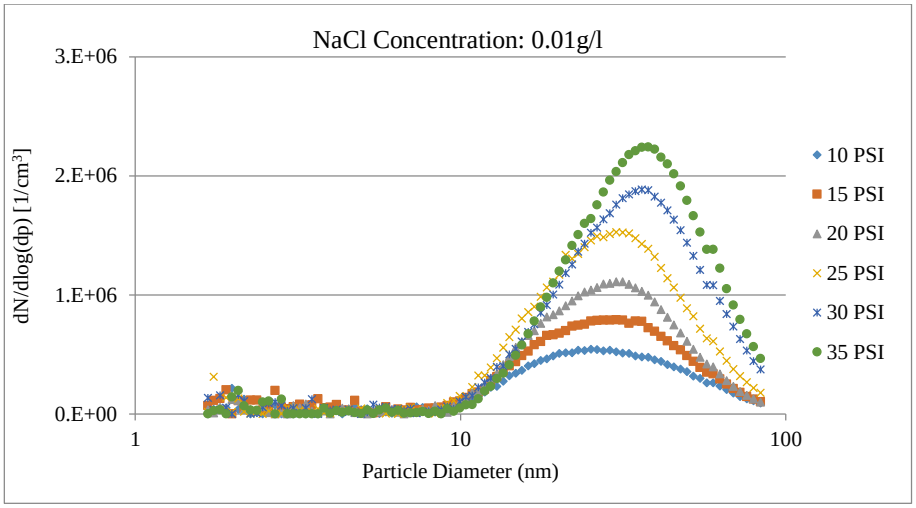

Figure 3-4. Particle number concentration distributions of NaCl nanoparticles at 0.01 g/l salt concentration

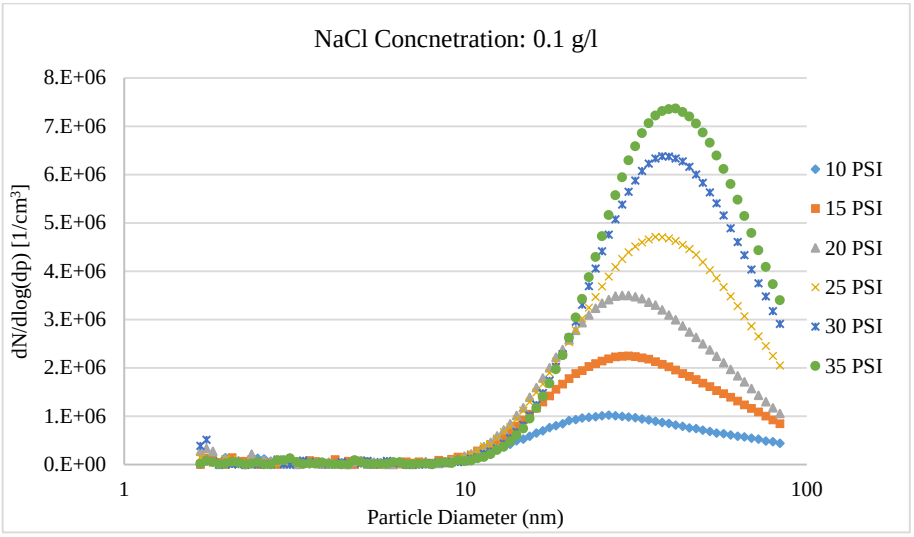

Figure 3-5. Particle number concentration distributions of NaCl nanoparticles at 0.1 g/l salt concentration

Results in Figure 3-4 and Figure 3-5 show that the particle number concentration distributions of generated nanoaerosols depend on both applied pressure and NaCl concentration in the solution. The particle number concentration distributions of NaCl particles at two different salt concentrations and three applied pressures of 10, 20, and 30 psi are shown in Figure 3-6 for easy comparison. It shows that particle concentration increases as either the applied pressure or salt concentration increases. Figure 3-7 shows that the mean number concentration increased linearly as a function of applied pressure at both NaCl concentrations.

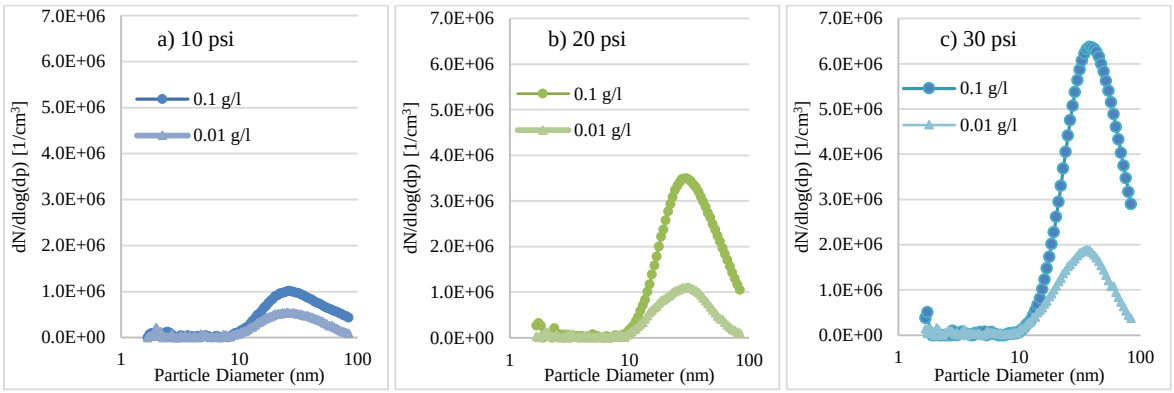

Figure 3-6. Particle number concentration distributions of NaCl nanoparticles at an aerosol flow rate of 1 lpm

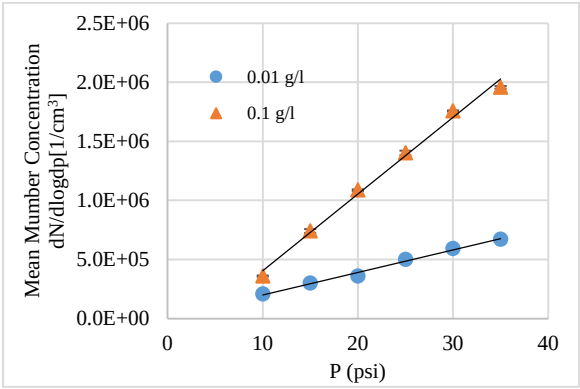

Figure 3-7. Mean number concentration of NaCl particles as a function of applied pressure

Experimental results also show that the geometric mean diameter is a function of both applied pressure and salt concentration (Figure 3-8). The mean particle diameter for higher salt concentration

is greater than the one for lower concentration. The results also show that the mean particle diameter increases linearly as the applied pressure increased.

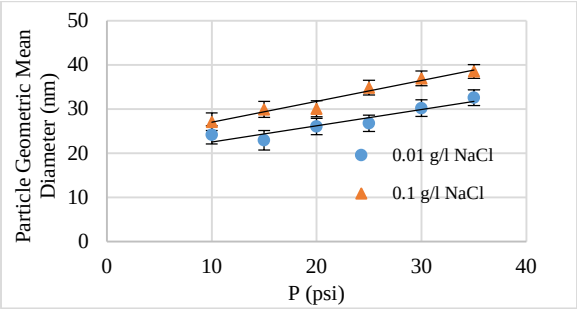

Figure 3-8. Geometric mean particle diameter

Figure 3-9 shows the effect of sodium chloride concentration in the solution on the generated particle concentration as a function of particle diameter measured at 1 lpm aerosol flow rate. The ratio was determined for all of the applied pressures (10, 15, 20, 25, 30 and 35 psi), and their averages with standard deviations shown. As the concentration of sodium chloride in the solution is increased to 10 times the first value, the particle concentration increases; however, the rate of increase is greater for larger particles.

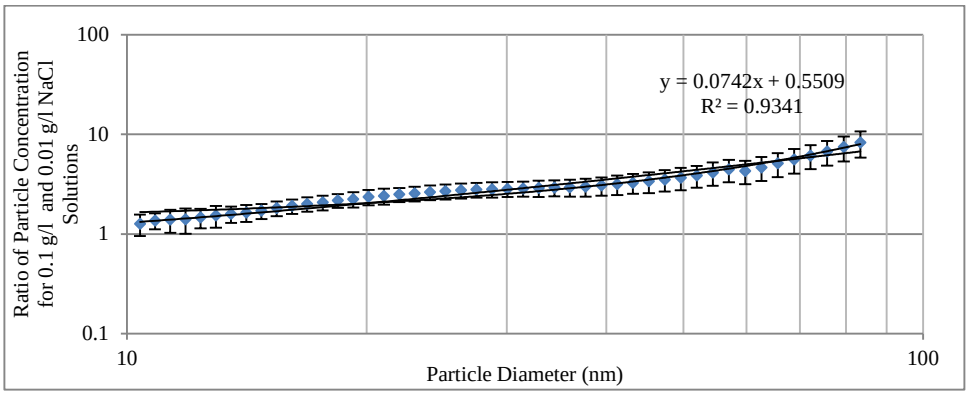

Figure 3-9. Ratio between NaCl particle concentration for 0.1 and 0.01 g/l salt

3.4.1.2 Tungsten oxide generator

Three factors are important for generated tungsten oxide nanoparticles: the tungsten air flow rate, carrier air flow rate, and diluting air flow rate. From now on, I will always use these three flow rates as

the specifications of the generated tungsten aerosols. For example, WOx 6 50 100 shows that the tungsten air flow is 6 $l.h^{-1}$, carrier air flow is 50 $l.h^{-1}$ and diluting air flow is 100 $l.h^{-1}$. The effects of these flow rates on generated nanoparticle number concentration distribution are investigated in the following.

A. Effect of tungsten air flow rate on generated nanoparticle number concentration distribution

The nanoparticle number concentration distribution for the three different tungsten air flow rates (6, 9, and 11 $l.h^{-1}$) for a carrier air flow of 50 $l.h^{-1}$, and without diluting air flow is shown in Figure 3-10. The effect of tungsten air flow rate on the size of generated nanoparticles is negligible; however, it is significant for the concentration of nanoparticles. As the tungsten air flow increases, the particle concentration increases.

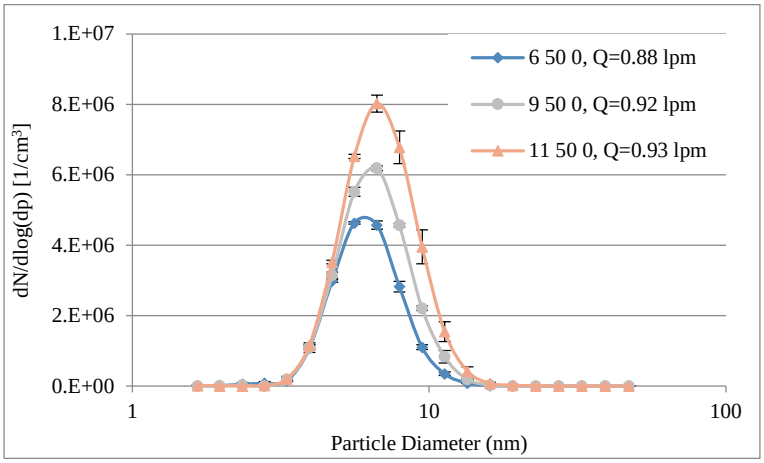

Figure 3-10. Particle number concentration distributions at different tungsten air flow rates (a, b, c in the figure present the tungsten air flow rate, carrier air flow rate and diluting air flow rate in the WOx generator, respectively)

B. Effect of carrier air flow rate on generated nanoparticle number concentration distribution

The nanoparticle number concentration distribution for four different carrier air flow rates (50, 100, 200, 300 and 400 $l.h^{-1}$) is shown in Figure 3-11. As the carrier air flow increases, the geometric mean

particle diameter decreases as shown in Figure 3-12. However, the effect of carrier air flow on particle concentration is not straightforward. The trend is increased at first and then decreased.

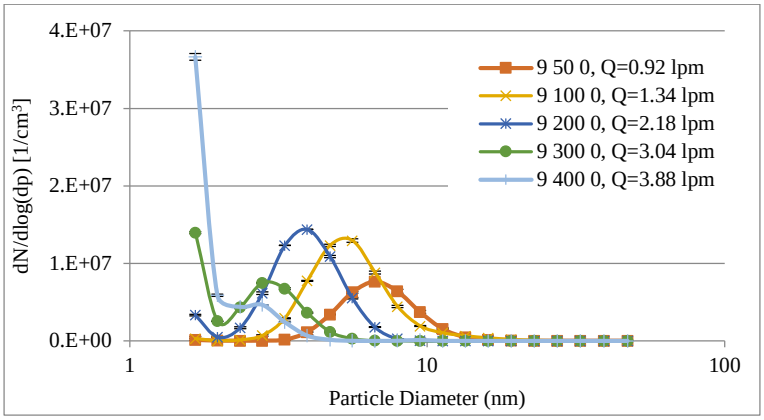

Figure 3-11. Particle number concentration distributions at different carrier air flow rates (a, b, c in figure present tungsten air flow rate, carrier air flow rate and diluting air flow rate in WOx generator, respectively)

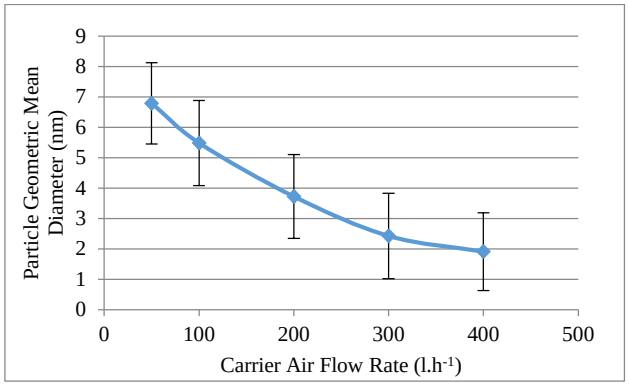

Figure 3-12. Geometric mean particle diameter as a function of carrier air flow rate

C. Effect of diluting air flow rate on generated nanoparticle number concentration distribution

Figure 3-13 shows the nanoparticle number concentration distribution for four different diluting air flow rates (0, 200, 300, and 400 $l.h^{-1}$). Without diluting air flow, larger particles are generated; however, increasing the diluting air flow rate generates smaller nanoparticles, at higher concentrations.

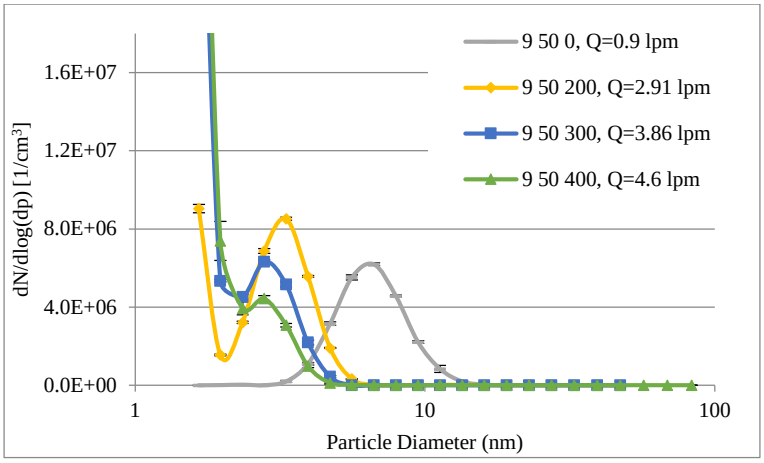

Figure 3-13. Particle number concentration distributions at different diluting air flow rates (a, b, c in figure present the tungsten air flow rate, carrier air flow rate and diluting air flow rate in WOx generator, respectively)

3.4.2 Parameters considered for SMPS+E

As explained, a number of parameters are involved when the particle number concentration distribution is measured using SMPS+E. Employing GRIMM SMPS+E is relatively new, and to the best of our knowledge, almost no studies have been studied the effects of these parameters on nanoparticle number concentration distribution measurement. Thus, this section explains the effect of these parameters and methods to detect nanoparticles in higher resolutions to measure the particle number concentration distribution.

One of the important parameters that may cause errors in particle classification is mobility shift, which is affected by the number of channels and the ratio of the sheath air to sample air flow rate. Another parameter that causes errors in measurement is the low particle concentration limit of FCE, which will be discussed in this section.

3.4.2.1 Number of channels

The number of channels shows the number of stepwise applied voltages to a DMA. Channel width is a function of sample air, sheath air, DMA temperature, and DMA pressure. Figure 3-14 shows the transfer function of an S-DMA for sheath air to sample air flow ratios of 5:1 and 10:1 for four different numbers of channels. This figure shows the transfer function for a lower particle detection limit up to

4 nm. Particles with diameters in the area of each triangular transfer function are classified as having the same particle diameter in each channel. It is shown that the particle diameter bandwidth is greater at larger particle diameters. The electrical mobility of larger particles is smaller (Eq.(3-2)), which leads to the smaller particle electrical mobility bandwidth (Eq.(3-5)) and larger particle diameter bandwidth.

Comparison of figures in the same columns shows the effect of the number of channels on particle classification. As expected, the lower particle size detection limit is constant for different numbers of channels. For smaller numbers of channels, triangular transfer functions have no intersection with each other (12 channels for a 5:1 ratio, and 12, 23 channels for a 10:1 ratio). Thus, particles with a diameter between these triangular transfer functions are not classified because they lie outside the channels, which leads to significant errors in the measurement. At larger numbers of channels, triangular transfer functions may intersect with one another, and as the number of channels increases, the intersection areas of triangular transfer functions increases. Thus, any channels that intersect with each other can classify particles. This issue is the main reason for measurement errors and mobility shifts of particles. Consequently, to minimize the mobility shift errors, the number of channels must be optimized. The optimized number of channels for the sheath air to sample air flow rate ratios of 5:1 and 10:1 are 23 and 45, respectively. With these numbers of channels, the tested particle range are classified with the minimum intersections, which minimizes mobility shift.

Comparison of the paired results in the various rows in Figure 3-14 shows that as the ratio of sheath air to sample air flow rate increases, both the particle lower detection limit and particle diameter bandwidth decreases. Thus, the higher ratio of sheath air to sample air flow rate leads to more accurate classification of polydispersed particles.

To better understanding the effect of number of channels on particle number concentration distribution measurement, Figure 3-15 and Figure 3-16 show the particle number concentration distributions measured at three numbers of channels (23, 45, and 89) for WOx and NaCl particles, respectively, with the same sheath air to sample air flow rate ratio of 5:1. The number of channels shows the number of particle size intervals; thus, the size range of particles in each bin is determined based on the chosen number of channels and the number of particles is measured for the selected bin size. As a consequence, the particle number concentration distribution chart is chosen to determine the number of channels on the measurement performance of SMPS+E.

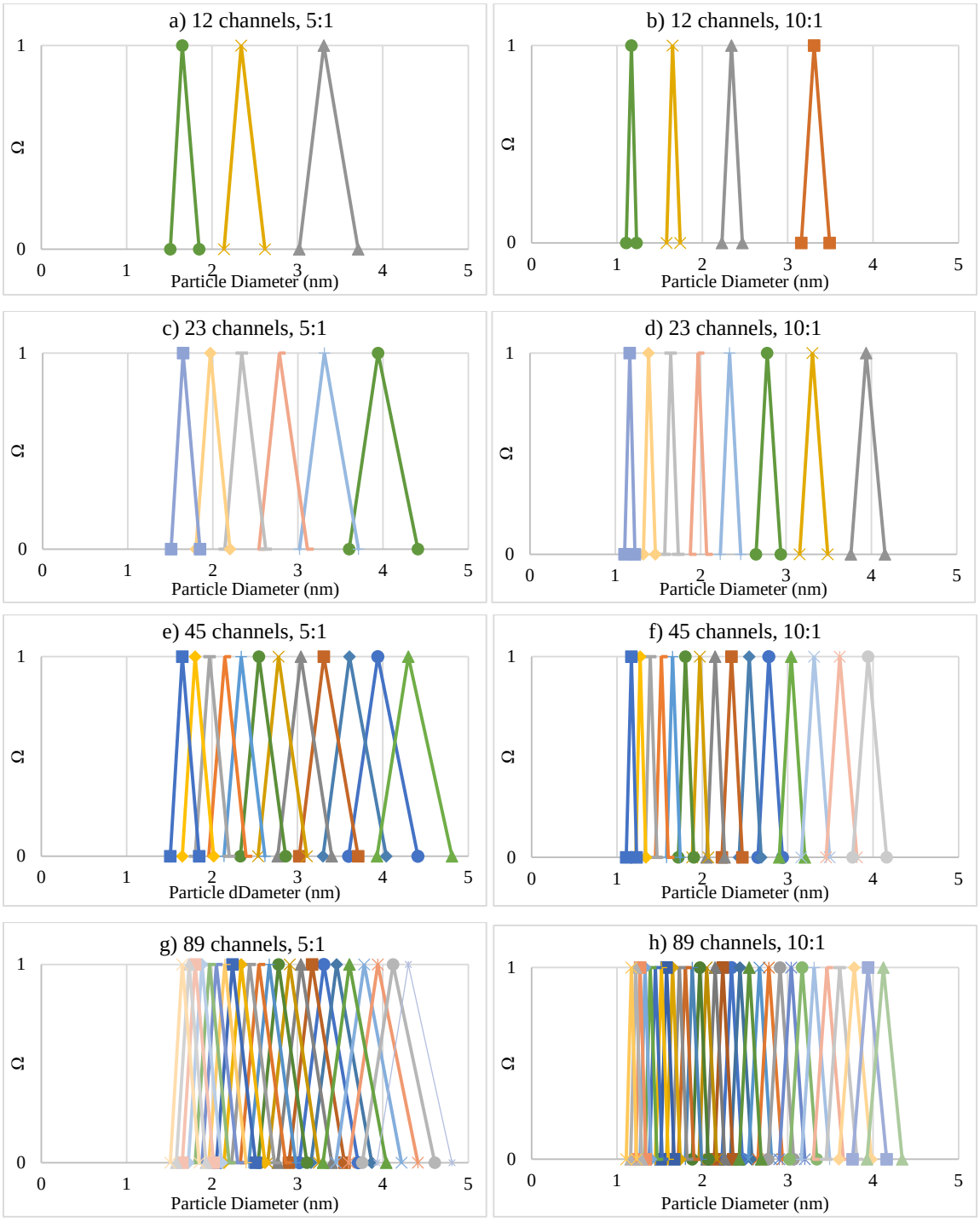

Figure 3-14. TRF of the DMA for various numbers of channels and sheath air to sample air flow rate ratios

Comparing the particle number concentration distributions for different numbers of channels shows that, for both NaCl and WOx particles, both the geometric mean diameter and total particle concentration slightly increase; but not statistically significant (Table 3-3). As the number of channels increases, the intersection area between triangular transfer functions increase, which may cause particles with electrical mobility in intersection areas to be classified by either of the neighboring channels. The increases in particle concentration for larger numbers of channels are more obvious in the peaks of particle number concentration distributions in both Figure 3-15 and Figure 3-16; but these increases are not significant (less than 2% difference at the concentration of mode size). In this study, in order to minimize possible errors, the number of channels is selected based on the sheath air to sample air flow rate ratio and by considering minimizing the intersection areas between the DMA transfer functions (Figure 3-14). The recommended numbers of channels are 23, 45 and 89, for the sheath air to sample air flow rate ratios of 5, 10 and 20, respectively.

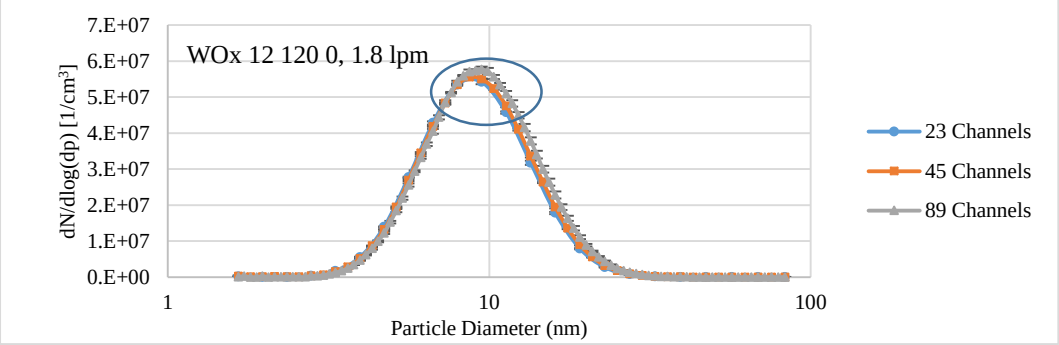

Figure 3-15. WOx particle number concentration distribution measurements at three different numbers of channels

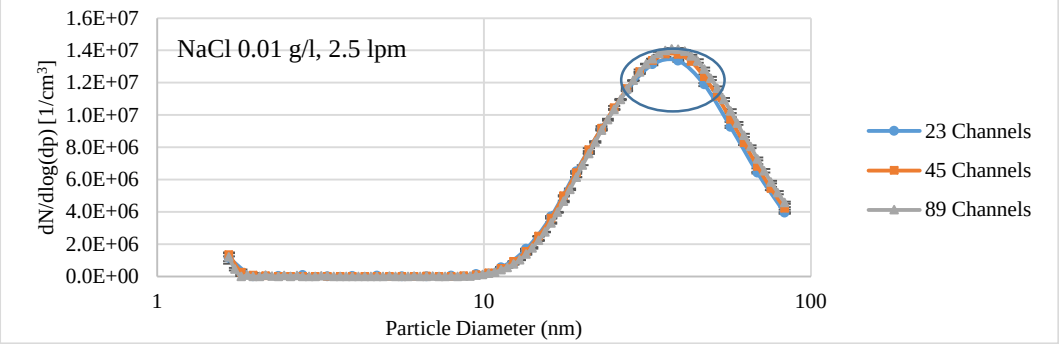

Figure 3-16. NaCl particle number concentration distribution measurements at three different numbers of channels

Table 3-3. Geometric means and total particle concentrations for particle number concentration distributions in Figure 3-15 and Figure 3-16

Number of channels	WOx particles (Figure 3-15)			NaCl particles (Figure 3-16)		
	23	45	89	23	45	89
Geometric Mean Diameter (nm)	8.97 ±1.46	9.12 ±1.47	9.25 ±1.146	33.79 ±1.81	34.77±1.68	35.46±1.64
Total Particle Concentration $x10^4$ (1/ccm)	2310±77.4	2340±10.1	2450±43.3	733±1.63	739±9.14	740±2.17

3.4.2.2 Effect of sheath air to sample air flow rate ratio on measured particle number concentration distribution

Figure 3-17a shows WOx (2-22 nm) and NaCl (10-83 nm) particle number concentration distributions at an aerosol flow rate of 2.25 lpm for three different sheath air to sample air flow ratios (5:1, 10:2, and 10:1). S-DMA classifies particles up to 56.79 nm, and 83.11 nm for a sheath air flow rate of 10 lpm, and 5 lpm, respectively (More explanation in 3.4.2.3).

Surprisingly, results showed that for both particle types, particle number concentration distribution measurement depends strongly on the selection of sheath air and sample air flow rate ratios. The selection of sheath air to sample air ratio of 5:1 for NaCl particles gives the highest particle concentration (a peak concentration of $1.2x10^7/cm^3$ @32.75 nm for NaCl, and $8x10^7/cm^3$ @7.26 nm for WOx); which followed by the sheath air to sample air ratios of 10:1 (a peak concentration of $5.5x10^6/ cm^3$ @32.75 nm for NaCl, and $2.9x10^7/cm^3$ @7.26 nm for WOx), and 10:2 (a peak concentration of $4.1x10^6/ cm^3$ @32.75 nm for NaCl, and $2.4x10^7/cm^3$ @7.26 nm for WOx).

For the sheath air to sample air ratio of 20:2, the GRIMM SMPS could not give valid data for particle concentration measurement, so it is not shown in the figure. In this case, the sheath air flow rate entering the DMA diluted the introduced aerosol flow, causing a much-diluted aerosol flow to enter the FCE. The particle concentration in the FCE is lower than the detection limit of the system ($\sim10^3 /cm^3$), leading to the invalid data. Thus, the higher the sheath air flow rate, the more diluted the aerosol flow exiting the DMA, which cause low measured particle concentration issue in FCE.

Overall, the results in Figure 3-17a show that although the peak concentration occurs with the same particle size for the selected sheath air to sample air flow rate ratios, the corresponding particle number

concentrations differ. The sheath air flow rate introduced through the DMA affects the concentrations of polydispersed particles entering the DMA, and the new particle concentration is measured with an FCE. Comparison between the measured particle number concentration distributions for sheath air flow rate to sample air flow rate ratios of 5:1 and 10:1 in Figure 3-17a shows that the higher the sheath air flow rate, the lower the particle concentrations introduced through the FCE, a situation that decreases the particle concentration measurement. The difference between these particle number concentration distributions shows that the GRIMM SMPS+E software does not have the correction factor to determine the original particle number concentration distribution measurement (i.e., the particle number concentration distribution introduced into the DMA).

Figure 3-17b shows the normalized particle size distributions for both WOx and NaCl particles. The normalized particle size distributions for NaCl particles are the same for all three sheath air to sample air flow rate ratios, and no mobility shift is observed. For WOx particles, the particle sizes for the peak for three sheath air to sample air flow rates are the same; however, the normalized peak with a sheath air to sample air flow rate of 2:10 differs by 3% from that with a 1:10 sheath air to sample air flow rate. Thus, changes in the sample air flow rate did not cause mobility shift of particles. However, the polydispersed particle number concentration distribution measurement of sub-100 nm at sample air flow rates of 1 lpm and 2 lpm in TSI SMPS showed a particle mobility shift to smaller particles at a sample air flow rate of 2 lpm (Lasher 1999). In this case, the particle diameter for peak concentration shifted at least 6 nm to smaller particles, when the sample air flow rate was increased from 1 lpm to 2 lpm. The same result was not observed for the measurement of monodispersed polystyrene sphere particle, because of the delayed time calculation in TSI SMPS or insufficient bipolar chargers at high polydispersed sample air flow rates (Lasher 1999). Thus, employing GRIMM SMPS+E is one of the best options for particle number concentration distribution measurement as it eliminates the unwanted mobility shift of nanoparticles.

It has been shown that for the aerosol flow rate (2.25 lpm) in Figure 3-17, all three sheath air to sample air flow rate ratios (5:1, 10:1, and 10:2) can be employed to measure nanoparticle number concentration distributions. However, in some cases, based on the aerosol flow and original particle concentrations, employing a sheath air flow rate of 10 lpm is not the proper option. For example, Figure 3-18 shows that at a low aerosol flow rate of 1 lpm, the SMPS+E measures the particle number

concentration distributions of nanoparticles at sheath air to sample air flow rate ratios of 5:1, and in some cases 10:2. At sheath air flow rate to sample air flow rate ratios of 10:2 and 20:2, the GRIMM SMPS+E could not measure particle number concentration distribution accurately because the aerosol flow rate is lower than the sample air flow rate that introduces errors in the measurement. Also, for the sheath air to sample air flow rate of 10:1, aerosols were diluted to the particle concentration of lower than 10^3 /cm^3, and the FCE could not measure the particle concentration. Thus, at a low aerosol flow rate (~1 lpm), choosing the sheath air to sample air flow rate ratio of 5:1 is the only option in order to measure the particle size distribution with SMPS+E.

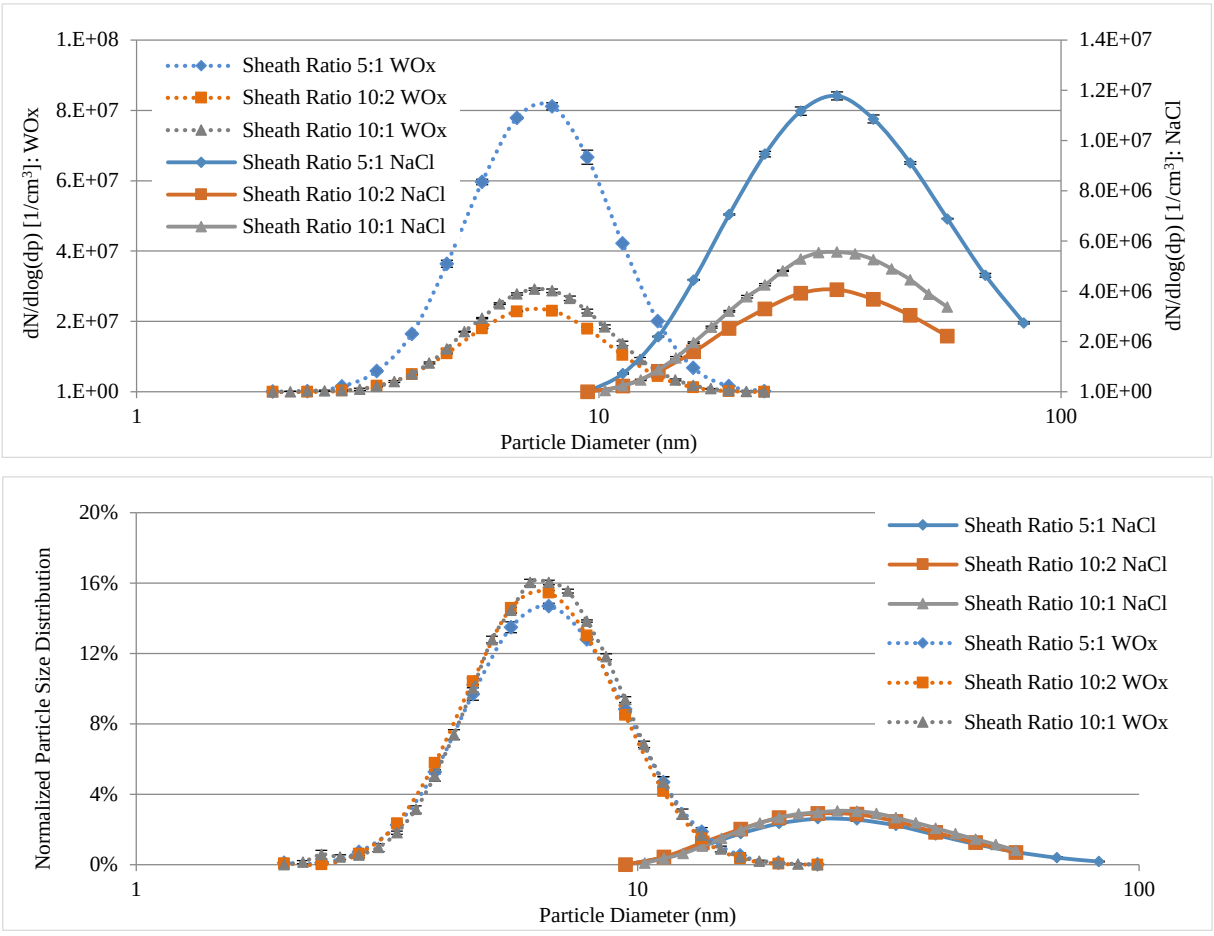

Figure 3-17. WOx and NaCl particle number concentration distribution and normalized particle size distribution measurements at an aerosol flow rate of 2.25 lpm

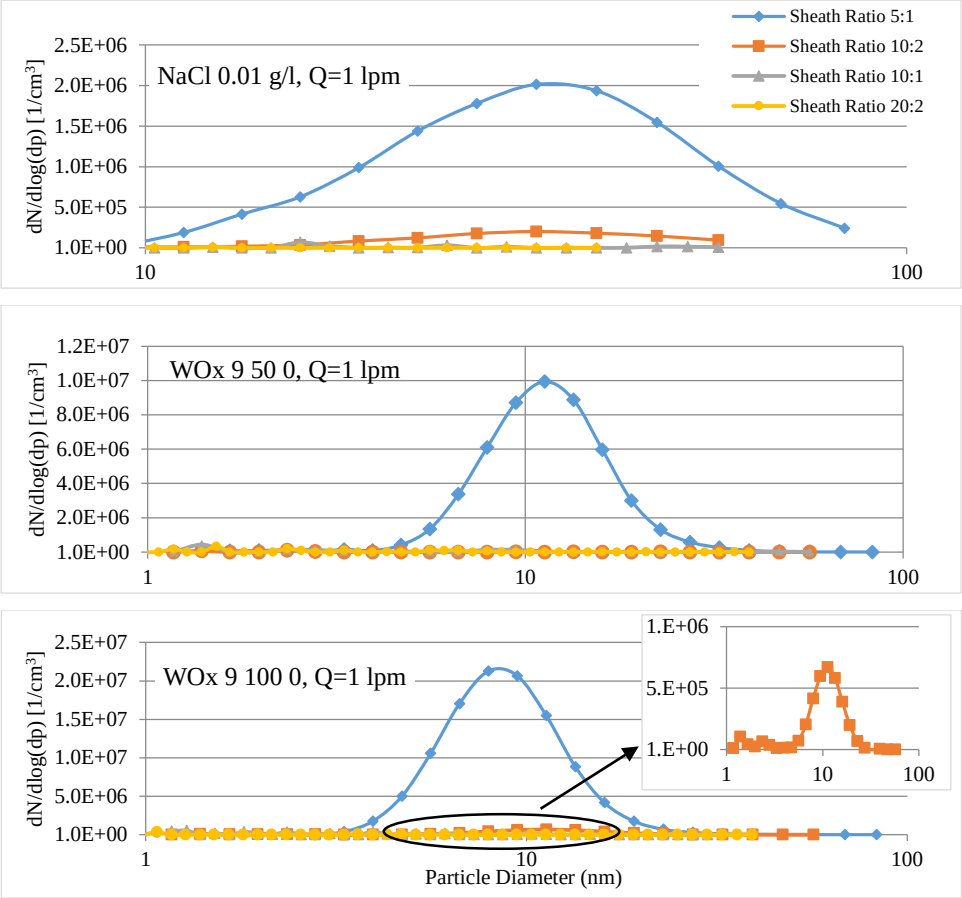

Figure 3-18. NaCl and WOx particle number concentration distribution measurements at different sheath air and sample air flow rates (WOx a, b, c in the figure present the tungsten air flow rate, carrier air flow rate and diluting air flow rate in the WOx generator, respectively)

Besides the aerosol flow rate, the initial particle concentration is also important to choose the sheath air to sample air flow ratio. Figure 3-19 shows the particle number concentration distribution of WOx particles at an aerosol flow rate of 1.5 lpm for two different WOx filaments. Results show that the sheath air to sample air flow rate ratios of 5:1, 10:2, and 10:1 could be employed to measure particle number concentration distribution in Figure 3-19a. However, when the peak particle concentrations decreased by the order of two magnifications, only the sheath air to sample air flow rate ratio of 5:1 could be employed. Thus, employing a sheath air flow rate of 10 lpm diluted particles to a level lower than the detection limit of the device. Therefore, the selection of sheath air to sample air flow rate ratio depends strongly on both the aerosol flow rate and original particle concentration.

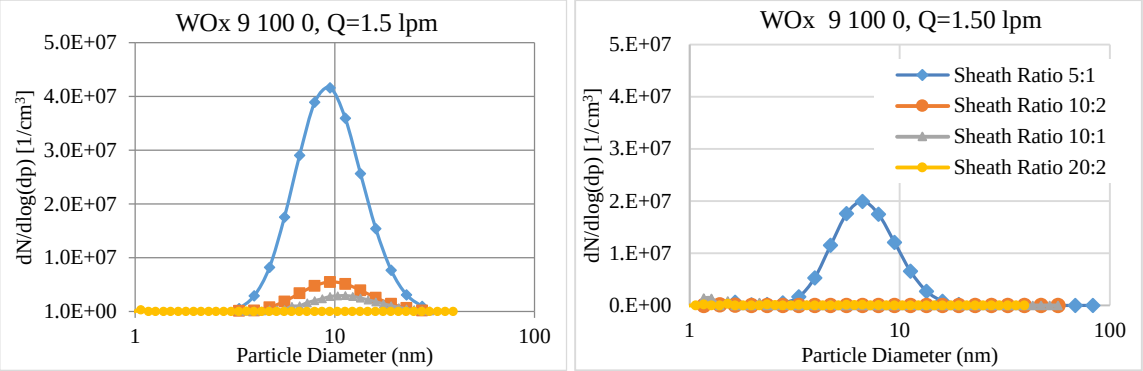

Figure 3-19. WOx particle number concentration distribution measurements at different sheath air and sample air flow rates (WOx a, b, c in figure present the tungsten air flow rate, carrier air flow rate and diluting air flow rate in WOx generator, respectively)

The DMA design also affects particle number concentration distribution measurement. A short height is used for classification of nanoparticles. The short height reduces the residence time of aerosols in the DMA, minimizes the diffusion loss and improves the transfer function. The same effects can be obtained by employing a high sheath air flow rate and sample air flow rate (Wang and Tronville 2014). Previous studies showed that, for TSI SMPS, the recommended sheath air to sample air flow rate ratio was 10:1 (Japuntich et al. 2007); however, due to the differences in the DMA designs of GRIMM and TSI, the recommended sheath air to sample air flow rate ratio for GRIMM DMA could be different. The height of the DMA in TSI (Nano DMA 3085: 203 mm, Long DMA 3081: 610 mm) is larger than that of the GRIMM S-DMA (total height: 157 mm, active length of electrode: 15 mm). Thus, particles have smaller residence time in the GRIMM DMA than in the TSI DMA, leading to less diffusion loss. Thus, in GRIMM DMA, the same monodispersity of particles can be achieved at a lower sheath air to sample air flow rate ratio.

Although high sheath air to sample air flow rate ratio minimizes the mobility bandwidth of classified nanoparticles and improves the monodispersity of particles (Eq.(3-5)), it led to more diluted aerosols from the DMA, which caused low concentration issue for the counting device. Employing FCE GRIMM for particle counting has limitations in low particle concentrations and introduces errors; it is more accurate for higher particle concentrations. On the other hand, the CPC employed light scattering for counting nanoparticles, and as a result, it can detect particles with a greater accuracy at lower particle concentrations. Thus, due to the differences between GRIMM SMPS+E and TSI SMPS, the

recommended sheath air to sample air flow rate ratios differ. The recommended sheath air to sample air flow rate ratio for TSI DMA is 10:1, and this value can be decreased to 5:1 for the GRIMM DMA. As it has been shown previously that in some cases, the only way to measure particle number concentration distribution with GRIMM SMPS+E is by selecting the sheath air to sample air flow rate ratio of 5:1.

3.4.2.3 Effect of sheath air to sample air flow rate ratio on the lower and upper size detection limits

Figure 3-20 shows two different particle number concentration distributions of WOx particles. All of the sheath air to sample air flow rate ratios enable the measurement of generated sub-2 nm particle number concentration distribution, and the size range of measured particle number concentration distribution depends on sheath air flow rate. For a lower sheath air flow rate of 5 lpm, particles can be measured down to 1.65 nm; however, for a sheath air flow rate of 10 lpm, particles can be measured down to 1.17 nm, and the sheath air flow rate of 20 lpm for particles down to 0.83 nm. As the sheath air flow rate increases, smaller particles can be detected (Eq.(3-4)). Thus, for detecting small nanoparticles (sub-2 nm), the higher sheath flow ratio is recommended (20 lpm).

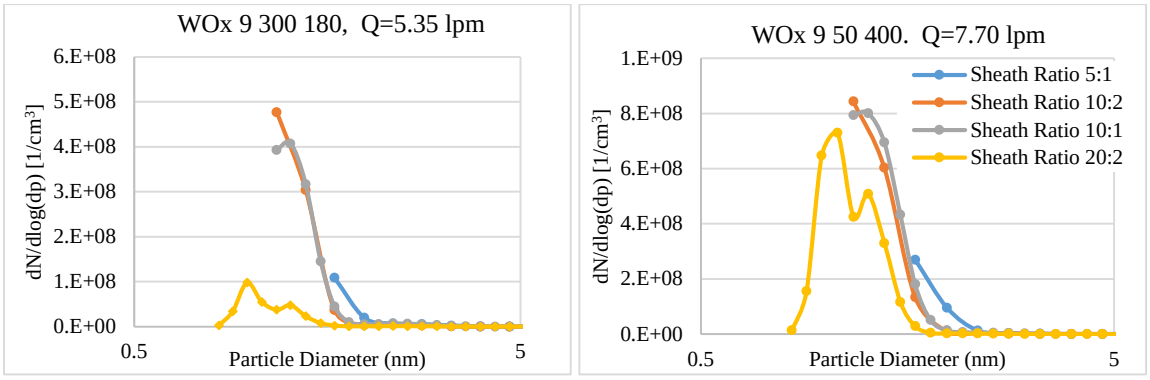

Figure 3-20. WOx particle number concentration distribution measurements at different sheath air and sample air flow rates (WOx a, b, c in figure present the tungsten air flow rate, carrier air flow rate and diluting air flow rate in the WOx generator, respectively)

Figure 3-21 shows the measured particle number concentration distribution of NaCl particles generated at two salt concentrations (0.01 g/l and 0.1 g/l), at four different sheath air and sample air flow rates. Results show that the sheath air flow rate also affects the upper size detection of particles.

In S-DMA the sheath air flow rates of 5 lpm, 10 lpm, and 20 lpm, can classify particles up to 82.92 nm, 56.65 nm, and 39.13 nm, respectively.

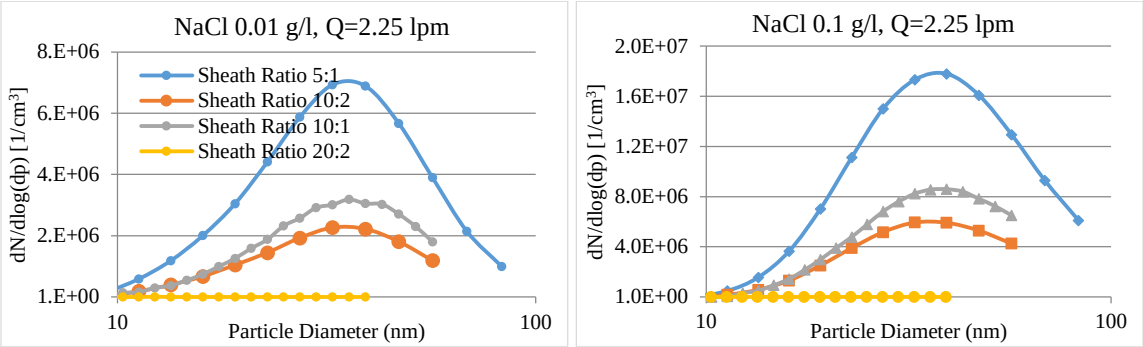

Figure 3-21. NaCl particle number concentration distribution measurements for two sodium chloride solutions at different sheath air and sample air flow rates

In order to better understand the previous experimental results, theoretical investigation of GRIMM SMPS theory was performed. Figure 3-22 shows the selected range of particle diameters as a function of applied voltage for six different values of sheath air and sample air flow rates. The mean particle diameter is calculated based on Eq.(3-4) and the lower and upper particle diameters are calculated based on the particle diameter bandwidth, which will be classified at a specific applied voltage (Eq.(3-5)). At each applied voltage, a narrow size distribution of particles exits from the DMA and is dependent on the selected sheath air to sample air flow ratio. As the applied voltage increases, both mean particle diameter, and particle diameter bandwidth increase (Eq.(3-4) and Eq.(3-5)).

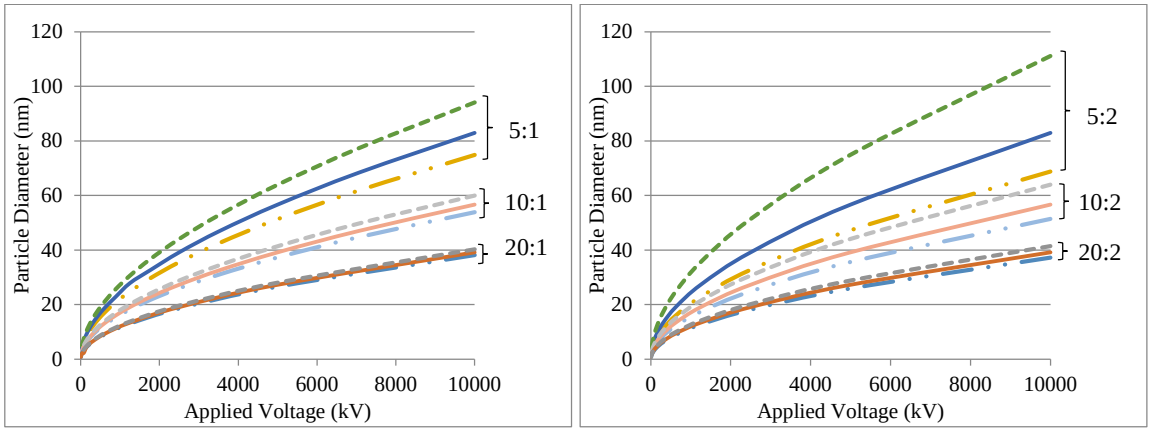

Figure 3-22. Particle diameter as a fucntion of applied voltage at various aerosol to sheath air flow rates (-------: upper particle diameter, _____: mean particle diameter, _ . . _: lower particle diameter)

Figure 3-22 shows the effect of sheath air flow rate on nanoparticle size classification. The detection size range of nanoparticles strongly depends on the sheath air flow rate. The detected range of nanoparticles for sheath air flow rates of 5, 10, and 20 lpm are 1.65<dp<82.93 nm, 1.17<dp<56.66 nm, and 0.83<dp<39.17 nm, respectively. As the sheath air flow rate increases, a narrower range of particles, with a narrower diameter bandwidth is detected, which leads to the measurement of particle number concentration distribution at higher resolution.

Comparison between Figure 3-22a and Figure 3-22b shows that as the sample air flow rate increases, the mean particle diameter does not change (Eq.(3-4)); however, the particle diameter bandwidth increases (Eq.(3-5)), which means more particles can be classified for a specified voltage. This feature led to particle number concentration distribution measurement with a lower resolution. Although more particles were classified at a higher sample air flow rate (less dilution), the mean particle diameter did not change as expected, which shows the high resolution of the measurement device for particle classification and prevents mobility shift at various sheath air and sample air flow rates. Since employing GRIMM SMPS did not show any mobility shift for different sample air flow rates, it can be used at high resolution for polydispersed particle number concentration distribution measurement, even at high sample air flow rates. However, in order to minimize the particle diameter bandwidth, a smaller sample air flow rate is recommended.

3.4.2.4 Determining the response time of SMPS+E

It has been shown that for multiple samples of polydispersed particles without purging between samples, large particles from the previous sample are counted as smaller ones in the next sample, resulting in artifacts in the TSI SMPS (Japuntich et al. 2007). Experiments were carried out to determine whether the purging time is necessary for our experimental setup employing the GRIMM SMPS+E. Figure 3-23 shows the original particle number concentration distribution along with three particle number concentration distributions when the SMPS+E was disconnected from the introduced upstream particle concentration, and connected immediately. The SMPS+E was disconnected only for about 2 s, which was nevertheless sufficient to cause changes in the introduced particle number concentration distribution.

For all three tests (1, 2 and 3 in Figure 3-23), the SMPS+E was disconnected when it was classifying particles of 19.17 nm. Results show that although the introduced particle number concentration

distribution was changed after these 19.17 nm particles were classified, the SMPS+E could still measure the next particle size, 16.06 nm, in their original particle concentrations, because of the residual samples in the system. However, for the other three particle sizes, 13.46 nm, 11.29 nm and 9.47 nm, the SMPS+E could not be measured in their original concentrations because of unstable particle concentrations introduced through the system. Therefore, measurement error occurs at a particle size of 16.06 nm, at which size the particle concentrations were not the same as the original ones; however, the GRIMM SMPS+E showed the original particle concentration. Each data point is the average of three concentration measurements with a time interval of ¼ s. Thus, the total time for the SMPS+E to measure the new particle number concentration distribution is less than 1 s (3 × ¼ s).

It is concluded that for even multiple sample measurements without purging time, the GRIMM SMPS+E measures the newly introduced particles at high accuracy. The fast response time of this device is because of the rinse air flow in the FCE which causes the FCE to be sensitive in particle concentration changes in about 200 ms. Thus, for this device, purging is not necessary between multiple samples.

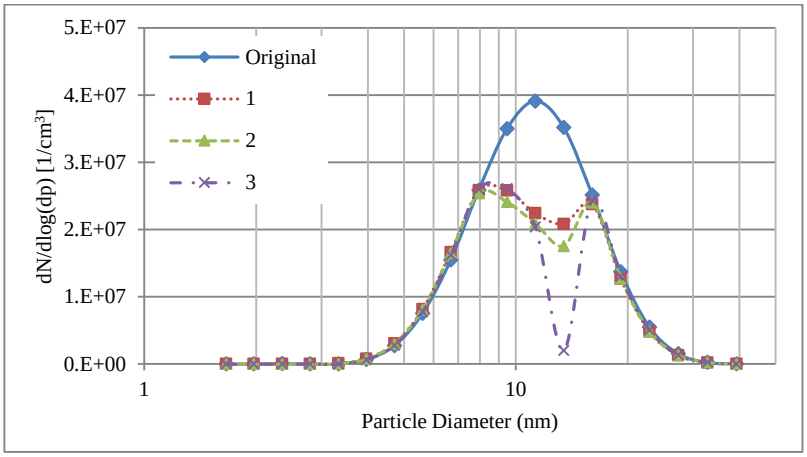

Figure 3-23. Particle number concentration distributions of WOx nanoparticles for the original and disturbed (1, 2 and 3) particle number concentration

3.4.3 The performance of emission sampling system for nanoparticle dilution

Figure 3-24 and Figure 3-25 show the original particle number concentration distribution of NaCl and WOx particles, at a sample flow rate of 1 lpm, respectively. The original particle number concentration distribution was diluted by employing ESS with one or two dilution stages for three replicated

experiments at low sampling probe temperature. Results showed that employing ESS using one or two dilution stages decreases the particle concentration for both NaCl and WOx nanoparticles. However, the calculated dilution ratios are not as specific as those claimed by the company (at a sample flow rate of 1 lpm, 10:1 and 100:1 for one and two dilution stages, respectively).

The first look at Figure 3-24 shows that the dilution ratios for each particle size for one and two dilution stages are about 10 and 100, respectively; however, the dilution ratio decreases for sub-20 nm particles. Calculations showed that the dilution ratios over a selected particle range employing one and two dilution stages are 5.83±5.88 and 41.35±48.69, respectively. The high standard deviation indicates the discrepancy between the dilution ratios for sub-20 nm particles and larger ones. Excluding sub-20 nm particles leads to having the dilution ratios of 12.23±1.28 and 98.87±23.94 for employing one and two dilution stages, respectively. Thus, for NaCl particles larger than 20 nm, the ESS properly diluted the introduced particles; however, the dilution ratio decreases for sub-20 nm particles. If the total particle concentration is considered, the dilution ratios are calculated as 11.34±0.17 and 70.25±3.98, for one and two dilution stages, respectively (dp>10 nm).

Figure 3-25 shows the particle number concentration distributions for sub-20 nm WOx particles. Although ESS is able to dilute generated particles, the dilution ratios for each particle size are not 10 or 100 for one or two dilution stages, respectively. The dilution ratio is much higher than the expected one associated with the high standard deviation for the tested size of WOx particles (38.36±76.79 and 3048.58±8420.25 for one and two dilution stages, respectively). Considering the total concentrations of particles for the tested sizes, the dilution ratios are calculated as 9.96±0.1 and 53.58±1.80, for one and two dilution stages, respectively. Thus, the ESS could work better to decrease the total particle concentration compared to reducing the particle concentration for each particle size.

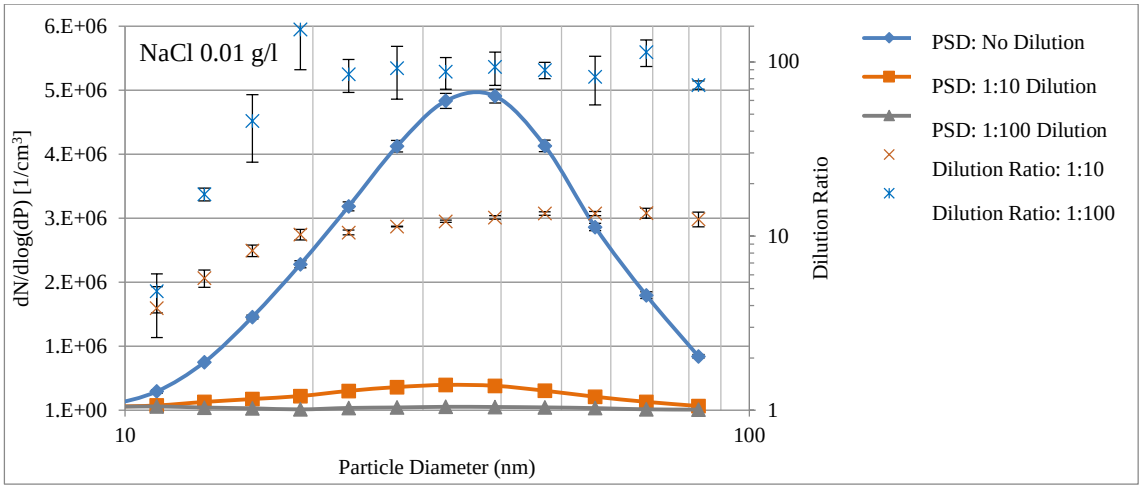

Figure 3-24. Particle number concentration distributions and dilution ratio for NaCl particles

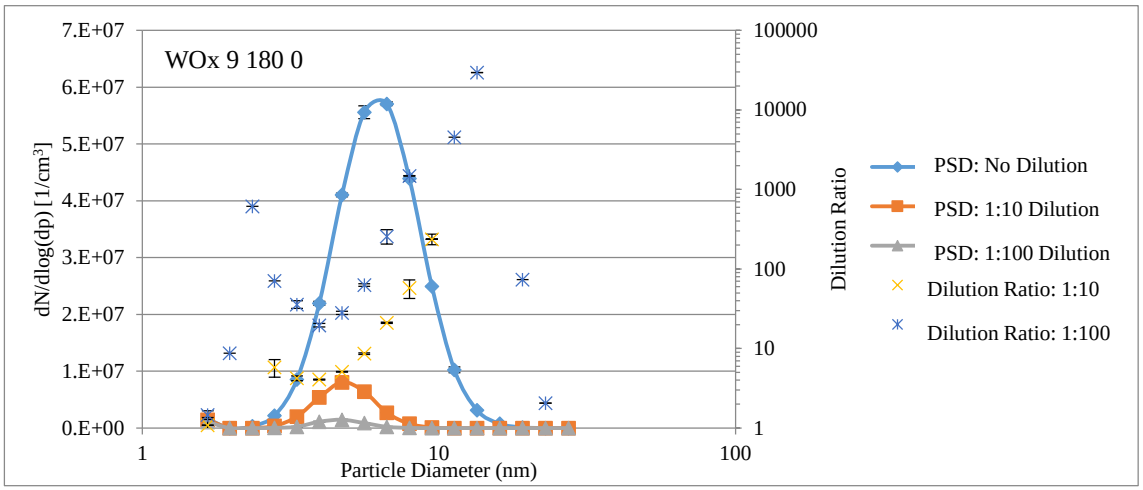

Figure 3-25. Particle number concentration distributions and dilution ratio for WOx particles

Various parameters, including the ESS design, particle size, particle loss, and aerosol temperature, may affect ESS performance. The GRIMM ESS employed re-circulating mass flow to dilute nanoparticles. In this case, a portion of the aerosol flow introduced into the ESS is filtered and then employed as a diluent. This factor is the main reason why the calculating the dilution ratio is impossible (Crayford et al. 2012). Employing ESS causes particles to pass extra tubes, resulting in more particle loss. It has been shown that the particle loss in the ESS increases as the size of nanoparticles decreases. The particle loss percentage of 100 nm graphite soot particles is about 25%, and that for 15 nm is about

45% (Crayford et al. 2012). Thus, this particle loss in the ESS is one reasons behind difficulty in calculating the dilution ratio.

Another possible reason for the dilution ratio to deviate from what was expected of the ESS manual is the temperature of the introduced aerosol flow. The ESS is usually employed for sampling aerosols from hot gas. However, in this study, the temperature of generated particles was about room temperature (22.6±0.4 ^{o}C), and the temperature of the sampling probe was set to 25 ^{o}C. In ESS, the diluting air is preheated prior to being mixed with the aerosol flow to avoid condensation. However, it seems that because of the low temperature of the sampling probe, the diluting air did not preheat, thereby increasing the re-condensation rates of nanoparticles. This effect was more dominant for smaller nanoparticles. Thus, due to the system design of ESS, its performance may be more efficient at high temperatures.

In summary, ESS is usually employed for sampling particles with concentrations higher than the detection limit of measurement devices. Consequently, if the original particle concentration is high, the ESS is employed to dilute particles, and then an original particle number concentration distribution is calculated by applying a correction factor (e.g., 10 or 100 for one or two dilution stages, respectively, at a sample flow rate of 1 lpm). However, as it has been shown in this study, this procedure is associated with significant errors, and it is not accurate to calculate the original particle number concentration distribution by applying a default dilution factor stated by the device. Thus, in this thesis ESS is employed to dilute particles; however, we cannot trust the dilution ratio set by the manual, and the new particle number concentration distributions should be considered instead of calculating the original particle number concentration distribution considering specified correction factors.

3.5 Conclusions

This chapter has discussed the experimental setup used to determine the performance of the scanning mobility particle sizer coupled with a Faraday cup electrometer (GRIMM SMPS+E 7.860) for the measurement of nanoparticle number concentration distribution. For this aim, the principals of the GRIMM SMPS+E were compared to those of the TSI SMPS. The GRIMM SMPS+E can measure particle number concentration distribution with stepping intervals down to ~0.1 s without producing artifacts, whereas TSI FCE 3068B is limited to time intervals larger than 1 s. The GRIMM SMPS classifies particles from large diameter down to smaller (lower electrical mobility up to larger electrical

mobility); however, the TSI works opposite direction. The GRIMM SMPS+E employed FCE to measure nanoparticle concentration; however, TSI SMPS employ CPC for that purpose. The difference between the designs of these two instruments caused their different performances. The FCE can measure particle concentrations up to 10^8 /cm^3 with a lower limit of 10^3 /cm^3. On the other hand, CPC can detect particles down to concentrations of 1 /cm^3, but it has limitations for higher particle concentrations, which depends on CPC type. On the other hand, FCE does not have a lower particle size detection limit; however, the CPC has a lower particle size detection limit due to its dependence on optical measurement. Thus, the investigations of the measurement devices showed that a state-of-the-art measurement method is required to minimize errors in nanoparticle number concentration distribution measurement to within an accepted level of confidence.

In this chapter, experiments were done to determine the GRIMM SMPS+E's performance for different particle types, particle sizes, and particle concentrations. Two types of NaCl and WOx particles at various particle number concentration distributions were tested. The parameters which need consideration in order to adjust the size distributions of generated particles were discussed in this chapter (e.g., number of channels, sheath air flow rate, sample air flow rate, response time). ESS performance was investigated, and results showed that although it can be used for diluting nanoparticle concentrations, the dilution ratio cannot be trusted, especially for sub-20 nm particles.

Employing GRIMM SMPS+E needs more attention to the following parameters: particle concentration, aerosol flow rate, sheath air flow rate, sample air flow rate, and particle properties. The selection of appropriate sheath air flow rates and sample air flow rates greatly depends on the initial particle concentration, size of nanoparticles, and aerosol flow rate. For low particle concentrations, a sheath air flow rate of 5 lpm is recommended; however, the sheath air flow rate can be increased to greater values for smaller nanoparticles or higher particle concentrations. It is recommended that the results to compare to those for TSI SMPS to gain better information about the selection of a sheath air to sample air flow ratio.

By the end of this chapter, the principals and performances of the GRIMM SMPS works accurately for nanoparticle number concentration distribution measurement were better understand. Thus, the GRIMM SMPS+E will be employed in the following chapters for filtration tests.

Chapter 4

Filtration of WOx Nanoparticles using Micron-sized Wire Screens

4.1 Summary

With the knowledge gained in Chapter 3, the GRIMM SMPS+E was employed to evaluate the filtration performance of the filters of interest. Although various studies have been done on employing SMPS for the measurement of nanoparticle filtration efficiency, there have been limited studies on the effects of filtration testing method (e.g., monodispersed or polydispersed particles) and instrumental operating parameters (e.g., sheath air to sample air flow rate ratios) on the measurement of nanoparticle filtration efficiency. Therefore, prior to the main goal of this chapter, which is evaluating the filtration efficiency of wire screens for various WOx particle number concentration distributions, the effects of these factors on the measurement of filtration efficiency were investigated.

Uncharged stainless-steel wire screens were used for testing the filtration of WOx and NaCl nanoparticles with a broad range of diameters and concentrations at different face velocities. Wire screens made of micron-sized wires were chosen because of the uniform structure of the wires in each single-layer screen. The filtration efficiency results for both monodispersed and polydispersed measurements agreed well, thus it is unnecessary to employ monodispersed particles in the filtration tests. Furthermore, the measured filtration efficiency showed that the sheath air to sample air flow rate ratios of 5:1 and 10:1 did not affect the measurement.

Results showed that NaCl and WOx particles behave differently in air filtration. The filtration efficiency for NaCl nanoparticles agreed with the conventional filtration theory of Cheng and Yuh (1980) for wire screens. The filtration efficiency increased as the size of NaCl nanoparticles decreased from 100 nm to 10 nm in diameter. Moreover, the filtration efficiency of NaCl particles decreased slightly as the particle concentration decreased. On the other hand, the measured filtration efficiency of WOx nanoparticles depended on upstream particle number concentration distributions. For particles smaller than the size of peak concentration (the left side of the particle number concentration distribution), the filtration efficiency followed the conventional filtration model, which decreased with increasing particle size. However, for particles larger than the size of peak concentration (the right side of the particle number concentration distribution), the measured filtration efficiency deviated from the

model prediction dramatically. This surprising behavior of WOx nanoparticles may be due to their different morphology, which affects both particle charging and measurement performance.

4.2 Introduction

Nanoparticle filtration has become a challenging research over the last few decades due to the growing concerns over the potential adverse impact of nanoparticles on human health (Ferreira et al. 2013; Kreyling et al. 2006a). Various studies have been conducted recently on the filtration of nanosized particles (Givehchi et al. 2015; Liu et al. 2011b; Rengasamy et al. 2009; Shaffer and Rengasamy 2009); however, there were disagreements between experimental and theoretical studies due to the complicated behaviour of nanoparticles down to 1 nm through filters (Givehchi and Tan 2014; Givehchi and Tan 2015; Kim et al. 2006).

Although various studies have been done on nanoparticle filtration efficiency, a standard method for nanofiltration testing is still lacking. Currently, two methods, monodispersed and polydispersed nanoparticles, are used for filtration test measurements in literature. In the first method, researchers employ a specific size of monodispersed particles classified by a DMA and use either a CPC (Alonso et al. 1997; Boskovic et al. 2005; Chen et al. 2013; Heim et al. 2005; Kim et al. 2007; Thomas et al. 2013; Yang and Lee 2005) or an electrometer (Furuuchi et al. 2010; Ichitsubo et al. 1996) for counting the particles. In this method, classified monodispersed particles, mostly carrying single ion, pass through a radioactive neutralizer to achieve Boltzmann charge equilibrium. Neutralized monodispersed particles are introduced through a filter; upstream and downstream particle concentrations are measured with a particle counter.

In the second method, researchers employ polydispersed particles and measure the particle number concentration distribution with an SMPS (Bałazy et al. 2006; Balazy et al. 2006; Brochot et al. 2011; Buha et al. 2013; Cyrs et al. 2010; Eninger et al. 2008; Golanski et al. 2009; Golshahi et al. 2009; Huang et al. 2007; Lore et al. 2011; Otani et al. 2007; Rengasamy et al. 2009). Polydispersed nanoaerosol particles pass through a radioactive neutralizer prior to the filter testing. The SMPS measures the particle number concentration distributions upstream and downstream of the test filter, which are used to calculate filtration efficiencies.

Japuntich et al. (2007) reported that the particle number concentration distribution measurement of polydispersed particles for multiple sampling without purging time or time interval led to measurement errors, especially for particles smaller than 30 nm, which may be attributed to thermal rebound effect. The TSI SMPS usually measures polydispersed particles by scanning from small to large diameters. In this case, the fraction of large particles from the previous sample may remain in the system and be counted as small ones in the next sample (Japuntich et al. 2007). This error becomes serious if downstream particle concentrations are measured immediately after upstream particle concentration measurement. Error due to the measurement of concentration distribution of polydispersed particles can be eliminated by using a proper sampling method, either by employing a time interval (Lore et al. 2011) or by introducing purge time (Japuntich et al. 2007) between measurements for upstream and downstream particle number concentration distribution. Thus, both upstream and downstream concentrations reach equilibrium between consecutive sampling. In this case, the error due to measurement of polydispersed particles is eliminated. A recent study also confirmed that passing polydispersed nanoparticles and monodisperse nanoparticles in the range of 20 nm to 300 nm through identical filters resulted in nearly the same particle penetration measurement (Li et al. 2012).

Although both polydispersed and monodispersed particles can be employed as tested particles, some researchers still suggest employing monodispersed particles for filtration tests to minimize possible errors in the classification of nanoparticles in a measurement device. If errors are associated to the measurement device, there is no need to separate CPC and DMA from each other to produce monodispersed particles for filtration tests. One of the issues that were not considered in previous studies is the different behaviors of nanoparticles introduced to the same filter in these two testing methods. In the first method, monodispersed particles pass through the filter; however, in the second one, polydispersed particles pass through the filter. Particles have different interactions with each other in these two cases, which could affect the measured filtration efficiencies. In order to eliminate the possible differences, the SMPS can be employed downstream of the filter; polydispersed particles are introduced through the filter, and the SMPS is set to measure the concentration of each discrete particle size (monodispersed particles) or polydispersed particle number concentration distributions. In this case, comparison between the filtration efficiency measurements for polydispersed particles with those for monodispersed particles is more accurate than that with the previous method because the same particles pass through the tested filter.

One of the parameters discussed in the previous chapter was the sheath air to sample air flow rate, which affected the measurement of nanoparticle number concentration distribution. This rate ratio did not affect the factional particle number concentration distributions, even though the particle concentrations were different due to the different dilution rates in the DMA (see Section 3.4.2.2 in Chapter 3). A sheath air to sample air flow rate ratio of 10:1 is typically used for a good resolution of particle number concentration distribution (Chen et al. 1998) for accurate filtration efficiency measurement; however, as explained in the previous chapter, if the particle resistance time in the DMA is reduced due to its short height, lower sheath air to sample air flow rate ratios can be employed too. In this chapter I investigate the effects of sheath air to sample air flow rate ratio on the measurement of nanoparticle filtration efficiency.

After the concerns associated with the particle number concentration distribution measurement device had been addressed, experiments were done to achieve the goal of this study, that is, to determine the effect of WOx particle number concentration distribution on the filtration efficiency of wire screens. Under realistic situations, polydispersed particles at different number concentration distributions and concentrations are applied to filters. Thus, in this study, unlike other researchers who employed monodispersed particles, I used polydispersed particles at different particle number concentration distributions as the test aerosol particles to determine whether varying particle number concentration distributions affect the measured filtration efficiency.

NaCl and WOx nanoparticles with a broad range of diameters and concentrations at different particle number concentration distributions were employed as the teste aerosols. Micron-sized stainless-steel wire screens were employed as the test filters. Results showed that WOx and NaCl nanoparticles behave differently during filtration. The filtration of NaCl nanoparticles does not depend on introduced nanoparticles; however, for WOx particles, the introduced nanoparticle number concentration distribution significantly affects filtration efficiency.

4.3 Materials and Method

The experimental setup for the measurement of particle number concentration distribution was shown in Figure 3-2. This setup was modified in order to determine the filtration efficiency of the test filter, as shown in Figure 4-1. In this setup for filtration test, a grounded cone shape filter holder with an inner diameter of 25 mm was employed upstream of the measurement device and purged with clean air before

each test. Polydispersed aerosol particles (NaCl, WOx) were then introduced at a specific flow rate through the filter holder.

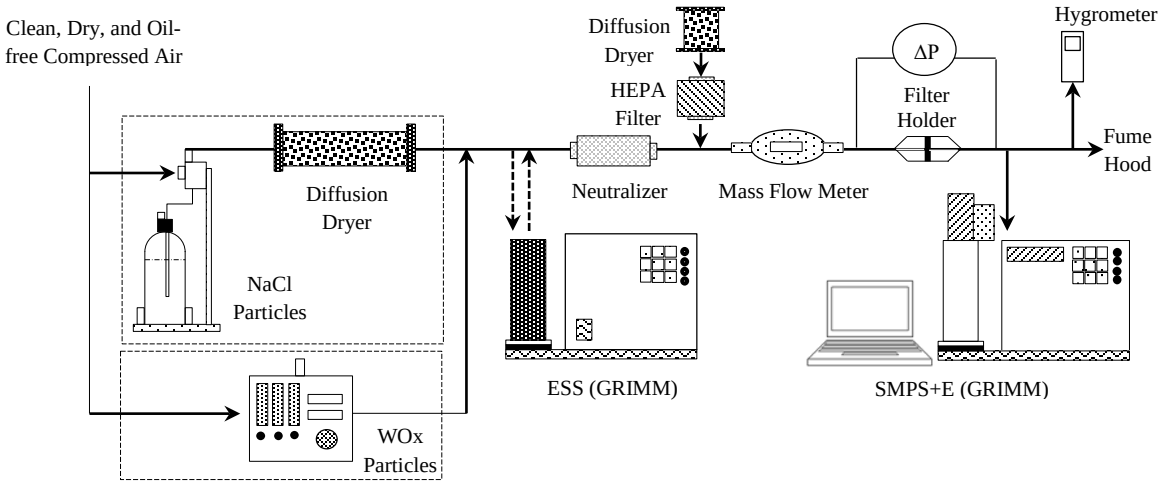

Figure 4-1. Schematic diagram of the experimental setup for filtration efficiency testing

Wire screens made of micron-sized wires were chosen as the test filters because they have uniform wires in a single layer. The wire screens herein are low efficient; thus any modification to the experimental conditions will lead to obvious changes in calculated filtration efficiency. The characteristics of these wire screens are shown in Table 4-1. Generally speaking, wire screens 4212120 and 4212125 are similar to each other in terms of wire diameter and filter thickness. Wire screen 4212140 has the thinnest wire and filter thickness. Prior to tests, these wire screens were dipped into liquid isopropanol for 10 minutes or so followed by drying under a fume hood to remove electrical charges (Martin Jr and Moyer 2000).

Table 4-1. Specifications for stainless steel wire screens

Filter	d_f (μm)	L(μm)	Opening Size(μm)	α
W-4212120	41	82	86	0.538
W-4212125	41	82	61	0.64
W-4212140	25	50	38	0.64

As mentioned above, two filtration tests are widely used for determining nanoparticle filtration efficiency by either monodispersed or polydispersed particles. In this thesis work, due to the necessity of combining FCE and DMA for high resolution and to minimize loss due to particle diffusion, the SMPS+E was employed downstream of the filter holder. Thus, polydispersed particles were passed through the filter and, based on the selection of a single channel or multiple channels, either monodispersed or polydispersed particle concentrations could be measured. In the first test, a single channel setting was employed to measure the concentrations of the sizes of nanoparticles without and with the filter in the holder. In the second test, SMPS+E measured the particle number concentration distribution of nanoparticles without and with the test filter in the holder. Difference between the filtration efficiencies determined by these two approaches is considered as the inaccuracy of SMPS for polydispersed measurement.

Nanoparticle concentrations measured downstream of the filter holder without and with a test filter represent upstream (C_{up}) and downstream (C_{down}) concentration, respectively. Each data point was repeated at least three times. The corresponding filtration efficiency was then calculated by

$$\eta = 1 - P = 1 - \frac{C_{down}}{C_{Up}} \tag{4-1}$$

With this identical sampling method, the error due to particle loss is minimized, and there is no need to employ a correction factor, which Japuntich et al. 2007 had to use due to their sample train difference, to compensate for particle loss differences. For frequent sample measurements, we have to make sure that the device measures new particles; thus, we need to wait to get a stable reading from the equipment. The FCE is a fast measurement device, and changes in particle number concentration distributions immediately affect the measurement in a few second (Section 3.4.2.4).

Theoretical filtration models have been reviewed in Chapter 2, and they are briefly summarized as follows. The filtration efficiency of particles through the filter is:

$$\eta_{theory} = 1 - \exp\left[\frac{-4\alpha EL}{\pi d_f(1-\alpha)}\right] \tag{4-2}$$

where η is the filtration efficiency, L is the filter thickness, α is the solidity of the filter, d_f is the diameter of the fiber, and E is the corresponding single fiber efficiency. The single fiber efficiency for

nanoparticles was believed to depend primarily on the Brownian diffusion, and it is calculated using (Cheng and Yeh 1981; Kirsch and Fuchs 1968):

$$E_D = 2.7Pe^{-2/3} \tag{4-3}$$

where Pe is the Peclet number, calculated using Eq.(2-2).

Conventional filtration model is compared with experimental data. As explained in the previous chapter, the electrical mobility particle sizer classifies particles based on their electrical mobility diameter, which is independent of particle properties such as density (Austin et al. 2002). For spherical particles, the electrical mobility diameter equals the geometric particle diameter (DeCarlo et al. 2004).

4.4 Results and Discussion

4.4.1 Filtration testing methods

Figure 4-2 shows the particle filtration efficiencies of two wire screens (4212140, 4212120) for WOx nanoparticles. The filtration efficiencies were measured for both polydispersed and monodispersed WOx particles. In polydispersed measurement, the filtration efficiencies were calculated using the measured particle number concentration distributions upstream and downstream of the filter. For monodispersed measurement, the filtration efficiency for each size of particle was calculated using its concentrations upstream and downstream of the filter measured over 3 min.

As expected, the filtration efficiencies of the wire screen 4212140 were higher than those of 4212120 for the sizes of tested particles because the screen 4212140 has finer wires and larger solidity. However, it is not the case for particles larger than 12 nm in diameter. The Comparison between the efficiencies based on the monodispersed and polydispersed measurements shows that, for both filters, the filtration efficiencies determined by these two methods agreed well with each other except for 2 nm particles through the screen 4212120. Also, it is shown that for screen 4212140, the filtration efficiencies drop when particles are smaller than 2.35 nm for both polydispersed and monodispersed measurements. The standard deviations for both cases are great for sub-2.79 nm particles and for both wires. Further investigation is needed to determine the sources of errors in the measurement of filtration efficiency for particles smaller than 2.79 nm and those larger than 12 nm.

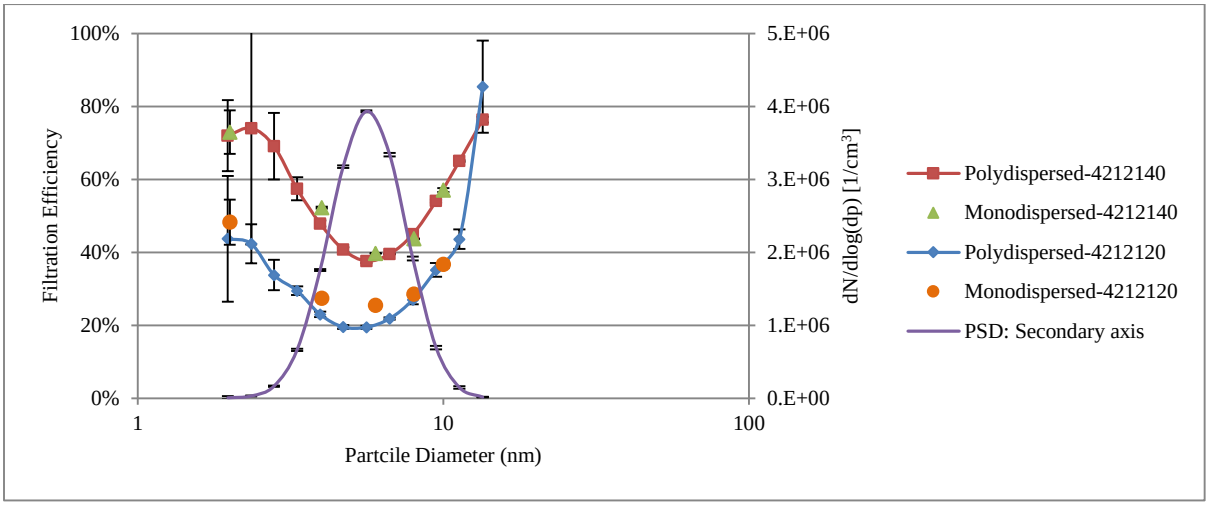

Figure 4-2. Comparision between filtration efficiencies for the measurement of polydispersed and monodispersed WOx particles at an aerosol flow rate of 2.5 lpm

Figure 4-3 shows the concentrations of particles measured by monodispersed mode for diameters of 2, 4, 6, 8, and 10 nm for upstream and downstream of the screen 4212140. For each particle size, the measurement lasted for 3 min with a time interval of ¼ s. Because the measured concentrations were stable over time, only the results over the first 60 seconds are shown here. The total measurement points for each particle size during 60s are 240. Results showed that for each selected particle size, the first measurement point is different from others, and it reaches to the same measurements for the further measurements after only ¼ s. Thus, any changes in the particle concentrations in the SMPS+E affects the measurement at only ¼ s, which shows the fast measurement of SMPS+E.

Results in Figure 4-3 also show that, except for particle sizes of 2 and 12 nm, the other concentration measurements are above the lower detection limit (10^3 /cm^3), with a standard deviation of less than 2% of the averaged data, which shows high accuracy and stable measurements. Both upstream and downstream particle concentrations for the sizes of 2 nm and 12 nm are lower than the detection limit of the SMPS+E as shown in Figure 4-4 and Figure 4-5. Due to the low accuracy of SMPS+E for low particle concentration, false negative concentration measurements were observed for both 2 nm and 12 nm particles. The average upstream and downstream particle concentrations for 2 nm particles are 130.71±121.88, and 33.98±128.03, respectively (Figure 4-4). These negative false measurements and large standard deviations led to great errors the calculated in filtration efficiencies. For 12 nm particles (Figure 4-5), the average particle concentrations were negative for both upstream and downstream

measurements (-32.84±89.90, and -39.87±87.96), which reveals the invalidity of the measurement for this particle size. For polydispersed measurements the negative values were corrected by the correction factor of the FCE, which may affect calculated filtration efficiency too. The same results were also observed for wire 4212120, which are not shown here. In summary, regardless of particle sizes and whether they are measured when polydispersed or monodispersed, caution must be taken when working with particle number concentrations lower than the detection limit of the GRIMM SMPS+E.

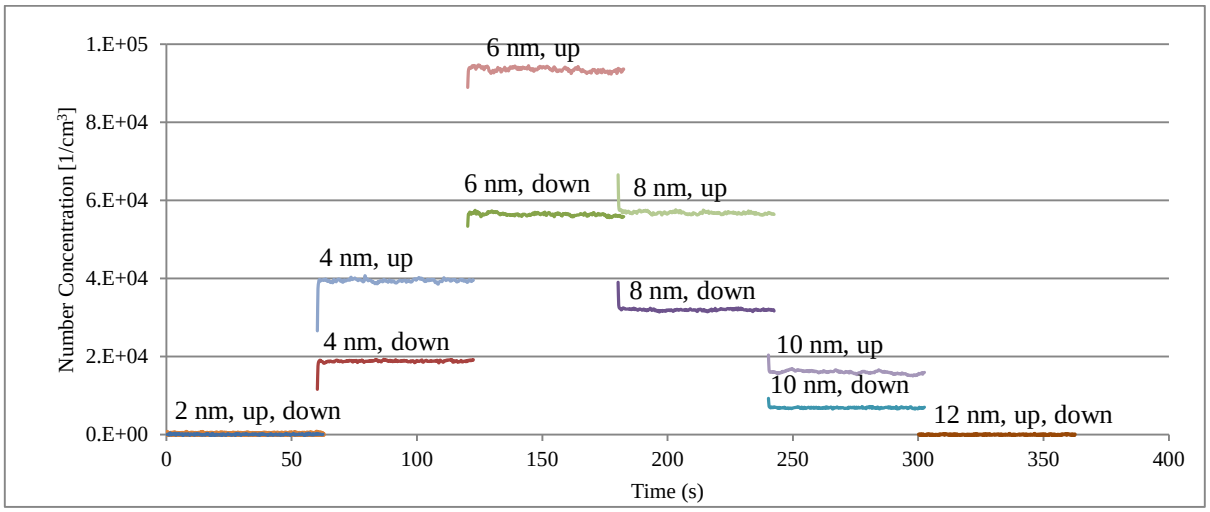

Figure 4-3. Monodispersed concentrations of particles with diameters of 2, 4, 6, 8, 10 and 12 nm for upstream and downstream of wire screen 4212140

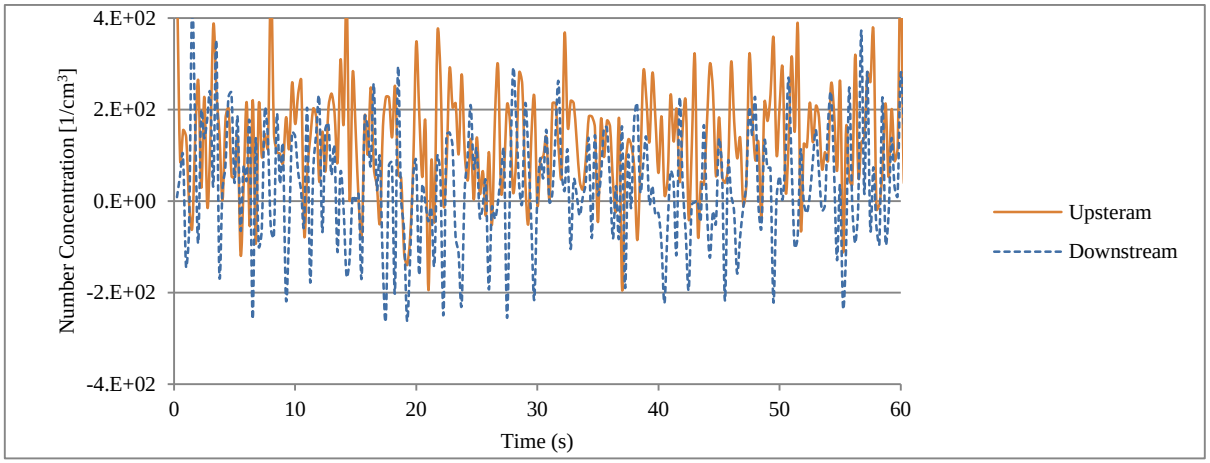

Figure 4-4. Monodispersed concentrations of particles with diameter of 2 nm for upstream and downstream of wire screen 4212140

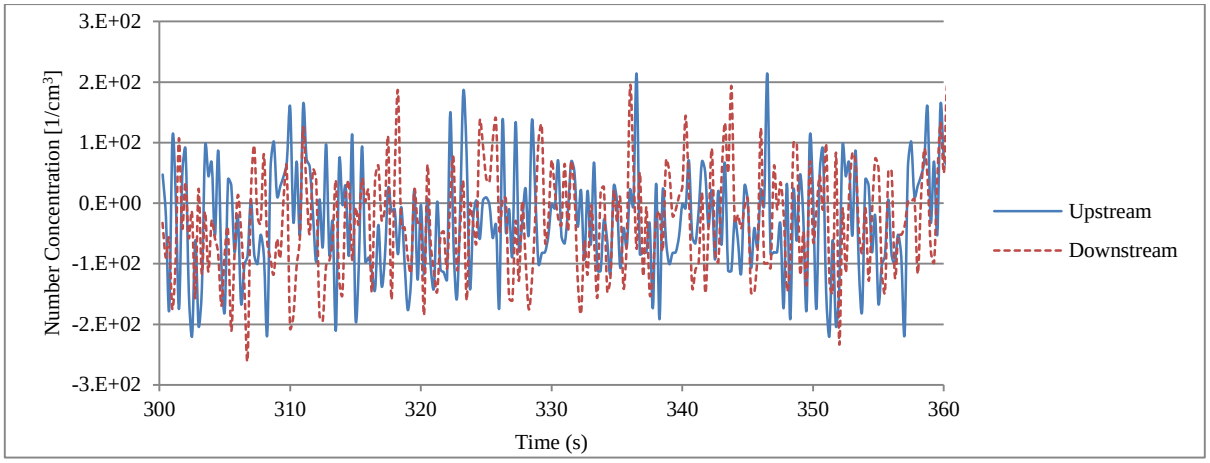

Figure 4-5. Monodispersed concentrations of particles with diameter of 12 nm for upstream and downstream of wire screen 4212140

Another issue that may lead to the discrepancy between the calculated filtration efficiencies for monodispersed and polydispersed measurements is the instability of WOx nanoparticles over a long time. The WOx particle concentrations may differ due to changes in the tungsten filament over time. The monodispersed measurements are time consuming (each particle diameter requires 3 min scan time). The measurement of polydispersed particles before and after the measurements of monodispersed particles may vary due to the long measurement time of 65 min in this experiment. Figure 4-6 shows the upstream and downstream particle number concentration distributions measured with a time interval of 65 min and the resultant filtration efficiencies. The particle concentration decreases due to the usage of the WOx filament over time. However, the calculated filtration efficiencies did not change (except for two particle sizes, sub-2.79 nm and supper-11.28 nm, with low particle concentrations), because each downstream particle number concentration distribution was measured after its associated upstream measurement. Furthermore, the constant filtration efficiency over 65 min time interval showed the impossibility of charge build up during filtration.

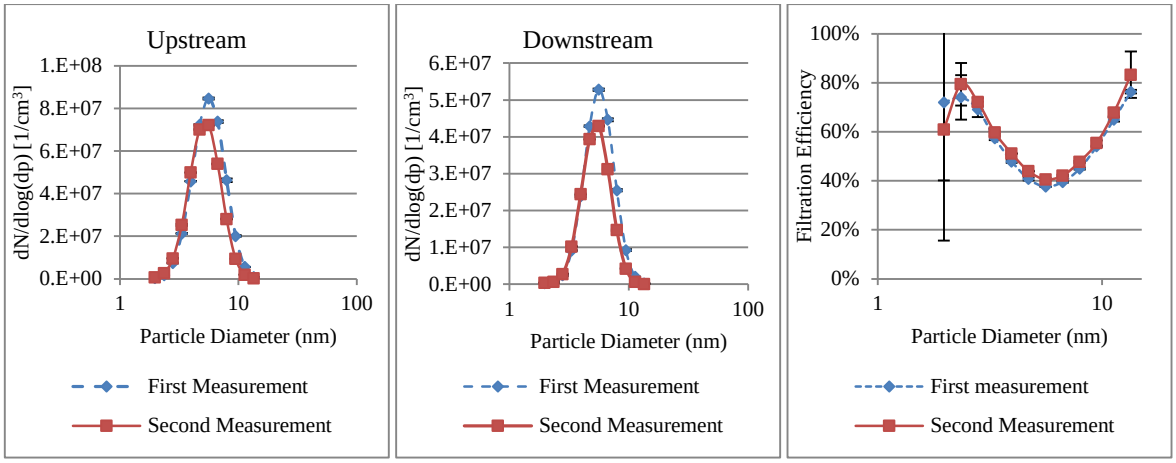

Figure 4-6. Particle number concentration distributions and filtration effciencies in time interval of 65 min

One question that arises here is whether the particle concentration changes between the upstream polydispersed measurement and downstream polydispersed measurement. In order to check whether that particle number concentration distributions would remain constant, the upstream polydispersed measurements were done twice, before and after the downstream measurement. As shown in Figure 4-7, the particle number concentration distributions agreed well with each other, which indicates the stability of WOx particle number concentrations over a period of time of 6 min in this experiment. Therefore, for accurate filtration efficiency measurement, the downstream particle concentrations were measured after the upstream ones with short time intervals to ensure stable particle concentration.

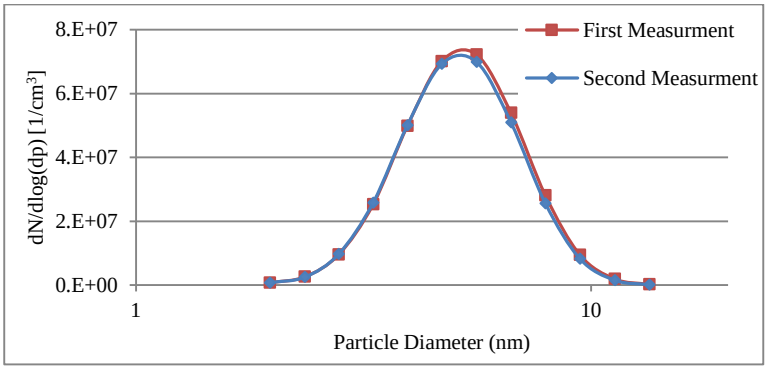

Figure 4-7. Upstream particle number concentrations in time interval of 6 min

In summary, it has been shown that measured filtration efficiencies are the same for both polydispersed and monodispersed measurement. The error due to polydispersed measurement for TSI SMPS is not presented here; it is due to employing a high resolution FCE that is sensitive to changes in particle concentration with a fast response time of ¼ s. In contrast to previous experimental studies, our experiments employed mobility classifier, which classifies particles from larger to smaller with high accuracy and reduces measurement errors for smaller particles. Thus, using GRIMM SMPS with either polydispersed or monodispersed particles can assess the filtration efficiency of a specific filter. However, careful consideration must be given for low particle concentrations.

In this study, for the rest of experiments, polydispersed measurement is used, and upstream and downstream particle concentrations were measured, respectively.

4.4.2 Effect of sheath air to sample air flow rate ratio on filtration efficiency measurement

Figure 4-8 shows the measured upstream particle number concentration distributions and corresponding filtration efficiencies of three wire screens; the particle number concentration measurements were taken with sheath air to sample air flow rate ratios of 5:1 and 10:1 at an aerosol flow rate of 2.5 lpm. Although the measured upstream particle number concentration distribution depends on the sheath air to sample air flow rate ratio, the particle filtration efficiencies calculated with the concentrations measured with ratios of 10:1 and 5:1 agree well with each other. Discrepancy occurs for particles smaller than 2.79 nm and larger than 16.04 nm because of their low concentrations (Section 4.4.1).

As explained in the Section 3.4.2.2, changes in the sheath air to sample air flow rate ratio did not cause mobility shift in the measurement of particle number concentration distribution, nor did it affect the calculated filtration efficiency. This indicates that diffusional broadening of particles was negligible for the selected sheath air to sample air flow rate ratios. Otherwise, it would have affected the accuracy of the measured particle number concentration distribution and the consequent calculation of the filtration efficiency. The effective length of the electrometer in the S-DMA employed herein was short, and it could be operated with smaller ratios than the typical sheath air to sample air flow rate ratio of 10:1. Thus, in cases with low particle concentration, the sheath air to sample air flow rate ratio of 5:1 is preferable.

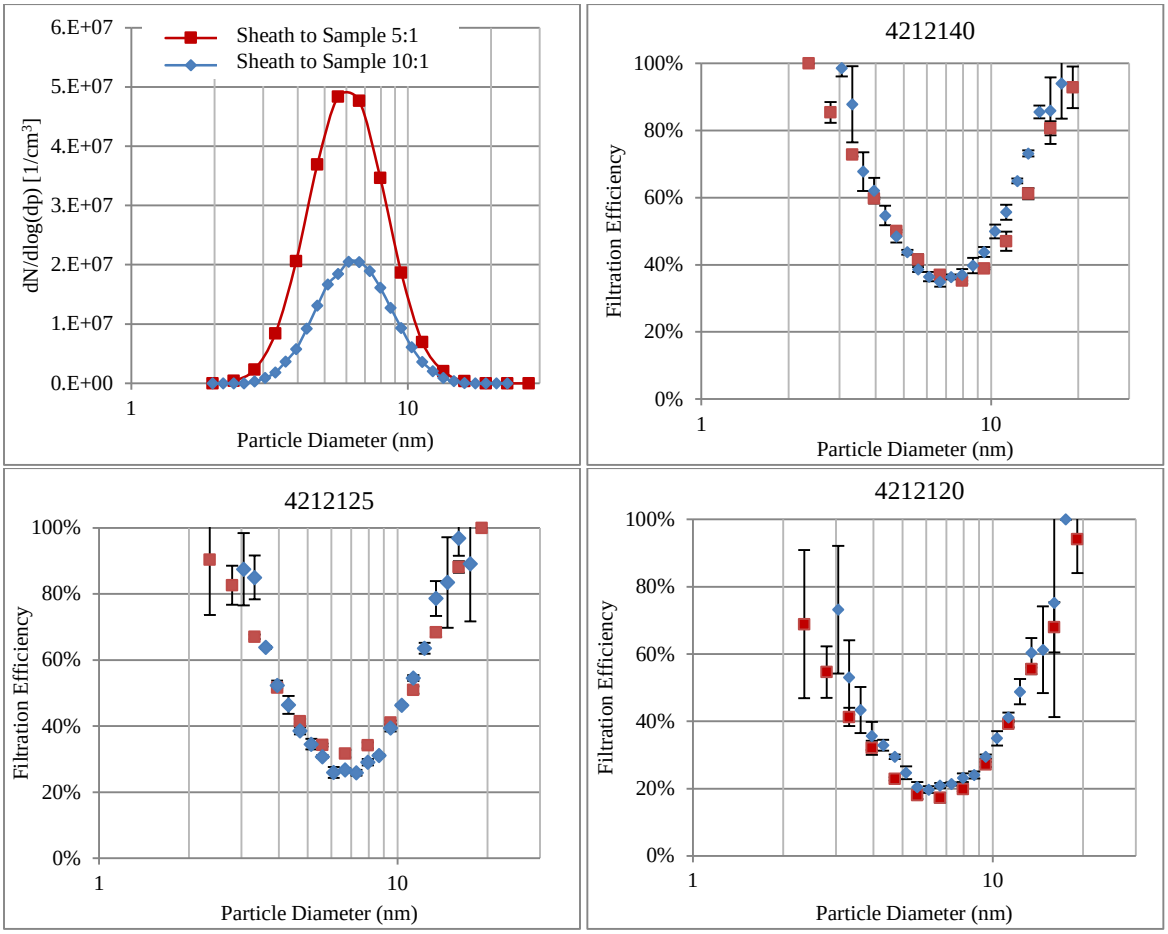

Figure 4-8. Filtration efficiencies of three wire screens for two sheath air to sample air flow rate ratios

4.4.3 Effect of polydispersed particle number concentration distributions on filtration efficiency

In this section, experiments were carried out to investigate the effect of a shift in the WOx particle number concentration distribution on the resultant nanoparticle filtration efficiency. For this aim, three different upstream particle number concentration distributions of WOx particles were introduced through three wire screens at two aerosol flow velocities of 3.9 cm/s and 5.4 cm/s. WOx particle number concentration distributions in this section vary with the carrier air flow rate. Greater carrier air flow rate leads to the generation of smaller nanoparticles with narrower size distributions and lower particle concentrations (more information can be found in section 3.4.1.2). The upstream particle concentration

is affected by face velocity, which is adjusted by a valve upstream of the filter holder. Closing the valve decreases the face velocity and, as a result, fewer particles enter the measurement device, and the measured particle concentrations are lower. Figure 4-9 shows the filtration efficiencies of three wire screens vs. particle diameter corresponding to different upstream particle number concentration distributions. The aerosol flow rate was fixed at 1.1 lpm and 1.5 lpm corresponding to the face velocities of 3.9 cm/s and 5.4 cm/s, respectively.

Table 4-2 summarizes the mode sizes and the most penetrating particle size for these three wire screens. The mode sizes are 6.65 nm, 4.69 nm, and 3.95 nm for WOx 13 200 0, WOx 13 120 0 and WOx 13 400 0, respectively. Although the mode sizes differ from each other for these three particle number concentration distributions, the most penetrating particle size is 5.59 nm for all three wires tested at a face velocity of 3.9 cm/s, except for one that is WOx 13 200 0 and wire 4212140, which is 6.65 nm. However, at a higher face velocity of 5.4 cm/s, the most penetrating particle size occurs at 6.65 nm for WOx 13 200 0 for all three filters. For the second WOx particle number concentration distribution, the most penetrating particle sizes are 4.69 nm, 5.59 nm and 6.65 nm for screens 4212120, 4212125 and 4212140, respectively. For WOx 13 400 0 at a face velocity of 5.4 cm/s, the most penetrating particle size was not observed, and the filtration efficiency decreased as the particle size increased. However, for the particle diameter of 6.66 nm, the standard deviation was high, and we could not conclude affirmatively that the efficiency decreased at these particle sizes.

No specific correlation was observed between the aerosol flow rate and the most penetrating particle size. However, the most penetrating particle size was close to the mode size. Therefore, the filtration efficiency of WOx particles through the wire screens depends on upstream particle number concentration distribution. A lower filtration efficiency is associated with a higher particle concentration. The most penetrating particle sizes for these three particle number concentration distributions occurred in the range of 4.69-6.65 nm.

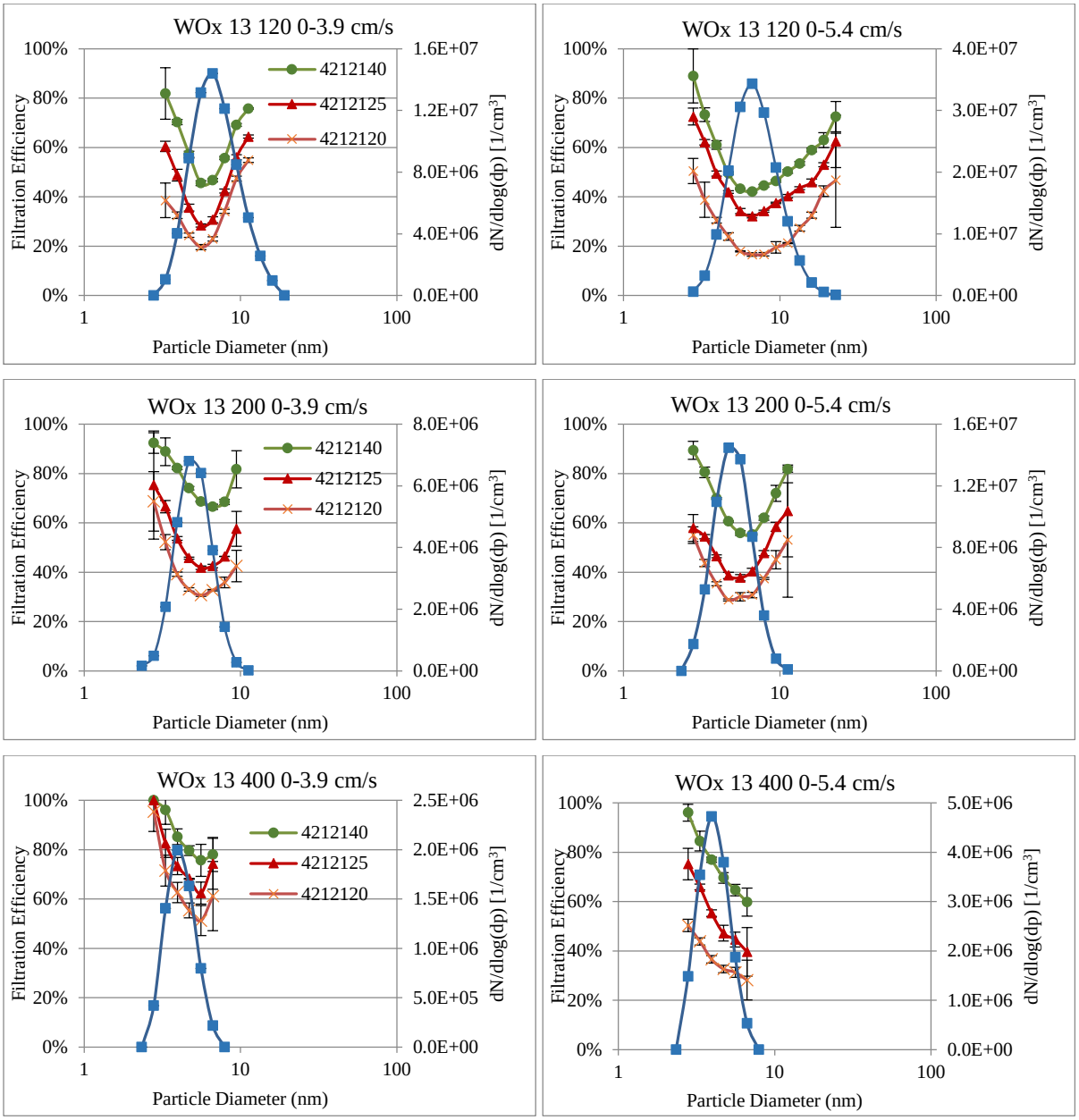

Figure 4-9. Particle number concentrations for WOx and filtration efficiencies of three wire screens as a function of particle diameter for different upstream particle number concentration distributions at face velocities of 3.9 cm/s and 5.4 cm/s

Table 4-2. Mode size and most penetration particle size

Particle number concentration distribution	**WOx 13 120 0**	**WOx 13 200 0**	**WOx 13 400 0**
		Face velocity=3.9 cm/s	
Mode size (nm)	6.65	4.69	3.95
MPPS for 4212120 (nm)	5.59	5.59	5.59
MPPS for 4212125 (nm)	5.59	5.59	5.59
MPPS for 4212140 (nm)	5.59	6.65	5.59
		Face velocity=5.4 cm/s	
Mode size (nm)	6.65	4.69	3.95
MPPS for 4212120 (nm)	6.65	4.69	-
MPPS for 4212125 (nm)	6.65	5.59	-
MPPS for 4212140 (nm)	6.65	6.65	-

In the conventional air filtration model, the most penetrating particle size occurs when both diffusion and interception mechanisms are weak. For the tested WOx particles smaller than 20 nm, the interception mechanism is negligible and diffusion mechanism is believed to be dominating by a simple calculation using Eq.(4-3). For these particle sizes, we expect an increase in filtration efficiency with decreasing in particle size, and we did not expect the most penetrating particle sizes. However, experimental results show that the most penetrating particle size for WOx particles was between 4.69 nm to 6.65 nm. In the next section, experimental data is compared with conventional filtration models.

4.4.4 Comparison between experiments and conventional filtration model

Experimental and modeling filtration efficiencies of various particle number concentration distributions are shown in Figure 4-10. Results show the upstream particle number concentration distributions of NaCl and WOx particles and the filtration efficiencies of these three wire screens at a face velocity of 5.4 cm/s. NaCl filtration efficiency followed conventional filtration theory; however, WOx particles did not. NaCl nanoparticles have been widely used as test particles in filtration studies and their filtration efficiencies are well known to agree with conventional models. As expected, the filtration efficiency increases as the particle diameter decreases. The filtration efficiencies of NaCl nanoparticles that were generated at two different salt concentrations (0.01 g/l and 0.1 g/l) differ slightly from each other. The filtration efficiencies of particles generated with 0.1 g/l NaCl concentration are slightly higher than those with NaCl 0.01 g/l. Similar results were reported by others for N95 filters (Kang 2011). The P-values in the one-way Anova test for NaCl particles are 0.274, 0.257 and 0.127, for wire

screens 4212140, 4212125 and 4212120, respectively, for the significance level of 0.05. Therefore, the effect of NaCl particle concentration on filtration efficiency is not significant.

Surprisingly, however, the filtration efficiencies of WOx nanoparticles do not agree with conventional filtration model. The discrepancy between theory and experiments occurred for particles larger than the mode sizes. The experiments showed that the filtration efficiency increased as the size of nanoparticles increased, and the gap between model and experimental data increases with the particle size. Moreover, comparison between the particle size distribution and the filtration efficiency curves shows that the higher the particle concentration, the lower the filtration efficiency is. Thus, it seems that particle concentration affects the filtration efficiency for particles larger than the mode size; however, it does not affect the efficiency for particles smaller than the mode size.

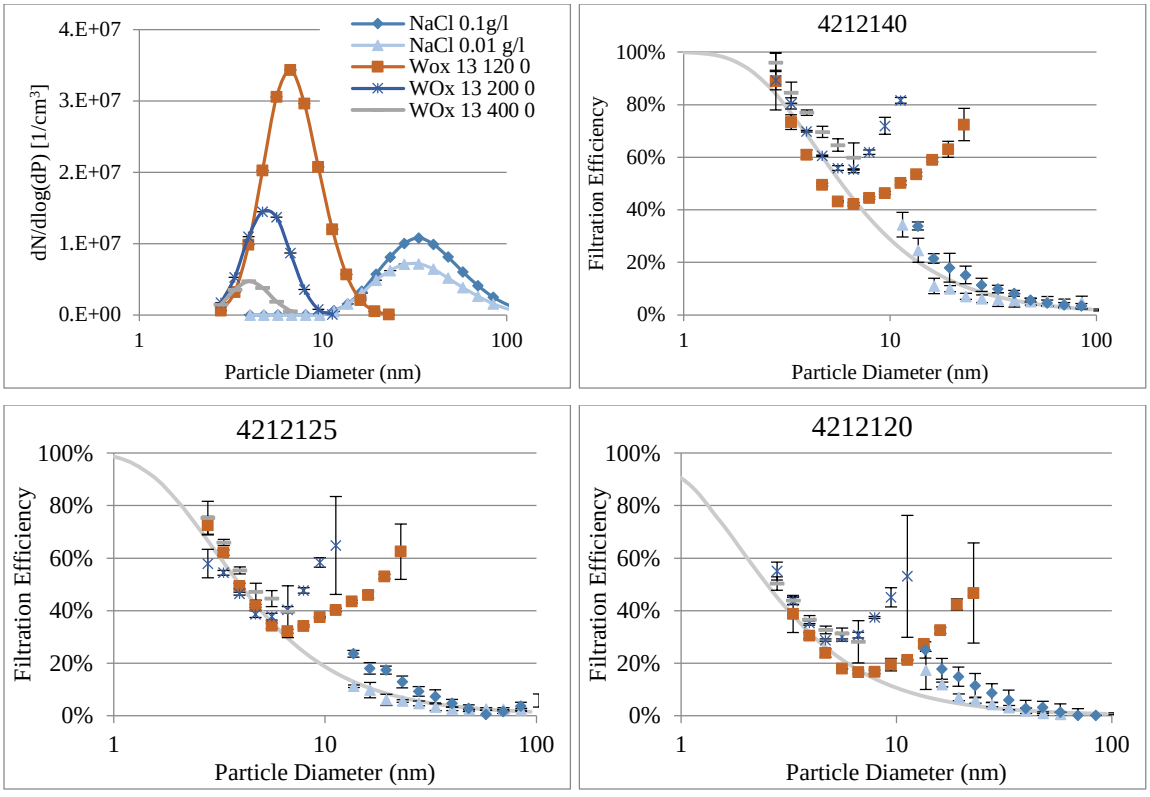

Figure 4-10. Particle number concentration distribution for WOx and NaCl and filtration efficiencies of three wire screens as a function of particle diameter for different upstream particle number concentration distributions at an aerosol flow rate of 1.5 lpm, 5.4cm/s

In order to determine the effect of particle concentration on filtration efficiency, the emission sampling system was employed to dilute introduced particles prior to filtering tests. The results are shown in the next section.

4.4.5 Effect of particle concentration on filtration efficiency

This section describes experiments carried out to investigate whether NaCl and WOx particle concentrations affect filtration by wire screens. The emission sampling system was employed to dilute introduced WOx and NaCl particles at dilution ratios of 1:10 and 1:100. For NaCl particles generated at a concentration of 0.1 g/l, employing two dilution stages reduced the particle concentrations below the detection limit of the system. Therefore, the experiments were done with salt concentrations of 1 g/l to avoid measurement of concentration lower than the detection limit of 1000/cm^3.

Figure 4-11 shows the upstream particle number concentration distributions at three levels of concentration: no dilution, 1:10, and 1:100, along with the filtration efficiencies of WOx and NaCl particles through wire screen 4212140 at a face velocity of 5.4 cm/s. Without employing ESS, the WOx particle concentration is high for the tested range of particles (2.35-13.45 nm); however, employing ESS dilutes introduced particles and may decrease the concentration of certain particles to a level that is lower than the detection limit of the SMPS+E. That is why the reported range of particle size decrease in the efficiency curves. In this experiment, the detectable WOx particle size range decreased to 2.79-9.47 nm and 3.32-6.67 nm when the dilution ratio was 1:10 and 1:100, respectively. For NaCl particles, the lower detectable size changed down to 3.67 and 17 nm particles for the dilution ratio of 1:10 and 1:100, respectively.

As the WOx particle concentration decreased, the particle filtration efficiencies for smaller particles increased slightly. The change rates in filtration efficiency are much lower than the dilution rates. One-way Anova analysis for this range of particles showed that the effect of upstream particle concentration on filtration efficiency of nanoparticles in the range of 2.35-5.59 nm is not significant (P-value=0.51, 0.32 and 0.15 for wires 4212140, 4212125 and 4212120, respectively). These results are consistent with conventional filtration model, where the filtration efficiency is independent of upstream particle concentration. As expected, the filtration efficiency of these particles was independent on the dilution rate. Diffusion is the most important deposition mechanism for filtration of these particles. For particles larger than 6.67 nm, the discrepancies between the filtration efficiencies are greater at 1:10 dilution and

no dilution. The standard deviation is also high. Thus, for particles in these sizes as it was shown in previous section, the lower filtration efficiency may be associated with the higher particle concentration.

For NaCl particles, the filtration efficiency curves corresponding to all three dilution rates are close to each other; however, closer investigations showed the weak positive correlation between filtration efficiency and particle concentration. As the particle concentration decreases, the filtration efficiency decreases slightly. For the dilution ratios of 1:10 and 1:100, the filtration efficiencies are almost the same. We can conclude that the filtration efficiency of NaCl particles follows conventional filtration theory, which is almost independent of particle concentration.

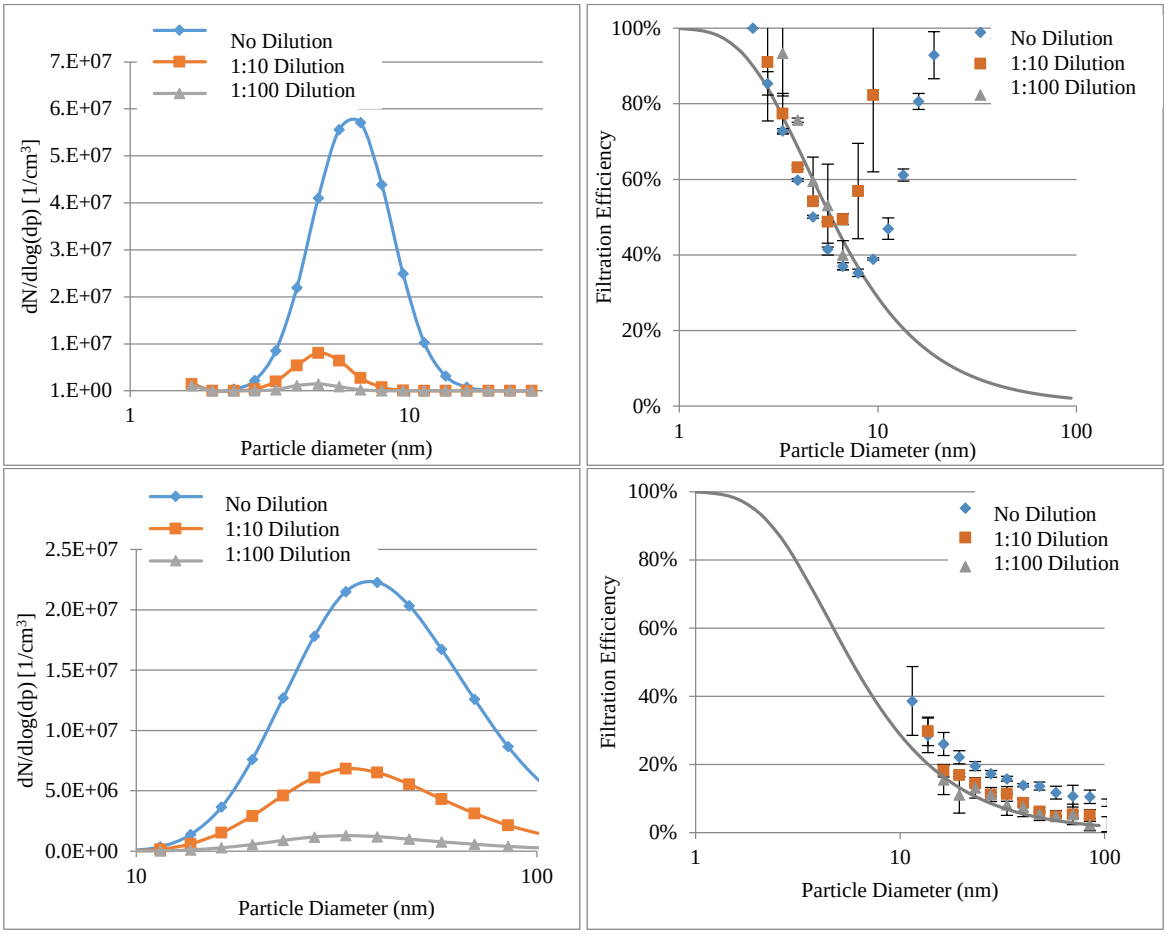

Figure 4-11. Effect of employing emission sampling system on filtration efficiency

As shown above, the filtration efficiency of WOx particles with sizes larger than about 5 nm does not follow the conventional filtration model if only diffusion mechanism is considered. Experimental results showed the strange behavior of WOx nanoparticles larger than about 5 nm as follows:

- It is contradictory to conventional filtration theory that filtration efficiency increases as the size of nanoparticles increases.
- The filtration efficiency depends on the incoming particle concentration.

One of the possible reasons for this behavior is the charge states of WOx particles. In all of the experiments, neutralized particles and uncharged wire screens were employed to eliminate electrostatic forces. The neutralizer is replaced every year based on the recommendation of the company. Thus, it is expected that it can charge the aerosol particles to Boltzmann equilibrium. Because a population of neutralized particles have a Boltzmann equilibrium charge rather than being completely uncharged for individual particles, they may also contribute to the image force between particles and filter. Thus, some researchers suggest that electrostatic forces between neutralized particles and uncharged filters should also be taken into account (Brown 1993). It is thus speculated that the neutralizer does not completely neutralize highly charged WOx particles larger than about 5 nm, which increase the filtration efficiency.

Thus, in the next section, experiments are done to determine whether the charge states of WOx particles affect their filtration efficiency.

4.4.6 Effect of particle charges on filtration efficiency for WOx nanoparticles

The effect of electrostatic forces on nanoparticle filtration efficiency is controversial. Kim et al, 2006 showed that the filtration efficiency for sub-100 nm NaCl particles is lower for uncharged particles than for charged particles at a face velocity of 2.5 cm/s, and this discrepancy decreases with a decrease in particle size (Kim et al. 2006). Another study on filtration of sub-80 nm NaCl particles using electrospun filters showed that nanoparticle removal efficiency was independent on the charge state of particles, indicating the negligible effect of columbic force compared to strong diffusion force (Kousaka et al. 1990; Yun et al. 2007). Thus, a simple test was done to determine the possible influence of electrostatic force on filtration efficiency.

Figure 4-12 shows the filtration efficiencies of wire screen 4212140 for three different WOx particle number concentration distributions with (W) and without (WO) employing the neutralizer upstream the test filter. The particle number concentration distributions in both cases differ from each other. Overall, without employing the neutralizer, particles have lower concentrations. It is likely that some of these highly charged particles were lost while they travel in the tubes. The lower particle concentration could not be attributed to the coagulation of particles; otherwise, there should have been more larger particles and less smaller ones, with the curve shifting to right.

The GRIMM SMPS+E considers the effect of multiple charges for particles greater than 40 nm (Giechaskiel et al. 2008). The electrical mobility of multiple charged particles increases, causing the particles to be collected in the upper part of the DMA cylinder, i.e., with the smaller particles (Willeke and Baron 1993). In this case, the concentration of larger particles decreases and that for smaller particles increases. The particle measured number concentration distributions in Figure 4-12 show the same results as for multiple charged particles. Without employing the neutralizer, the particle concentration for larger particles is lower than that achieved using the neutralizer. Moreover, the particle concentration for smaller particles is greater than that when employing the neutralizer. It seems that, without the neutralizer, WOx particles may carry multiple charges, causing the minor shift of the curve toward the lower end. In fact, multiple charged particles affect the concentration measured using the GRIMM SMPS+E and the consequent calculation of filtration efficiency.

For all three particle number concentration distributions, the filtration efficiency without the neutralizer is higher than that with the neutralizer. In summary, it believed that electrostatic forces affected the filtration of nanoaerosol particle. The electrostatic forces increase with particle size. The effect of electrostatic force is negligible for smaller particles; however, it is more profound for larger ones. Figure 4-12 shows that the particle size below which the effect of electrostatic force is negligible depends on the introduced particle number concentration distributions. The particle sizes are 5.64, 4.74, and 3.98 nm for Figure 4-12a, b and c, respectively.

Despite previous studies showing the effect of electrostatic forces is negligible on the filtration of nanoparticles, the results of this study show its positive effect for WOx particles using micron-sized wire screens. The WOx particles were generated by evaporation and condensation; their properties differ from those NaCl particles which were generated in aqueous solution. A great number of the

nanoparticles produced by evaporation and condensation method carry charges. However, the polarity of the net charge depends on the particle material and temperature. Other researchers (Peineke and Schmidt-Ott 2008) have shown net positive polarity for silver nanoparticles generated with hot wire at temperatures below its melting point (~1200 K). For palladium, the net charge was positive for low temperatures but changed to negative for temperatures higher than 1730 K. However, there has been no report in public literature on the charge states of WOx nanoparticles. Tungsten oxide particles used in current study are generated at high temperatures of 1000 K, which is lower than those for silver and palladium particles. As a result, we speculate that a large amount of these WOx nanoparticles may be positive. Employing a neutralizer reduces the charges of nanoparticles, and as a result, decreases their filtration efficiency.

Figure 4-12 shows that the neutralizer affected the filtration efficiencies for particles larger than 5.64, 4.74 and 3.98 for WOx distributions of 10 70 0, 10 100 0 and 10 200 0, respectively, and the effect is negligible for smaller particles. The neutralizer changed the charge states of nanoparticles. Figure 4-13 shows the theoretical probabilities of ion collision with the particles based on the Alonso theory vs. particle diameter (more information is available in Appendix E). For sub-5 nm particles, the probability of positive ions attaching to negative particles is greater than that of negative ions attaching to positive particles. The trend is opposite for larger particles. Moreover, for sub-5 nm particles, the probability of negative ions attaching to neutral particles is almost equal to the probability of positive ions attaching to neutral particles; however, it is greater for larger particles. After passing through the neutralizer, positively charged sub-5 nm particles and negatively charged larger particles dominate. Consequently, particles below 5 nm or so and larger ones behave differently when they pass through the same filter. Earlier study on the particle number concentration distribution of 1.7 nm WOx particles also showed that the concentrations of positively charged particles are higher than those of negatively charged particles (Winkler et al. 2007). In their study, WOx particles were passed through a neutralizer prior to a DMA. The polarity of particles exiting the DMA was determined based on the polarity of a classifier electrode. For both polarities the particle number concentration distributions were measured using a differential mobility particle spectrometer.

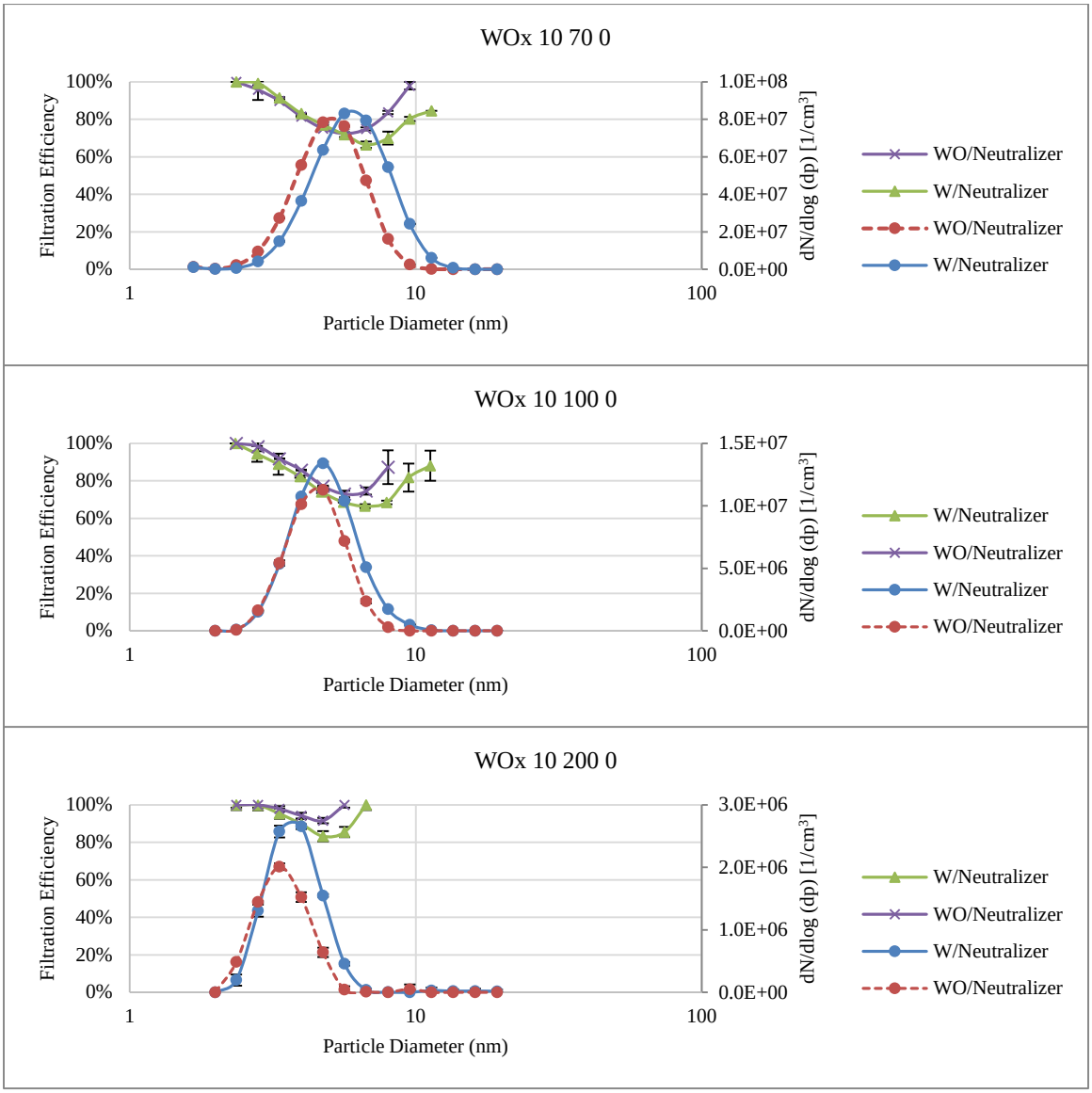

Figure 4-12. Filtration efficiencies of WOx particles at a face velocity of 5.4 cm/s (neutralized and charged)

As mentioned above, a large amount of tungsten oxide particles is positively charged right after generation and the neutralizer changes the charge states of sub-5 nm and larger particles (here we speak of sub-20 nm) differently in terms of polarity and number of charges, which in turn reduces filtration efficiency for particles larger than 5 nm. However, for smaller particles, employing the neutralizer causes more positive particles than negative ones, and it only reduces the number of positive particles.

Because it does not change the polarity of particles, it has less effect on filtration efficiency. Furthermore, as the size of particles decreases, the probability of them carrying ions decreases, which in turn reduces the effect of electrostatic forces.

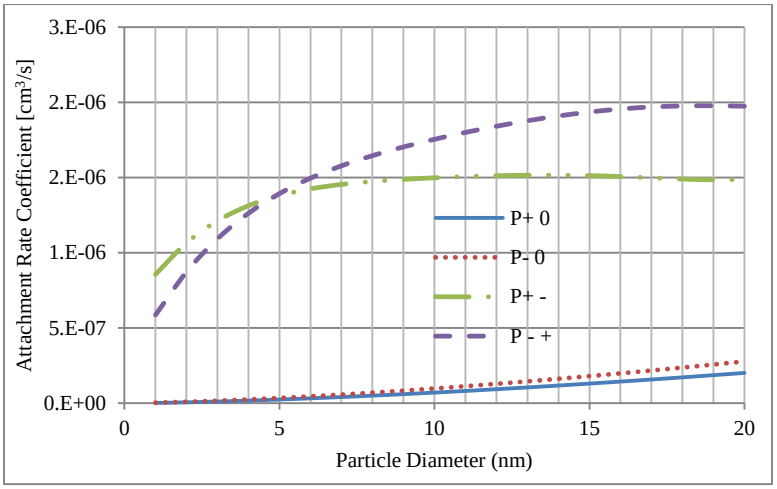

Figure 4-13. Diagram of charging probability via particle diameter

For particles larger than about 5 nm, the filtration efficiency of neutralized particles differs from that of charged particles. Thus, it can be concluded that even the neutralizer does not completely neutralize all the nanoparticles larger than 5 nm, a large portion of them still carry ions. As a consequence, the measure filtration efficiency was greater than that predicted by conventional model based on pure diffusion.

The performance of the neutralizer may vary at different nanoparticle concentrations. The number of ions within the neutralizer is constant; thus, when particle concentrations are low, nanoparticles have a higher chance of being neutralized than when the particle concentrations are high. Consequently, the measured filtration efficiency for particles at lower concentrations will deviate less from that predicted by the theoretical model than that at higher concentrations. However, results showed greater deviation for lower particle concentrations. Thus, it cannot be concluded that the neutralizer performs differently at tested particle concentrations.

Another reason for this discrepancy may be the charge states of the wire screens under test. In this study, screens were dipped in isopropanol for 10 min and dried overnight. It was assumed that the wire

screens were completely uncharged. However, they may still be partially charged, and isopropanol may reduce the charges of wires rather than removing them completely.

Results suggest not only that one of the reasons for this discrepancy between theory and experiments may be the charge of wire screens, but also that the charge states of WOx particles affect filtration efficiency. However, electrostatic forces are often ignored in conventional filtration theory models for sub-100 nm particles. It is possible that employing additional neutralizer prior to filtration testing would help to determine whether the filtration efficiency follows conventional theory. Further investigation is needed to determine the charge states of WOx particles after both generation and neutralization.

The interactions among WOx particles may affect filtration efficiency. This interaction depends on the sizes and concentrations of the introduced particles. This interaction may be another reason for the dependency of filtration efficiency on introduced polydispersed particle number concentration distributions.

We have to exclude the possibility that the discrepancy was due to measurement errors. In previous studies, measurement errors in particle classification occurred for smaller particles, which led to thermal rebound; however, the results of this study show an opposite trend. The filtration efficiency of particles down to 2.35 nm follows the theoretical model; however, based on the introduced particle number concentration distributions, the filtration efficiency for particles larger than the size of peak concentration may not follow the theoretical model. The filtration efficiency increases as the particle diameter increases. The SMPS+E classifies particles from larger to smaller, and so any small particles in the device left over from previous samples may count as large particles in the consequent sample (opposite trend as TSI SMPS). If this is the case, the particle concentrations of large particles must increase, leading to reduced filtration efficiency; however, this result is opposite to those of this study. Thus, measurement error cannot be then the reasons for this discrepancy.

4.5 Conclusion

This chapter investigated filtration of WOx and NaCl nanoparticles using uncharged stainless-steel wire screens at different particle sizes and concentrations. Results showed that both polydispersed and monodispersed measurements can be employed for accurate measurement of filtration efficiency. The

results also showed that filtration efficiency measurements are the same for sheath air to sample air flow rate ratios of both 10:1 and 5:1.

This study challenged the filtration efficiencies of NaCl and WOx particles with different number concentration distributions. Results showed that NaCl and WOx particles behave differently during filtration. The behavior of WOx nanoparticles during filtration was likely due to the different morphology of WOx particles, which affects particle charging and therefore both filtration efficiency and measurement performance. WOx particles produced with evaporation/condensation method are highly charged, causing them not to follow conventional filtration theory. For particles larger than 5 nm, higher particle concentration leads to lower filtration efficiency.

Moreover, results showed that the measured filtration efficiencies of particles between 2.35 nm and 5 nm or so follow conventional filtration model. Thus, it can be concluded that the GRIMM SMPS+E is accurate for the sizes of concern, especially for particles with diameters smaller than the size of peak concentration, allowing us to continue working with it for the next chapters.

In this study, thermal rebound was not observed for particles down to 2.35 nm. Thus, in the next chapter, a new model for thermal rebound theory is developed to determine the size of nanoparticles for which thermal rebound occurs.

Chapter 5
Theoretical Study on Thermal Rebound in Nanosized Particle Filtration[1]

5.1 Summary

The results in Chapter 4 did not show thermal rebound for particle sizes down to 2.35 nm. Therefore, this chapter investigates the theoretical model of thermal rebound theory. The chapter begins by considering the effect of material properties on thermal rebound, followed by presenting the effects of electrostatic and capillary forces on nanoparticle filtration.

This chapter also presents a new model for airborne nanoparticle filtration, by taking into account the effects of electrostatic and capillary forces and plastic behavior impaction. This model was validated using experimental data both from the literature and collected during this research. The capillary force between both particle and filter surfaces was shown to increase with relative humidity levels, leading to reduced rebound of nanoparticles from a filter media. Therefore, thermal rebound of nanoparticles may occur at low relative humidity.

5.2 Problem Statement

Since the introduction of thermal rebound theory by Wang and Kasper (1991), many experimental studies have been conducted to examine the thermal rebound theory (Alonso et al. 1997; Brochot et al. 2011; Golanski et al. 2009; Heim et al. 2005; Heim et al. 2010; Huang et al. 2007; Ichitsubo et al. 1996; Japuntich et al. 2007; Kim et al. 2006; Kim et al. 2007; Otani et al. 1995; Rengasamy et al. 2008;

[1] Similar contents of this chapter were published as:

Givehchi, R., and Tan, Z. (2014). Thermal Rebound in Nanosized Particle Filtration. *Proceedings of The Canadian Society for Mechanical Engineering International Congress*.

Givehchi, R., and Tan, Z. (2015). The Effect of Capillary Force on Airborne Nanoparticle Filtration. *Journal of Aerosol Science*. 83:12-24.

Scheibel and Porstendörfer 1984; Shin et al. 2008b; Skaptsov et al. 1996; Steffens and Coury 2007b; Van Gulijk et al. 2009; Van Osdell et al. 1990; Wang et al. 2007b; Yamada et al. 2011). However, very few of them have reported experimental evidences to support the phenomena of thermal rebound in nanoparticle filtration (Ichitsubo et al. 1996; Kim et al. 2006; Otani et al. 1995; Rennecke and Weber 2013a; Van Gulijk et al. 2009). Despite the large body of literature substantial uncertainty still remains in this area of research, and the reasons why some have observed the thermal rebound of nanoparticles while others have failed are unclear.

Researchers stated that the results produced by Otani et al. (1995) and Ichitsubo et al. (1996) might be inaccurate due to the mobility shift in the particle size classification devices, when particles are classified from polydispersed particles mainly consists of much larger particles (Alonso et al. 1997; Heim et al. 2006). Only, the experimental results of the following groups of researchers were not openly challenged. Kim et al. (2006) employed monodisperse NaCl nanoparticles down to 1 nm through a fibrous glass filter at 1.22% relative humidity; they showed the possible evidence of drop of nanoparticle filtration efficiency for sub-2 nm particles. Van Gulijk et al. (2009) then tested polydispersed NaCl, $CaCl_2$, $(NH_4)_2SO_2$, and $NiSO_4$ particles passing through a stainless steel grid and a wire screen; they also demonstrated the drop in filtration efficiency of NaCl and $NiSO_4$ particles. Both groups of the researchers claimed that they have successfully observed thermal rebound in nanoparticle filtration. Recently, Rennecke and Weber (2013) investigated the thermal rebound of nanoparticles under low pressure and demonstrated the possibility of thermal rebound for dense NaCl particles in the range of 20 nm to 60 nm.

Existing nanoparticle filtration models with the consideration of thermal rebound were built on the Bradley-Hamaker (BH) or Johnson-Kendall-Roberts (JKR) elastic adhesion energy models (Mouret et al. 2011; Wang and Kasper 1991), and they did not consider the Derjaguin-Muller-Toporov (DMT) elastic adhesion energy model for the calculation of adhesion efficiency, which seems to be more applicable to nanoparticles. Furthermore, all researchers have assumed elastic impact between nanoparticles and filter media. However, latest advances in molecular dynamic simulation have proven the plastic deformation of nanoparticles upon impact with the surface of the filter media (Awasthi et al. 2006; Awasthi et al. 2007; Ayesh et al. 2010; Gilabert et al. 2006; Ikeda et al. 1999).

Adhesion energy models also require the exact value of the mechanical constant, Hamaker constant, and the specific adhesion energy between bodies; however, exact values are unavailable for most materials. Also, studies show that the material properties of nanoscale bodies differ from those of bulk materials (Richter et al. 2009). For example, studies revealed that the Hamaker constant of nanoparticles differs from those larger ones (Esquivel-Sirvent and Schatz 2012; Pinchuk 2012). Thus, incorporating the material properties of nanoparticles based on those bulk materials may lead to inaccuracy in the thermal rebound.

Another factor missing in the theory of airborne nanoparticle filtration is the effect of capillary force between the nanoparticle and the surface of the filter media. Studies have shown the increase of the adhesion energy between a particle and a solid surface at high relative humidity (Bateman et al. 2014; Chen et al. 2011; Stein et al. 1994; Vasiliou et al. 1999). It has also been reported that the filtration efficiencies for micron particles increase with the level of relative humidity (Brown 1993; Miguel 2003; Mullins et al. 2003; Xu et al. 2014); however, it is not clear whether this applies to nanosized particles.

Furthermore, the effect of electrostatic force on nanoparticle filtration was not considered in earlier studies of nanoaerosol filtration and thermal rebound. Previous models were developed based on consideration of uncharged particles and filters; however, in reality, most aerosol particles and filters carry ions. Studies conducted to determine how the charge states of micron particles affect filtration and have shown that as the particle charge increases, the penetration of particles through a filter decreases (Chen and Huang 1998; Lundgren and Whitby 1965); however, only a few studies have been done to determine how a sub-100 nm particle charge state affects filtration (Kim et al. 2006; Yun et al. 2007). Kim et al. (2006) showed that the filtration efficiency of sub-100 nm sodium chloride particles is lower for uncharged particles than for charged particles at the face velocity of 2.5 cm/s, and this discrepancy decreases with a decrease in the particle size (Kim et al. 2006). Another study on the use of electrospun filters for sub-80 nm NaCl particles showed that the nanoparticle removal efficiency is independent of the charge state of particles, thus showing the negligible effect of columbic force compared to that of a strong diffusion force (Kousaka et al. 1990; Yun et al. 2007).

The main objective of this chapter is to develop a new nanoparticle filtration model by considering the effects of thermal rebound, electrostatic force and capillary force between nanoparticles and the filter media. This chapter presents a new approach using the plastic deformation of nanoparticles upon

impaction to determine the particle critical velocity above which thermal rebound occurs. The new model is then validated using our experimental data and those in literature. In the experimental phase of this study, the removal filtration efficiencies of WOx and NaCl nanoparticles through stainless-steel wire screens were evaluated as a function of particle size at air flow rate of 2 lpm.

5.3 Theoretical Analysis

Theoretical analyses have been reviewed in Chapter 2 and they are briefly summarized as follows. The penetration efficiency of particles through the filter is (Cheng and Yeh 1980)

$$P = \exp\left[\frac{-4\alpha\varepsilon EL}{\pi d_f(1-\alpha)}\right] \tag{5-1}$$

where P is the penetration efficiency, L is the filter thickness, α is the solidity of the filter, d_f is the diameter of the fiber, E is the corresponding single fiber efficiency, and ε is the adhesion efficiency of nanoparticles to the surface of the filter media. The diffusional single fiber efficiency of nanoparticles through a wire screen is determined by Cheng and Yeh (1981) theory, which was explained in section 2.3.1.

It should be noted that the maximum value for single fiber efficiency is 1. Previous studies (Mouret et al. 2011; Wang and Kasper 1991) employed diffusion deposition equation (Lee and Liu 1982b) for the calculation of single fiber efficiency, which led to values of greater than 1 for sub-10 nm particles. Many researchers did not correct the error of the equation, and supper-1 single fiber efficiency was used in their works. The multiplication of these values by an adhesion efficiency with a maximum value of 1 leads to a high filtration efficiency for small nanoparticles.

5.3.1 Thermal rebound

In order to include the effect of thermal rebound in an air filtration model, the adhesion efficiency of nanoparticles (ε) is employed for the calculation of single fiber efficiency based on the thermal rebound effect ($E_{eff} = E.\varepsilon$). The fractional adhesion efficiency is defined as (Wang and Kasper 1991)

$$\varepsilon = \int_0^{v_{cr}} f(v_{im})dv_{im} \Big/ \int_0^{\infty} f(v_{im})dv_{im} \tag{5-2}$$

With a Boltzmann distribution for the particle impact velocity, Eq.(5-2) becomes

$$\varepsilon = \int_0^{v_{cr}} v_{im}^2 exp\left(-\frac{mv_{im}^2}{2K_bT}\right) dv_{im} \Big/ \int_0^{\infty} v_{im}^2 exp\left(-\frac{mv_{im}^2}{2K_bT}\right) dv_{im} \tag{5-3}$$

The numerator and denominator of Eq.(5-3) are, respectively:

$$\int_0^{v_{cr}} v_{im}^2 exp\left(-\frac{mv_{im}^2}{2K_bT}\right) dv_{im} = \frac{\sqrt{\pi}\text{erf}\left(\sqrt{\frac{m}{2K_bT}}x\right)}{4\left(\frac{m}{2K_bT}\right)} - \frac{x.exp\left(-\frac{m}{2K_bT}x^2\right)}{\frac{m}{K_bT}} \tag{5-4}$$

$$\int_0^{\infty} v_{im}^2 exp\left(-\frac{mv_{im}^2}{2K_bT}\right) dv_{im} = \frac{\sqrt{\pi}}{4\left(\frac{m}{K_bT}\right)^{1.5}} \tag{5-5}$$

The adhesion efficiency is then calculated as

$$\varepsilon = \text{erf}\left(\sqrt{\frac{m}{2K_bT}}v_{cr}\right) - \sqrt{\frac{2m}{\pi K_bT}}v_{cr}exp\left(-\frac{m}{2K_bT}v_{cr}^2\right) \tag{5-6}$$

Recall that

$$\bar{v}_{im} = \sqrt{\frac{8K_bT}{\pi m}} \tag{5-7}$$

Eq.(5-7) becomes

$$\varepsilon = erf\left(\frac{2}{\sqrt{\pi}}\frac{v_{cr}}{\bar{v}_{im}}\right) - \frac{4}{\pi}\frac{v_{cr}}{\bar{v}_{im}}\ exp\left[-\frac{4}{\pi}\left(\frac{v_{cr}}{\bar{v}_{im}}\right)^2\right] \tag{5-8}$$

where $\bar{v}_{im}$ is the mean impaction velocity of a particle as follows:

$$\bar{v}_{im} = \left(\frac{48K_bT}{\pi^2\rho_P d_P^3}\right)^{1/2} \tag{5-9}$$

When a particle collides with the surface of the filter media, a complex deformation (elastic and plastic) occurs; it is difficult to simulate the exact process. However, in the present study, we can carry on the analysis by considering a fully elastic deformation or fully plastic deformation assumption. The particle critical velocity is described as (Dahneke 1971)

$$v_{cr} = \left(\frac{12E_{ad}}{\pi\rho_p d_p^3 e^2}\right)^{1/2} \tag{5-10}$$

where ρ_p is the density of the particle, d_p is the diameter of the particle, e is the coefficient of restitution, and E_{ad} is the adhesion energy.

The coefficient of restitution for nanoparticles is not unity, and the absolute value is unknown for nanosized particles (Ayesh et al. 2010; Givehchi and Tan 2014; Sato et al. 2007; Wall et al. 1990). The coefficient of restitution varies with the material of the nanoparticles, the filter media, and the impact velocity of the nanoparticles. For impact velocity close to the critical velocity, the coefficient of restitution is small, leading to small rebound velocity (Rennecke and Weber 2013a). The molecular dynamic simulation by Ayesh et al. (2010) also confirmed the small coefficient of restitution for nanoparticles, which is less than 0.6 for solid nanoparticles.

The adhesion energy can be calculated based on the JKR, DMT, MP and WM models that were comprehensively explained in Chapter 2 (2.4.1), and are summarized in Table 5-1.

Table 5-1. Adhesion energy in different models

Model	Adhesion Energy
JKR	$E_{ad} = \left(6\Delta\gamma^{\frac{5}{2}}\pi^{\frac{5}{2}}R^{*2}/K^*\right)^{2/3}$
DMT	$E_{ad} = \left(2\Delta\gamma^{\frac{5}{2}}\pi^{\frac{5}{2}}R^{*2}/K^*\right)^{2/3}$
MP	$E_{ad} = 2\pi\Delta\gamma^2 R^*/H$
WM	$v_{Cr} = \left(4\Delta\gamma^2/5.3^{\frac{1}{3}}\rho_P Y R^{*2}\right)^{1/2}$

The calculation of adhesion energy using Eq.(2-50) requires known mechanical constants, the Hamaker constants, the specific adhesion energies, and the elastic yield of particles. However, these parameters are unknown for most nanomaterials (Givehchi and Tan 2014). In addition, more and more studies have shown that the material properties of nanoscale materials differ from those of bulk materials (Gu et al. 2008; Rennecke and Weber 2013b). Some of these material properties are not available for nanosized particles (Hartland 2004). Incorporating the material properties of the nanoparticles based on those of the bulk materials may thus lead to discrepancies between the model

and experiment. In this work, the bulk material properties of the particles and filters required for the calculation of the nanoparticle adhesion efficiency are shown in Table 5-2.

Table 5-2. Bulk material properties (Ahmadi et al. 2007; Eichenlaub et al. 2002; Rennecke and Weber 2013b; Soltani and Ahmadi 1995; Wang and Kasper 1991)

Quantity	Steel	WOx	NaCl	Silver	Copper	Glass	Polystyrene
A $(.10^{-20}\mathrm{J})$	21.2	12.1	7.9	34.2	33.0	8.5	7.9
$\Delta\gamma_{RH=0\%}$ $(.10^{-3}\mathrm{J/m^2})$	35.14	20.15	13.09	56.69	54.70	14.09	13.09
v	0.27	0.284	0.252	0.37	0.33	0.2	0.33
E $(.10^{9}\ \mathrm{N/m^2})$	215	411	39.98	10.5	130	69	2.8
K$(.10^{-11}\mathrm{m^2/N})$	0.137	0.07	0.746	2.617	0.218	0.443	10.130
ρ $(\mathrm{Kg/m^2})$	7840	7160	2165	10500	8890	2180	1005
Y $(.10^{6}\ \mathrm{N/m^2})$	500	550	600	330	70	1900	22

5.3.2 Effects of electrostatic force

Another factor which may enhance the adhesion force for nanoparticles and a surface is the effect of electrostatic force due to the attachment of charged nanoparticles to the surface. Most particles and filters carry ions; however, the levels of their charge are not high to increase the electrostatic force between the nanoparticle and the filter. Therefore, in this section it is assumed that nanoparticles are highly saturated unipolar charged, which have the highest electrostatic force among other charge states of nanoparticles. The electrostatic force (F_e) on unipolar charged nanoparticles in a gas with a permittivity ε_0 and the electric field of E is as follows:

$$F_e = qE + \frac{q^2}{16\pi\varepsilon_0 Z^2} + \frac{qEd_P^3}{16Z^3} + \frac{3\pi\varepsilon_0 d_P^3 E^2}{128Z^4} \qquad (5\text{-}11)$$

where the terms on the right hand side of the Eq.(5-11) are Columbic force, image force, dielectrophoretic force and polarization force, respectively. The image and polarization forces are toward the surface; however, the other two forces may be toward or away from the surface based on the type of charge carried by a particle. E is the electric field, ε_0 is the permittivity of a vacuum

(8.859×10^{-12} C^2/(N.m^2)), Z is the distance between a particle and a surface ($Z = Z_0 + d_P/2$), and q is the electrical charge on particles:

$$q = ne \tag{5-12}$$

where e is the elementary unit charge of an electron (1.6×10^{-19} C), and n is the number of charges carried by the particle. The number of saturated charges (n) carried by an individual nanoparticle in unipolar diffusion charging during a time t is

$$n = \frac{d_P K_b T}{2e^2 K_e} \ln\left(1 + \frac{d_P K_e C_i \pi e^2 N_i t}{2K_b T}\right) \tag{5-13}$$

where K_b is the Boltzmann constant (1.38×10^{-23} J/K), T is the temperature, K_e is a proportionality constant ($1/4\pi\varepsilon_0=9\times10^9$ Nm^2/C^2), C_i is the mean thermal speed of ions (240 m/s at standard condition), and N_i is the ion concentration typically in the order of 5×10^{14} ions/m^3 (Tan and Wexler 2007). However, for small nanoparticles in which the average number of charged per particles is less than unity, the effective value of the $N_i t$ decreases as the size of nanoparticles decreases (Hogan Jr. et al. 2009). So the number of charged per particle is overestimated.

To include the effect of electrostatic force on nanoparticle filtration, it is assumed that nanoparticles attach to the surface of the filter by van der Waals force and the electrostatic force. As a result, the effective pull-off force can be calculated as follows:

$$F_{Pull-off} = F_{Pull-off}^{F_e=0} + qE + \frac{q^2}{16\pi\varepsilon_0 Z^2} + \frac{qEd_P^3}{16Z^3} + \frac{3\pi\varepsilon_0 d_P^3 E^2}{128Z^4} \tag{5-14}$$

The effective surface adhesion energy for the JKR and WM models, is then described using the following equation.

$$\frac{3}{2}\pi\Delta\gamma R^* = \frac{3}{2}\pi\Delta\gamma_{F_e=0} R^* + qE + \frac{q^2}{16\pi\varepsilon_0 Z^2} + \frac{qEd_P^3}{16Z^3} + \frac{3\pi\varepsilon_0 d_P^3 E^2}{128Z^4}, \tag{5-15}$$

and for the DMT and MP models, it is calculated using the following equation.

$$2\pi\Delta\gamma R^* = 2\pi\Delta\gamma_{F_e=0} R^* + qE + \frac{q^2}{16\pi\varepsilon_0 Z^2} + \frac{qEd_P^3}{16Z^3} + \frac{3\pi\varepsilon_0 d_P^3 E^2}{128Z^4} \tag{5-16}$$

5.3.3 Effects of capillary force

The preceding adhesion energy models did not include the effect of air humidity on particle adhesion energy, and air was assumed to be dry. In reality, air contains moisture, and most air filtration takes place in humid air. When there is moisture in the air, meniscus is formed by the condensation of vapor on the contact surface. As a result, the capillary force may affect filtration performance, and it is thus necessary to quantify this effect.

The condensation of water vapor in the small gap between a particle and a surface in humid air forms a meniscus neck between the particle and the surface (Chen and Soh 2008; Chen and Lin 2008; Orr et al. 1975). The meniscus grows until evaporation rate and condensation rate reach equilibrium with the ambient air (Pakarinen et al. 2005), leading to the capillary force which increases the adhesion force between particle and the surface of the filter media (Ahmadi et al. 2007; Zhang and Ahmadi 2007). Although studies have been done to determine the meniscus profile (Pakarinen et al. 2005), it is beyond the scope of this work.

As depicted in Figure 5-1, the capillary force on hydrophilic surface is a function of the surface tension of water

$$F_c = 2\pi\sigma d_P[sin\alpha \sin(\alpha + \theta) + cos\theta] \tag{5-17}$$

where F_c is the capillary force, σ is the surface tension of water (0.0735 *N/m* at STP condition), d_P is the particle diameter, θ is the wetting angle, and α is the angle between the imaginary lines perpendicular to the filter surface and meniscus. Since α and θ are typically small, Eq.(5-17) is simplified as

$$F_c = 2\pi\sigma d_P \tag{5-18}$$

Eq.(5-18) is the standard approximation for sphere particles larger than 1 μm. It may not apply for nanosized particles for the following reasons. First of all, for nanoparticles, the capillary force depends on relative humidity (Pakarinen et al. 2005). And, the surface tension force also depends on the size of nanoparticles, which attenuates the total capillary force for such small nanoparticles (Israelachvili 1991; Pakarinen et al. 2005).

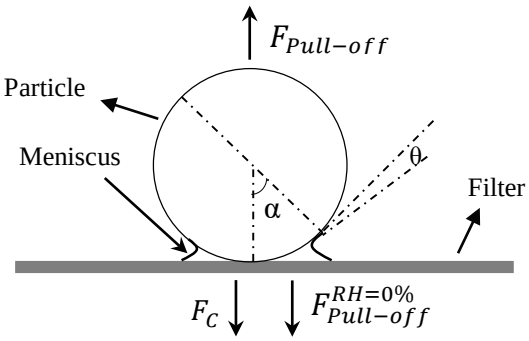

Figure 5-1. Schematic diagram for the attachment of a spherical particle to a filter surface with capillary force

Pakarinen et al. (2005) calculated the capillary force between nanoparticles and solid surface as a function of particle size, relative humidity, and surface tension. Their results showed that the capillary force on nanoparticles depends on relative humidity, and that Eq.(5-18) can be only used for 100% relative humidity. In order to quantify the effect of relative humidity on capillary force, a new term of β is defined as the ratio of the standard approximation of total capillary force calculated using Eq.(5-18) to the actual capillary force at certain relative humidity level. Then, the capillary force for nanoparticles with the consideration of relative humidity is described as

$$F_c = 2\beta\pi\sigma d_P \tag{5-19}$$

where β is size dependent, and it can be determined using the experimental data by Pakarinen et al. (2005) (Figure 3 of the original paper). The capillary force for other sizes and relative humidities can be calculated by extrapolation.

The consequent pull-off force may be enhanced by the consideration of capillary force. The effective pull-off force shown in Figure 5-1 is then calculated as follows:

$$F_{Pull-off} = F_{Pull-off}^{RH=0\%} + 2\beta\pi\sigma d_P \tag{5-20}$$

where $F_{Pull-off}^{RH=0\%}$ is the adhesion force at $RH = 0\%$. Then, the effective surface adhesion energy ($\Delta\gamma$) for the JKR and WM models becomes

$$\Delta\gamma = \Delta\gamma_{RH=0\%} + \frac{8}{3}\beta\sigma \tag{5-21}$$

and that for the DMT and MP models becomes

$$\Delta\gamma = \Delta\gamma_{RH=0\%} + 2\beta\sigma \tag{5-22}$$

where $\Delta\gamma = \Delta\gamma_{RH=0\%}$ is the surface adhesion energy at $RH = 0\%$.

5.4 Experimental Setup

Experimental setup used in this chapter is the same as that explained in Chapter 4. Polydispersed aerosols (NaCl, WOx) were introduced through a circular filter holder at a flow rate of 2 lpm. Polydispersed particles were chosen as feed aerosol particles because they are close to real applications. Stainless-steel wire screens were tested as filters. The wire screens had uniform wires with a diameter of 25 μm and the screen thickness was 50 μm. The filter solidity was 0.64. These single-layer filters with well-defined structures minimize the effect of depth on the filtration efficiency. Prior to test, the stainless-steel wire screen was treated with isopropanol alcohol in order to remove the possible charges on the filter media for diminishing the electrostatic force on the filter (Martin Jr and Moyer 2000).

A scanning mobility particle sizer with a Faraday cup electrometer (SMPS+E, S-DMA GRIMM) was used for measuring the nanoaerosol particle number concentration distribution. The ratio of the aerosol and sheath flow rates through the SMPS+E was 1:10 in all experiments. Pre-calibration of aerosol instruments was conducted by the supplier, and the accuracy of the instrument was deemed acceptable for the scope of the work described herein.

The concentrations of monodispersed nanoparticles were measured downstream of the filter with a scanning time of 2 min with and without the filter, representing downstream (c_{out}) and upstream (c_{in}) particle concentrations, respectively. The error of calculated efficiency due to particle loss is minimized by the identical sampling line. The sizes of nanoparticles were selected based on the mean diameter of nanoparticles that SMPS+E measured at the aerosol to sheath flow air ratio of 1:10. The sizes of the NaCl particles were 12.3 nm, 14.66 nm, 17.5 nm, 20.9 nm, 22.84 nm, 29.88 nm, 35.8 nm, and those of the WOx particles were 3.04 nm, 3.32 nm, 3.95 nm, 4.7 nm, 5.13 nm, 6.11 nm. Each data point was repeated for at least three times to ensure repeatability. The nanoparticle penetration (P) and removal filtration efficiency of the filter (η) for each particle size are calculated as

$$P = 1 - \eta = \frac{C_{out}}{C_{in}} \tag{5-23}$$

5.5 Results and Discussion

5.5.1 Effect of material properties

Figure 5-2 compares impact velocity and critical velocity calculated using different adhesion models for NaCl and WOx particles impacting a stainless-steel and glass filter. The particle's critical diameter (the intersection between impact velocity and critical velocity) depended on adhesion energy models (Table 5-3). The variations between these values are mainly due to the differences in the material properties of particles and filters. For elastic impaction models (JKR, DMT), the Hamaker constant, mechanical constant, and particle density; and for plastic impaction models (MP, WM), the Hamaker constant of materials, and yield stress and density of particles are important factors affecting particle's critical diameters.

Comparing the figures in each column reveals the importance of the filter material on particle's critical diameter. Overall, for both NaCl and WOx particles, considering all adhesion energy models, the particle critical velocity is smaller for glass media, which results in the larger critical particle diameter. The particle critical velocity is proportional to $\Delta\gamma^{5/6}.\rho_P{}^{-1/2}.K^{*-1/3}$, and $\Delta\gamma.\rho_P{}^{-1/2}.Y^{-1/2}$, for elastic and plastic impaction models, respectively. The lower the Hamaker constant (lower specific adhesion energy) of glass filter than that of the stainless steel filter decreases the critical velocity of both NaCl and WOx particles, and increases the critical particle diameter for all of the impaction models. The effects of Hamaker constants overcome the adverse effect of mechanical constants (a lower composite Young's modulus (K^*)) on the critical velocity for glass filter.

Comparing the figures in each row reveals the importance of a particle's material on its critical diameter. Overall, considering the elastic impaction models (JKR, DMT), the particle critical diameter for WOx particles is greater than that for NaCl particles if either filters of steel or glass filter are considered. The larger the particle density and mechanical constant (lower composite Young's modulus) of WOx particles, the lower the particle critical velocity, and as a result, the greater the particle critical diameter. However, if plastic impaction (MP, WM) is considered, the particle critical

diameter is smaller for WOx particles than NaCl ones, if either a steel or glass filter is considered due to the smaller elastic yield of WOx particles.

Figure 5-2 also shows that the elastic yield velocity depends on the target particle and filter. The difference between the elastic yield velocity values occurs due to differences in the hardness, mechanical constant, and density of particles. Based on Eq.(2-45) for tested particles, the lower the mechanical constant of a filter, the higher the composite mechanical constant, thus lowering the elastic yield velocity and increasing the probability of plastic impaction at lower impact velocities. Results show that the particle critical diameter for all tested particles and filters, occurs for small nanoparticles where the impact velocity is higher than the elastic yield velocity, implying the probability of plastic impaction, which has not been considered in previous studies.

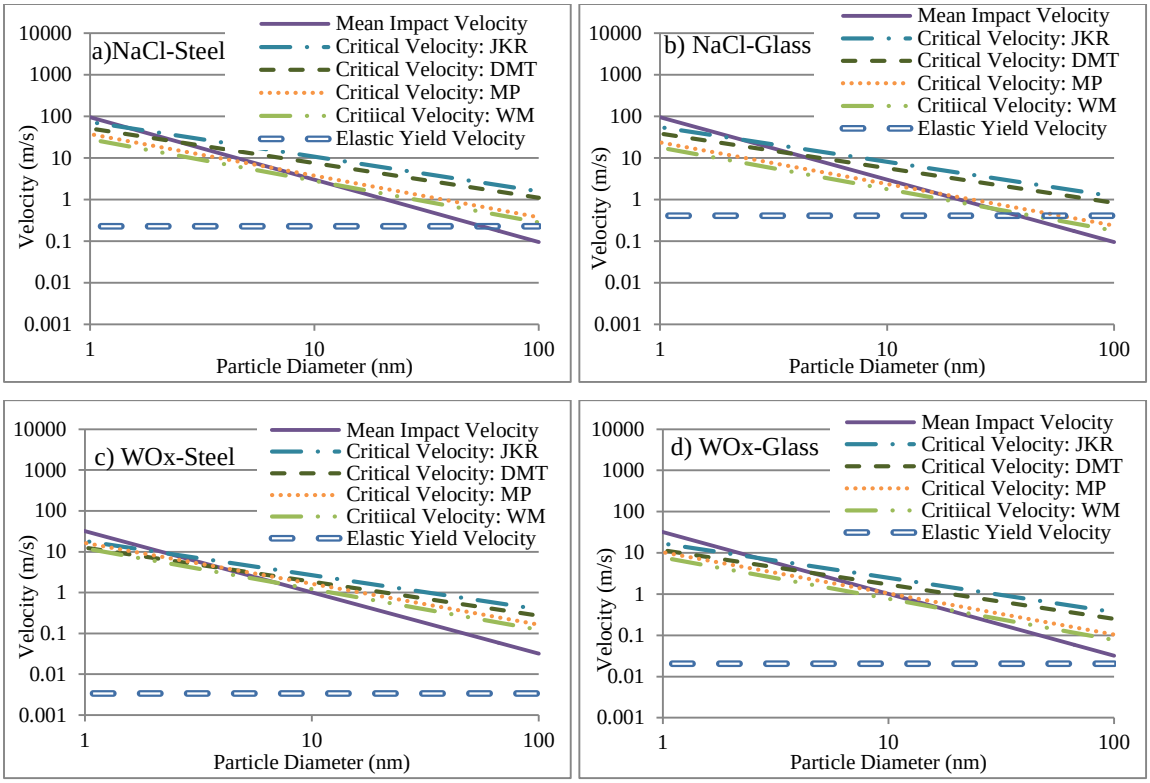

Figure 5-2. Comparison of impact velocity and critical velocities calculated using different adhesion models

Table 5-3. Particle critical diameters

	Adhesion energy models			
Particle-Filter	JKR	DMT	MP	WM
NaCl- Stainless steel	1.5 nm	2.6 nm	6.5 nm	11.6 nm
NaCl-Glass	2.3 nm	3.9 nm	16 nm	28.8 nm
WOx- Stainless steel	2.4 nm	4.1 nm	3.9 nm	7 nm
WOx-Glass	2.7 nm	4.6 nm	9.6 nm	17.3 nm

The critical diameters for different kinds of particles and filters are calculated at two temperatures for elastic and plastic models (Figure 5-3). In this figure, the Y axis represents the critical diameter, and the X axis indicates the interaction between the particle and the filter materials, respectively. Temperature affects thermal impaction velocity, and as a result, a particle's critical diameter. The critical diameter increases at higher temperatures due to the higher thermal impact velocity, causing larger particles to bounce off the filter surface. Thus, a strong recommendation is to decrease the temperature of the aerosol flow rate and so decrease the probability of thermal rebound.

The critical diameter depends strongly on the particle and filter materials involved. For most interactions, the critical diameter for plastic impaction is greater than that for elastic impaction, due to the lower adhesion energy between the particles and the surface. If the nanoparticle material is known, the filter surface can be selected to minimize the critical diameter.

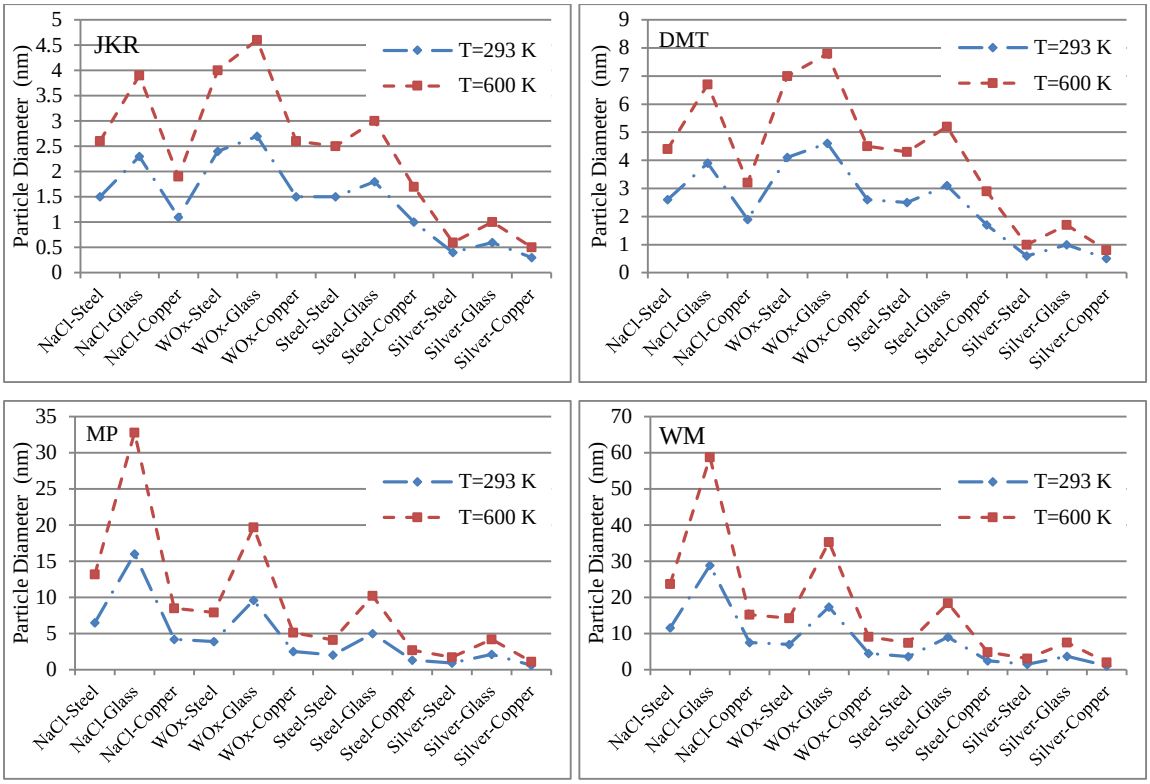

Figure 5-3. Comparison of critical diameters for a variety of particle-surface material interaction

For a variety of particle and filter materials, Figure 5-4 shows the analytical filtration efficiency based on the new thermal rebound theory plotted as a function of particle diameter. Although the conventional efficiency curves are the same for all particles and filter materials, the efficiency curves based on consideration of thermal rebound differ for different materials. If elastic impaction is considered, the removal efficiency for WOx particles directed through a steel filter is smaller than for other material interactions, followed by the efficiency for NaCl particles through a glass filter and steel particles through a glass filter. Considering plastic impaction, the removal efficiency for NaCl particles moving through a glass filter is lowest, followed by interaction of NaCl and steel. Comparison between these charts showed that filtration efficiency differs based on consideration of these elastic and plastic impaction models. Particle-removal efficiency based on consideration of plastic impaction is lower than that assumed for elastic impaction.

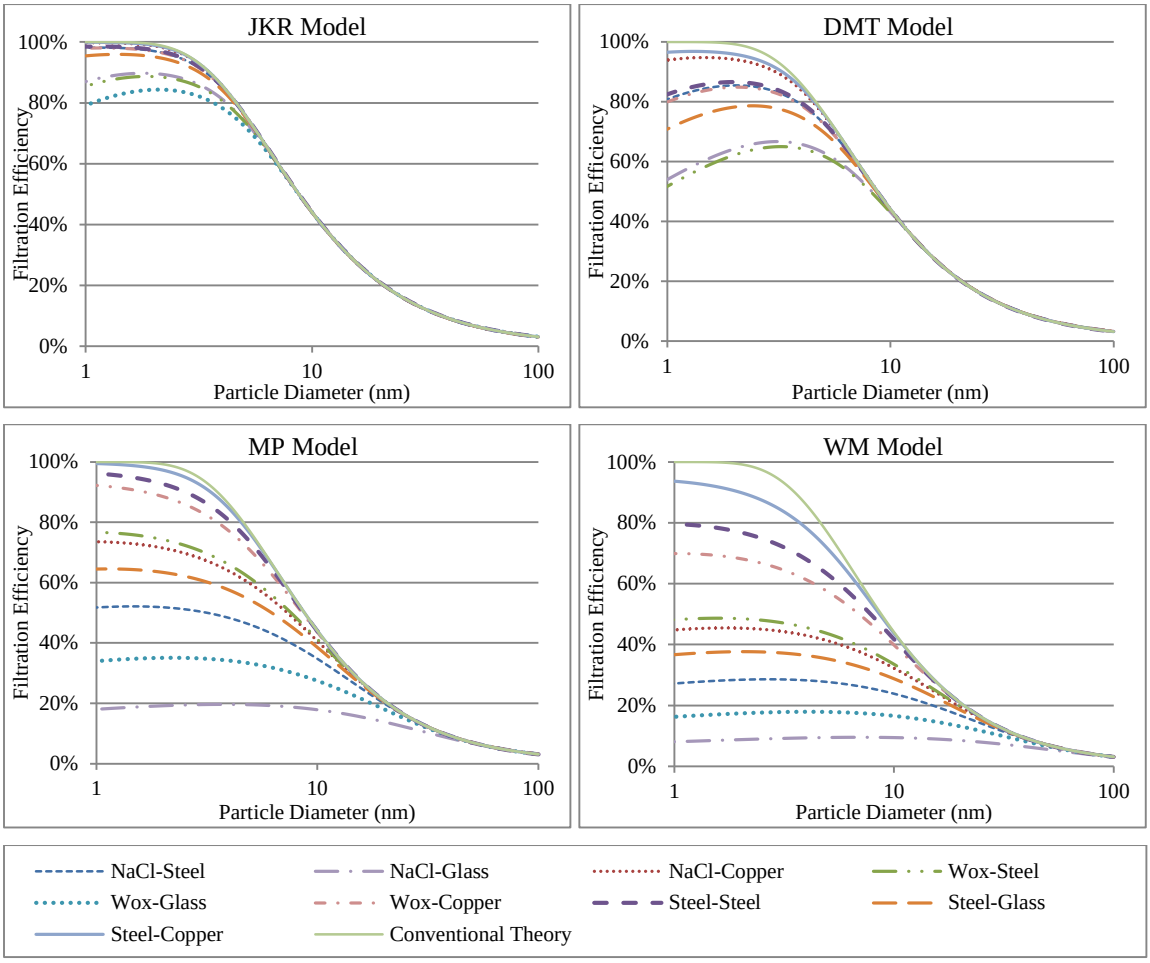

Figure 5-4. Particle removal efficiency of a filter as a function of particle size for a variety of particle and filter material

In summary, preliminary results show that, based on the adhesion energy models and the properties of particle and filter, filtration efficiency may start dropping when particle size is decreased to a certain critical diameter. Thus, proper matching between target particle and filter material is important to the effective particle-gas separation. To this point of this thesis, all adhesion models have been employed without determining which predicts thermal rebound better. Thus, in the next section, different models will be compared with each other, and a suitable model will be chosen for developing thermal rebound theory.

5.5.2 Comparison of different models for nanoparticle filtration

To compare the different adhesion energy models, the interaction between NaCl and a stainless-steel filter is illustrated here. Figure 5-5 shows the comparison of the calculated adhesion efficiency and filtration efficiency of spherical NaCl nanoparticles passing through a stainless-steel wire screen. The calculation was based on a volumetric flow rate of 2 lpm and for elastic (JKR, DMT) and plastic (MP, WM) deformation of nanoparticles upon impaction to the surface of the filter media. These calculated results indicate that the nanoparticle adhesion efficiency drops as the size of the nanoparticle decreases; however, the particle critical diameter and the drop rate depend on the model of choice. The JKR model predicts the greatest adhesion efficiency, followed in the decreasing order by the DMT, MP, and WM models.

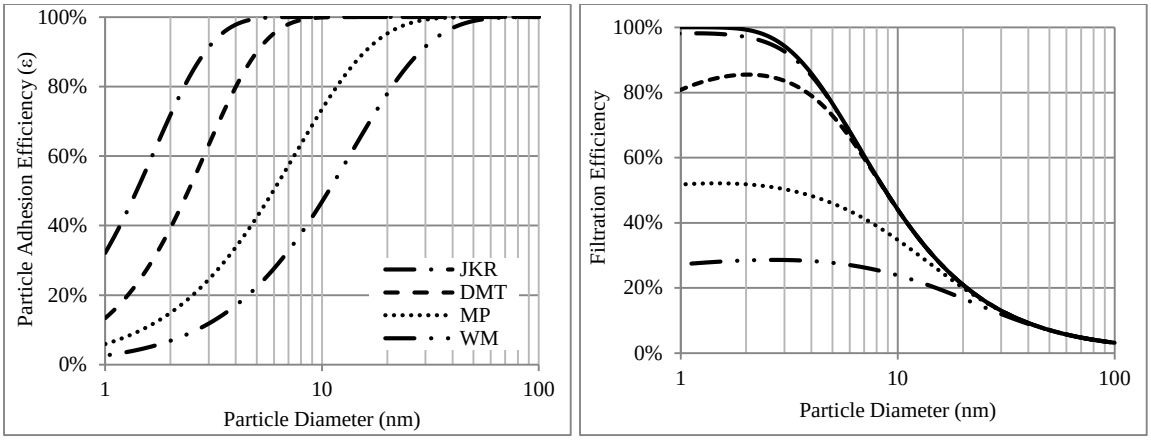

Figure 5-5. NaCl nanoparticle adhesion efficiencies and filtration efficiencies of the stainless-steel wire screen as a function of particle size using different adhesion energy models

Nonetheless, all calculated filtration efficiencies do not follow the conventional filtration theory. All models predict lower filtration efficiency than that calculated using conventional filtration model. In addition, the predicted filtration efficiency depends on the model of choice. Fully elastic deformation and fully plastic deformation represent two extremes of nanoparticle impaction. In reality, the removal efficiency should fall between the curves assumed for fully elastic and fully plastic impactions.

Within these four models of concern, the particle removal efficiencies calculated by considering plastic deformation effect (MP and WM models) are lower than those for elastic deformation (JKR and DMT models). This seems to be against our common sense, because one would expect elastic impaction

leads to less energy loss than plastic impaction, and consequently higher chance for transported nanoparticles to rebound from the surface of the filter media. This discrepancy is resulted from the assumptions of the plastic models. In WM and MP models, the plastic deformation cannot be recovered as energy required for particle rebound. However, as the energy lost through plastic deformation increases, greater energy is stored in the secondary elastic deformation (Xu et al. 1993), which leads to a higher probability of the rebound of nanoparticles. That is why the curves corresponding to MP and WM plastic deformation models in Figure 5-5 are much lower than those from JKR and DMT elastic deformation models.

For the elastic impact models (JKR and DMT), the Tabor parameter is employed herein to determine the applicable elastic deformation model between JKR and DMT models. The calculated Tabor parameter based on Eq.(2-38) using the properties of NaCl particle and stainless steel filter media is less than 0.1 for sub-100 nm particles. As introduced above and confirmed by other researchers, the JKR model applies to a large-value Tabor parameter ($\mu > 5$), and the DMT model is more applicable for a small value ($\mu < 0.1$) (Greenwood 1997; Johnson and Greenwood 1997; Muller et al. 1980; Tsai et al. 1991). Therefore, the DMT model shown in Figure 5-5 provides a better approximation of the elastic impaction of NaCl nanoparticles and a stainless steel surface than the JKR model does.

On the other hand, DMT model cannot represent the actual nanoparticle adhesion energy and filtration either. As explained in the theoretical analysis part above (Section 2.4.1), the comparison between the particle elastic yield velocity and particle impact velocity to the filter media defines the plastic and elastic deformation zone. Figure 5-6 shows the particle impact and critical velocity vs. particle diameter for NaCl particles. The calculated elastic yield velocity of NaCl particles striking a stainless-steel wire is 0.22 m/s. Nanoparticles with impact velocity greater than this value have a higher chance of plastic deformation. Our calculation using NaCl nanoparticles showed that particles smaller than 56 nm corresponds to an impact velocity greater than 0.22 m/s. The direct measurement of nanoparticle critical velocity also shows that plastic deformation regime occurs for sub-20 nm particles (Rennecke and Weber 2013b), which is in agreement with the results. There is no thermal rebound for particles greater than 56 nm, and the filtration efficiencies calculated using both elastic and plastic deformation models agree with conventional filtration theory. Therefore, plastic deformation models (MP and WM) will be used for further discussion in the text that follows.

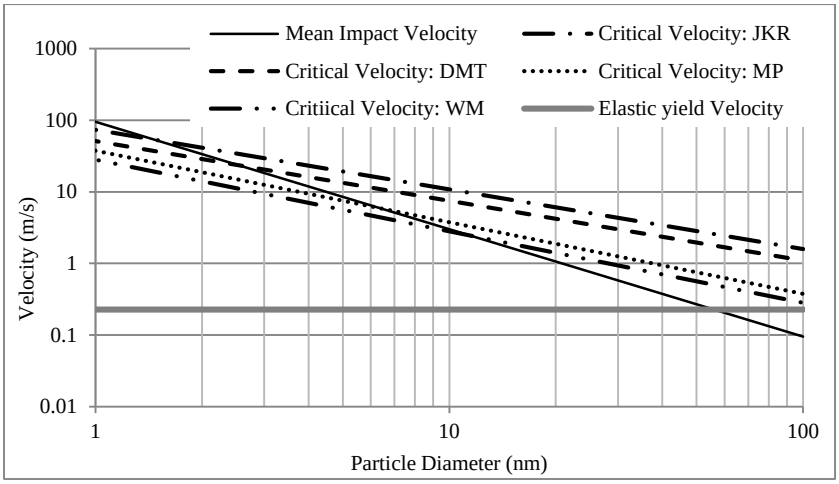

Figure 5-6. Comparison of the impact velocity, critical velocity and elastic yield velocity calculated using different adhesion energy models

5.5.3 Nanoparticle filtration with the consideration of electrostatic force

Figure 5-7 shows the adhesion efficiency and filtration efficiency of unipolar saturated charged nanoparticles through the stainless steel wire mesh filter. Comparison between Figure 5-6 and Figure 5-7 demonstrates the negligible effect of electrostatic force on the thermal rebound and adhesion efficiency of nanoparticles. In this section, the electrostatic force was calculated based on the assumption of fully saturated charged nanoparticles, and results show that even the maximum electrostatic force and the saturated charge levels of nanoparticles do not affect the adhesion efficiency between these nanoparticles and the filter. This phenomenon occurs because Brownian diffusion is the most dominant mechanism in capturing sub-100 nm particles, and the electrostatic force may not affect the particle filtration efficiency for small nanoparticles (Kim et al. 2006; Lee et al. 2002b; Li and Xia 2004; Wang and Otani 2013). The results are in agreement with a study that showed that the penetration of charged, uncharged, and neutralized sub-100 nm particles is the same (Yun et al. 2007). Even in electret filters, Brownian diffusion has been shown to be more significant than electrostatic forces (Lee et al. 2002b). Even the maximum electrostatic force between charged particles and filters does not affect adhesion efficiency or filtration efficiency.

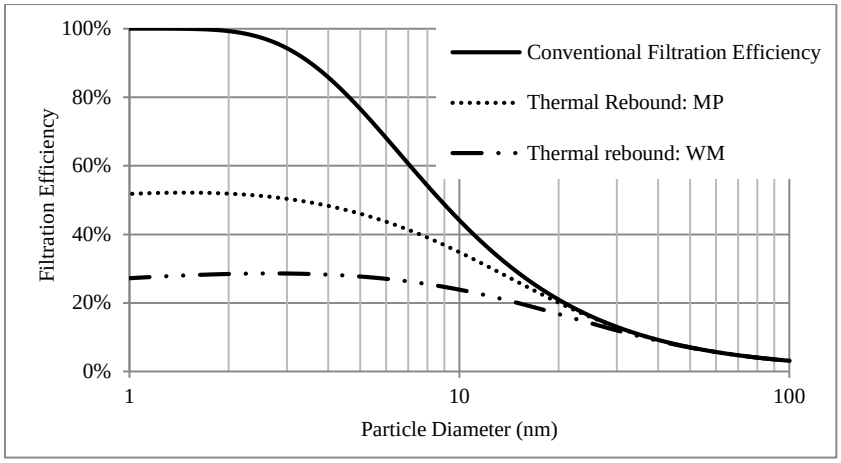

Figure 5-7. NaCl nanoparticle filtration efficiency of a stainless-steel wire screen as a function of particle size for a variety of adhesion energy models with the presence of electrostatic force

5.5.4 Nanoparticle filtration with the consideration of capillary force

Figure 5-8 shows the pull-off forces based on adhesion energy models and the capillary forces at various relative humidity levels as a function of particle diameter. It shows that the pull-off forces attempting to detach the nanoparticles from the surface increase with the nanoparticle size. Results also show that as the relative humidity increases, the pull-off force increases due to the stronger capillary force. The discrepancy between the pull-off forces for WM and MP model decreases with the increase in the relative humidity. As there is almost no difference between the pull-off forces for WM and MP models at a relative humidity of 100%. It indicates that the pull-off force at this relative humidity is approximately equal to the capillary force. Therefore, the capillary force should be considered for the calculation of the pull-off force and nanoparticle filtration.

Figure 5-9 shows the filtration efficiency calculated using MP and WM models for NaCl nanoparticles passing through a stainless-steel wire screen at three relative humidity conditions (0%, 5%, and 10%). The particle critical diameters in the absence of capillary force (RH=0%) are approximately 21 nm and 37 nm for MP and WM plastic deformation models, respectively. The critical diameters decrease to 7 nm and 9 nm for MP and WM models, respectively, as the relative humidity increases to 5%. At higher relative humidity conditions (RH>5%), capillary force has an additive effect on the adhesion energy between a particle and a filter surface, and therefore, increases the adhesion energy. Therefore, the calculated filtration efficiency curve approaches the conventional filtration

curve. Thus, the calculated particle filtration efficiency strongly depends on air relative humidity, as the filtration efficiency increases with relative humidity.

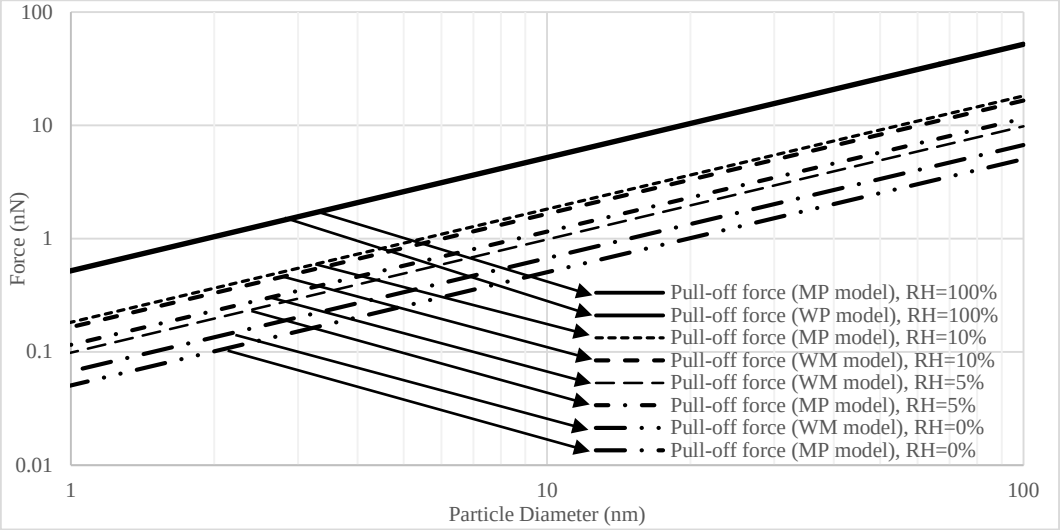

Figure 5-8. Variation of the pull-off forces as a function of particle diameter at various relative humidity levels

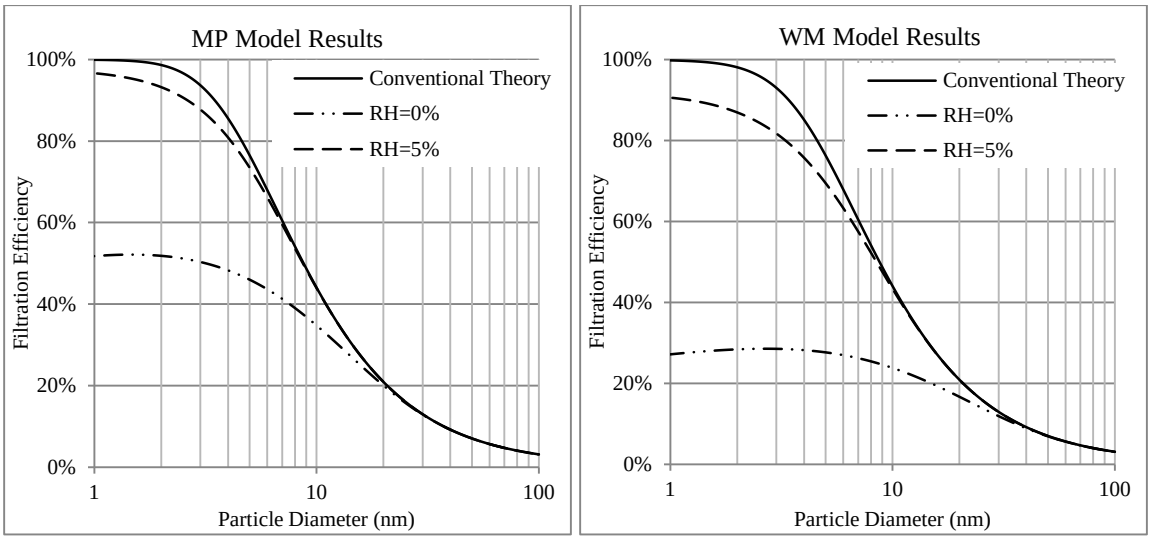

Figure 5-9. NaCl nanoparticle filtration efficiency of the stainless-steel wire screen at various relative humidity levels for plastic deformation models

The preceding analysis might help explain why many researchers could not observe thermal rebound in their experiments. Even at a relatively low relative humidity of RH=5%, the meniscus bridge water

is formed between the nanoparticle and the filter surface, leading capillary force to enhance the adhesion between nanoparticles and the surface. Most experiments were conducted at normal relative humidity level in the range of 25% to 40% (Mullins et al. 2003; Van Gulijk et al. 2009) except for the one by Kim et al. (2006). Kim et al. (2006) conducted their experiments at the relative humidity level of 1.22% as reported. According to the theoretical analysis above, thermal rebound could occur at such this low relative humidity, where the capillary force is minimized. As to be introduced shortly, our analysis herein concurs their experimental observations.

5.5.5 Validation of the model with experimental data

The experimental results of this study and those published by Alonso et al. (1997), Boskovic et al. (2005), Brochot et al. (2011), Heim et al. (2005) and Kim et al. (2006) are compared with the filtration efficiency calculated using the new model by considering capillary effect.

Figure 5-10 shows the comparison between the experimental data and filtration model for the present study. Overall, the model agreed well with the experimental results. In our experimental work, we used nanosized WOx and NaCl particles as test aerosol. The comparison between the filtration model (Eqs.(4-2,3)) and the experimental data obtained at air relative humidity level of about 20% is shown in Figure 5-10. The NaCl particles are believed to be completely dry at this relative humidity. According to the deliquescence phenomenon, NaCl particles lose water when RH<45% (Martin 2000; Van Gulijk et al. 2009). At this condition, the NaCl particles are in cubic shape (Martin 2000; Wise et al. 2007). Because of this relatively high relative humidity, the capillary force enhanced the adhesion efficiency between nanoparticles and the surface of the filter and diminished rebound of nanoparticles.

The capillary force for non-spherical particles is lower than that for spherical ones (Pakarinen et al. 2005). Therefore, under the same condition, the probability of thermal rebound should be higher for non-spherical particles. In addition, spherical particles could slide or roll upon collision to the fiber, whereas cubic ones may either slide or tumble. As a result, cubic particles may contact with the fiber via edge, which increases the probability of detachment from the surface of the filter media (Boskovic et al. 2005). Overall, non-spherical particles have a higher chance of thermal rebound because of the lower capillary force and the higher probability of detachment upon collision. Our experiments did not show thermal rebound for non-spherical cubic particles in the tested size range. Therefore, there is very low probability of thermal rebound for spherical particles for the same conditions.

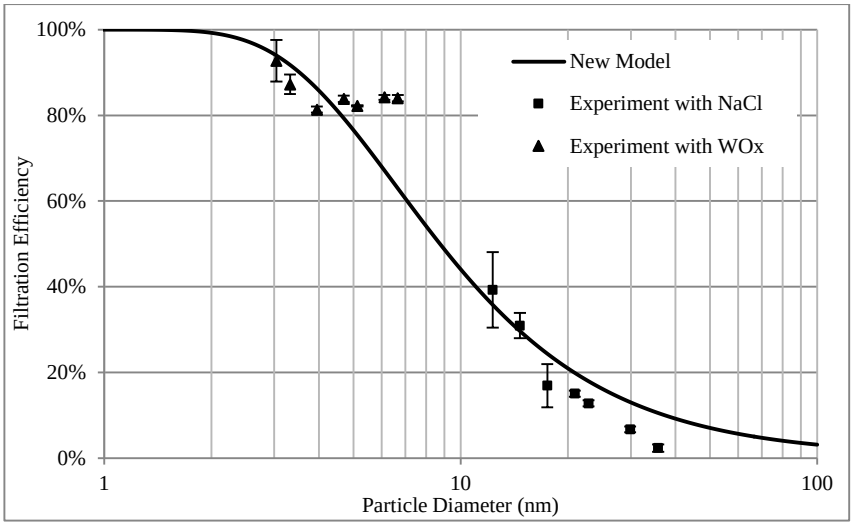

Figure 5-10. Comparison between experimental and modelled filtration efficiencies for NaCl and WOx nanoparticles

Figure 5-11 shows the comparison between the other experimental data and the model results, which did not show thermal rebound. Alonso et al. (1997) used stainless steel wire screen to filter NaCl nanoparticles in the size range of 2 nm to 7 nm with an air flow rate of 1 lpm. Boskovic et al. (2005) tested HEPA filters for the removal of PSL particles at a face velocity of 2 cm/s. Heim et al. (2005) focused on filtration of sub-20 nm NaCl particles by a nickel mesh filter at face velocity of 1.4 cm/s. Brochot et al. (2011) conducted their experimental studies with glass fibrous filters and neutralized NaCl particles in the size range of 5 nm to 50 nm with a face velocity of 5.3 cm/s.

Overall, Figure 5-11 shows that the published experimental data agreed with the models. The relative humidity in these studies is unknown. In their experimental setup, the aerosol flow was usually open to the filtered air prior to the filter holder; as a result, the relative humidity may be at room humidity, which is unlikely to be 0-10%. In calculating the filtration theory, we used a realistic value of 30%. As a result, at such high relative humidity, rebound of nanoparticles is diminishing. And the nanoparticle filtration efficiency can be predicted by conventional filtration models.

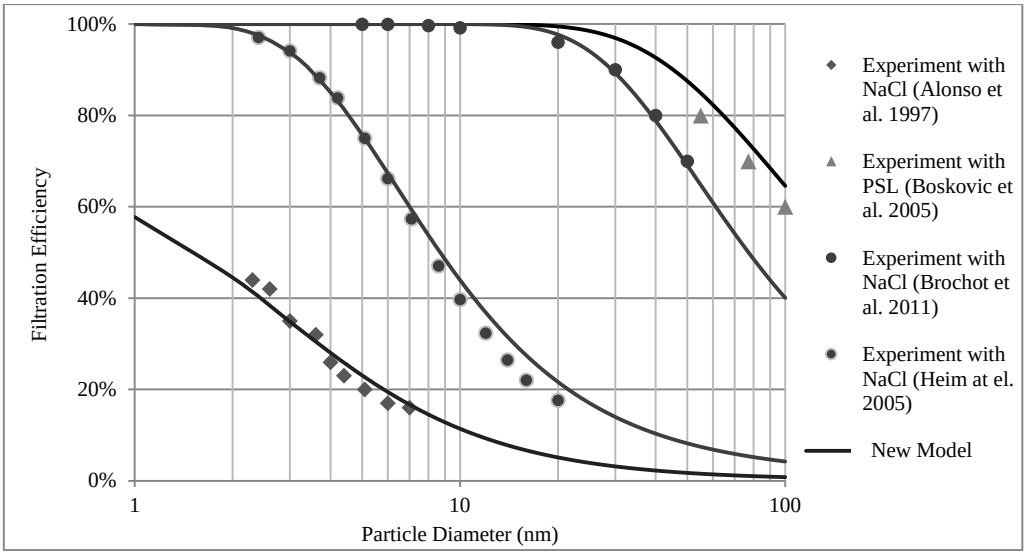

Figure 5-11. Filtration efficiency for nanoparticles: comparison between published experiments and model

Figure 5-12 shows the comparison between the penetrations of uncharged NaCl nanoparticles through the fibrous glass filter reported by Kim et al. (2006). The filtration model results were obtained by considering plastic deformation assumption and capillary force at different relative humidity levels. They reported the drop of efficiency that was attributed to thermal rebound for sub-1.3 nm particles. Penetration curve is chosen for the ease of presentation. The experimental data was collected at RH=1.22%, The NaCl nanoparticles are in the size range of 1 nm to 100 nm. Their tests were conducted at a face velocity of 5.3 cm/s. The model calculations correspond to RH=0%, 5% and 10%.

The models and the experimental data agreed qualitatively, but quantitatively speaking, there is an obvious discrepancy. The experimental data is expected to agree with the model at relative humidity of 1.22 %. However, the experimental results fall between the curves corresponding to RH=5% and 10%. The penetration of nanoparticles in the range of 1.3 to 3 nm does not follow the conventional penetration curve and follows theoretical model at 10% relative humidity. The increased penetration was observed for sub-1.3 nm particles and the experimental data is close to the theoretical model at a relative humidity level between 5% and 10%.

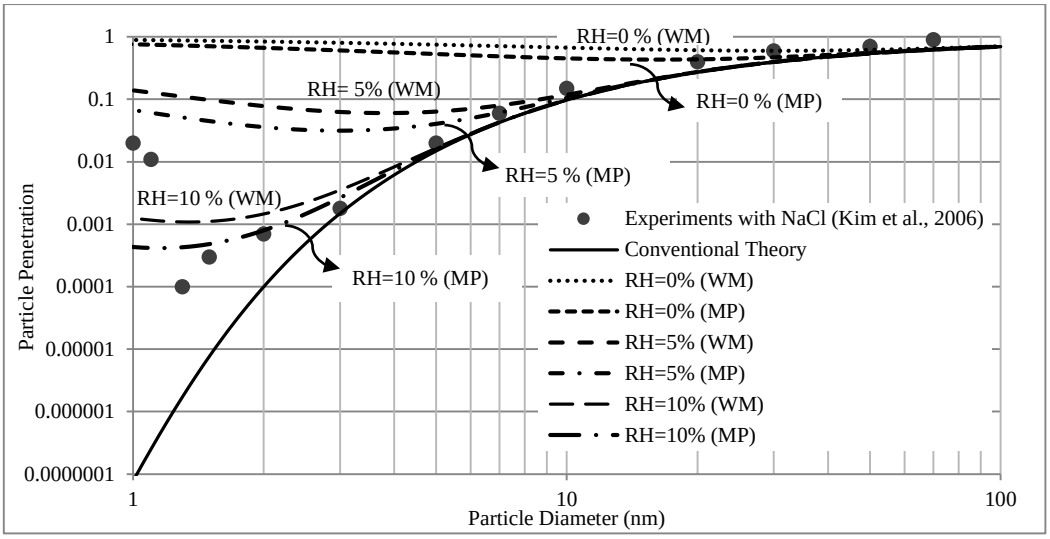

Figure 5-12. Penetration of NaCl nanoparticles: comparison between experiments and models

The quantitative discrepancy between the experiments and models may be attributed to several factors, such as shape. The model could not take shape factor into consideration and all particles are assumed to be spherical. However, in the experimental work, the NaCl particles are cubic. The capillary force for spherical particles are greater than that for non-spherical ones (Pakarinen et al. 2005). This is a possible reason why the experiments by Kim et al. (2006) matches a nanoparticle filtration model at higher relative humidity than what was reported in their experiments.

In addition, there are other uncertainties and limitations in this work. First of all, in general, the following factors were excluded from the model: shape and morphology of nanoparticles, smoothness of the surface, oblique impaction of nanoparticles, and limited database for nanomaterial properties. Secondly, the calculation of capillary force can also be further improved. The relation between the capillary force and relative humidity for sub-30 nm particles at relative humidity of smaller than 10% was calculated using extrapolating of data by Pakarinen et al. (2005). We assumed zero capillary force at dry condition, which may cause some errors. In addition, the capillary force was calculated for spherical particles; however, the contact angles and the meniscus shape could affect the capillary force strength, and should be considered in future work. Neither NaCl nor WOx particles used in our experiments is spherical, and the actual pull-off force based on capillary force may be smaller than the calculated values based on the assumption of spherical particles.

5.6 Conclusion

This chapter has explored the nanoparticle filtration by theoretical analysis and experimental investigation, with a focus on understanding the effect of capillary force at various relative humidity conditions on the filtration of nanoparticles. The following conclusions can be drawn from the studies herein.

First, results demonstrate that the thermal rebound of nanoparticles strongly depends on the material properties involved (no capillary force and no electrostatic force); thus, thermal rebound theory cannot be viewed as a general theory; instead, it must be adapted from one particle and filter type to another due to changes in the mechanical constant, Hamaker constant, density, and hardness. Second, when nanoparticles collide on a solid filter media, it is more likely for plastic deformation to occur than elastic deformation. Therefore, a nanoparticle filtration model should be based on the assumption of plastic deformation of nanoparticles upon impact on to the surface of the filter media. Third, thermal rebound is independent of electrostatic force. Thus the charge state of particles does not affect the adhesion efficiency between nanoparticles and a filter, and as a result, filtration efficiency. Finally, the filtration of nanoparticles and related thermal rebound effect are dependent on the relative humidity of the air. The probability of nanoparticle rebound increases inversely with relative humidity, which attenuates the capillary force. Thermal rebound may only take place under conditions where relative humidity is extremely low.

So far, the filtration efficiency of wire screens with low filtration efficiency has been investigated. To enhance filtration efficiency for nanoparticles, nanofibrous filters are next employed. These nanofibrous filters reveal superior performance for nanoparticle removal. Thus, the next chapter investigates, a method to fabricate PVA nanofibrous filters, along with characterization in terms of fiber size distributions and filter quality factor.

Chapter 6
Characterization of Polyvinyl Alcohol Electrospun Nanofibrous Filters for Nanoparticle Filtration[1]

6.1 Summary

PVA nanofibrous filter samples were fabricated in a laboratory under eight different electrospinning conditions, and characterized in terms of fiber size distributions by both manual and automatic SEM analysis. Both automated and manual image analysis methods provided similar findings for SEM images with high magnification. For low-magnification images, the manual method was time consuming and inaccurate; and, only the automated method could be employed.

The quality factors of these nanofibrous filters were then evaluated using sodium chloride nanoparticles in the size range of 10-125 nm. Results showed that, as expected, single layer filters with smaller fiber diameters and greater solidity were more efficient. However, these characteristics led to lower quality factors due to their greater pressure drops. Single layer filters made with higher applied voltage, longer tip to collector distance and shorter deposition time corresponded to greater filter quality factors. Multilayer filters made by stacking thin nanofibrous filters greatly increased the filter quality factors.

6.2 Introduction

Air filtration is the most effective approach for separating nanoparticles from gases, and filters with fiber diameters in the order of micrometers are widely used for nanoparticle filtration (Givehchi and Tan 2014). Nanofibrous filters are promising alternatives for the removal of airborne nanoparticles with higher efficiencies and low pressure drops; they appear to be a cost-effective option for nanoparticle

[1] A similar version of this chapter was published as:

Givehchi, R., Li, Q., Ni. C., Tan, Z. (2015). Quality Factors of PVA Nanofibrous Filters for Airborne Particles in the Size Range of 10-125 nm, *Fuel, In Press.*

filtration owing to their long lifetime, high loading capacity, low air resistance, low basis weight and great permeability (Bahk and Wang 2014; Givehchi and Tan 2014; Podgórski et al. 2006).

Electrospinning is widely used for the production of nanofibrous filters for air filtration (Ahn et al. 2006; Song et al. 2015). In typical electrospinning, a polymer solution is injected through a capillary needle into an electrical field. Nanofibers produced by this method have diameters ranging from a few to several hundred nanometers. These fibrous nanomaterials are believed to be less likely airborne and thus more environmentally friendly (Yoon et al. 2008).

Researchers have characterized polyvinyl alcohol (PVA) nanofibers and their use as filter media. Through the analysis of scanning electron microscopy (SEM) images, Wang et al. (Wang et al. 2007a) reported that nanofibrous PVA filters were not uniform, and beads were observed along fibers. They also showed that PVA nanofibers deposited on a conventional cotton scaffold had higher filtration efficiencies and a lower pressure drop for particles in the range of 0.3-5 μm than conventional fibrous filters (Wang et al. 2011a). Although PVA nanofibers can be employed for air filtration, only limited information is available on their characterization and performance in capturing nanoparticles, which prevail in flue gases. Furthermore, the effects of the electrospinning parameters on the filter characteristics and the performance of nanoparticle removal are not clear.

In addition, with the rapid growth of nanofiber research and development, there is need for an automatic method for characterizing the size distribution of nanofibers. Nanofibers are now commonly characterized by their SEM images, with the image analysis mostly performed manually using software such as ImageJ. Manual image processing may work for high-magnification SEM images, although it is time consuming. However, it is not effective for low-magnification images.

The objectives of this chapter are 1) to characterize PVA nanofibrous filters produced by electrospinning with an automated image analysis method, and 2) to determine the relationship between electrospinning parameters and the filter quality factor for nanoaerosol filtration. PVA nanofibers were made with different applied voltages, tip to collector distances and deposition times. The morphologies of these electrospun filters were then characterized by SEM images coupled with an automated image analysis method. Using NaCl airborne nanoparticles in the size range of 10-125 nm, the single-layer and multilayer filters were also evaluated in terms of filter quality factor. The effects of the

electrospinning parameters on filter quality factor were determined to identify the important factors affecting filtration performance of PVA nanofibrous filters.

6.3 Materials and Methods

A custom-made electrospinning setup was used in this study for filter sample preparation (Figure 6-1). The relative humidity and temperature of the air inside the housing were 39±4% and 23±3°C, respectively. A 5-ml syringe was loaded with a solution of PVA polymer, which has a molecular weight of 89,000-98,000 $g \cdot mol^{-1}$ (Sigma Aldrich Canada). The desired solution concentration of 10% w/w was prepared by diluting the PVA in distilled water at 90°C and stirring overnight (Appendix B). A 22-gauge stainless steel capillary needle with an inside diameter of 0.413 mm was attached to the syringe. The syringe was mounted on a syringe pump (Kd Scientific), which was used to control the flow rate to 0.3 $ml \cdot hr^{-1}$ (Appendix B). A lab jack was used to adjust the vertical distance between the capillary needle and the grounded collector. A high-voltage power supply (Gamma High Voltage, ES50P-5W) was employed to apply the high voltage between the capillary needle and an aluminum collector.

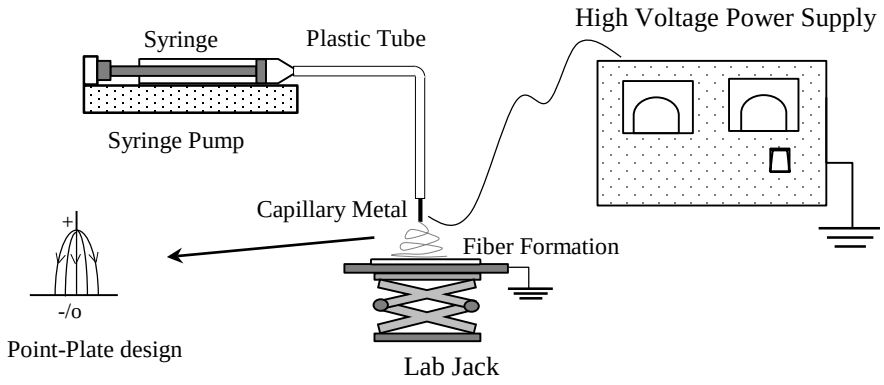

Figure 6-1. Schematic diagram of the electrospinning setup

Stainless-steel wire screens with a diameter of 140 µm and an opening size of 368 µm were used to support the nanofibrous filters. Filter samples were then left in lab environment overnight, allowing charges to dissipate from the collector and enabling the nanofibers to dry. Table 6-1 summarizes the eight conditions for the electrospun sample filters. The sample thickness was measured using a digital micrometer (Tresna IP65, series M18) with a resolution of 1 µm. Thickness was measured at the filter

center, which may be greater than that at the edges due to the random deposition pattern of fibers in an electric field (Zhang et al. 2010).

Table 6-1. Operating conditions for fabricating nanofibrous electrospun filter

Filter #	Tip-to-collector distance (cm)	Voltage (kV)	Duration (min)
NF1, NF1-A, NF1-B	10	15	15
NF2	12.5	15	15
NF3	15	15	15
NF4	10	12.5	15
NF5	10	17.5	15
NF6, NF6-A, NF6-B, NF6-C	10	15	5
NF7, NF7-A, NF7-B	10	15	30
NF8	10	15	60

6.3.1 Characterization of nanofibrous filters

These sample filters were then characterized using field emission scanning electron microscopy (FE-SEM) analysis. Samples were coated with gold particles for 139s prior to imaging. The SEM images were then quantitatively analyzed using an automated method developed by us to determine the distribution of nanofiber diameters.

6.3.1.1 Automated image analysis of fiber size distribution

An image analysis algorithm was developed based on fiber individualization using MATLAB. It consists of 5 steps, being pretreatment, local thresholding, smoothing, edge detection and skeletonization (Shin et al. 2008a). Figure 6-2 demonstrates the processing of a nanofiber SEM image with high magnification using the automated method:

1. The original image (Figure 6-2 (a)) was pretreated by median filtering, image intensity adjustment and histogram equalization to reduce noise and increase contrast to ensure the most accurate results (Figure 6-2 (b)).

2. Instead of simply taking the threshold of a whole image, a local thresholding method using Sauvola binarization was utilized to transform the image into binary one, i.e., black and white (Figure 6-2 (c)).

3. Undesirable noise was further reduced using repeatedly morphological opening and closing (Figure 6-2 (d)).
4. Fiber boundaries were detected using canny edge detection, as shown in Figure 6-2 (e). Dilation was used to seal the openings in order to accurately detect edges. Subsequent thinning fixed the edge profile, so that they were no longer inaccurately thickened.
5. In the final stage of image processing, the fiber centerlines were defined using a skeletonization process. A pruning process was then used to delete sporadic branches (Figure 6-2 (f)).

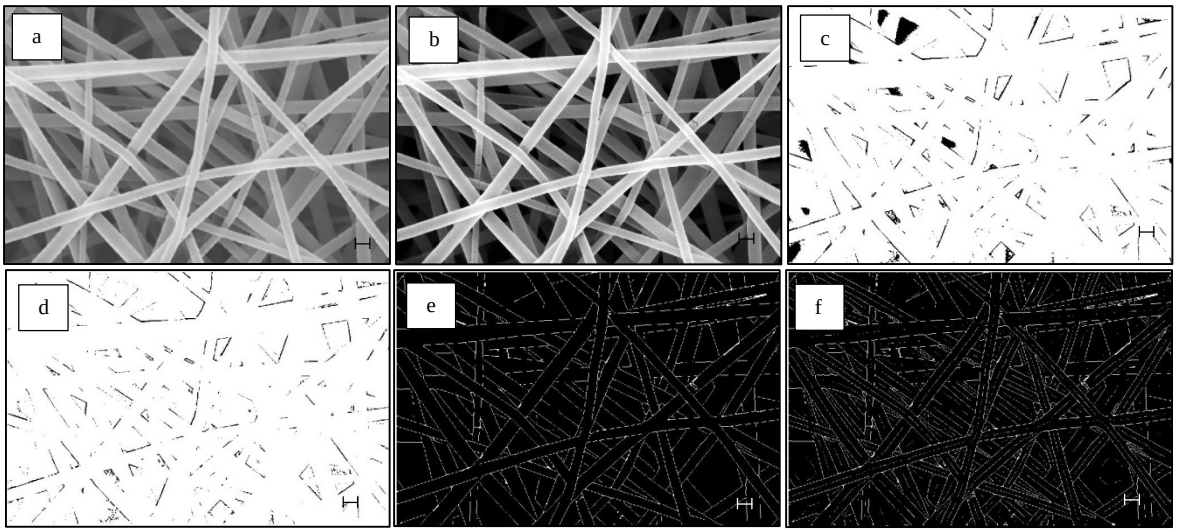

Figure 6-2. a) Original SEM image, scale: 200 nm, b) filtering: median, image histogram equalization, c) local threshold, d) smoothing and noise reduction, e) edge detection, and f)skeletonization

The fiber diameters are then calculated according to the distance between edge of the fiber and centerline using the Euclidean distance transform matrix (Shin et al. 2008a; Tomba et al. 2010). For more reliable statistical data, the fiber size distribution must be calculated based on several images at different locations and with different magnifications. For this purpose, the automated process was applied to a low-magnification image, and the resulst are shown in Figure 6-3.

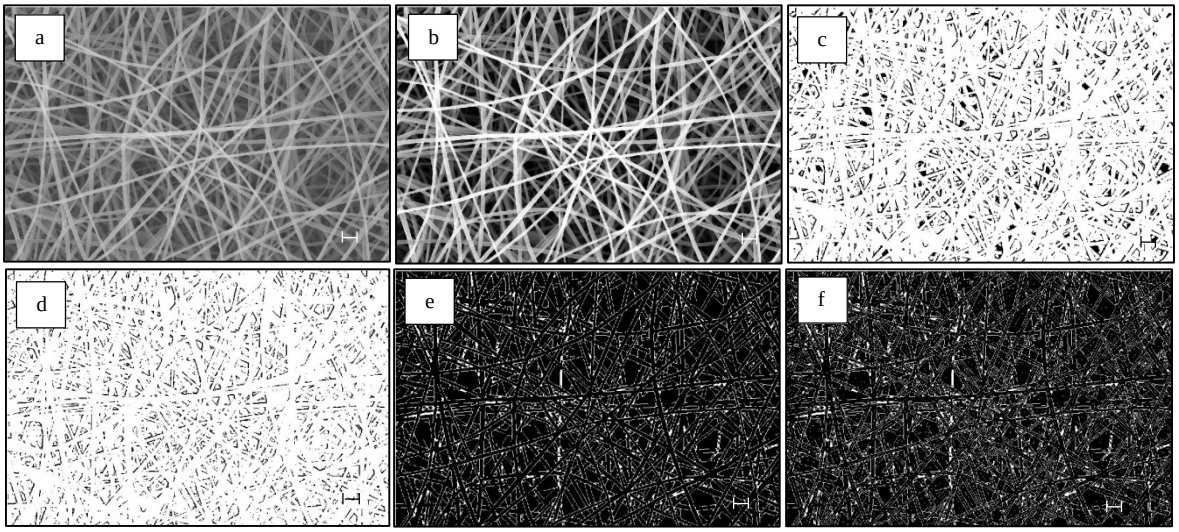

Figure 6-3.a) Original SEM image, scale: 1000 nm, b) filtering: median, image histogram equalization, c) local threshold, d) smoothing and noise reduction, e) edge detection, and f)skeletonization

Figure 6-4 shows two SEM images for an electrospun nanofibrous filter at two different magnifications, 20.00 KX and 5.00 KX, with the fiber size distribution determined by the automated method. As shown in Figure 6-4, fiber size distributions for the selected images had different mean fiber diameters and standard deviations. These two images were captured from various places of the sample at two different magnifications.

For more reliable statistical data, the fiber size distribution was calculated considering several images with different magnifications as shown in Figure 6-5. The average fiber diameter and standard deviation in the new size distribution were more similar to the low-magnification image, because the low-magnification images contain a larger area of the sample and the results, therefore, are more realistic. However, the high-magnification images also have to be utilized to determine the low fiber size diameters.

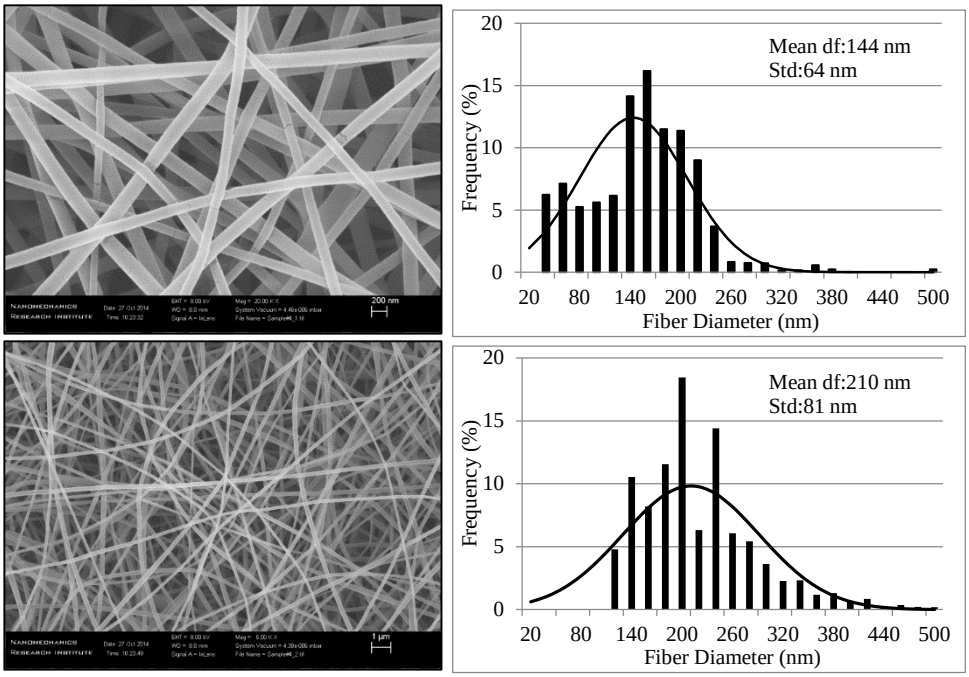

Figure 6-4. SEM images of electrospun nanofibrous filters at two different magnifications (20.000 KX and 5.00 KX), and their corresponding fiber distributions

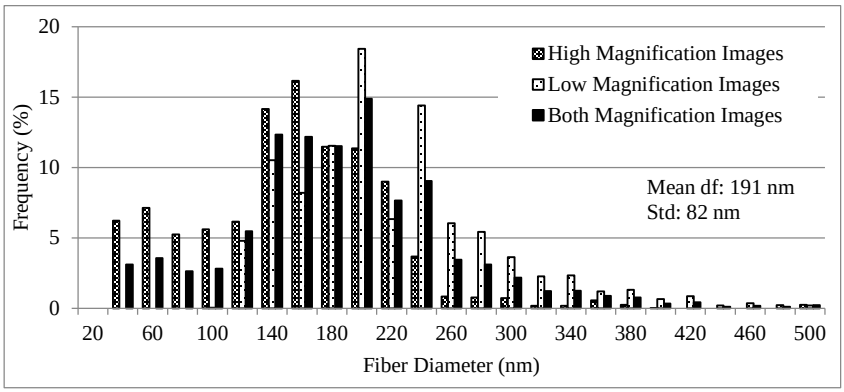

Figure 6-5. Fiber size distribution for two images at different magnifications

6.3.1.2 Manual image analysis of fiber size distribution

The manual tool used to validate the automated image analysis technique was the open source ImageJ image processing software package. As this manual method can only be used for high-magnification images, the results of ImageJ in the process of high-magnification images were used to validate the

automated image analysis algorithm. The fiber size distribution was determined with at least 100 measurements.

6.3.1.3 Comparison between automated and manual image analysis

The fiber size distributions determined by these two methods for high magnification SEM images are presented in Figure 6-6 and Table 6-2. A t-test showed that the differences between mean fiber diameters are not statistically significant (significant level 0.05). The mean fiber diameters provided by both approaches were close to each other; however, the standard deviations were different. This may have been due to the much smaller number of fibers utilized in the manual method than in the automated method.

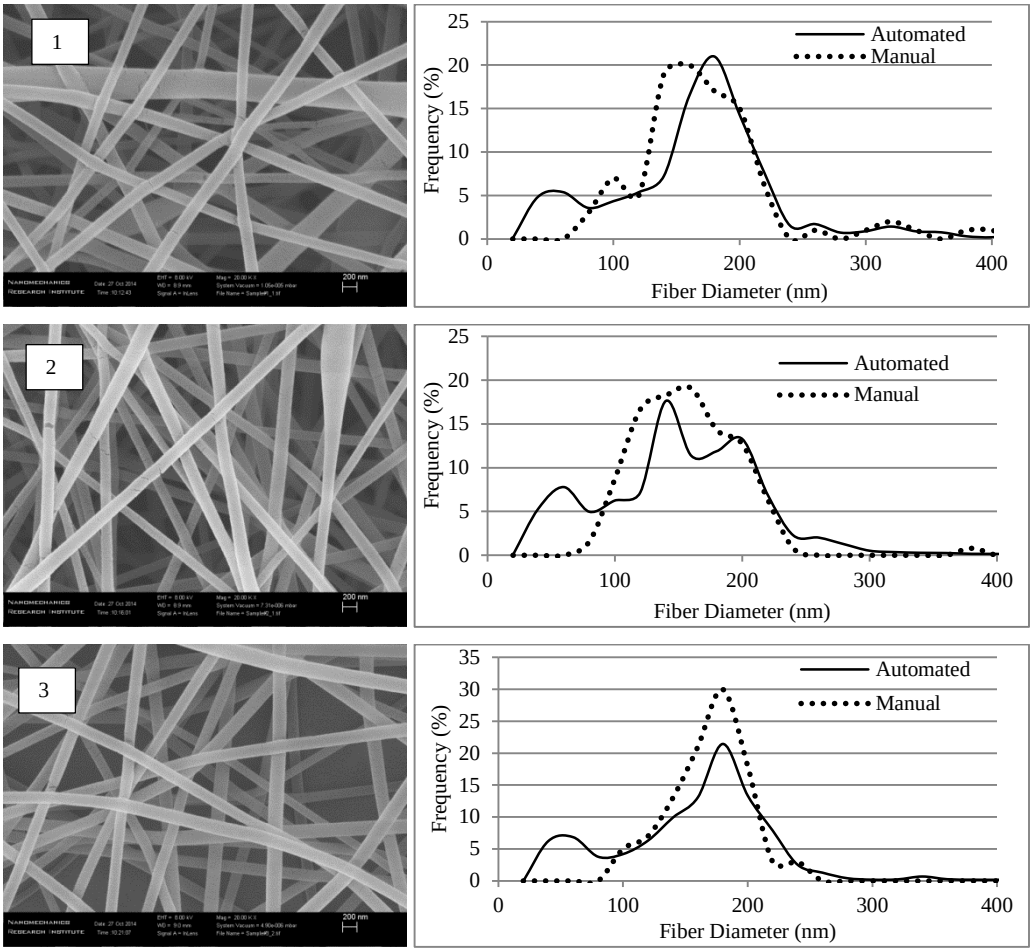

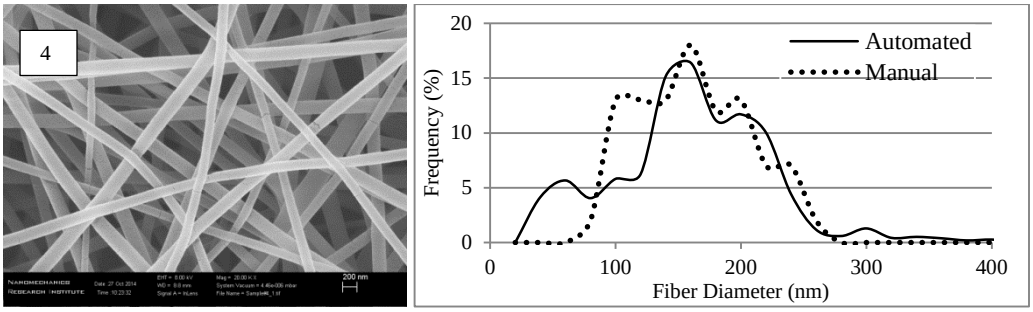

Figure 6-6. Fiber size distribution for different samples: comparison between manual and automated methods

Table 6-2. Comparison between automated and manual methods

Sample#	Automated Method		Manual Method		P-value (t-test)
	Mean (nm)	Std (nm)	Mean (nm)	Std (nm)	
1	162	79	166	63	0.308
2	142	62	148	48	0.121
3	150	68	158	31	0.103
4	144	64	152	44	0.096

Figure 6-7 shows a parity plot comparing the mean fiber diameters given by automated and manual methods for four filters. The results demonstrate that the manual and automated methods had a linear relationship with a high coefficient of determination ($R^2 = 0.92$), indicating that the automated method was validated by the results of the manual approach.

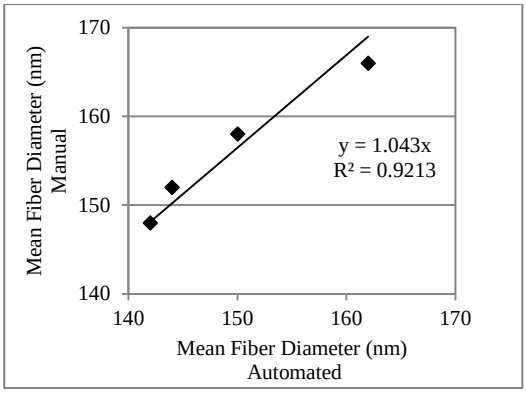

Figure 6-7. Correlation between the mean fiber diameters for automated and manual methods

6.3.2 Performance of nanofibrous filter for nanoaerosol filtration

Meanwhile, samples made at identical conditions were tested for the filtration performance and pressure drop. The experimental setup for air filtration test was similar to that reported in Chapter 4; only a brief description is provided as follows. Polydispersed sodium chloride particles in the range of 10-125 nm were generated by a constant output atomizer (TSI model 3076). These aerosol particles were then passed through a diffusion dryer (TSI Model 3062) to reduce air humidity followed by neutralization using a radioactive neutralizer (Staticmaster Model P-2031). These polydispersed aerosol particles then pass through the test filter at an air flow rate of 2 lpm, which corresponds to a face velocity of 6.7 cm/s.

The pressure drop across the test filter was measured using a differential pressure gauge (Omegadyne, Model DPG409). A scanning mobility particle sizer with a Faraday cup electrometer (SMPS+E, GRIMM model 5.705) was used to determine the concentrations of the nanoaerosol particles downstream of the 25-mm filter holder, with and without tested filter, to determine the filtration efficiency (η). With this method, the error due to particle loss is minimized by the same sampling line. The corresponding filter quality factor (Q_F) is calculated from the measured pressure drop (ΔP) and particle filtration efficiency (η) (Hinds 1999).

$$Q_F = -\frac{\ln(1-\eta)}{\Delta P} \tag{6-1}$$

Although the higher pressure drop is preferable for HVAC systems (Zaatari et al., 2014), it is not preferable for some applications such as respiratory dust masks (e.g., Appendix F). Based on the measured pressure drop and filter thickness, the solidity of nanofibrous filters is determined using the Davies equation (Davies 1952):

$$\Delta P = \frac{64\mu U L \alpha^{\frac{3}{2}}(1+56\alpha^3)}{d_f^2} \tag{6-2}$$

where μ is the air viscosity, U is the face velocity, L is the filter thickness, α is the solidity of filter, and d_f is the mean diameter of the fibers. With the density of the filter (ρ_f), the basis weight of the filter (w) is determined by

$$w = \alpha L \rho_f \tag{6-3}$$

6.4 Results and Discussion

Figure 6-8 shows the SEM images, size distributions, mean diameters and standard deviations, thicknesses, solidities and basis weights of the nanofibrous filters fabricated under eight electrospinning conditions (Table 6-1). SEM images were taken at two magnifications of 20.00 KX and 5.00 KX for each sample.

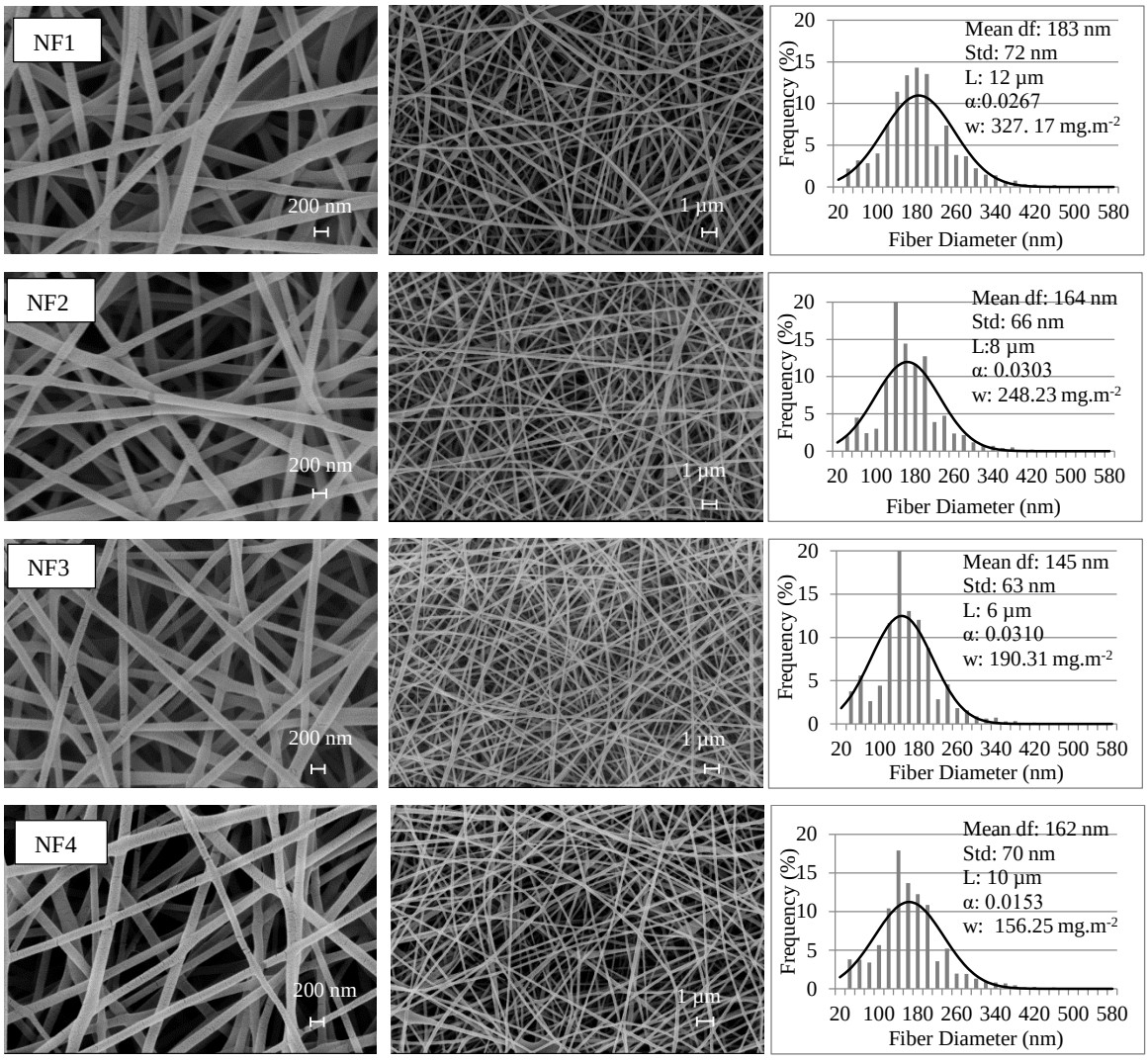

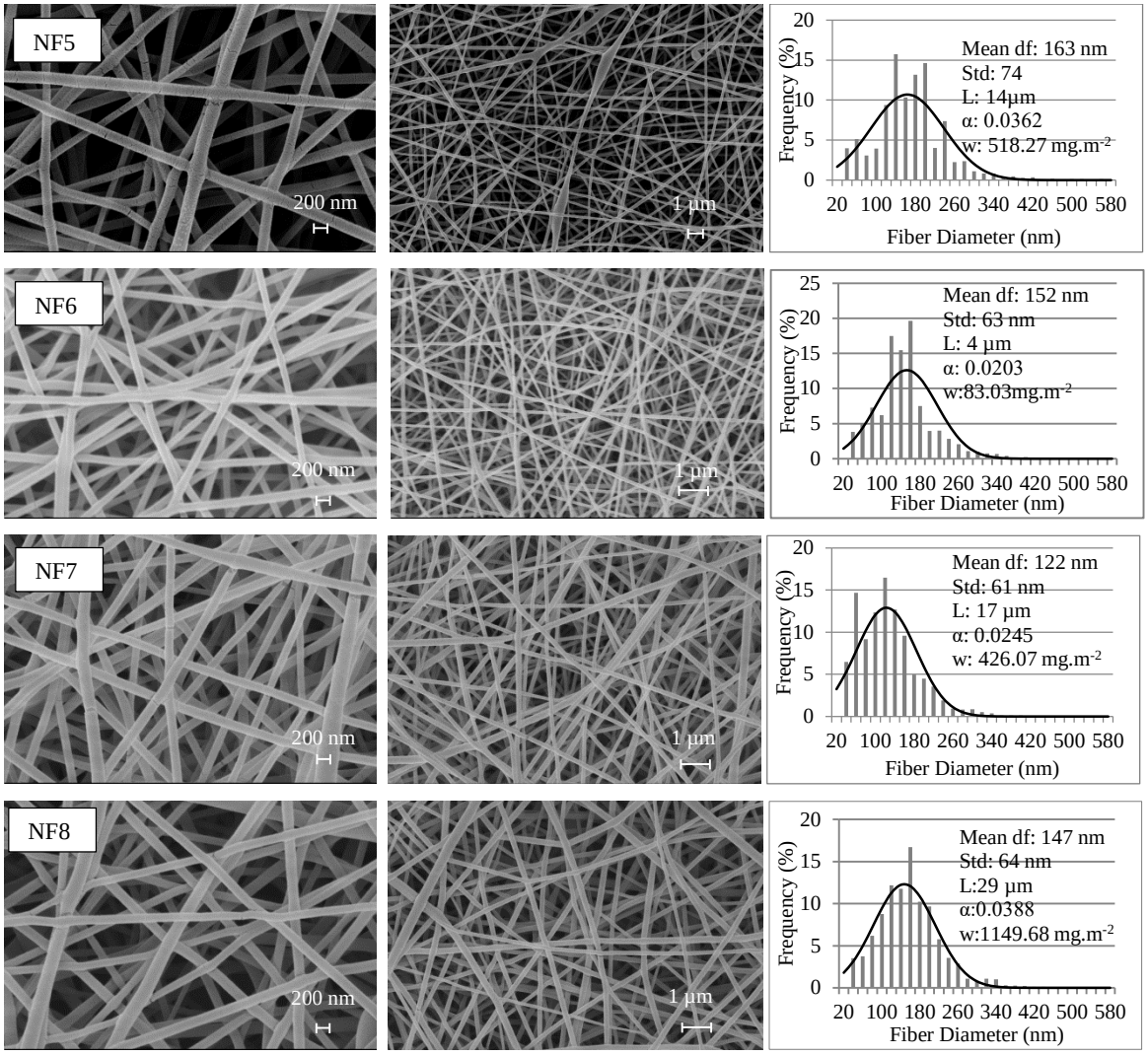

Figure 6-8. SEM images and fiber diameter distributions of nanofibrous filters

6.4.1 Effects of tip-to-collector distance on nanofiber size distribution and morphology

NF1, NF2, and NF3 were fabricated at applied voltage of 15 kV, deposition time of 15 min and different tip-to-collector distances of 10, 12.5 and 15 cm, respectively. Numerical values in Figure 6-9 show that the mean fiber diameter decreased with the tip-to-collector distance. The mean diameters are 184 nm, 164 nm and 145 nm with respective standard deviations of 72 nm, 66 nm and 63 nm when the distances were 10, 12.5 and 15 cm, respectively. Both the mean fiber diameter and standard deviation decreased

with the distance resulting in more uniform fibers. These values and the SEM images indicate that relatively uniform fibers were produced without beaded fiber formation.

Comparison of NF1, NF2 and NF3 shows that the tip-to-collector distance directly affects solidity. With higher solidity and lower thickness, the basis weight of the filter decreased with the increasing tip-to-collector distance. The increase in the distance reduced the electric field intensity. It also affects the deposition time, the evaporation rate, and the jet instability. Longer distance allows more time for the fluid jet to stretch thinner and for the solvent to evaporate more completely, resulting in thinner nanofiber and thinner sample filters.

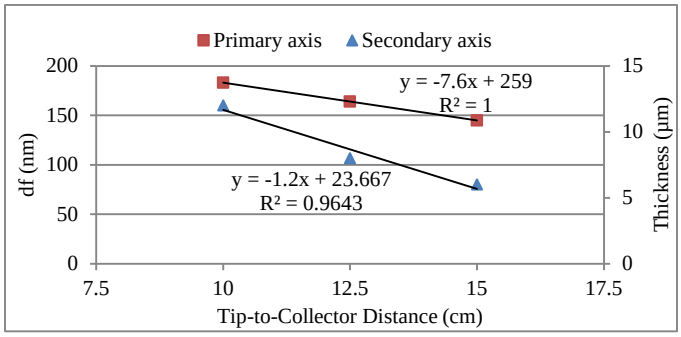

Figure 6-9. Effect of tip-to-collector distance on mean fiber diameter and filter thickness

6.4.2 Effects of applied voltage on nanofiber size distribution and morphology

NF4, NF1 and NF5 were fabricated at same tip-to-collector distance of 10 cm, same deposition time of 15 min, and different applied voltages of 12.5, 15, and 17.5 kV, respectively. As seen in Figure 6-8, the initial average fiber diameter increased from 162 nm to 183 nm when the applied voltage changed from 12.5 to 15 kV, and then it decreases to 163 nm when the applied voltage further increased to 17.5 kV. This finding indicates that there should be an optimum voltage in electrospinning for the thicker nanofiber. Actually, the effect of applied voltage on the diameter of nanofibers has not been conclusive. Some researchers reported that the applied voltage had a negligible effect on the nanofiber diameter (Reneker and Chun 1996; Sener et al. 2011); others reported its direct effect (Yuan et al. 2004; Zhang et al. 2005) or its inverse effect on the mean fiber diameter (Lee et al. 2002a; Megelski et al. 2002). Some researchers believe that increasing the voltage would increase the electrostatic repulsive force on the jet, leading to thinner nanofibers (Zong et al. 2002), while others believed that voltage increase could increase the volume of the solution ejected from the Taylor cone, resulting in larger nanofibers

(Demir et al. 2002). These contradictory results indicate that other parameters such as the solution properties also affect the nanofiber size (Fallahi et al. 2010). Our high-speed video camera recorded stable jets for all of the applied voltages. The SEM images in Figure 6-8 also show that none of these filter samples had beads along the nanofibers. The fabrication of filters with stable jets may have prevented bead formation, due to the balance between the electrospinning and feeding rates.

The results in Figure 6-8 above also show that the voltage affected the solidity and thickness of nanofibrous filters. As the applied voltage increases, both solidity and thickness of the filter samples increase linearly (Figure 6-10). At a higher voltage, the electrostatic force at the needle tip is greater due to a higher electric field intensity and greater columbic forces in the jet, increasing the jet flow rate (the jet flow rate is independent of the feeding flow rate) (Fallahi et al. 2010). Consequently, it increased the solidity and basis weight of the filter.

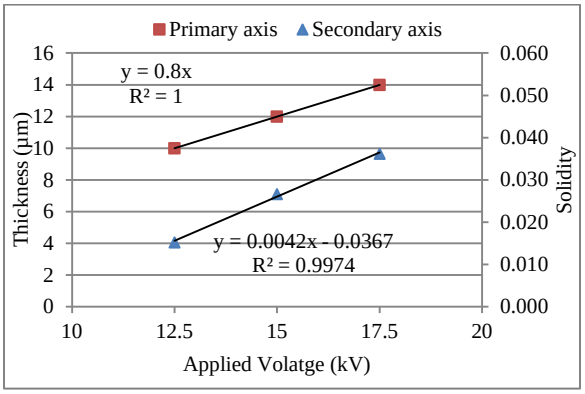

Figure 6-10. Effect of applied voltage on filter's thickness and solidity

6.4.3 Effects of deposition time on nanofiber size distribution and morphology

NF6, NF1, NF7 and NF8 were fabricated at applied voltage of 15 kV, tip-to-collector distance of 10 cm and deposition times of 5, 15, 30 and 60 min, respectively (Table 6-1). Results in Figure 6-8 show that the deposition time also affects the average diameter, the solidity and the basis weight of the nanofibers. The mean fiber diameter was 152 nm, 183 nm, 122 nm and 147 nm when the deposition time increased from 5 min to 15 min, 30 min and 60 min, respectively. First of all, this finding is quite different from the assumptions made by other researchers that the nanofiber size distributions of electrospun nanofibers remain constant over time (Mei et al. 2013; Zhang et al. 2010). Actually, at the beginning of the electrospinning process, the jet enters into a homogenous electric field and deposits

on the collector with such a good contact that it allows efficient charge dissipation. After a certain time, heterogeneous charges accumulating on the deposited area cannot dissipate quickly due to the low conductivity of the PVA polymer. Thus, the jet behaves differently due to the heterogeneous electric field (Ahirwal et al. 2013; Nedjari et al. 2015). The incidence of charge buildup prevents the effective deposition of incoming fibers, leading to different fiber deposition pattern and a decreasing production rate (Sun et al. 2015; Wittmer et al. 2014). In this study, up to the deposition time of 60 min, no obvious reduction in nanofiber production rate was observed as indicated by the increased thickness and basis weight of the filter samples. However, deposition time did affect the filter quality and fiber size distribution.

When the deposition time increased to 15 min, so did the mean fiber diameter, likely because the buildup of residual charges on the deposited fibers reduced the spiral motion of the incoming jet and decreased the elongation rate. As a result, the process produced thicker nanofibers (Zhang et al. 2010). However, when the deposition time was 30 min, the mean fiber diameter decreased unexpectedly to 122 nm. We believe that the changes in the buildup charges on deposited fibers may be one of the reasons for this result. The number of contacts between the deposited fibers affects the charge dissipation (Wittmer et al. 2014). It seemed that for a 30 min deposition time, the number of contacts between fibers was great enough to enable timely charge dissipation, leading to thinner fibers. Newer deposited fibers are likely to have smaller diameters than previously deposited ones. For the deposition time of 60 min, the mean fiber diameter again increased due to the buildup residual charges. Another reason for this nonlinear behavior might be the uncertainty in image analysis. One of the issues in this study is employing SEM images, which show only the top layers of deposited fibers in 2D structure. This factor deserves further investigation in the future.

As shown in Figure 6-11, the deposition time affects both the thickness and solidity of a filter. The longer the deposition time, the more fibers are compressed on the substrate, leading to greater filter solidity. As the deposition time increases, so do the thickness and solidity of filters, leading to a greater basis weight too. This finding agrees with those reported in literature (Mei et al. 2013).

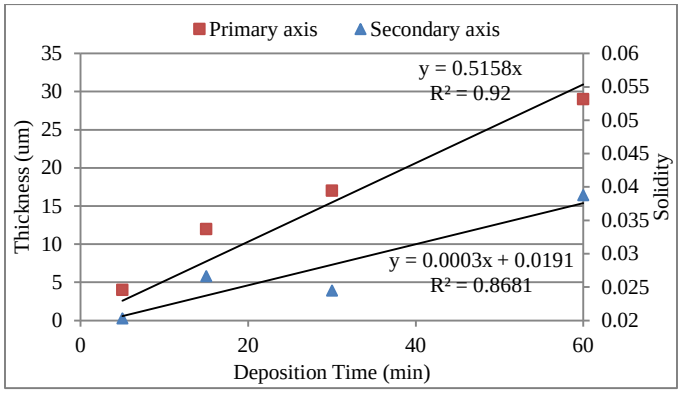

Figure 6-11. Effect of deposition time on filter's thickness and solidity

6.4.4 Performance of nanofibrous filters for the filtration of nanoaerosol

Figure 6-12 shows the particle filtration efficiencies and quality factors of the nanofibrous filters tested at a consistent air flow rate of 2 lpm. The fiber diameters of the tested filters were mostly less than 500 nm (Figure 6-8), which should enable gas slip effect in nanoparticle filtration (Barhate and Ramakrishna 2007; Mei et al. 2013). Results in Figure 6-12 show that samples NF8, NF7 and NF5 have the highest filtration efficiencies (>95% for tested particle size). However, they do not have high quality factors due to their great pressure drops. Both NF8 and NF7 were fabricated at the same long deposition time and are thick. NF7 has the lowest quality factor due to its great thickness (17 µm) and smaller mean fiber diameter (122 nm). NF8 is the thickest (29 µm) with the greatest solidity (0.0388); however, due to its larger fiber size, NF8 has a greater quality factor than NF7. Despite the fact that thickness does not affect the quality factor of conventional filters (Huang et al. 2013; Leung et al. 2010), it could be one of the important parameters for electrospun nanofibrous filters.

NF4 has the lowest filtration efficiency for the size range of tested particles, followed by NF6, NF1 and NF2. Comparison between the characteristics of these filters show that the filtration efficiency decreases with solidity of a filter. NF4 has the lowest filtration efficiency among all samples, which led to the lowest quality filters. Although NF6 does not have high filtration efficiencies, it has the greatest quality factors for the tested particle sizes.

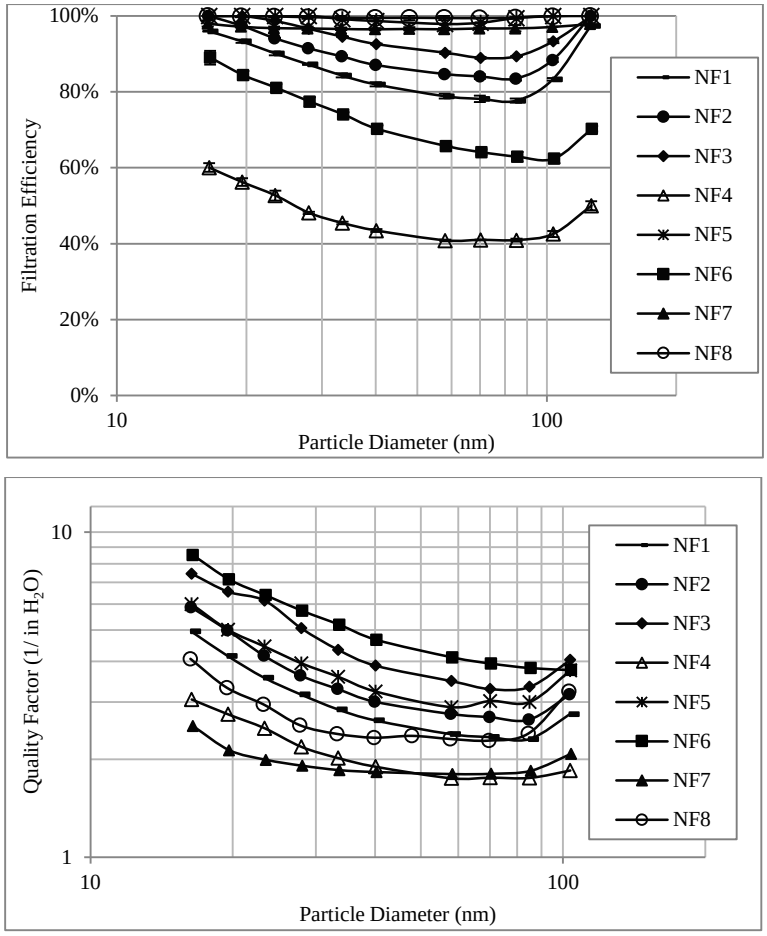

Figure 6-12. Filtration efficiency and quality factor of nanofibrous filters

6.4.4.1 Effect of tip-to-collector distance on filtration performance

Figure 6-13 presents the effect of tip-to-collector distance on the corresponding total filtration efficiencies and quality factors of NF1, NF2 and NF3. The total filtration efficiency of a filter is calculated based on the ratio of total nanoparticles downstream of the filter to those upstream of the filter. There is a positive correlation between the tip-to-collector distance and either filtration efficiency or quality factor. Tip-to-collector distance directly affects the solidity of the filter; however, it has an adverse effect on filter thickness and mean fiber diameter. Increasing the filter solidity and decreasing the mean fiber diameter have positive effects on the filtration efficiency. On the other hand, decreases in the thickness of the filter have an adverse effect on filtration efficiency but a positive effect on the pressure drop across the filter, which increases the filter quality factor.

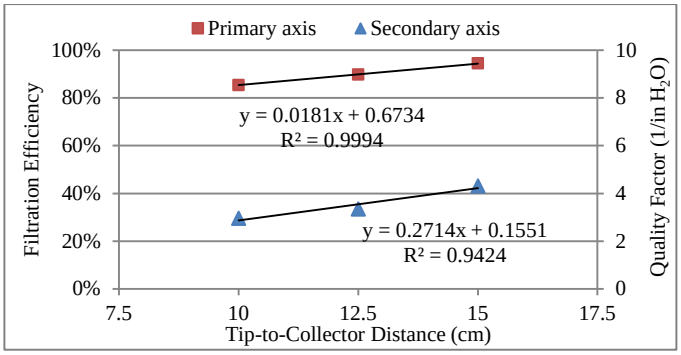

Figure 6-13. Filtration efficiency and quality factor of filters versus tip-to-collector distance

6.4.4.2 Effect of applied voltage on filtration performance

Figure 6-14 shows the total filtration efficiencies and quality factors of samples NF4, NF1 and NF5. The applied voltage has a positive effect on both filtration efficiency and quality factor of an electrospun filter. As the voltage increases, so do both thickness and solidity, and consequently, both the filtration efficiency and pressure drop across the filter increase; however, the increasing rate of filtration efficiency is greater than that of the pressure drop, which ultimately increases the quality factor.

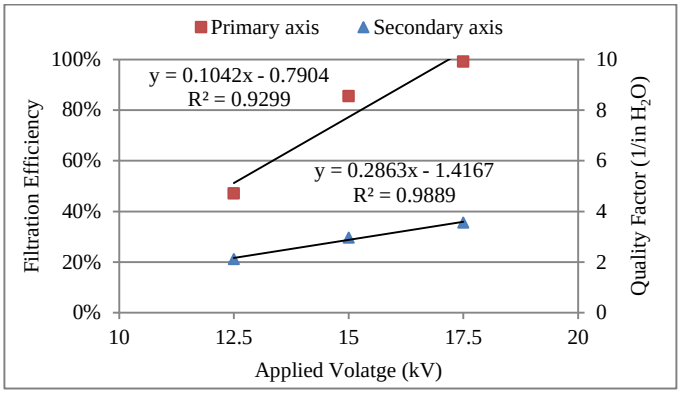

Figure 6-14. Filtration efficiency and quality factor of filters versus applied voltage

6.4.4.3 Effect of deposition time on filtration performance

Figure 6-15 presents the total filtration efficiencies and quality factors of samples NF6, NF1, NF7 and NF8, which are different in terms of deposition time. The total filtration efficiency positively correlates to the electrospinning deposition time; however, the increasing rate decreases as the deposition time increases. As shown in Figure 6-11, the deposition time directly affects the thickness and solidity of

the filters, resulting in increased total filtration efficiency. On the other hand, deposition time has a negative effect on the total quality factor because the filter thickness increases with deposition time and it affects pressure drop more than filtration efficiency. As a result, the quality factor of filters decreases greatly as the deposition time increases from 5 min to 15 min. The gap between total filtration efficiency and pressure drop grows with deposition time, and it may be due to the fabrication of non-uniform filters with deposition time (Zhang et al. 2010).

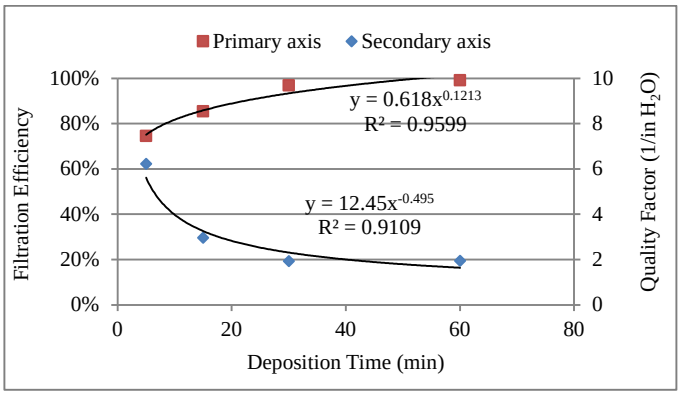

Figure 6-15**.** Filtration efficiency and quality factor of filters versus deposition time

This means that a shorter deposition time may result in more uniform and thinner filters of higher quality factor. Our finding herein is different from other researchers who reported that "*the quality factor of filters is independent of filter thickness* (Huang et al. 2013; Leung et al. 2010)". Again, deposition time may affect the deposition pattern over time, consequently reducing the filter quality factor (Zhang et al. 2010).

6.4.4.4 Performance of multilayer filters

Figure 6-16 shows the comparison of the filtration efficiency and quality factor of single layer and multilayer nanofibrous filters. Both filtration efficiency and quality factor of multilayer filters are generally higher than the corresponding single layer filters. Multilayer filters 3*NF6 (3 layers of NF6, which were made with deposition time of 5 min), 2*NF1 (2 layers of NF1, which were made with deposition time of 15 min), and 2*NF7 (2 layers of NF7, which were made with 30 min deposition time) perform much better than the respective single layer filters. This observation is quite different from the theoretical analysis that follows. Theoretically, increases in the layers of filters will lead to the

increase in filtration efficiency according to Eq.(6-4) (Yeh and Liu 1974); however, it shall not affect the quality factor calculated using Eq.(6-1) because the term L (filter thickness) is canceled out.

$$\eta = 1 - \exp\left[\frac{-4\alpha EL}{\pi d_f (1-\alpha)}\right] \tag{6-4}$$

In reality, electrospun nanofibers may not be uniform due to the random deposition of fibers. Thus, the fabrication of multilayer filters using single layer filters may result in different fiber orientations, which overcomes the non-uniform nature of final filter and increases total filter quality factor. Similar results were also reported for PAN nanofibrous filters (Zhang et al. 2010). However, in another study, which employed PEO nanofibrous filters, the quality factor of a single layer filter was the same as those of 2-layer and 3-layer filters (Leung et al. 2010). The PEO nanofibrous filters might be more uniform than PVA and PAN nanofibrous filters.

One would expect the identical filtration performances for all filters fabricated using with same electrospinning parameters; however, results in Figure 6-16 show otherwise. For example, NF6-A, NF6-B and NF6-C were fabricated under the same operating conditions but their filtration efficiencies and quality factors are not exactly the same, although they are close to each other. Both filtration efficiencies and quality factors of filters created in the shorter time deposition time of 5 min deviate less from one another than those made with longer deposition times (15 and 30 min). Due to the random nature of electrospinning, the characteristics of filters may differ even under the same electrospinning parameters.

Figure 6-17 shows the comparison of the filtration efficiency and quality factor of multilayer filters and associated single layer filters with the same total electrospinning deposition time. In any one of these three figures, the same amount of energy, time and materials were used to fabricate these single layers and the corresponding multilayer filters. However, results show that both filtration efficiency and quality factor of the multilayer filters of 3*NF6 and 2*NF1 are higher than those of the corresponding single layer filters being NF1 and NF7, respectively. This comparatively higher quality factor of the multilayer filters is likely due to the higher quality of electrospun filters at shorter deposition times, which lead to more uniform spatial distribution of the fibers and better performances.

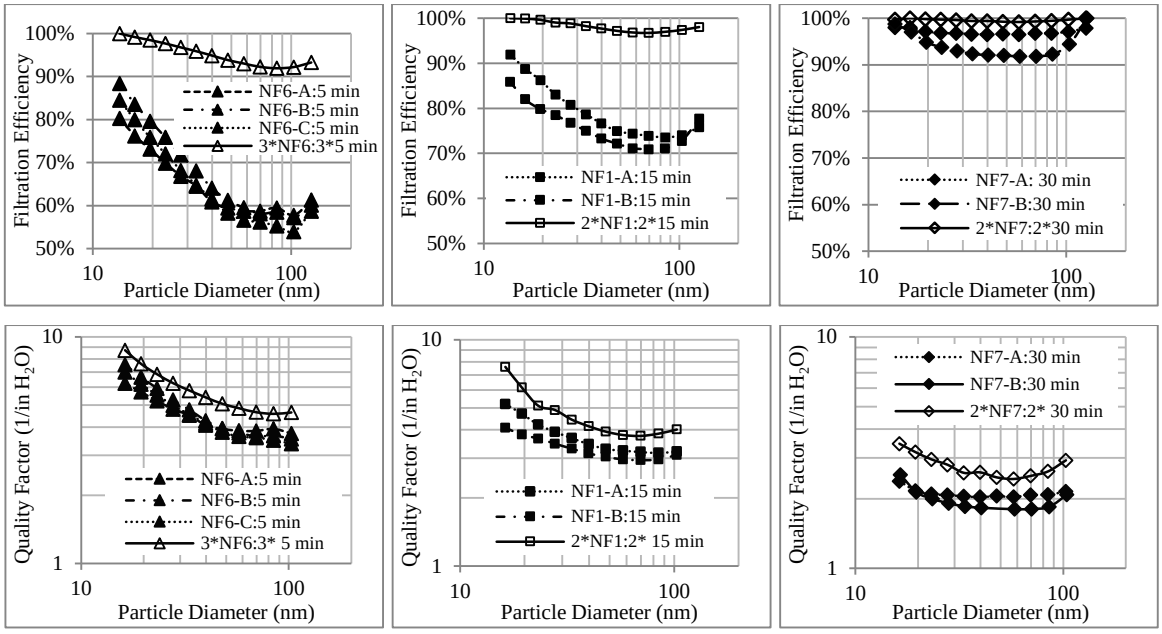

Figure 6-16. Comparison between the filtration efficiency and quality factor for single layer and multilayer filters

However, the differences between the filtration efficiencies and quality factors 2*NF7 and NF8 is negligible, indicating that at such a long deposition time of 60 min, the improvement of filter is no longer obvious, and it is likely due to the lower quality of nanofibers as explain above. Comparing the thickness of single-layer and multilayer filters revealed the differences between the thicknesses of multilayer filters and corresponding single layer filters at longer deposition times. The thickness of 3*NF6 (equivalent 15 min deposition time) is 3×4μm, which is the same as that for NF1 (12 μm for 15 min deposition time); however, the thickness of 2*NF1 (equivalent 30 min deposition time) is 2×12 μm, which is greater than that of NF7 (17 μm for 15 min deposition time). The thickness of 2*NF7 (2×17 μm) is also greater than that of NF8 (29 μm) filter. At a longer deposition time, the difference between the thickness of multilayer and single layer filters increased; it is non-linear. The higher thickness lead to the lower quality factor for both multilayer and single layer filters.

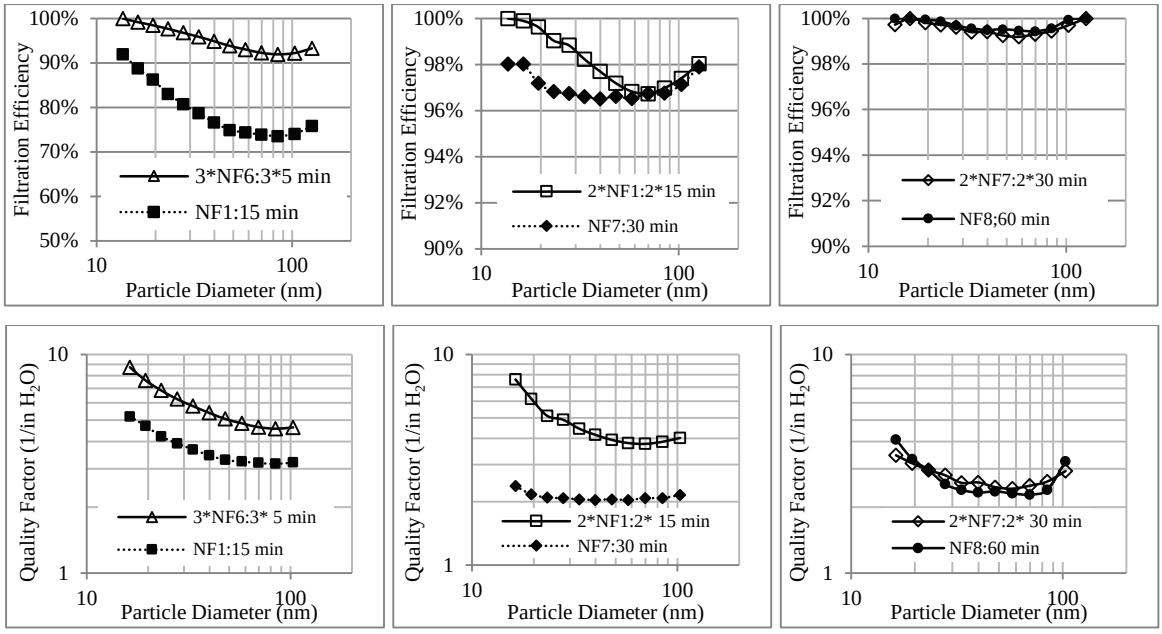

Figure 6-17. Comparison between the filtration efficiency and quality factor for single layer and corresponding multilayer filters

6.5 Conclusion

Nanofibrous filters were fabricated by electrospinning of PVA nanofibers on micro scale wire screens at different parameters, such as applied voltage, tip-to-collector distance, and electrospinning deposition time. An automated method was developed to determine nanofiber size distribution for the characterization of the electrospun nanofibrous filters. Electrospun nanofibrous filters were employed to elevate the filtration efficiency for NaCl nanoparticles. Results show that the applied voltage, tip-to-collector distance, and deposition time of the electrospinning process affected the fiber size, solidity and thickness of the nanofibrous filters, as well as the quality factors. Employing multiple layer thin nanofibrous filters with different fiber diameters and solidities greatly increased the filter quality factors of the PVA nanofibrous filters.

In the next chapter, in order to determine the behavior of small nanoparticles through filtration, thin layers of nanofibrous filters are employed. Employing these thin nanofibrous filters with randomly deposited fibers, in which filtration is characterized by surface loading instead of depth loading (Yoon et al. 2008), may eliminate the problems associated with both commercial filters (e.g., thick multilayers) and wire screens (sieving problems).

Chapter 7
On the Effects of Concentration on Nanoparticle Filtration Efficiency and Thermal Rebound

7.1 Summary

In previous chapters, it was shown that thermal rebound was not observed for WOx particles down to 2.35 nm and a relative humidity of about 20%. Theoretically, thermal rebound might happen when relative humidity is less than about 5%. There is no research on the effects of particle concentration on nanoparticle filtration and thermal rebound. In this chapter, the possibility of thermal rebound is revisited by measuring the filtration efficiency of WOx nanosized particles in the size range of 0.9-3.3 nm at different dilution ratios, passing through PVA nanofibrous filters at the low relative humidity of 2.9%.

Triple modal particle number concentration distributions with peaks at 1.07 nm, 1.27 nm and 2.54 nm were introduced through the filter. The particle concentrations for the first two peaks were in the order of 10^8 /cm^3; however, that of for the third peak was about 100 times lower. A great drop in filtration efficiency was observed at the particle size of 1.96 nm, a finding that contradicts conventional filtration theory. This drop is likely due to the higher particle concentrations for particles smaller than 1.96 nm. Comparing the filtration efficiencies measured for sub-1.8 nm at three different dilution ratios showed that the filtration efficiencies were elevated for the lower upstream particle concentration. Thus, for these small particles, the conventional filtration theory that works independence of particle concentration is no longer valid. Nanoparticles at these small sizes may behave like gas molecules. Thus, in addition to deposition mechanisms in filtration, another mechanism that depends on the concentration of particles is also expected to be important. This mechanism is somehow similar to adsorption of gas molecules onto a solid surface. As the concentration of particles increases, more of the filter's surfaces are covered by particles. Thus, at higher concentrations, there are fewer chances for incoming particles to collide on the surface of the filter media, leading to reduced filtration efficiency. It was shown that, for particles smaller than 1.07-1.17 nm, the drop of filtration efficiency occurred. This reduction was more obvious as the particle concentration decreased, because particles have more chance to collide with the surface and, as a result, to rebound from the surface.

7.2 Problem Statement

Uncertainties about the behavior of nanoparticles for sufficiently small size remain open questions. So far, three studies have shown evidences of thermal rebound. Kim et al. (2006) observed a drop in the filtration efficiency of a glass filter for uncharged sub-1.3 nm NaCl nanoparticles at 1.22% relative humidity. Van Gulijk et al. (2009) compared the penetration of different particles with a similar size distribution through a wire screen, and found the possibility of thermal rebound for NaCl and $NiSO_4$ particles. However, they did not determine the particle critical diameter below which thermal rebound occurred. Rennecke and Weber (2013) then investigated the thermal rebound of nanoparticles under low pressure and demonstrated the possibility of thermal rebound for dense NaCl particles in the range of 20 nm to 60 nm. They showed that thermal rebound is pressure dependent. At an ambient pressure, gas friction reduces the kinetic energy of a particle prior to rebounding, and causes its adhesion to a surface.

The focus of this chapter is to explore the complicated behavior of sub-3.3 nm particles in air filtration. Several parameters were taken into consideration, including ambient conditions, tested filter properties, nanoparticle properties and their measurement devices. The effects of these parameters on air filtration have been investigated in previous chapters.

Ambient conditions such as relative humidity, temperature and pressure all affect filtration performance. First, the adhesion energy between particles and filter media surfaces increases with the level of relative humidity due to capillary force (Bateman et al. 2014; Chen et al. 2011; Givehchi and Tan 2015; Pakarinen et al. 2005; Stein et al. 1994). The increase in the adhesion energy may decrease the probability of thermal rebound. Second, temperature directly affects the Brownian diffusion of nanoparticles. Therefore, the possibility for nanoparticles to rebound from a surface may increase at high temperatures (Mouret et al. 2011). The last but not least important ambient parameter is pressure. A numerical and experimental study using a low-pressure impactor showed the possibility of thermal rebound at low pressure (Rennecke and Weber 2013a).

The characteristics of filters are also crucial to thermal rebound. Most experimental studies employed commercial fibrous filters to test nanoparticle penetration through the filter and concluded that no thermal rebound was associated with their tested particles (Golanski et al. 2009; Huang et al. 2007; Japuntich et al. 2007; Kim et al. 2007; Van Osdell et al. 1990). It is believed that thermal rebound may

not happen for thick and multilayer filters, because rebounded particles may be captured by the next layers of the filter (Givehchi and Tan 2014). Consequently, single layer filters such as wire screens are expected to eliminate this artifact. In this case, if particle rebound takes place, a second layer will not capture the rebounded nanoparticles. The two experimental studies that showed the possibility of thermal rebound for sub-2 nm particles used wire screens as their filter media (Ichitsubo et al. 1996; Otani et al. 1995). However, wire screens have well-defined wires and openings. These open spaces may be sufficiently large for nanoparticles to pass through without collision with the wires, according to sieving mechanism. In this scenario, the low efficiency of small nanoparticles may attribute incorrectly to thermal rebound. Given the possible artifacts of test filters during the observation of thermal rebound effect, nanofibrous filters are considered an alternative to conventional filters in this study. The filtration is then characterized by surface loading instead of depth loading because of the extra thin thickness of nanofibers. In addition, the media surface on which nanoparticles can collide is greatly increased due to the large surface area of nanofibers. Moreover, nanofibers are bonded together, which eliminates openings.

Another important factor that affects thermal rebound is the properties of nanoparticles. Although various methods have been used to produce nanoaerosol particles, few can generate nanoparticles down to 1 nm in sufficient numbers. Previous studies have usually employed nanoparticles greater than 2 nm, and did not observe thermal rebound. Only a few researchers utilized sub-2 nm particles along with larger ones (Alonso et al. 1997; Heim et al. 2010; Ichitsubo et al. 1996; Kim et al. 2006; Otani et al. 1995), and three of them reported the possibility of thermal rebound for sub-2 nm particles (Ichitsubo et al. 1996; Kim et al. 2006; Otani et al. 1995). As a result, the tested nanoparticles' size is important to the occurrence of thermal rebound, and the majority of studies did not observe thermal rebound, probably because they used nanoparticles above 2 nm.

Another missing factor in air filtration theory is the effect of upstream particle concentration on filtration efficiency. If small nanoparticles behave like gas molecules upon their impaction with the surface of the filter media, the concentration also becomes important. Therefore, besides deposition mechanisms in filtration, another mechanism similar to adsorption for gas molecules has to be taken into consideration.

In addition, the accuracy of nanoparticle measurement devices also affects the calculation of filtration efficiency and may lead to the artifact of thermal rebound. In Chapter 3, it was explained that the GRIMM SMPS+E employing high resolutions of DMA and FCE for sizing and quantifying nanoparticles down to 0.8 nm at high accuracy. GRIMM FCE is also employed as a reference device for particles smaller than 3 nm (Wimmer et al. 2013), and shows FCE's higher accuracy for smaller particles than CPC's. Thus, the former device is employed to determine the particle concentration distribution at this small size.

The main goal of this chapter is to determine the effects of nanoparticle concentration on nanoaerosol filtration and thermal rebound. The filtration efficiency for triple modal number concentration distributions of WOx particles, ranging from 0.82 nm to 4 nm, at different particle concentrations and moving through PVA nanofibrous filters, was measured under ambient conditions. A GRIMM emission sampling system (ESS) was employed to dilute nanoaerosol at two rates, 10x and 100x. The GRIMM SMPS+E was used to measure the particle number concentration distributions upstream and downstream of the filter with a sheath air to sample airflow rate ratio of 20:2.

Results showed that nanoparticle filtration efficiency depended on the upstream nanoparticle concentration. As the particle concentration increases, the nanoparticle filtration efficiency decreases. At higher particle concentrations, less surface on the filter media is available for nanoparticles to deposit themselves on. Thus, at higher particle concentrations, nanoparticles have less chance to collide on the filter media surface, causing reduced in filtration efficiency. It was shown that, for particles smaller than 1.07-1.17 nm, the reduction in filtration efficiency occurred with decreases in particle size. This reduction is more obvious at lower particle concentrations, because nanoparticles have more chance to collide with the surface of filter media, revealing thermal rebound.

7.3 Materials and Methods

The experimental setup used to determine the filtration efficiency of WOx nanoparticles is the same as that in Chapter 4. In present work, the tungsten air flow was in the range of 7-10 $L.h^{-1}$; the carrier air was in the range of 120-200 $L.h^{-1}$; and the diluting air flow was in the range of 200-250 $L.h^{-1}$. Nanoparticles down to 0.8 nm were generated using the GRIMM WOx nanoparticle generator and their size distribution remained steady during the experiments. Since diffusion loss is significant for such small particles, particle concentrations have to be large enough to be sufficient when the flow reach the

measurement device. To detect these small particles, the aerosol flow rates must be relatively higher than the values employed in previous chapters (Q> 4 lpm). At a higher flow rate, the residence times of nanoparticles in the tubes are lower, which minimizes the diffusion loss of nanoparticles (Erickson et al. 2007).

The ESS was employed to dilute tested nanoparticles prior to filtration. Besides dilution rate, particles travel in extra tubes in ESS, which increases the diffusion loss and causes lower particle concentrations. The relative humidity and temperature of the aerosol flow were 2.9±0.4%, and 24.7±1.3 ^{o}C, respectively. The low relative humidity minimizes the capillary force and eliminates the adhesion energy between nanoparticle and a filter's surface due to capillary force (Givehchi and Tan 2015).

The GRIMM SMPS+E was used to measure the size distribution of nanoparticles down to 0.8 nm when a high sheath flow rate was chosen. For measuring small nanoparticles and minimizing the diffusion broadening, a sheath air to sample airflow ratio of 20:2 was used and remained constant in all experiments. In order to minimize the nanoparticle loss due to diffusion, the FCE and the DMA have to be apart from each other at a minimum distance. In this case, the particle size distribution measurements reached stable and equilibrium lognormal distribution as long as the particle concentration remained greater than 1000 /cm^3.

Electrospun polyvinyl alcohol (PVA) nanofibrous filters were used as the test filters. A full explanation of fabricating these filters has been given in Chapter 6. Differences in the electrospinning parameters for the fabrication of filters result in different mean fiber diameters, thicknesses, and solidities, as shown in Figure 7-1. SEM images were taken at two magnifications, 20.00 KX and 5.00 KX, for each sample. Table 7-1 summarizes the characteristics of the fabricated filters used in this chapter.

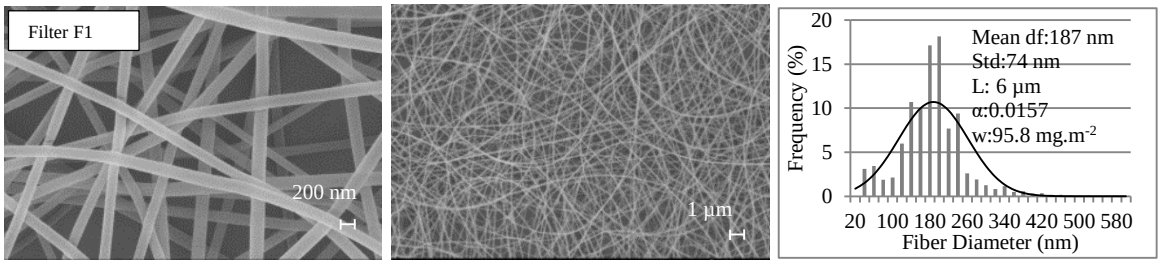

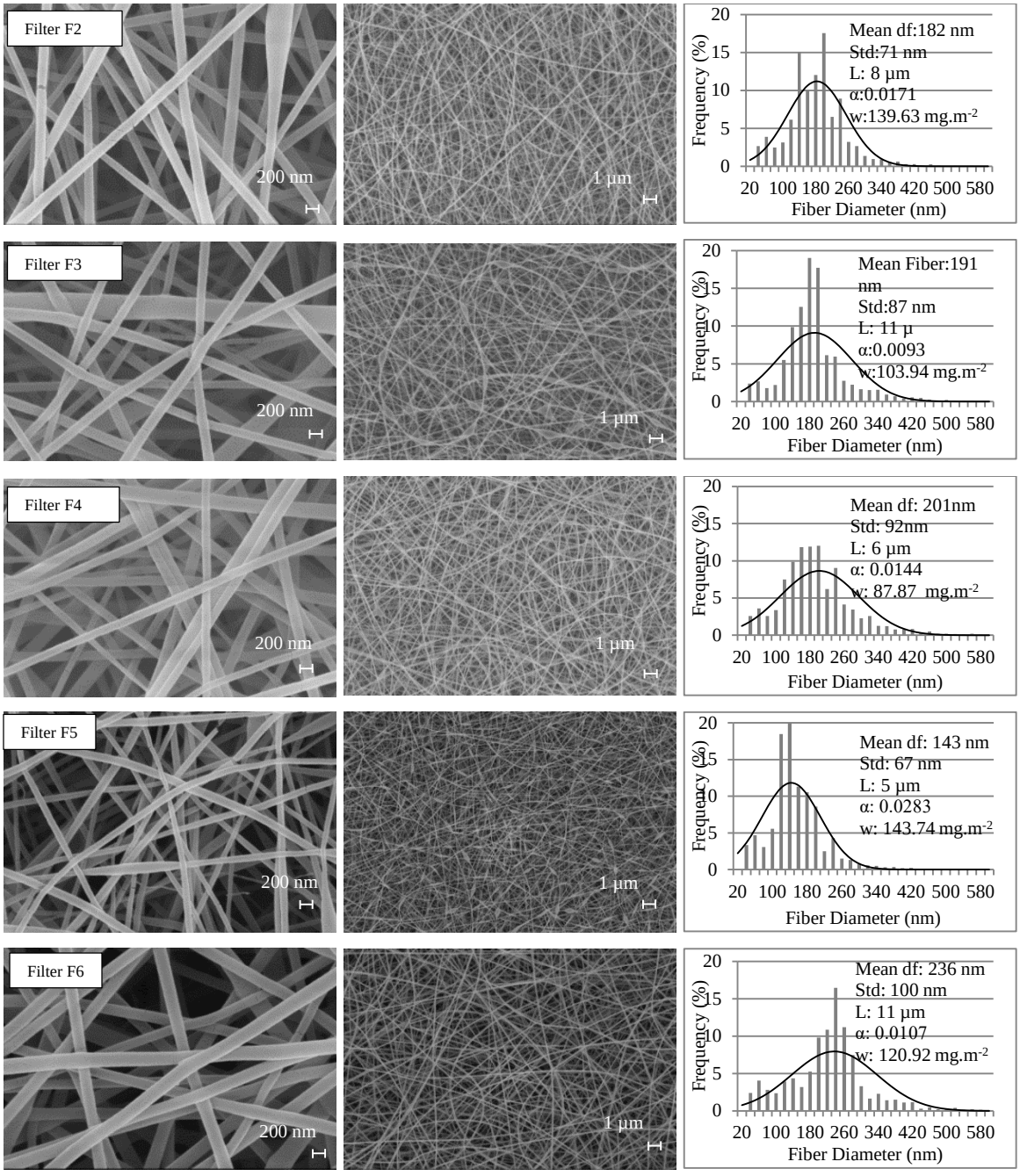

Figure 7-1. SEM images and fiber diameter distributions of nanofibrous filters

Table 7-1. PVA nanofibrous filter characteristics

Filter	d_f (nm)	σ_g (nm)	L (μm)	α	ρ_f (g/cm^2)	W (mg/m^2)	ΔP at 4 lpm (in H_2O)
F1	187	74	6	0.0157	1.019	95.80	0.22
F2	182	71	8	0.0171	1.019	139.60	0.38
F3	191	87	11	0.0093	1.019	103.94	0.17
F4	201	92	6	0.0144	1.019	87.87	0.18
F5	143	67	5	0.0283	1.015	143.74	0.92
F6	236	100	11	0.0107	1.023	120.92	0.15

7.4 Theoretical Analysis

Theoretical analyses have been reviewed in Chapters 2 and 4, and so only the equations used in this chapter are described. The total filtration efficiency is as follows:

$$\eta = 1 - \exp\left[\frac{-4\alpha E_T L}{\pi d_f (1-\alpha)}\right] \tag{7-1}$$

where E_T is the total single fiber efficiency. For the tested particle sizes in this chapter, the interception, electrostatic forces, and impaction are negligible. Thus, the only effective mechanism is Brownian diffusion. The single fiber efficiency of nanoparticles moving through fibrous filters in a gas slip flow based on the Brownian diffusion mechanism is defined as (Payet et al. 1992);

$$E_D = 1.6\left(\frac{1-\alpha}{Ku}\right)^{1/3} Pe^{-2/3} C_d C_d' \tag{7-2}$$

where

$$C_d = 1 + 0.388 Kn_f \left[\frac{(1-\alpha)Pe}{Ku}\right]^{1/3} \tag{7-3}$$

$$C_d' = \left[1 + 1.6\left(\frac{1-\alpha}{Ku}\right)^{1/3} Pe^{-2/3} C_d\right]^{-1} \tag{7-4}$$

where Ku is the Kuwabara hydrodynamic factor, Pe is the Peclet number, Kn_f is the fiber Kundesn number, and α is the solidity of the filter.

Small nanoparticles may behave like gas molecules during filtration. Thus, in this study, besides diffusion and thermal rebound, another mechanism which depends on particle concentration is also considered. The idea comes from adsorption theory, in which gas molecules travel toward a solid's surface and are attracted to the surface of that solid by van der Waals forces. This mechanism depends on the concentration of gas molecules. As the concentration increases, more and more of surfaces are covered by gas molecules. Therefore, at higher concentrations, molecules have less chance to collide on the surface, causing reduced adsorbent efficiency.

To borrow the adsorption theory from gas molecules for the nanoparticle adsorption, the following assumptions are considered:

- For each particle size, the transport of nanoparticle onto the filter's surface depends on particle concentration, which is valid according the aerosol dynamics (Tan 2014).
- If particles become deposited on the surface by this mechanism, they attach to the surface, and there is no rebound.

Among adsorption isotherms, the Freundlich model is an empirical one without many assumptions. Consequently, single fiber efficiency based on nanoparticle concentration (E_C) is defined based on the Freundlich model as follows:

$$E_C = KC^n \tag{7-5}$$

where K and n are constants for a specific nanoparticle and filter media at certain conditions. The relationship between the single fiber efficiency and particle concentration allows us to determine the constants empirically.

The total single fiber efficiency (E_T) required in Eq.(7-1) is calculated as:

$$E_T = 1 - (1 - \varepsilon . E_D)(1 - E_C) \tag{7-6}$$

where E_D is the single fiber efficiency based on the diffusion mechanism, ε is the adhesion efficiency of nanoparticles based on thermal rebound theory and considering capillary force as explained in Chapter 5, and E_C is the single fiber efficiency based on the effect of concentration.

7.5 Results and Discussion

7.5.1 Filtration efficiencies of tested filters for sub-3.3 nm particles

Figure 7-2 shows number concentration distribution of tungsten oxide nanoparticles averaged over at least three consecutive measurements versus particle diameter, at an aerosol flow rate of 4 lpm. The tungsten air, the carrier air and the diluting air flow rates in the tungsten aerosol generator were 10, 220, and 250 $L.h^{-1}$, respectively. The particle number concentration distribution of these particles remained stable. As shown in this figure, the generated nanoparticles have a diameter range between 0.82 and 4 nm, associated with three concentration peeks at diameters of 1.07 nm, 1.27 nm, and 2.54 nm. The particle concentrations for the first two peaks are in the order of 10^8 particles/cm^3; however, the particle concentration for the third peak is about 100 times lower than the others (in the order of 10^6 particles/cm^3).

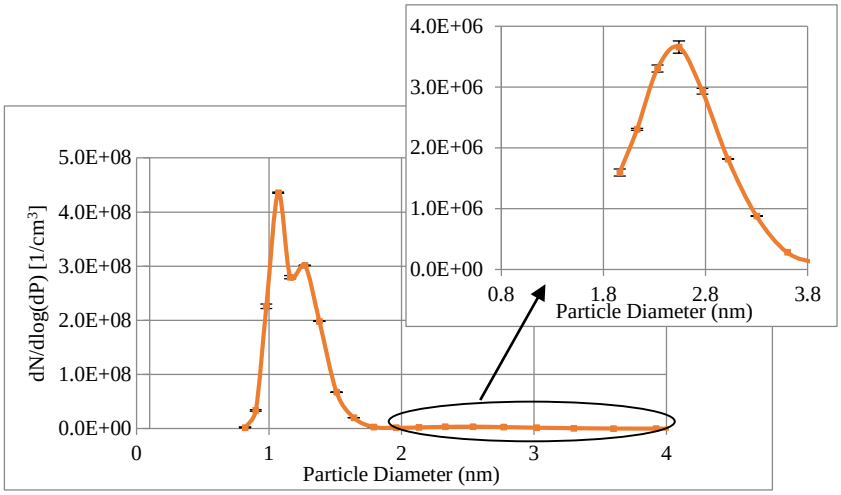

Figure 7-2. WOx nanoparticle size distribution generated by the tungsten oxide generator at an aerosol flow rate of 4 lpm

Figure 7-3 shows the upstream particle concentrations and the removal filtration efficiencies of six different electrospun nanofibrous filters for WOx nanoparticles vs. particle diameter. Although the particle sizes were in the range of 0.82-4 nm, the filtration efficiency was able to be determined only for particles in the range of 0.9-3.3 nm, because the particle concentrations of both lower and upper ends dropped below the lower detection limit of FCE (in-depth explanation was provided in Chapter 4) in downstream of the filters. Comparison between the filtration efficiencies for particles in the range of

0.9 to 3.3 nm for different tested filters show that the particle concentration affects the filtration efficiencies for these small nanoparticles. The filtration efficiencies for particles smaller than 1.96 nm are much lower than those for larger nanoparticles, and a sharp drop in filtration efficiency occurred at this size. Particle concentrations for sub-1.96 nm particles are in the range of 10^8 particles/cm^3; however, the concentrations of larger particles are in the range of 10^6 particles/cm^3. Thus, the difference between the filtration efficiencies for these particles may be attributed to the differences in the incoming particle concentration.

Further investigations show that the concentrations of particles with a diameter of 1.79 nm is about the same as those with diameters of 2.77 nm and 2.33 nm. However, the filtration efficiency for 1.79-nm particles is much lower than the efficiency for those other two diameters. Thus, in addition to particle concentrations, another mechanism may also cause the drop in filtration efficiency for smaller size of particles.

In the conventional filtration theory, it is believed that filtration efficiency increases as the size of small nanoparticles decreases; however, results of this study showed a significant drop in filtration efficiency as the size of nanoparticles decreased (even at the same upstream particle concentration). Thus, the conventional filtration theory is no longer valid for these tested sizes of WOx particles through the PVA nanofibrous filters under test, because it does not consider the effect of particle concentration on filtration efficiency.

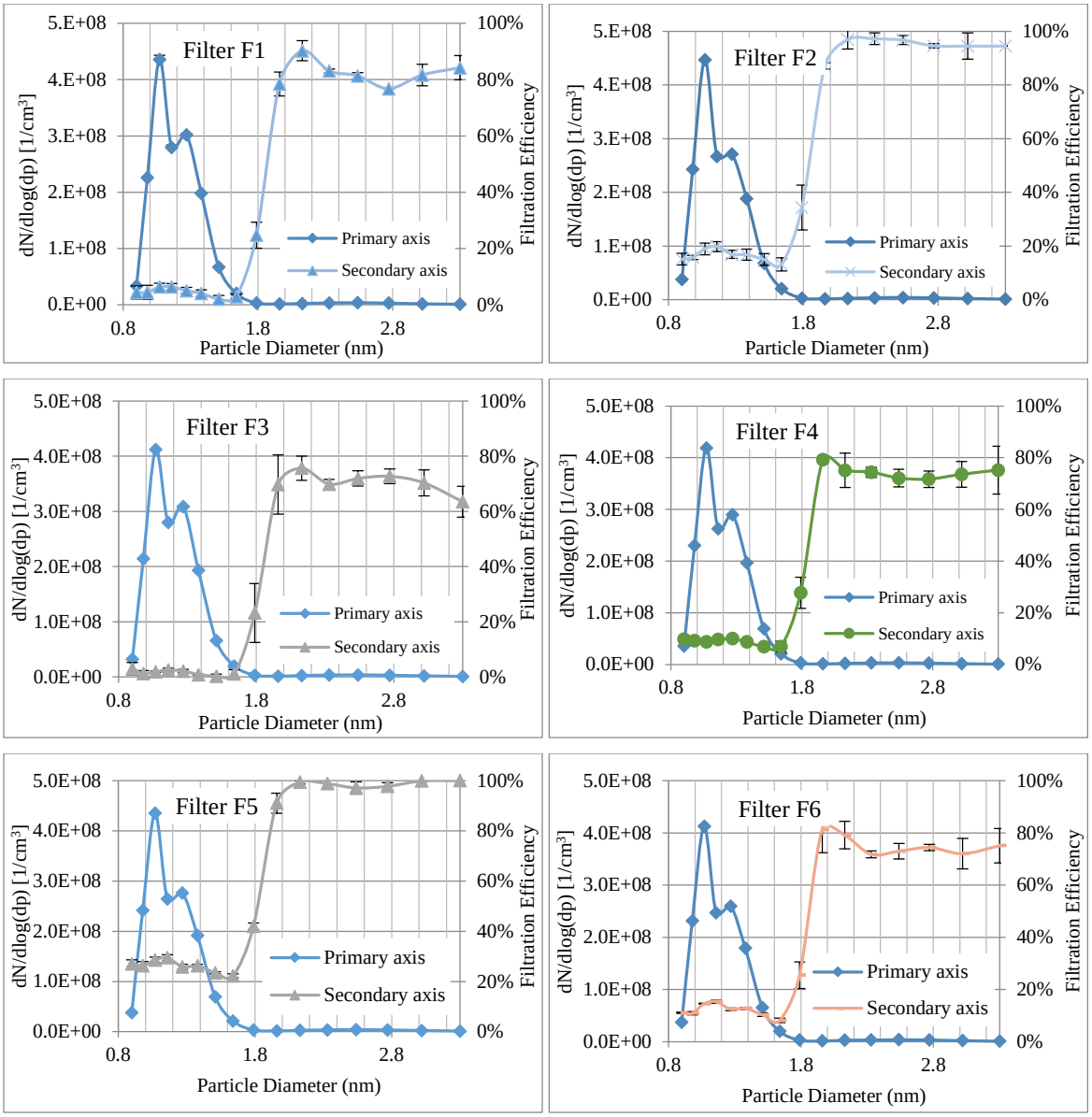

Figure 7-3. Nanoparticle size distributions along with particle removal efficiencies of different nanofibrous electrospun filters

7.5.2 Effect of particle concentration on filtration efficiency of nanoparticles

To investigate the effect of particle concentration on air filtration efficiency, the ESS was employed to dilute the incoming aerosol concentration prior to filtration testing. For particles larger than 1.96 nm, the particle concentrations fell below the detection limit of the FCE and, consequently, the filtration

efficiency measurements are inaccurate. Thus, the effect of particle concentration on filtration efficiency is only evaluated herein for smaller particles. Three particle number concentration distributions, which correspond to three dilution ratios (no dilution, 1:10, and 1:100) were employed as tested particles, as shown in Figure 7-4. The particle concentrations have three different orders of magnitude: from 10^8 to 10^7 and 10^6 /cm^3. Results show that the error bars in the particle size range were less than 1% for a high particle concentration (in the order of 10^8), about 3% for median (in the order of 10^7), and about 4% for low particle concentration (in the order of 10^6). In all three figures, there are two peaks at 1.07 nm, and 1.27 nm.

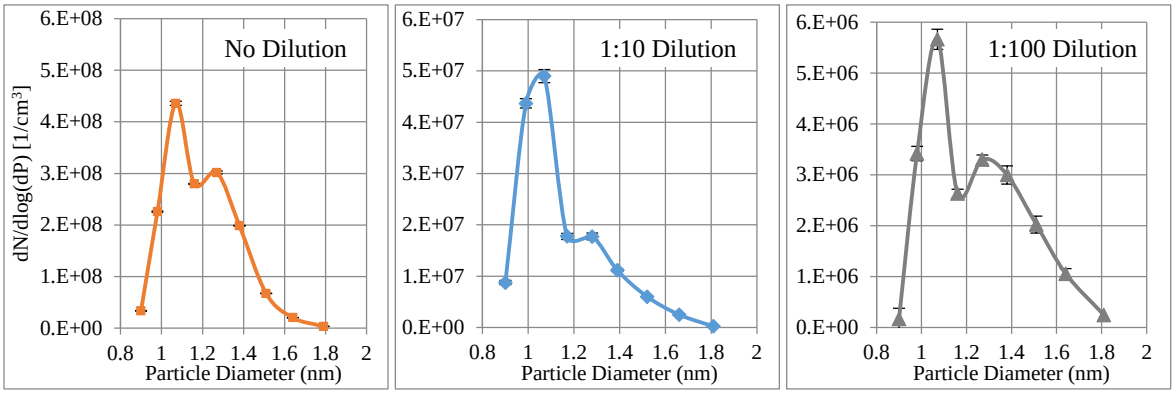

Figure 7-4. WOx nanoparticle number concentration distributions generated by the tungsten oxide generator at an aerosol flow rate of 4 lpm for three dilution ratios

The filtration efficiencies of the electrospun nanofibrous filters for three particle number concentration distributions (Figure 7-4) are shown in Figure 7-5. For all filters, as the dilution ratio increases and consequently upstream particle concentration decreases, the filtration efficiency is elevated, which shows the dependency of filtration efficiency on particle concentration. Shi and Ekberg also showed that the filtration efficiency of particulate matters in the range of 0.3-0.5 μm decreases as the upstream particle concentration increased (Shi and Ekberg 2015).

The upstream particle concentrations for sub-1.8 nm particles when employing the second dilution stage of ESS are in the same magnitude as those for larger particles. Even at the same concentration level, the filtration efficiency for sub-1.8 nm particles is lower than that for larger ones for all tested filters, which shows the complicated behavior of nanoparticles at these small sizes.

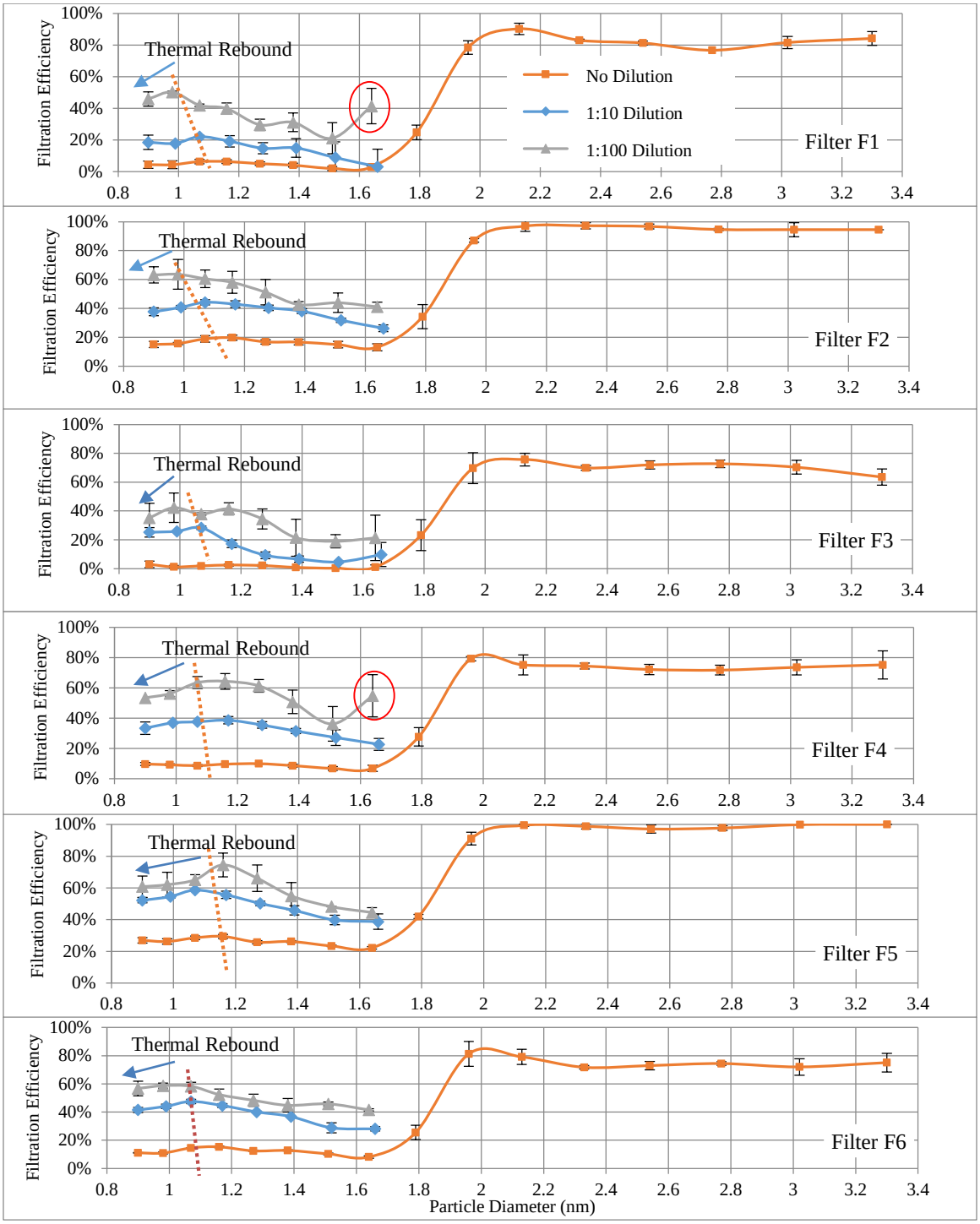

Figure 7-5. Particle filtration efficiencies of nanofibrous filters at three particle concentrations

Nanoparticles at these small sizes may behave like gas molecules upon their impact with the surface of the filter media. Thus, another mechanism, which becomes important at this size of nanoparticles, may be similar to adsorption, and it is concentration dependence. Adsorption is a surface phenomenon caused by van der Waals forces, where gas molecules will stay on the surface of an adsorbent. In this process, as the concentration of gas molecules increases, more surfaces of solid is covered with gas molecules. Thus, the availability of surface area decreases at higher concentration (Namasivayam et al. 1996). Qualitatively speaking, at low concentrations, the filtration efficiency for nanoparticles is high because of the availability of a filter's surface, and filtration efficiency decreases at higher concentrations.

Further investigations of particles smaller than 1.66 nm in Figure 7-5 show that, at three levels of dilutions, the filtration efficiency increases as the size of nanoparticles decreased to about 1.07-1.17 nm. At a particle size of 1.66 nm for two filters F1 and F4 and employing second dilution stage, the efficiency drops and then increases. This finding may be due to experimental errors as indicated by the large standard deviations than other points. For particles smaller than 1.07-1.17 nm, the filtration efficiency decreases as the size of nanoparticles decreases, perhaps due to thermal rebound. The filters tested in this study are extra thin, and act as single layer media; as a result, if a particle rebounds from the surface, there will be little chance for them to be captured again by the filter media.

The critical particle diameters are almost constant for various dilution ratios; however, the drop in filtration efficiency is more obvious at lower particle concentrations (i.e., higher dilution ratios). At lower particle concentrations, particles have more chance to collide with the surface, and as a result, rebound from the surface, thus increasing the probability of particle rebound from the surface, and decreasing the adhesion efficiency of particles to the surface. All of these situations lead to a decreasing rate of filtration efficiency for particles smaller than the critical diameter. The critical particle diameters are also almost constant for different filters. Since all tested filters were made of the same polymer with the same Hamaker constant, elastic mechanical constant and specific adhesion energy, we would expect the particle critical diameter to be the same for the filtration of WOx particles using PVA filters.

The average filtration efficiency for sub-1.8 nm particles as a function of upstream particle concentration for different electrospun tested filters is shown in Figure 7-6. Filtration efficiency

decreases with increasing particle concentration. Therefore, the upstream particle concentration has a significant effect on sub-1.8 nm particle filtration efficiency.

In a practical application, one of the ways to improve the filtration efficiency of these nanoparticles is employing makeup air and mixing it with recirculated polluted air, which gradually becomes cleaner as the polluted air goes through the filter. In this case, the filter removes the portion of upstream contamination and then outlet air with a low particle concentration goes through the filter again for further cleaning. This air has a lower particle concentration and causes higher filtration efficiency.

Filter F5 has the highest filtration efficiency for sub-1.8 nm particles at the three levels of particle concentrations, and filter F3 has the lowest filtration efficiency. Although F5 has the smallest thickness of 5 µm, it has the smallest mean fiber diameter (143 nm) and the greatest solidity (0.0283). The larger ratio of the solidity to mean fiber diameter increases the filtration efficiency for nanoparticles, at a price of relatively large pressure drop of 0.92 in H_2O. Filter F3 has the relatively large bed thickness of 11 µm, which is greater than those of the other filters. Its mean fiber diameter is between those of filters F1 and F4. However, it has the smallest solidity among all the filters, which decreases its filtration efficiency. The pressure drop of this filter is relatively lower than those of other filters (0.17 in H_2O). Thus, for these sizes of particles, which behave like gas molecules, a filter with a smaller mean fiber diameter and larger solidity has the highest filtration efficiency, and the thickness of a filter has only a negligible effect on the filtration efficiency for these nanoparticles.

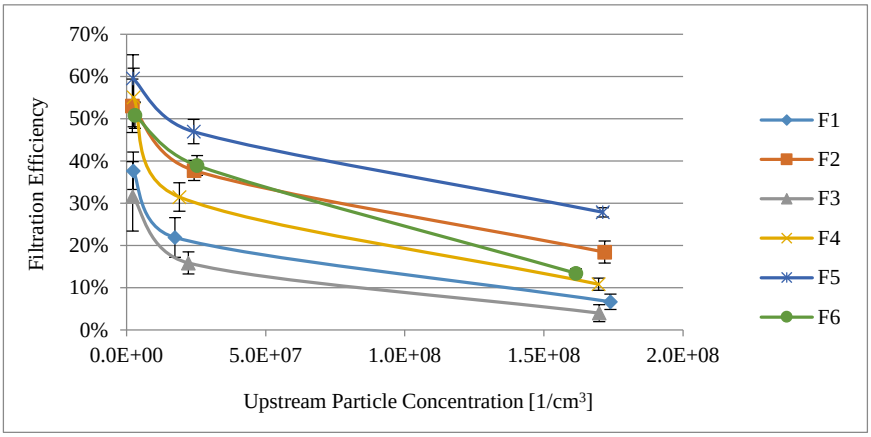

Figure 7-6. Total filtration efficiencies of electrospun filters as a function of upstream particle concentration

7.5.3 Validation of empirical model

7.5.3.1 Single fiber efficiency based on adsorption

For particles with diameters smaller than 1.8 nm at high concentrations, it is assumed that Brownian diffusion is not significant, an assumption counter to conventional filtration theory. However, in this study, the assumption makes sense because if Brownian diffusion is significant, the filtration efficiency for sub-1.8 nm must be at least as the same level as that for larger particles. Therefore, another mechanism, which is concentration dependent, more effectively explains the deposition mechanism for these sizes of particles.

The parameters of K and n in Eq.(7-5) have to be determined experimentally. Thus for each particle size in the range of 0.9 nm to 1.64 nm, the single fiber efficiency as a function of upstream particle concentrations for six different filters are plotted. The single fiber efficiency is determined based on Eq.(7-1) by considering the total filtration efficiency and filter characteristics. Figure 7-7 shows the results for particles with diameters of 1.07 nm and 1.64 nm. Results show K values of 127.18 and 950.42, for particles with a diameter of 1.07 nm and 1.64 nm, respectively. The n values are -0.348 and -0.567, for particles with a diameter of 1.07 nm and 1.64 nm, respectively. The trends for other particles are similar to these figures and are not shown here.

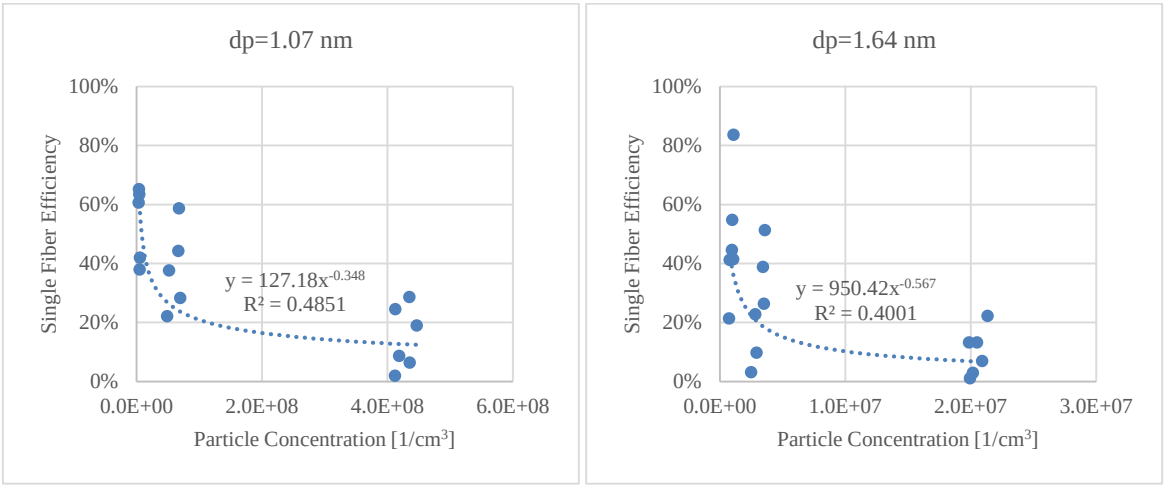

Figure 7-7. Single fiber efficiency versus particle concnetration for particle sizes of 1.07 nm and 1.64 nm

For each particle size, the parameters of K and n are determined and plotted as a function of particle diameter, as shown in Figure 7-8. Applying the least mean square method, these parameters are determined for particles larger than 1.64 nm and employed in Eq.(7-5) to determine the single fiber efficiency affected by concentration. Both the K and n parameters are size dependent and are shown as follows:

$$K = 2171.9d_p^3 - 5192.9d_p^2 + 3628d_p - 524.1 \tag{7-7}$$

$$n = -0.3134d_p - 0.0113 \tag{7-8}$$

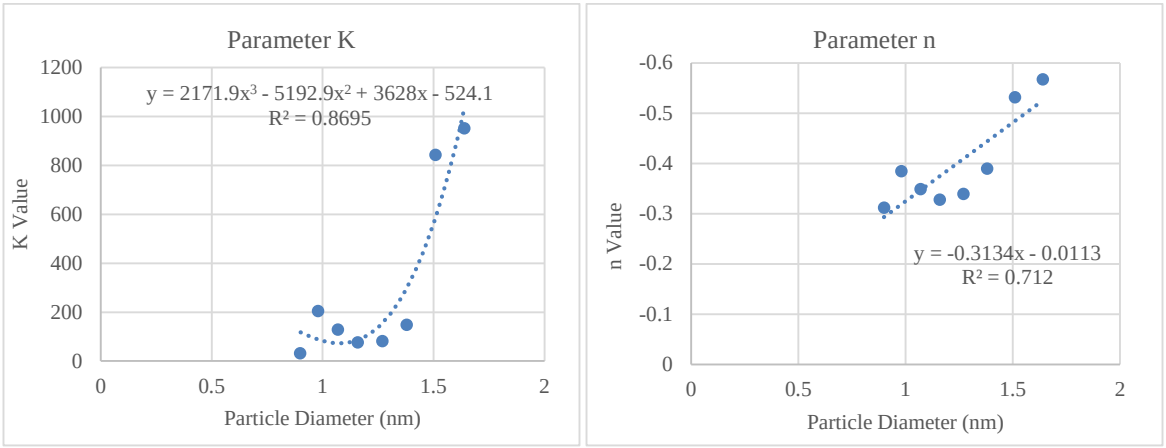

Figure 7-8. Parameters of n and K as a fucntion of particle diameter

7.5.3.2 Single fiber efficiency based on diffusion and thermal rebound

The relative humidity of the aerosols in this set of experiments was 2.9%. Based on the results in Chapter 5, at this relative humidity level, the thermal rebound of particles may happen. The Hamaker constant of PVA polymer is $37 \times 10^{-20} J$ (Vial and Carré 1991). The mechanical constant of PVA electrospun filters is calculated based on Eq.(2-27) by considering the poison ratio 0.42, and elastic Young's modulus $250 \times 10^9\ N/m^2$ (Yao et al. 2014), leading to $1.05 \times 10^{-12}\ m^2/N$.

The calculated elastic yield velocity (Eq.(2-45)) is 0.00241 m/s, which is much lower than the particle impact velocity (Figure 7-9). This comparison shows the high possibility for particles to impact the surface in a plastic regime. Thus, both adhesion energy models WM and MP are suitable for determining the adhesion energy of nanoparticles. The particle critical diameter based on the WM adhesion energy model is 2.13 nm, and that for the MP adhesion energy model is 1.38 nm.

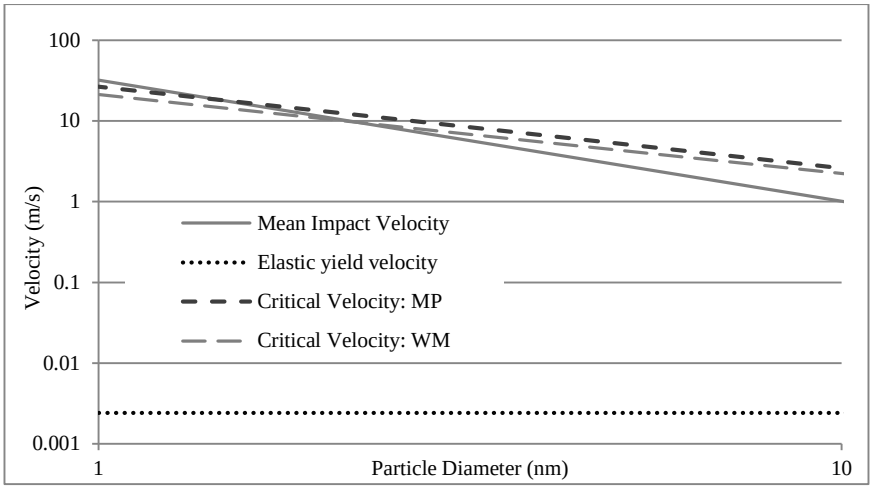

Figure 7-9. Comparison of the impact velocity, critical velocity and elastic yield velocity calculated using different models

The particle filtration efficiency based on both MP and WM models without and with considering thermal rebound at two relative humidities of 0% and 2.9% for filter F1 are shown in Figure 7-10. The filtration model employing MP model gives slightly higher filtration efficiency than that with WM model. Due to the similarity between these two models, this study considers only WM. The filtration efficiency model based on WM adhesion efficiency at a relative humidity of 2.9% starts dropping at a particle diameter of about 7 nm. Thus, for sub-7 nm particles, there is a decreasing rate in the model.

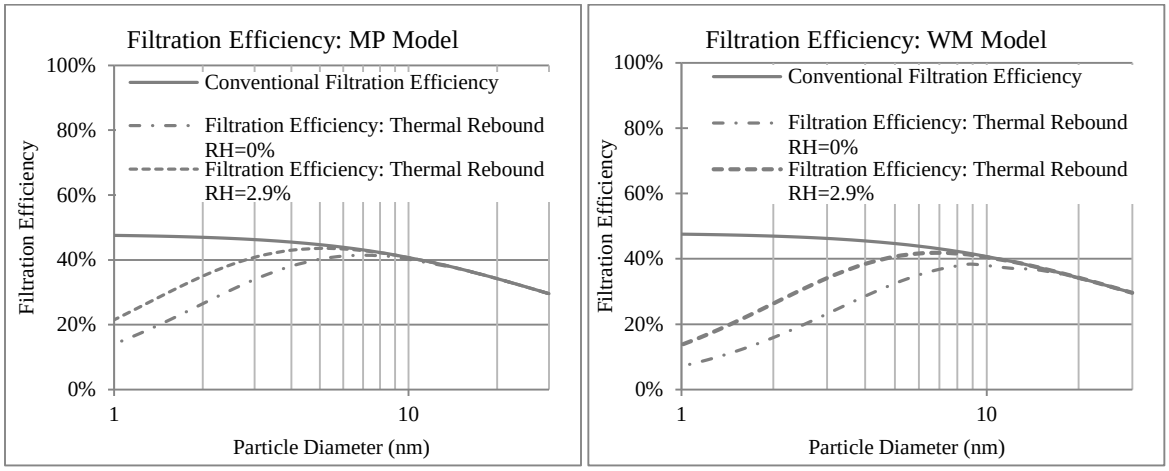

Figure 7-10. WOx nanoparticle filtration efficiencies of filter F1 at two relative humidity levels for plastic deformation models

7.5.3.3 Comparing experimental filtration efficiency and theory

Figure 7-11 shows the filtration efficiency of nanoparticles for both experiments and the developed model at three different particle number concentrations for six different filters. The model was developed by considering Brownian diffusion mechanism, thermal rebound effect and concentration-dependent single fiber efficiency. For all three dilution ratios, the models and the experimental data agreed qualitatively, but quantitatively, there is obvious discrepancy.

For higher particle concentrations (no dilution), the model underestimates the filtration efficiency for larger particles and overestimates that for smaller particles. As shown in Figure 7-10 for filter F1, even without consideration of the effect of particle concentrations, the filtration efficiency model drops to 38% for 4 nm particles, a level much lower than the experimental finding. Therefore, the filtration theory based on diffusion and thermal rebound underestimates the filtration efficiency for those particles larger than 1.96 nm, probably because of errors in determining the characteristics of the nanofibrous filters under test.

For sub-1.96 nm particles, without dilution, the experimental filtration efficiencies are almost constant over the tested particle sizes, and thermal drop in filtration efficiency is not obvious for particles smaller than 1.07-1.17 nm. However, the filtration efficiency based on the model decreases as the size of nanoparticles decreases. For lower particle concentrations (one or two dilution stages), the model and experimental data intersect with each other and are almost in the same range. Overall, for sub-1.96 nm, the filtration efficiencies based on the model decrease (or are almost constant) as the size of nanoparticles decreases to the critical sizes of 1.07-1.17 nm. After that, filtration efficiency drops more obviously.

To further this work, it would be useful to employ thin fibrous filters with micron scale fibers and determine if the same phenomenon is observed for those filters. Micron-scale fibers have a lower surface area to volume ratio than nano-scale fibers, and it is expected that particles would cover more surfaces. Therefore, based on the developed theory, one would expect to observe the same results or even more obvious ones. Furthermore, using different types of particles and filters would lead to the identification of different particle critical diameters. Considering the effect of particle resuspension may also improve the model (e.g., Boor et al. 2013).

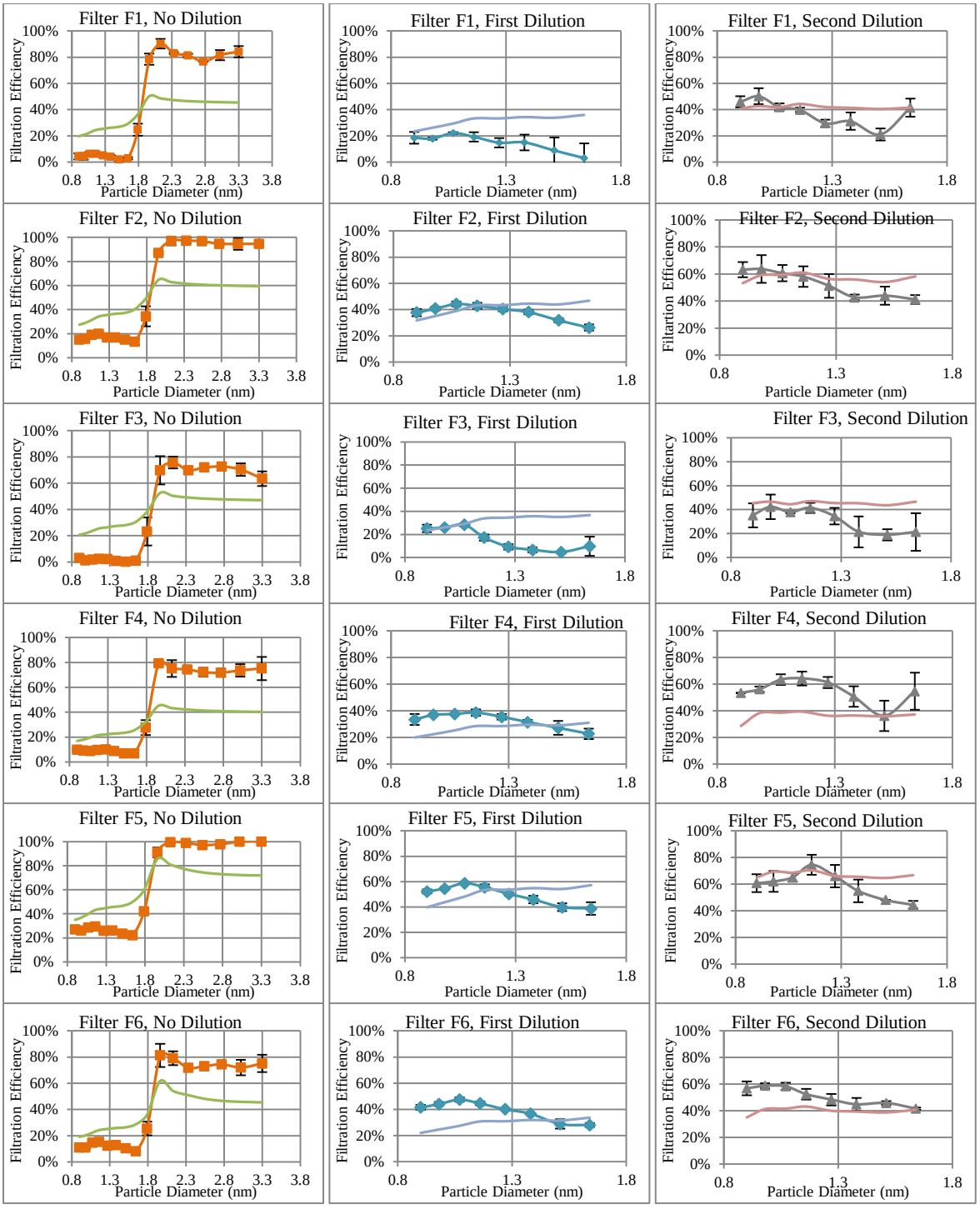

Figure 7-11. Filtration efficiency of filters at three particle concentrations (line:model, dots:exp)

7.6 Conclusion

This chapter has studied the filtration efficiency of sub-4 nm tungsten oxide particles moving through different electrospun nanofibrous filters, with a focus on understanding the effect of upstream particle concentration on the filtration of nanoparticles. Results showed the different behaviors for nanoparticles smaller and larger than 1.96 nm during filtration. A significant drop occurs for particles smaller than 1.96 nm, a drop due to the difference in particle concentrations rather than thermal rebound. It is shown that in addition to the deposition mechanisms in filtration, adsorption is also important for these particles. Based on adsorption theory, at higher particle concentrations, particles have less chance to collide on the filter's surface, and cause reduction in filtration efficiency. Further investigations for sub-1.8 nm particles show that as the particle size reduces, the filtration efficiency increases, until particle diameters of about 1.07-1.17 nm are reached. For smaller particles, reduction in filtration efficiency occurs, perhaps due to thermal rebound.

Chapter 8
Conclusions and Future Work

8.1 Conclusions and Contributions

The research presented in this thesis aimed to understand the interaction between different nanoparticles and various filter media. The key contributions and associated conclusions of the work are summarized as follows.

8.1.1 The performance of GRIMM SMPS+E for nanoaerosol sizing and quantifying

The performance of the GRIMM SMPS+E for sizing and quantifying airborne nanoparticles was first determined. For high-resolution measurements with minimum particle diffusion loss, the FCE has to be attached to the DMA. Due to the GRIMM FCE's fast response time (¼ s), purging between tests is not necessary. Even for multiple sample measurements without purging time, the GRIMM SMPS+E measures the newly introduced particles very accurately. The fast response time of this sensitive device occurs because of the rinse air flow in the FCE, which causes the FCE to respond to particle concentration changes in about 200 ms.

It was found that the sheath air to sample air flow rate affects the particle number concentration distribution measurements; the lower the sheath air flow rate, the higher the particle number concentration measurement. However, the sheath air to sample air flow rate does not affect the normalized particle size distributions, and mobility shift was not observed. Overall, although a high sheath air to sample air flow rate ratio minimizes the mobility bandwidth of classified nanoparticles and improves the monodispersity of particles, in this research, it led to more-diluted aerosols exiting from the DMA, which caused a low concentration challenge to the FCE GRIMM. Therefore, based on the initial particle concentration, sheath air flow rate to sample air flow rates of either 5:1 or 10:1 can be employed.

8.1.2 The behavior of WOx nanoparticles during filtration employing wire screens

Based on conventional filtration theory, in a Brownian diffusion regime, the filtration efficiency increases as the size of nanoparticles decreases. However, in this research, the filtration efficiency of WOx nanoparticles in wire screens did not show this trend, and the most penetrating particle sizes were

observed in the diffusion regime. The filtration efficiency of these WOx nanoparticles depended on upstream particle number concentration distributions. For particles smaller than the mode size, the filtration efficiency followed conventional filtration theory and decreased with increasing particle size. However, for particles larger than the size of peak concentration, the filtration efficiency deviated from conventional filtration theory. In this study, the most penetrating particle sizes and the sizes of peak concentration were in the same range: 4.69 nm to 6.65 nm.

The behavior of WOx nanoparticles during filtration was likely due to the different morphology of WOx particles, which affects particle charging and therefore both filtration efficiency and measurement performance. WOx particles produced with evaporation/condensation method are highly charged, causing electrostatic deposition as well as diffusion. Comparing the filtration efficiency of WOx nanoparticles with and without neutralization showed that the filtration efficiency was elevated for charged particles. The gap between the filtration efficiency for these two efficiency curves is attributed to the effect of electrostatic forces on filtration efficiency. The effect of electrostatic force is negligible for smaller particles (smaller than 3.98-5.64 nm); however, it is much more profound for larger ones. Theoretically, at the end of the neutralizing process, positive sub-5 nm particles and negative larger particles predominate, causing these small and large particles to behave differently during filtration. Furthermore, the particle size below which the effect of electrostatic force is negligible depends on the introduced particle number concentration distributions.

8.1.3 The effect of capillary force on thermal rebound

The thermal rebound of nanoparticles strongly depends on the material properties involved (no capillary and electrostatic forces); thus, thermal rebound theory cannot be viewed as a general theory; instead, it must be adapted from one particle and filter type to another due to changes in the mechanical constant, Hamaker constant, density, and hardness. Based on the adhesion energy models and the properties of particles and filters, filtration efficiency may start dropping when particle size is decreased to a certain critical diameter. Thus, proper matching between target particles and filter materials is important to effective particle-gas separation.

It has been shown that, when nanoparticles collide on a solid filter media, it is more likely for plastic deformation to occur than elastic deformation. Therefore, a nanoparticle filtration model should be based on the assumption of plastic deformation of nanoparticles upon impact with the surface of the

filter media. A new thermal rebound model was developed by taking into account the effects of electrostatic and capillary forces and plastic behavior impaction. Thermal rebound is independent of electrostatic force; however, it is affected by capillary force. The probability of nanoparticle rebound increases inversely with relative humidity, which attenuates the capillary force. Thermal rebound takes place only under conditions where relative humidity is extremely low (RH<5%).

8.1.4 The performance of PVA nanofibrous filters for nanoparticle removal

Electrospun PVA nanofibrous filters were employed to elevate the filtration efficiency for nanoparticles in the range of 10-125 nm NaCl particles. It has been shown that electrospinning parameters affect the characteristics of filters and nanofiltration performance. As the tip-to-collector distance increases, both fiber diameter and filter thickness decrease. As the applied voltage increases, both the solidity and thickness of the filter samples increase. The electrospun deposition time affects the mean fiber diameter, in addition to solidity and thickness of the filter. This finding is quite different from the assumption made by other researchers that the nanofiber size distributions of electrospun nanofibers remain constant over time. During electrospinning, the buildup of residual charges on the deposited fibers prevents the effective deposition of incoming fibers, leading to different fiber deposition patterns.

It has been shown that the higher the applied voltage and tip-to-collector distance and the shorter the deposition time, the higher the quality factors of nanofibrous filters. Therefore, the filter quality factor of a nanofibrous filter is not independent of filter thickness, because deposition time also affects the deposition pattern and other characteristics of nanofibrous filters. Employing multiple layers of thin nanofibrous filters greatly increased the filter quality factors of the PVA nanofibrous filters.

8.1.5 Effect of nanoparticle concentration on filtration efficiency of sub-4 nm WOx particles through nanofibrous filters

Finally, the possibility of thermal rebound was revisited by measuring the filtration efficiency for WOx nanosized particles in the size range of 0.9-3.3 nm, at different dilution ratios, passing through PVA nanofibrous filters at the low relative humidity of 2.9%. It has been shown that the upstream particle concentration affects the performance of nanofibrous filters, as it is elevated for lower particle concentrations. Nanoparticles at these small sizes may behave like gas molecules upon their impact with the surface of the filter media. Thus, another mechanism, termed here concentration dependence,

becomes important with this size of nanoparticles, and acts much as adsorption does. Therefore, at low concentrations, the filtration efficiency for nanoparticles is high because of the availability of a filter's surface.

It has also been shown that the particle critical diameter, below which thermal rebound may happen, is in the range of 1.07-1.17 nm, and the drop in filtration efficiency is more obvious at lower particle concentrations (i.e., higher dilution ratios), whereby nanoparticles have more chance to collide with the surface of the filter media. The filters tested were extra thin, and act as single layer media; as a result, if particles rebound from the surface, there will be little chance for them to be captured again by the filter media. Finally, empirical filtration efficiency was developed based on consideration of Brownian diffusion, thermal rebound and adsorption. The models and the experimental data agreed qualitatively, but quantitatively, they have discrepancies, which need further study.

8.2 Recommendations for Future Research

This section discusses potential areas of research that would extend the work initiated in this thesis.

The first limitation of this study is the low particle concentration detection limit of the GRIMM FCE. Because of this limitation, nanoparticle number concentrations of lower than 1000 /cm^3 cannot be measured by the FCE. Therefore, high efficient filters (e.g., commercial fibrous filters with micron scale fibers), which result in lower particle concentrations downstream of them could not be employed in this study. For all tests, particle concentrations had to be greater than 1000 /cm^3. Furthermore, as explained in Chapter 7, the effect of particle concentration was tested for sub-1.8 nm particles, not larger ones. Employing the ESS for particles in the range of 1.96-4 nm reduces the particle concentrations downstream of tested filters to lower numbers than 1000 /cm^3, which introduces significant errors in measurement. Employing CPC, which does not have a low particle concentration detection limit, may eliminate this issue.

Another limitation of this study was the necessity of attaching the FCE to the DMA. If the DMA was separated from the FCE and moved upstream of the filter, it could generate unipolar monodispersed particles. However, for filtration testing, these particles had to pass through a neutralizer to reach an equilibrium Boltzmann charge distribution. The FCE cannot measure the concentration of neutralized particles, and it could only measure the concentration of unipolar charged particles. Furthermore, the

concentration of monodispersed particles exiting from a DMA is low (because only unipolar charged particles are present), and it becomes lower due to high diffusion loss when they travel. Ultimately, the very low particle concentration reached the FCE and caused the false measurements. Therefore, for all experiments, the DMA and FCE were attached to each other. Due to this limitation, for all tests, polydispersed particles were passed through the tested filters, and a GRIMM SMPS+E was employed downstream of the filter to measure either polydispersed or monodispersed particles. The monodispersed ones were not investigated. It would be useful to employ the CPC (SMPS+C), and compare the filtration efficiency results when monodispersed particles pass through the filter and are measured by the CPC with those of this study (in which polydispersed particles pass through the filter and either monodispersed or polydispersed particles are measured with the GRIMM SMPS+E).

As explained in Chapter 3, the particle number concentration distributions measured by the GRIMM SMPS+E are affected by the sheath air to sample air flow rate, although the normalized particle size distributions are the same. This finding does not affect filtration testing, which was the main focus of this thesis; however, it strongly affects the results in orders of magnifications if particle number concentration distribution measurement is the main focus. Future research could compare the particle number concentration distribution measurements at different sheath air to sample air flow rates with those measured by other devices such as the TSI SMPS to determine the calibrations for the GRIMM SMPS+E.

It has been shown that WOx particles behave differently than NaCl particles during filtration. The filtration efficiencies of WOx particles with diameters larger than the size of peak concentration do not follow conventional filtration theory based on pure diffusion. This surprising behavior of WOx nanoparticles may be due to their different morphology, which affects both particle charging and measurement performance. To further this work, it would be useful to measure the charges of WOx nanoparticles after both generation and neutralization. For this aim, a mini electrostatic precipitator (ESP) could be employed to remove either positively or negatively charged particles prior to measurement.

The thermal rebound model was developed based on the effect of electrostatic and capillary forces; however, the model does not take shape factor, surface roughness, and oblique impaction into consideration. Furthermore, the calculation of capillary force can also be further improved. The relation

between the capillary force and relative humidity for sub-30 nm particles at a relative humidity of smaller than 10% was calculated by extrapolating from data by Pakarinen et al. (2005) and assuming of zero capillary force under dry conditions, which may cause some errors. In addition, the capillary force was calculated for spherical particles; however, contact angles and meniscus shapes could affect the capillary force strength, and should be considered in future work. The developed thermal rebound model was also compared with experiment filtration efficiency at a high relative humidity of 20%. Thus, future investigations could employ a humidifier to control the relative humidity of the aerosol flow and then compare the filtration efficiencies at various humidities with the developed thermal rebound model.

It has been shown that sub-1.8 nm particle behave like gas molecules and their filtration efficiencies through nanofibrous filters increase at lower particle concentrations. To further this research, it would be useful to employ thin fibrous filters with micron scale fibers and determine whether the same phenomenon is observed for those filters. Micron-scale fibers have a lower surface area to volume ratio than nano-scale fibers, and it is expected that particles would cover more surfaces. Therefore, based on the developed theory, one would expect to observe the same results or even more obvious ones.

Results of this study showed the possibility of thermal rebound for particles smaller than 1.07-1.17 nm for WOx particles through PVA nanofibrous filters. Using different types of particles and filters would lead to the identification of different particle critical diameters and has to be tested in future. In order to eliminate thermal rebound, it is suggested to employ multilayer filters; in this case, rebounded nanoparticles may be captured by successive layers.

Filtration efficiency based on the effect of particle concentration was developed by considering the Freundlich adsorption theory of gas molecules. The model and experiments agreed well qualitatively, but not quantitatively. For a more-accurate model, more experiments have to be done by considering different particles and filters and so determine the empirical parameters in different adsorption models for various interactions of particles and filters. Considering the effect of particle resuspension and the role of particle-particle interaction also helps improve the model.

8.3 Publications

The peer-refereed publications, related to the scope of this thesis, and authored by the candidate are listed below:

8.3.1 List of peer-reviewed journal articles

1. **Givehchi. R**., Li. Q., Tan. Z. (2015), Quality Factors of PVA Nanofibrous Filters for Airborne Particles in the Size Range of 10-125 nm. *Fuel*, In press.

2. **Givehchi. R**., Li. Q., Tan. Z. (2015), The Effect of Electrostatic Forces on Filtration Efficiency of Granular Filters. *Powder Technology*. 277:135-140.

3. **Givehchi. R**., Tan. Z. (2015), The Effect of Capillary Force on Airborne Nanoparticle Filtration. *Journal of Aerosol Science*. 83:12-24.

4. Tan. Z., **Givehchi. R**., Saprykina. A. (2015), Submicron Particle Sizing by Aerodynamic Dynamic Focusing and Electrical Charge Measurement, *Particuology*, 18:105-111.

5. **Givehchi. R**., Tan. Z. (2014), An Overview of Airborne Nanoparticle Filtration and Thermal Rebound Theory, *Aerosol and Air Quality Research*, 14: 45–63.

8.3.2 Peer- reviewed conference papers

1. **Givehchi. R**., Ni. C., Bardo. P., Tan. Z. Biodegradable Nanofibrous Filters for Air Filtration, *65th Canadian Chemical Engineering Conference*, Oct 4-7, 2015, Calgary, Alberta, Canada.

2. **Givehchi. R.**, Li. Q., Ni. C., Bardo. P., Tan. Z. Nanofibrous Filters for the Filtration of Nanoparticles, *The 8th International Symposium on Coal Combustion (8thISCC)*, July 19-22, 2015, Beijing, China.

3. **Givehchi. R**., Tan. Z. Thermal Rebound in Nanosized Particle Filtration, *Canadian Society for Mechanical Engineering International Congress*. June 1-4, 2014, Toronto, Canada.

4. **Givehchi. R**., Tan. Z., Yan. C., Li. Q. The Effect of Electrostatic Force on Granular Filtration of Nanoaerosol Particles, *the 9th International Green Energy Conference (IGEC-IX)*, May 25-28, 2014, Tianjin, China.

Glossary

BH	Bradley-Hamaker
CNC	Condensation Nuclei Counter
CPC	Condensation Particle Counter
DMA	Differential Mobility Analyzer
DMT	Derjaguin-Muller-Toporov
EC	Electrostatic Classification
ELPI	Electrical Low Pressure Impactor
ESP	Electrostatic Precipitator/Precipitation
FCE	Faraday Cup Electrometer
FMPS	Fast Mobility Particle Sizer
HEPA	High-Efficiency Particulate Arrestance
JKR	Johnson Kendall-Roberts
MP	Maugis-Pollock
PAN	Polyacrylonitrile
PEO	Polyethylene Oxide
PLA	Polylactic Acid
PM	Particulate Matter
PSM	Particle Size Magnifier
PVA	Polyvinyl Alcohol
SEM	Scanning Electron Microscopy
SMPS	Scanning Mobility Particle Sizer
TEM	Transmission Electron Microscope
UCPC	Ultrafine Condensation Particle Counter
VOC	Volatile Organic Compounds
WM	Weir and McGavin

Appendix A
Isokinetic Sampling

A.1 Summary

The goal of this section is to determine the effect of isokinetic sampling on the measurement of particle number concentration distribution. The behavior of nanoparticles in laminar flow was investigated with isokinetic and anisokinetic sampling procedure. Sub-10 nm polydispersed tungsten oxide nanoparticles were used as test particles. The particle number concentration distributions were measured at various main duct flow rates with and without the isokinetic sampling system.

Comparing the particle number concentration distributions for both cases (with and without isokinetic sampling) showed that, for the selected range of nanoparticles, the particle concentrations for isokinetic sampling procedure are lower than those without the isokinetic sampling procedure. However, the normalized particle size distributions in both cases are the same, which shows that employing isokinetic sampling in nanoparticle measurement is not necessary.

A.2 Introduction

Collecting representative samples from the gas stream using isokinetic sampling is essential to aerosol studies. In this method, a thin-walled sampling probe is aligned parallel to the gas streamline in the main tube, and a gas velocity in the probe is adjusted to the gas velocity in the main duct. The isokinetic sampling method is costly, because the size of the probe must change with changes in velocity.

Studies have shown the importance of isokinetic sampling for micron-sized particles (Barth et al. 2013; Ichitsubo and Otani 2012). It is believed that under anisokinetic conditions, sampling errors occur when particles cannot follow the gas streamline due to their inertia, which increases as the size of particles increases. Theoretical studies have shown that the error occurred for particles with a Stokes number of greater than 0.01 (Tan 2014).

The question arises of whether isokinetic sampling method is necessary for the measurement of nanoparticle number concentration distribution. For nanoparticles, inertia is negligible, so it seems that the isokinetic sampling procedure may not be necessary. A literature survey shows that several studies have measured nanoparticle number concentration distribution using isokinetic sampling method

(Golshahi et al. 2009; Heim et al. 2005; Lore et al. 2011; Motzkus et al. 2012). However, most of other studies did not employ the isokinetic sampling procedure to measure particle number concentration distribution (Brochot et al. 2011; Huang et al. 2007; Li et al. 2012; Van Gulijk et al. 2009). Arouca et al. 2010 employed NaCl particles in the range of 12 nm to 130 nm, using different nozzles, main ducts, aerosol flows and sampling flows; however, for all of the experiments, they employed a sampling tube for particle number concentration distribution measurements. They showed a negligible effect for using anisokinetic sampling procedure on normalized nanoparticle size distribution measurement (Arouca et al. 2010). As mentioned, some studies used the direct connection of aerosol flow rate to the measurement system, but before now no study has evaluated the effect of not employing isokinetic sampling tube for nanoparticle sampling, and pushing the aerosol flow directly to the measurement device. In this section, the difference between employing and not employing isokinetic sampling procedure is introduced.

In this section, sub-10 nm polydispersed tungsten oxide particles are sampled at different aerosol flow rates both with and without the isokinetic sampling procedure. The procedure involves a main duct, the isokinetic nozzle, and adjusting the sampling velocity to match the main velocity. The sampling point is selected from the fully developed region in the main duct, using the isokinetic nozzle.

A.3 Isokinetic Sampling Theory

Two parameters are important for the isokinetic sampling method: the nozzle geometry and the sampling velocity. At isokinetic conditions, the sampling flow rates in the nozzle and main duct must be adjusted, as the mean gas velocity in the sampling nozzle should be equal to the mean gas velocity in in the projected area in the main duct. If the mean sampling velocity is smaller than the mean gas velocity in the main duct, the nozzle is not able to draw particles from the projected area and so underestimates particle concentration. However, if the sampling velocity is greater than the mean gas velocity in the main duct, the nozzle draws particles from a larger projected area and thus overestimates nanoparticle concentration.

In anisokinetic sampling, the asperity ratio is defined as the ratio of the sample concentration to the ratio of the undisturbed concentration over the range of particle diameters,

$$A = \frac{C_s}{C_0} \tag{A-1}$$

where C_s is the nanopaticle concentration in the sampling probe, and C_0 is the nanoparticle concentration in the free stream. The Stokes number plays a major role in determining the importance of isokinetic sampling. This number is defined as

$$Stk = \frac{\rho_P d_P^2 C_c u_0}{18 \mu d_c} \tag{A-2}$$

where ρ_P is the particle density, μ is the gas viscosity, C_c is the Cunningham coefficienct, u_0 is the undisturbed mean air velocity, and d_c is the characteristics dimension. Various studies have been done to determine asperity ratios based on gas velocity and stokes number (Belyaev and Levin 1974; Krämer and Afchine 2004; Paik and Vincent 2002; Zenker 1971). Results have shown that the asperity ratio is not unity for large stokes numbers. However, for nanoparticles, $Stk < 0.01$, particle inertia in negligible and the asperity ratio is unity. As a result, isokinetic sampling may not necessary for the measurement.

The velocity profile in the main duct for a laminar situation is shown in Figure A-1. At the entrance section, the flow is uniform; however, as the flow hits the pipe wall, the velocity component near the wall change to zero and a fully developed region forms. In this region, the flow distribution is parabolic, with the maximum velocity at the center of the pipe. The entrance length in laminar flow is defined as:

$$\frac{L_e}{D} \approx 0.06\, Re_d \tag{A-3}$$

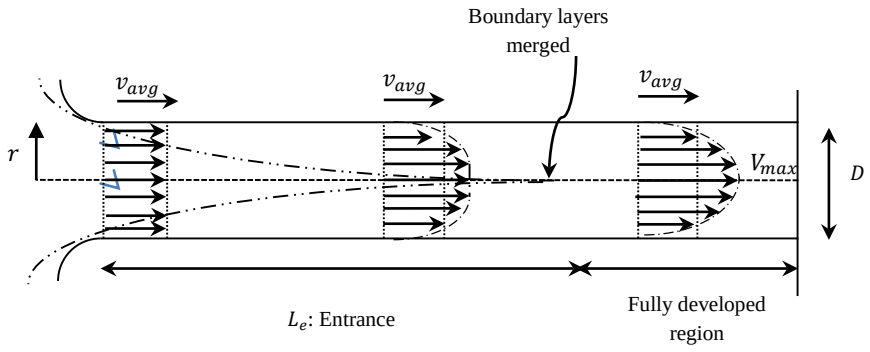

Figure A-1. Velocity profile in laminar flow

The sampling point is selected in the fully developed region as shown in Figure A-1. The average velocity in the main duct is defined as:

$$v_{avg} = \frac{v_{max}}{2} \tag{A-4}$$

$$v_{avg} = \frac{Q}{\pi D^2/4} \tag{A-5}$$

where Q is the aerosol flow rate. For a fully developed flow at laminar conditions, the velocity profile is given as:

$$v_{(r)} = v_{max}\left[1 - \frac{r^2}{(\frac{D}{2})^2}\right] \tag{A-6}$$

Thus:

$$v_{(r=0)} = v_{max} \tag{A-7}$$

$$v_{(r=d/2)} = v_{max}\left(1 - \frac{d^2}{D^2}\right) \tag{A-8}$$

The average velocity in the sampling nozzle (u_s) is calculated as:

$$u_s = \frac{v_{(r=d/2)} + v_{(r=0)}}{2} \tag{A-9}$$

$$u_s = \frac{8Q}{\pi D^2}(1 - \frac{d^2}{2D^2}) \tag{A-10}$$

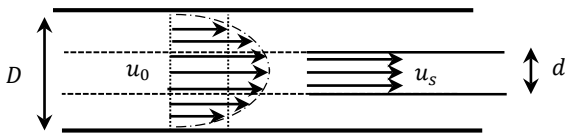

Figure A-2. Schematic diagram of duct flow and sampling flow

For isokinetic sampling, the mean particle velocity in the projected area (u_0) is equal to the mean sampling velocity and is calculated based on the nozzle diameter and the main duct as follows:

$$u_0 = u_s = \frac{8Q}{\pi D^2}\left(1 - \frac{d^2}{2D^2}\right) \quad \text{(A-11)}$$

A.4 Preliminary Results

Nanoparticle number concentration distributions were measured with and without the isokinetic sampling procedure by maintaining other factors as constants. For the first case (with the isokinetic procedure), an isokinetic sampling probe was employed in the fully developed region to avoid possible errors in the measurement of particle number concentration distribution. The diameter of the main duct was 1.5 inches and that of for the sampling nozzle 0.425 inches. The main duct length was about 10 times greater than its diameter to prevent any disturbances in the duct. Ideal isokinetic sampling happens when both geometric parameters and velocities are adjusted to match one another. The SMPS took samples at an aerosol sampling flow rate of 1 lpm. For isokinetic sampling, the mean particle velocity in the projected area is the same as the mean particle velocity in the isokinetic tube (Eq.(A-11)); as a result, an aerosol flow rate of 6.5 lpm is the ideal isokinetic sampling situation (the mean particle velocity in the projected area is 18 cm/s). For lower flow rates, superisokinetic and for higher flow rates, subisokinetic is performed. In the second case (without the isokinetic procedure), the whole system for isokinetic sampling was removed, and the entire flow was sampled directly with the measurement device.

Figure A-3 shows the particle number concentration distributions with and without the isokinetic procedure for various aerosol flow rates. Results showed that as the aerosol flow rate decreases, measured particle concentration decreases. At lower flow rates, smaller amounts of nanoparticles go through the tube, resulting in lower particle concentration.

Figure A-4 compares the particle number concentration distributions with and without the isokinetic procedure for three aerosol flow rates. With the isokinetic procedure, the ideal isokinetic sampling occurred at an aerosol flow rate of 6.5 lpm. For aerosol flow rates of greater than 6.5 lpm, subisokinetic sampling occurs, and for those lower than 6.5 lpm, superisokinetic. Each figure shows that particle number concentration distributions are significantly different in both cases. Employing the isokinetic sampling tube, decreases nanoparticle number concentration. Isokinetic sampling train may increase particle loss in the tube, because particles have a longer way to go, which increases the deposition rate

of nanoparticles on the tube's wall. Also, in isokinetic sampling, only a reprehensive sample goes through the isokinetic probe. However, without isokinetic procedure, all the aerosol flow goes directly to the measurement system which increases the nanoparticle number concentration measurement.

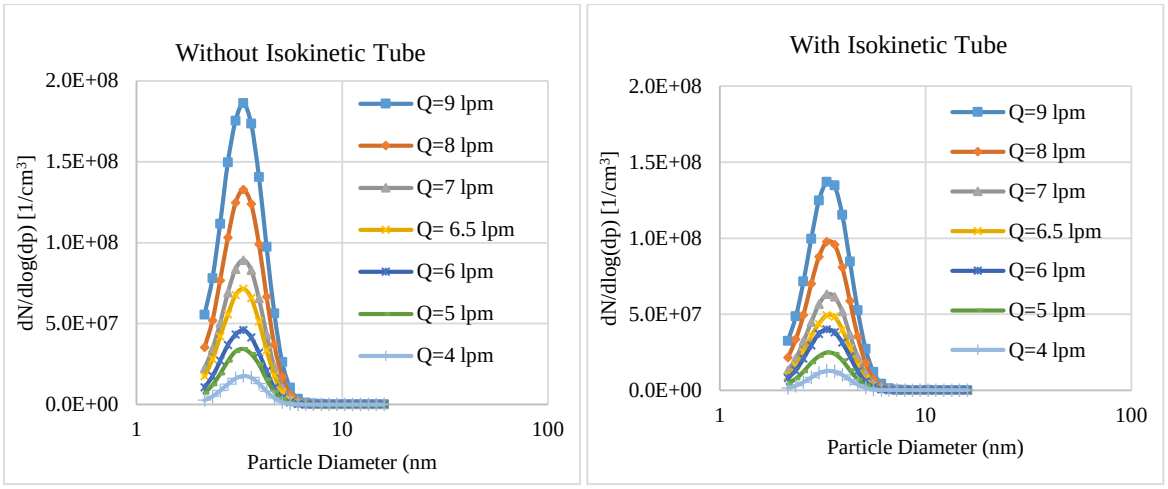

Figure A-3. Particle number concentration distribution measurements, for both with and without isokinetic sampling procedure

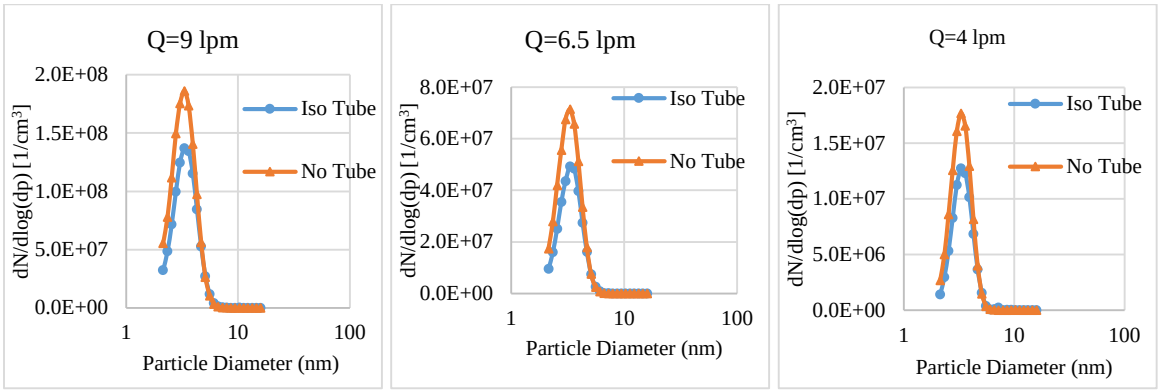

Figure A-4. Comparison between isokinetic procedure and non-isokinetic procedure for three aerosol flow rates

To highlight the differences in Figure A-3, the normalized particle size distributions for different aerosol flow rates in both cases (with and without isokinetic procedure) are shown in Figure A-5. The curves for all aerosol flow rates are similar to that for ideal isokinetic sampling (<0.5% difference).

Figure A-6 compares the normalized particle size distributions for isokinetic sampling procedure and non-isokinetic procedure at three aerosol flow rates. The normalized particle size distribution is not affected by the aerosol flow rates; as a result, the isokinetic sampling does not depend on main duct flow (Arouca et al. 2010).

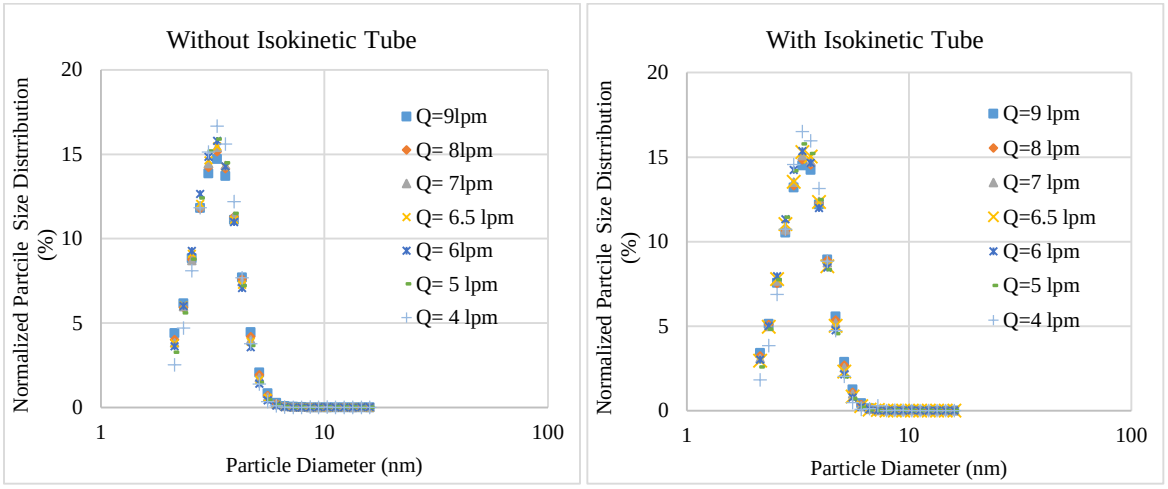

Figure A-5. Normalized particle size distributions for isokinetic sampling procedure

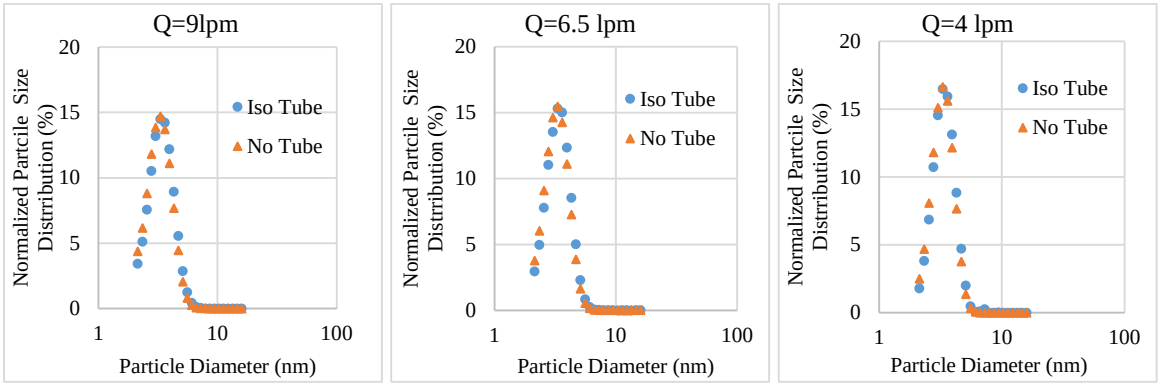

Figure A-6. Normalized particle size distributions (over-isokinetic, isokinetic, sub-isokinetic)

Comparison between the particle number concentration distributions for both cases (with and without isokinetic sampling) showed that for the selected range of nanoparticles, the particle concentration for isokinetic sampling is lower than that without isokinetic sampling. However, the normalized particle size distributions in both cases are the same, as are the normalized particle size distributions for ideal and non-ideal isokinetic sampling procedures.

If the goal of a study is to measure of nanoparticle number concentration distribution, anisokinetic sampling may affect the measurement, and an isokinetic tube is needed to get the repressive sample. However, for nanoparticle filtration studies, both upstream and downstream measurement are sampled under the same conditions. Thus, the effect of anisokinetic sampling is negligible, because, in this case, the particle penetration is calculated as the ratio of downstream measurement and upstream measurement so the error is minimized. In summary, although employing isokinetic sampling procedure is suggested for nanoparticle number concentration distribution, it is not necessary to have ideal isokinetic sampling through adjusting the main duct velocity to match the sampling velocity.

Appendix B
Electrospinning

B.1 Effect of PVA Concentration on the Morphology of Nanofibers

Figure B-1 shows the characteristics of three different filters that were fabricated at applied voltage of 10 kV, deposition time of 15 min, solution feeding rate of 0.3 ml·hr^{-1} and three different PVA polymer concentrations (8%, 10%, and 12%). It has been shown that both fibers and beads were generated when the polymer concentration was 8%. However, when the polymer concentration increased to 10%, smooth and uniform fibers were formed. As the concentration increased to 12%, the diameter of the fiber increased (Deitzel et al. 2001; Yun et al. 2007). Thus, as the polymer concentration increased, filters with a broad diameter distribution and greater mean fiber diameter were fabricated. Figure B-2 shows that the mean fiber diameter was exponentially proportional to the concentration of the PVA polymer. Previous studies have also reported an exponential relationship for nylon 4,6 and polyacetylene (PA) 6 (Huang et al. 2006; Mit-uppatham et al. 2004).

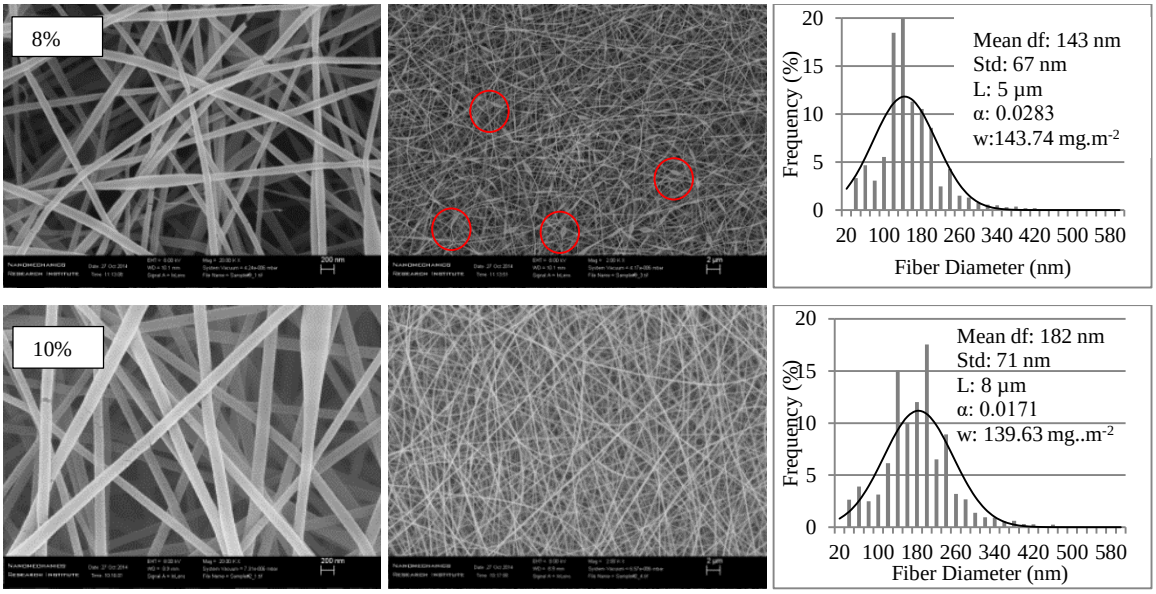

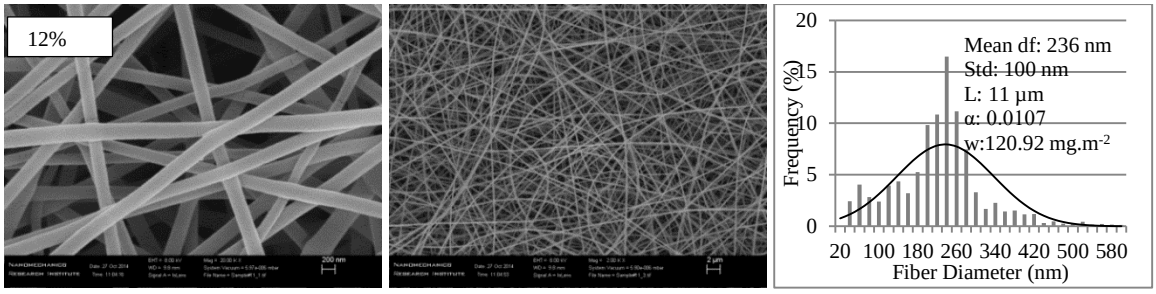

Figure B-1. SEM images and fiber diameter distributions of electrospun nanofibrous filters fabricated at 8%, 10%, and 12% w/w

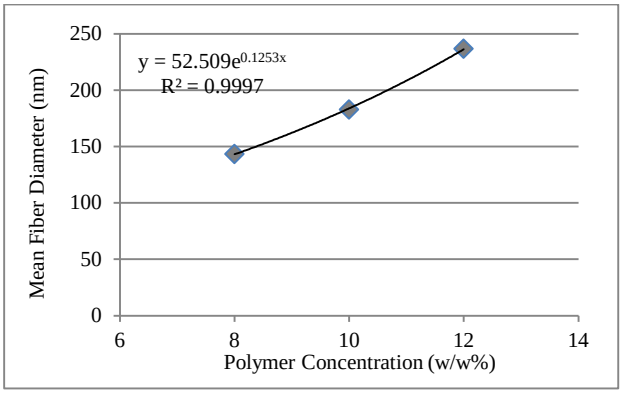

Figure B-2. Relation between the mean fiber diameter and polymer concentration

B.2 Effect of Polymer Feeding Rate on the Morphology of Nanofibers

One of the important operating parameters is the solution feeding rate. Experimental observations showed that fibers could not be formed until the feed rate reached 0.1 ml.hr^{-1}, due to the insufficient supply of solution. Figure B-3 shows the SEM images of three filters, which were fabricated at polymer concentration of 10%, applied voltage of 10 kV, tip-to-collector distance of 10 cm, and solution feeding rates of 0.1, 0.3, and 0.5 ml·hr^{-1}. The corresponding fiber size distributions using the developed automated method are also presented.

Fibers generated at the flow rate of 0.1 ml·hr^{-1} (Figure B-3 (a)) had a mean fiber diameter of 187 nm with a standard deviation of 74 nm. As the flow rate increased to 0.3 ml·hr^{-1} (Figure B-3 (b)), the fiber size distribution did not change significantly: the mean diameter and standard deviation of fibers were 183 nm and 72 nm, respectively. Thus, the extra flow rate resulted in more fibers, which increased the

solidity and basis weight of the filter. Figure B-3 (c) shows that, at the flow rate of 0.5 ml·hr^{-1}, undesired beads formed along the fibers. At a high flow rate, the solution did not have sufficient time for perfect polarization prior to ejection, which resulted in bead formation. The mean fiber diameter and standard deviation were 191 nm and 87 nm, respectively.

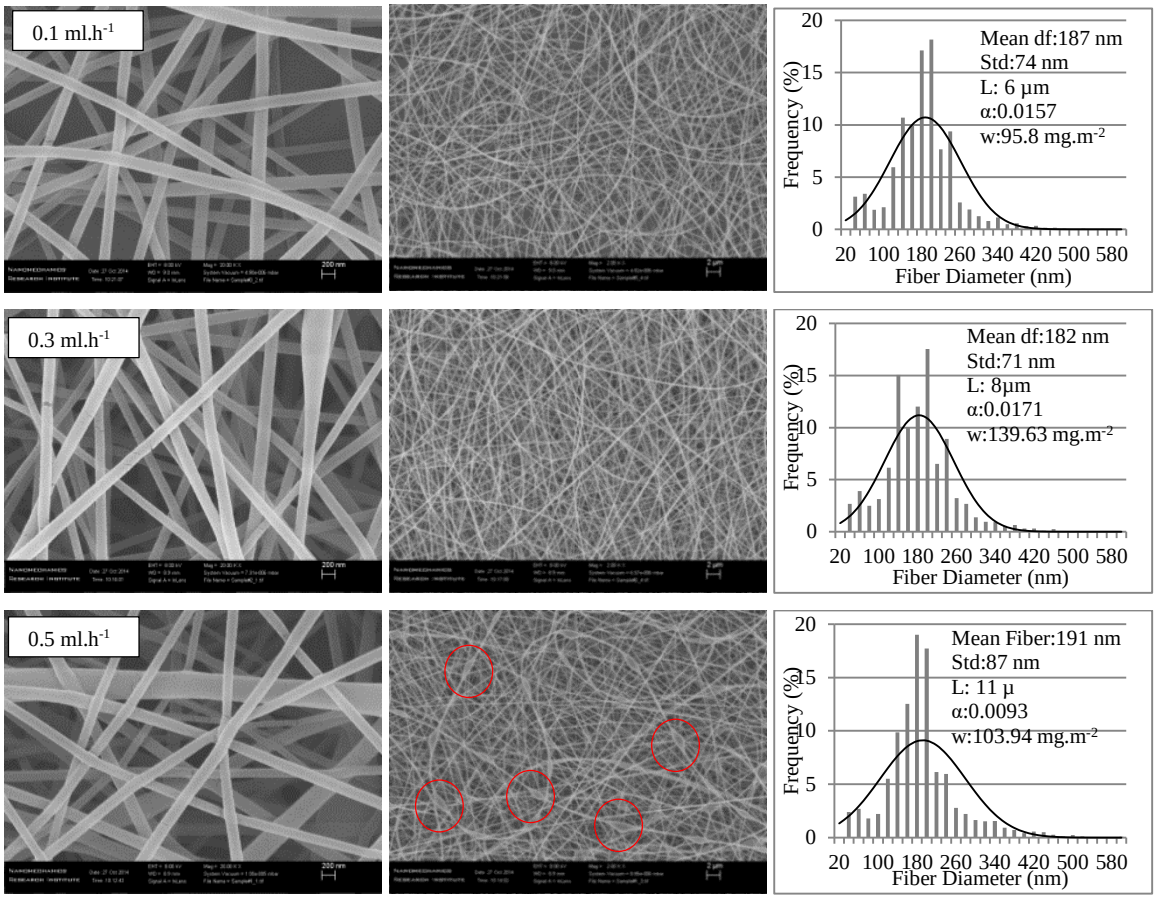

Figure B-3. SEM images and fiber diameter distributions of electrospun nanofibrous filters for solution feeding rates of 0.1, 0.3, and 0.5 ml.h^{-1}

Appendix C

MATLAB Code for Automated Method to Characterize SEM Images

The following is the code used to determine fiber size distributions. For this aim, the user needs to upload the SEM image in to the assigned folder and run the main file.

- **Main File**

% 1.Get the input image and resize properly (Based on SEM image size of 1024x768)

```
% Analyze the part of the SEM image with the scale to obtain the pixel length of the ruler  automatically
close all
clear all
file = 'Sample1.tif';
I = imread(file);
original = I;
% scale = imcrop(I, [800 682 224 78]);
[scale, noOfRegions] = bwlabel(scale, 4);

% Find the ruler:  it should be the object with the largest area
% Get the information about the image
measurements = regionprops(scale, 'Area', 'PixelList');
area = cat(1, measurements.Area);
[m, index] = max(area);
ruler = ismember(scale, index);

% Find the difference between the min and max X value to get the length
coordinates = measurements.PixelList;
x = coordinates(:,1);

% The measurement should actually start and end in the same position on the two opposite vertical lines.
% The correction is a measurement of the thickness of the bar and subtracting it so that the pixel length start from the left bar's first pixel, to the right bar's first pixel.
pixelDistance = range(x) - 2;
fprintf('The pixel length of the scale ruler is: %.2f pixels\n', pixelDistance)

scalevalue = input('Enter the scale (nm): ');
```

```
cannySensitivity = input(['\nEnter the Canny Border Detection sensitivity (0-0.999). \nThe lower the number, the easier matlab detects a region as an edge\n'...
   +'-If set less than 0.2 then a blurring filter will be done on the image (for high res)\n'...
   +'-If set above, no blurring is required (for low res)\nChoose 0.2 for high res images, and 0.21-0.3 for low res images: ']);

isBlur = false;
if cannySensitivity <= 0.2
   isBlur = true;
end

scale = pixelDistance/scalevalue;

% 2.Start the preprocessing image manipulation
I = imcrop(I, [0 0 1024 680]);
ASLI=I;

% 3. Initial noise reduction for the grayscale image
I = medfilt2(I);

% 4. Even out the contrast profile
I = imadjust(I);
I = histeq(I);

% 5. Noise Reduction
SE = strel('square', 2);
I = imclose(I, SE);
I = imopen(I, SE);
i = I;

% 6. Local thresholding method: This method goes to each pixel and processes the best threshold value for each pixel.
preprocessed = I;
BW = localthresh(I);
I = BW;

% 7. MAIN Noise Reduction
SE = strel('disk', 2);
I = imclose(I, SE);
```

```
I = imopen(I, SE);
I = bwmorph(I, 'majority');
I = bwmorph(I, 'clean');
BWreduced = I;

% Reverse colors of the binary image
I = imcomplement(I);

% 8. Store the edge profile of the image and combine with the binary image into N
        if isBlur
                i = gaussianFilter(i, 8);
        end
i = edge(i, 'canny', cannySensitivity);

% 9.Perfect the boundaries by first dilating (to seal openings) and thinning to reduce the edges to their
more accurate thickness
SE = strel('disk', 1);
i = imdilate(i, SE);
i = bwmorph(i, 'thin', Inf);
N = I | i;

% 10. Noise reduction. 'clean' gets rid of single pixel outliers
SE = strel('disk', 2);
N = imclose(N, SE);
N = bwmorph(N, 'clean');
N = imcomplement(N);
N = bwmorph(N, 'clean');
N = imcomplement(N);
withEdge = N;

% 11. Diameter Measurement
dist = bwdist(N, 'euclidean');
dist = dist*2/scale;

% 12. Create a skeleton image and use pruning to delete sporadic branches
skeleton = imregionalmax(dist, 4);
D = dist(find( skeleton == 1 ));

% 13.Display image with blue skeleton
```

```
% convert to rgb first
rgb = repmat(N, [1 1 3]);
rgb = cat(3, N, N, N);
rgb = repmat(double(N)./255,[1 1 3]);
finalImage = N | skeleton;
m = max(D);

% 14. Create the histogram from the measured distance data (radius x 2).
% Find the ranges necessary for plotting
range = 0:20:m-mod(m, 20)+20;
noOfRanges = length(range) -1;
frequency = zeros(1,noOfRanges);

% Store the diameters in the ranges
for i = 1:noOfRanges
   frequency(i)=length(find( D > range(i) & D < range(i+1) ));
end

% 15. Plot the data
figure('Position', [20 20 1200 760]), bar(range(2:end)-10 , frequency, 1)
endlimit = floor(range(end)/20)*20;
if mod(range(end), 20) > 0
   endlimit = endlimit + 20;
end
set(gca, 'XTick', [0:40:endlimit])
xlabel('Diameter [nm]')
ylabel('Frequency [%]')

disp('Press any button to see the sequence of image processing images')
pause
figure,imshow(preprocessed)
pause
NR=imcomplement(N);
BWreducedR=imcomplement(BWreduced);
FR=BWreducedR+NR;
F=imcomplement(FR);
figure, imshow(F);
pause
finalImageR=imcomplement(finalImage);
```

```
FINALR=BWreducedR+finalImageR;
FINAL=imcomplement(FINALR);
figure, imshow(FINAL);
```

- **Gaussian filtering**

```
function [ B ] = gaussianFilter( A, iterations )
        h = fspecial('gaussian', 6, 0.6) ;
        B = imfilter(A, h);
        for i = 2:iterations
                B = gaussianFilter(B, 1);
        end
end
```

- **Local thresholding**

```
function [ B ] = localthresh( A )
        w = 7;
        thickness = (w-1)/2;
        m, n] = size(A);
        B = zeros(m, n);
        k=0.3;
        I = zeros(m+w-1, n+w-1);
        I2 = zeros(m+w-1, n+w-1);
        [M, N] = size(I);
        int1 = integralImage(A);
        A2 = int64(zeros(m,n));
        A = int64(A);
        A2 = A.^2;
        int2 = integralImage(A2);
        I(thickness+1:M-thickness, thickness+1:N-thickness) = int1(2:end, 2:end);
        I2(thickness+1:M-thickness, thickness+1:N-thickness) = int2(2:end, 2:end);
        avg = mymean(I, w, M, N);
        S = mymean(I2, w, M, N);
        d = 0;
        for row = thickness+1:M-thickness
                for col = thickness+1:N-thickness
        std = sqrt(S(row, col) - (avg(row, col))^2);
       t = avg(row, col) * ( 1 + k*( std/128 - 1 ) );
                if A(row-thickness, col-thickness) <= t
```

```
                B(row-thickness,col-thickness) = 0;
            else
                B(row-thickness, col-thickness) = 1;
            end
        end
    end
end
```

In addition to the core contributions of thesis, the author also contributed to granular filtration (Appendix D), airborne nanoparticle sizing instrument development (Appendix E), and the application of nanofibrous filters to respiratory dust mask (Appendix F).

Appendix D
The Effects of Electrostatic Forces on Filtration Efficiency of Granular Filters[1]

D.1 Summary

The effect of electrostatic forces on the granular filtration of nanoaerosol NaCl particles in the range of 10 nm to 100 nm was investigated experimentally in this study. The test granular filters were made of 2 mm homogeneous glass beads at three media thicknesses (25, 76 and 127 mm), and they were tested at three air flow rates (23, 45 and 65 lpm). The filtration efficiencies were measured for neutralized and charged NaCl nanoparticles. The corresponding difference was considered as the filtration efficiency attributed to the electrostatic attraction between the charged NaCl particles and the glass granules. Results showed that the electrostatics played a great role in nanoaerosol filtration, which is different from conventional filtration theories. Its contribution to filtration efficiency increased with the size of the nanoparticles to a level of 30% or so. Results also showed a positive correlation between the filtration efficiency due to electrostatic forces and the residence time of the air flow. The correlation is relatively strong (between 0.6-0.9) for particles in the range of 20-100 nm. However, it is weak, although positive, for sub-20 nm particles.

D.2 Introduction

Clean air is a vital resource for human life. However, population growth, enhanced human activities, and the rapid expansion in industrial production have led to unprecedented demand on clean air all over the world. The report of the World Health Organization (2013) showed that over seven million premature deaths each year are attributed to air pollution. Among the air pollutants, nanosized aerosol (nanoaerosol) particles suspended in the air are proven to cause adverse impact on human health. In

[1] A similar version of this chapter was published as:

Givehchi, R., Li, Q., Tan, Z. (2015). The Effect of Electrostatic Forces on Filtration Efficiency of Granular Filters. *Powder technology*, 277:135-140.

addition, they also negatively impact on global climate change and extreme weather by interacting with the solar radiation. It is important to capture the nanoaerosol particles, at their sources and from the ambient air.

Among all of the technologies for removing nanoaerosol particles from their carrier gases, air filtration is the simplest and most widely used method. A great amount of works have been conducted with fibrous filters, membrane filters and fabric filters (Givehchi and Tan 2014; Kim et al. 2006; Wang and Otani 2013). However, much less attention has been paid to granular air filtration. Limited information has shown that granular air filtration has high removal efficiency for a wide range of particle size (Chen et al. 2009; Coury et al. 1987; El-Hedok et al. 2011; Golshahi et al. 2009; Wenzel et al. 2014). Granular filters may also be the only and promising option for air filtration at high temperature and high pressure (El-Hedok et al. 2011; Peukert and Wadenpohl 2001; Peukert and Löffler 1991; Saxena et al. 1985; Seville et al. 2003; Xiao et al. 2013).

The mechanisms of granular air filtration are similar to those of fibrous air filtration, except that the particles are deposited on surfaces of the granules. Among all the particle transport mechanisms, it has been widely accepted that diffusion is the dominant mechanism for removal of nanoparticles (1-100 nm in diameter), and the electrostatic effect is often ignored in conventional air filtration models that were developed based on single fiber theory (Lee and Liu 1982a; Yeh and Liu 1974), it is not certain for granular filtration. Aerosol particles and granules often carry electrostatic charges which may influence particle transport, and the consequent removal efficiency. The electrostatic forces between particles and granules may include image forces, dielectrophoresis due to collector charge, columbic force, space charge effect, columbic force due to external field, and dielectrophoresis due to external electric field. However, the columbic force due to particle charge and an external electrostatic field are the most dominated forces (Tien and Tien 1989).

Several researchers have employed external electric field in granular filtration to enhance the particle removal efficiency (Shapiro et al. 1986). The external electric field causes the granular beads to polarize. In this case, either neutral or charged particles are attracted to the polarized granules, leading to increased filtration efficiency. Particles travel a shorter distance in granular filters than in a conventional electrostatic precipitator to reach the collector surface. And, the collection surface area per volume of granules is larger than that of an electrostatic precipitator; therefore, the electrostatic

attraction effect is likely to increase the collision chance of particles and consequently filtration efficiency (Jaworek et al. 2007).

Although a number of studies have been conducted by considering external electric field to enhance electrostatic forces between micron sized particles and granular beads, there is very limited information about the effect of electrostatic forces on granular filtration of nanoparticles. In this work, experiments were carried out to investigate the effect of electrostatic forces on nanoaerosol filtration. The granular filters tested were made of uniform 2 mm glass beads at three media thicknesses of 25, 76 and 127 mm, and they were tested at three flow rates of 27, 45 and 65 liters per minute (lpm). The feed aerosol contained NaCl nanoparticles in the range of 10-100 nm.

D.3 Theoretical

The fractional filtration efficiency of a granular filter can be correlated with the single granule efficiency as (Shapiro et al. 1986):

$$\eta = 1 - \exp\left[-\frac{3}{2}\frac{(1-\varepsilon)}{\varepsilon}\eta_0\left(\frac{L}{d_g}\right)\right] \qquad \text{(D-1)}$$

where d_g is the granule diameter, L is the filter bed thickness, ε is the filter bed porosity, and η_0 is the single collector efficiency of the granular. The filter bed porosity of the filter is defined as follows (Pushnov 2006):

$$\varepsilon = 0.375 + \left(\frac{D}{d_g}\right)^{-2} \qquad for\ \ \frac{D}{d_g} > 2,\ L > 20d_g \qquad \text{(D-2)}$$

where D is the body diameter of the granular bed.

The single granule efficiency for nanoparticles based on diffusion and electrostatic attraction is defined as follows:

$$\eta_0 = 1 - (1-\eta_D)(1-\eta_E) \qquad \text{(D-3)}$$

where η_D and η_E are single granular efficiency due to Brownian diffusion and electrostatic forces, respectively. Tufenkji and Elimelech developed a model to calculate Brownian diffusion based single collector efficiency for each particle size as follows (Tufenkji and Elimelech 2004):

$$\eta_D = 2.4\, A_s^{\frac{1}{3}} \left(\frac{d_p}{d_g}\right)^{-0.081} Pe^{-0.715} N_{vdw}^{0.052} \tag{D-4}$$

where d_p is the particle diameter, d_g is the granular size, A_s is the porosity dependent parameter, Pe is the Peclet number, and N_{vdw} is the van der Waals parameter. A_s is defined as follows:

$$A_s = \frac{2 - 2(1-\varepsilon)^{\frac{5}{3}}}{\left[2 - 3(1-\varepsilon)^{\frac{1}{3}} + 3(1-\varepsilon)^{\frac{5}{3}} - 2(1-\varepsilon)^2\right]^{\frac{1}{3}}} \tag{D-5}$$

The Peclet number is defined as

$$Pe = \frac{d_g U}{D_i} \tag{D-6}$$

where D_i is the particle diffusion coefficient and U the superficial velocity. The van der Waals parameter is given by:

$$N_{vdw} = \frac{A_H}{KT} \tag{D-7}$$

where A_H is the Hamaker constant of interacting media (particles and granules). The Hamaker constant for glass beads is 0.85×10^{-19} J and that for NaCl particles is 0.79×10^{-19}J.

When charged particles pass through the granular filters, the single collector efficiency is enhanced by the electrostatic attraction. The charge states of particles and granules should be known in order to calculate the electrostatic forces. The calculation of single collector efficiency based on electrostatic forces needs complex trajectory analysis. For simplicity, Deutsch equation that was primarily developed for standard ESPs is employed. In this model, the electric field strength in granular filters is defined as the field induced by the net charge on the glass beads and aerosol particles (Shapiro et al. 1983). The single granule efficiency due to electrostatic force is then defined as (Guillory et al. 1981)

$$\eta_E = 1 - \exp\left[\frac{-2(1-\varepsilon)Lq_P C_c E}{\pi\mu U d_g d_P}\right] \tag{D-8}$$

where q_P is the particle charge, C_c is the slip correction factor, and E is the electric field strength. Eq.(D-8) shows that the single collector efficiency depends on the charge state of particles, glass beads,

and the electric field intensity. If the particles are charged to saturation, the maximum charge can be calculated as follows.

$$q_P = \frac{d_P K_b T}{2eK_e} \ln\left(1 + \frac{d_P K_e c_i \pi e^2 N_i t}{2K_b T}\right) \quad \text{(D-9)}$$

where c_i is the mean thermal speed of ions, K_b is Boltzmann constant, K_e is Columb's constant of proportionality, e is the electro charge, and N_i is the ion concentrations in the order of 5×10^{14} ions/m^3 (Tan and Wexler 2007).

D.4 Experimental Setup

Figure D-1 shows the experimental setup for measuring the removal efficiencies of the granular filters. A constant output atomizer (TSI model 3076) was used to generate polydispersed sodium chloride (NaCl) nanoparticles. The concentration of sodium chloride in the distilled water was 0.1 g/l as recommended by the manufacturer. A diffusion dryer (TSI model 3062) was used after the atomizer to dry the highly charged particles. Note that all aerosol particles carry charges after exiting the atomizer (Hoppel and Frick 1986). When these nanoparticles pass through the 20-mCi Po-231 neutralizer (NRD), the ions on the particles are neutralized and acquire Boltzmann equilibrium charge distribution. Without using the neutralizer, the charges on the nanoparticles cause electrostatic forces between the particles and filter collectors.

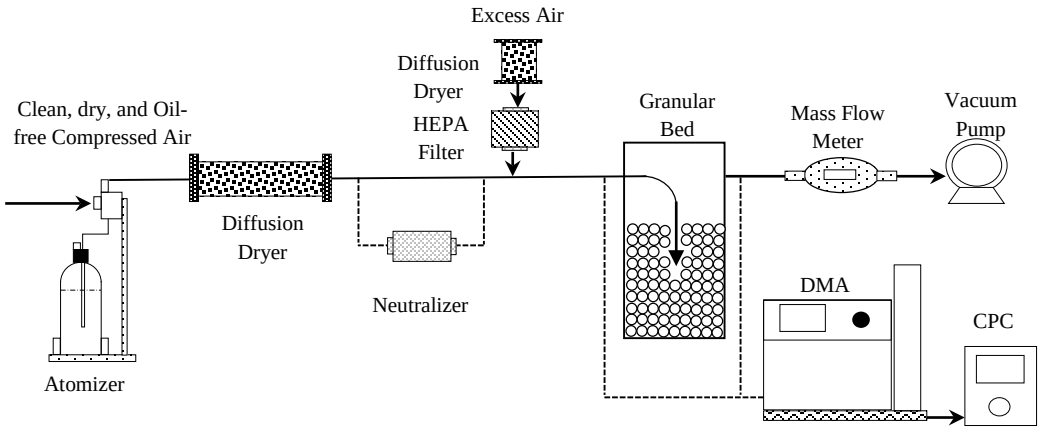

Figure D-1. Schematic diagram of experimental setup

Figure D-2 shows the schematic diagram of the cylindrical granular filter, which was the same as the one used by Golshahi et al. (2009). Air flow entered the filter from the bottom of the bed in a counter-current flow mode. There was a fixed height of 9 cm between the base of the filter unit and the level where the gas first interacted with the granules (h=0). This fixed thickness below h=0 was used to slow down the gas flow and it acted as a flow conditioner.

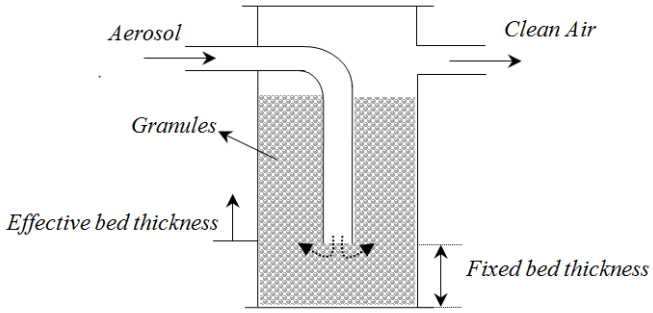

Figure D-2. Schematic diagram of the granular filter

The granular bed properties are shown in Table D-1. Glass beads with the uniform diameter of 2 mm in combination with three bed thicknesses (2.5, 7.6 and 12.7 cm) were used. The packed bed was purged for an hour prior to each experiment to allow the system to reach a steady state. Glass beads usually carry negative ions because of the free electrons in the air (Nieh and Nguyen 1988). While it is difficult to quantify the exact charges on the glass beads, it is expected to be profound when the air is pretty dry (RH<20%) in Calgary, Alberta, Canada. All the experiments were tested at room temperature (T=23 ^{o}C) to reduce the effect of temperature.

Table D-1. Granular bed properties

Granular filter parameter	**Value**
Granular size, d_g (mm)	2
Porosity, ε	0.375
Bed thickness, L (mm)	25, 76, 127
Flow rate, Q (lpm)	27, 45, 65

A thermal mass flow meter (TSI model 3063) meeting the criteria of the isokinetic sampling measured the main stream flow rate. A dust collector was used to make the system under vacuum condition and an opening was added after the aerosol generator to balance the air pressure in the system.

A scanning mobility particle sizer (SMPS) consisting of a long differential mobility analyzer (DMA) (TSI model 3081) and a condensation particle counter (CPC) (TSI model 3775) was employed to determine the particle concentration distribution. DMA was tuned for classifying particles in the range of 5.76 nm to 239 nm by adjusting the impactor nozzle to 0.075 cm. CPC was used to detect nanoparticles down to 4 nm in the range of 0 to 10^7 $particles/cm^3$. The sheath air flow to the sampling air flow was remained constant at 10, during all experiments.

The system was used both upstream and downstream the granular filters to determine the concentrations of particles before and after the granular filter. The fractional filtration efficiency of the granular filter is calculated by

$$\eta = \frac{C_{in} - C_{out}}{C_{in}} \times 100\% \qquad \text{(D-10)}$$

where C_{in} is the upstream particle concentration and C_{out} the downstream particle concentration. Both concentrations were measured at the inlet and the outlet of the granular bed. The removal efficiencies of granular filtration for nanoparticles were calculated by considering the average of three replications with the standard deviation of less than 2%.

The aerosol particle removal efficiencies were measured with and without employing the neutralizer by maintaining other factors constant. The difference between the filtration efficiency for charged and neutralized particles are attributed to the effect of electrostatic forces between charged particles and granular glass beads. It is deemed reasonable because it is the only factor that changes in the test for a certain particle size.

D.5 Results and Discussion

Figure D-3 shows the filtration efficiencies due to electrostatic force only. All the results show that the filtration efficiency by electrostatic attraction increased with particle size. The filtration efficiency by electrostatic attraction could increase to 20-30% when the particle diameter increased to 100 nm. This effect is much more profound than any other researchers reported in the past (Kim et al. 2006; Yun et

al. 2007). Almost all of other researchers concluded that the filtration efficiencies due to electrostatic forces are negligible for nanoparticles. For example, study on the electrospun filter for sub-80 nm NaCl particles showed that the nanoparticle removal efficiency is independent of charge state of particles, which showed the negligible effect of columbic force compared to the strong diffusive force (Kousaka et al. 1990; Yun et al. 2007). On the other hand, Kim et al. (2006) showed that the filtration efficiency of sub-100 nm sodium chloride particles is lower for uncharged particles than for charged particles at face velocity of 2.5 cm/s, and this discrepancy decreases with the decrease in the particle size. However, the discrepancy in their study is much lower than those shown in Figure D-3. The difference is likely related to differences in filter type and filter media.

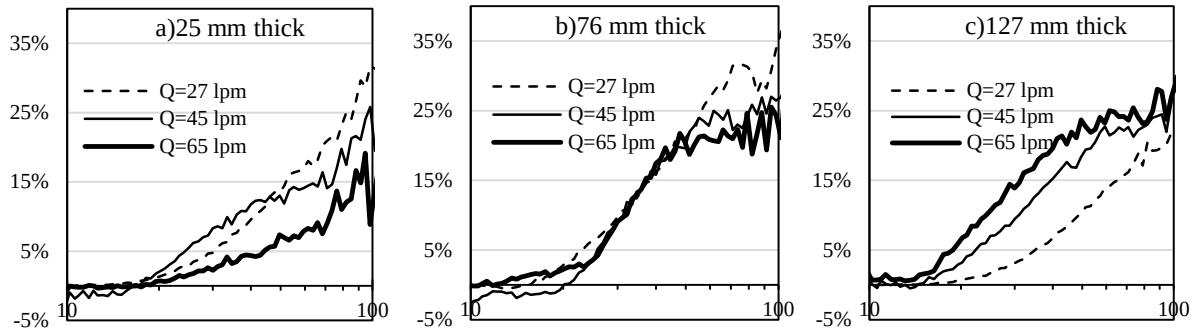

Figure D-3. Filtration efficiency for 2 mm glass beads at different media thicknesses and flow rates (x-axis is for particle diameter in nm; y-axis is for filtration efficiency due to electrostatic force)

D.5.1 Effects of particle size on electrostatic force

First of all, the filtration efficiency of sub-20 nm particles due to electrostatic attraction is negligible for most cases in Figure D-3, and even a closer examination shows the negative effect for most sub-20 nm particles. Therefore, the filtration efficiency of sub-20 nm particles is still dominated by diffusion. This agrees with conventional theory because of extremely small amount of ions that these small particles can be carried.

However, this may not be the case of larger nanoparticles. The filtration efficiency due to electrostatic forces increases to a maximum level of 30-35% when particle size increased to 100 nm. Results showed that the filtration efficiency of nanoparticles enhance if the neutralizer is not used, i.e. by the effect of electrostatic force. As most of nanoparticles generated by atomizer may carry positive ions and the

attraction force between positive particles and the negative glass beads is the dominant reason for the increase in the filtration efficiency.

One of the most important factors that contribute to the size dependent performance is the size-dependent charging and neutralization on nanoaerosol particles. First of all, although all aerosol particles carry charges after exiting the atomizer, there are only single ions (positive or negative) on the sub-20 nm particles. It is not enough to produce strong electrostatic forces. As indicated by Eq.(D-9), larger particles can acquire more charges leading to greater electrostatic forces in the same electrical field.

For nanoaerosol particles the analytical solution of the transient charging equation has been obtained following the Fuchs theory (Fuchs 1963). In this theory the space surrounding a particle was divided into two regions. In the outer region ions move according to the continuum diffusion equation, whereas in the inner region they move as in a vacuum, it means that they have no collision with air molecules. By assuming this ion attachment mechanism, Hoppel et al. (1986) showed that for aerosol particles smaller than 20 nm the probability that a particle acquires two or more net charges of either sign is practically zero. So there are only three different charges for aerosols below 20 nm: neutral, singly positive and singly negative. Alonso et al. (2002) recalculated the ion attachment rate coefficient of Fuchs theory (Fuchs 1963) for the particle diameter range between 2 nm and 20 nm with using the values of ionic mass of $m^+ = 150\ amu$ and $m^- = 80\ amu$, and ion mobilities of $Z^+ = 1.15\ \mathrm{cm}^2/\mathrm{v.\,s}$ and $Z^- = 1.65\ \mathrm{cm}^2/\mathrm{v.\,s}$ (Alonso et al. 2002). So the probabilities (denoted as *P*) of the ion attachments onto the neutral, positive and negative particles are as follow:

$$P^{+0} = 2.19 \times 10^{-9}\ d_P^{1.51} \tag{D-11}$$

$$P^{-0} = 3.02 \times 10^{-9}\ d_P^{1.51} \tag{D-12}$$

$$P^{+-} = (5.68 + 3.38\ d_P - 0.522\ d_P^2 + 0.042 d_P^3 - 0.0017 d_P^4 + 0.000027 d_P^5) \times 10^{-7} \tag{D-13}$$

$$P^{-+} = (2.15 + 4.20 d_P - 0.526 d_P^2 + 0.038 d_P^3 - 0.0014 d_P^4 + 0.000020 d_P^5) \times 10^{-7} \tag{D-14}$$

For example, P^{+0} shows the probability of attaching the positive ion to the neutral particle. Figure D-4 shows the probabilities of the ion collision onto the particles vs. the diameter of particles by the Alonso theory. As seen from this chart, the probability of attachment of negative ions into positive particles is greater than the probability of attachment of positive ions into negative particles. Besides,

the probability of attachment of negative ions into neutral particles is greater than the probability of attachment of positive ions into neutral particles. So at the end of the neutralizing process negatively charged particles are predominant over positive ones for particle smaller than 20 nm. Since the glass beads carry negative ions, the removal efficiencies for particles smaller than 20 nm were likely reduced because the glass beads tend to repel the incoming aerosol particles.

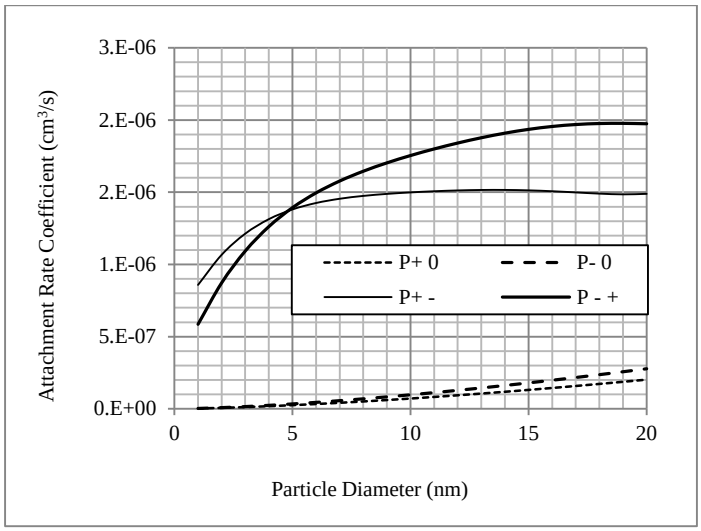

Figure D-4. Diagram of charging probability via particle diameter

On the other hand, researchers examined the positive unipolar diffusion charging in the range of 50-200 nm (Hogan Jr. et al. 2009). They showed that particles can get more net charges by increasing the size of them. For instance, the 200 nm particle can get eleven positive ions. So the electrostatic forces cause larger particles to be removed at a high efficiency with the present of electrostatic forces.

Marlow et al. (1975) demonstrated that there was a significant difference in polarity between the larger and smaller ones, when particles pass through the same bipolar charger (Marlow and Brock 1975), which is the neutralizer in this study. In the charging process of polydispersed particles, due to unequal charging rates, large and small particle may show different polarities. Since the polarity of the collector in the packed bed was certain, there must be a repulsive force for either large or small particles.

So by the above analysis we concluded that during the process of neutralizing, particles below smaller than 20 nm get different charges from the larger ones and because of this they have shown different behaviors through filtration. Small particles have the same charges as granules so the electrostatic

forces might have adverse effect on filtration efficiency. On the other hand, larger particles and granules have different charges so the electrostatic forces increase the filtration efficiency.

D.5.1 Effects of air flow on electrostatic force

Figure D-3 does not show obvious trend for dependency of filtration efficiency based on electrostatic forces on aerosol flow rate. Figure D-3a shows that the high air flow rate (65 lpm) corresponds to the lowest efficiency by electrostatic attraction; however, Figure D-3c shows the opposite trend: the higher air flow rate corresponds to the lowest filtration efficiency by electrostatic attraction. And the difference in filtration efficiency by electrostatic attraction in Figure D-3b is negligible. Since the charges carried by the aerosol particles are assumed to be stable and consistent during the tests, these results indicate that the filtration efficiency due to electrostatic forces depends on the air flow speed and the bed thickness. To understand the mechanism behind this discrepancy, the results were presented in terms of characteristic residence time, which is defined as

$$\tau = \frac{HA}{Q} \tag{D-15}$$

where A is the cross section area of the air flow, H the bed thickness, and Q the air flow rate. Since the area of the test apparatus was the same all the time, we can use H/Q as an indicator of the residence time. The particle separation efficiencies due to electrostatic force at different H/Q values are shown in Figure D-5 below. There is an overall trend that the effect of electrostatics increases with the residence time. This agrees with theoretical analysis in Eq.(E-8) above, which shows that higher air speed leads to lower residence time, and lower efficiency due to electrostatic attraction. It is physically plausible because, like what happens in a plate electrostatic precipitator, a longer resident time allows more particles to be precipitated on the collector surface.

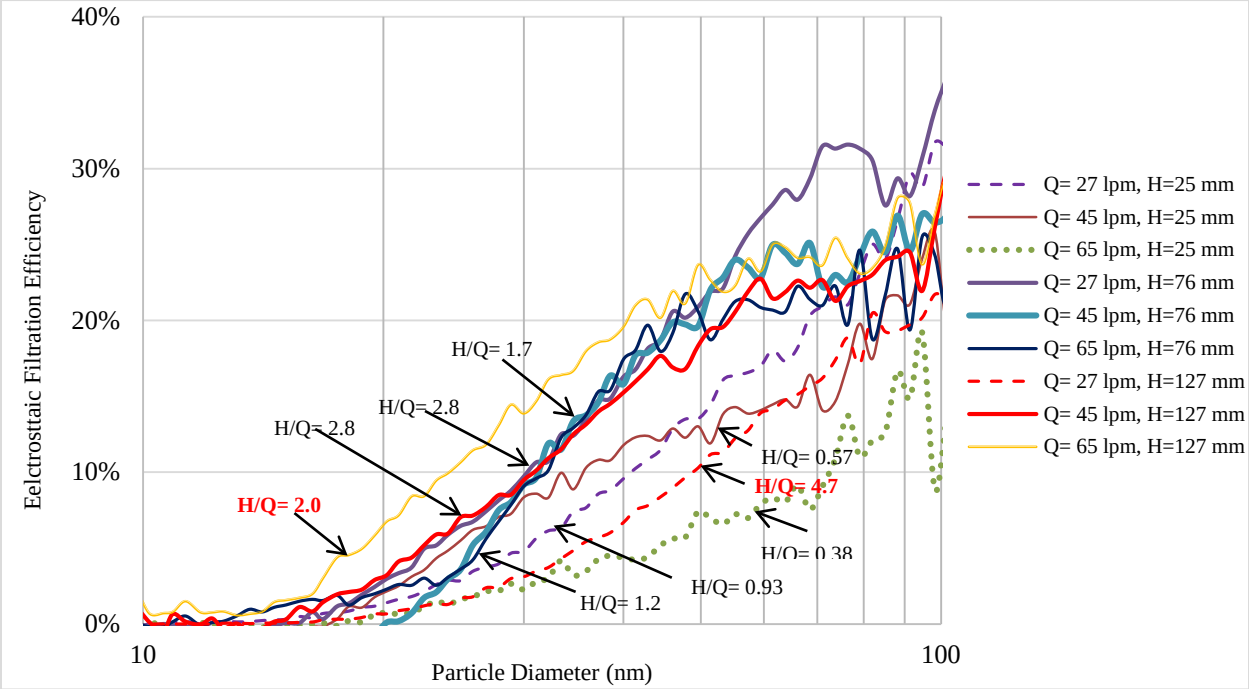

Figure D-5. Effect of residence time on the efficiency due to electrostatic forces

On the other hand, the same conclusion cannot be made quantitatively. A closer examination would reveal that some curves crossed each other. Furthermore, two of these nine curves do not support the conclusion, one is for $H/Q = 4.7$ (mm.min/l) and the other $H/Q = 2.0$ (mm.min/l). It indicates that there were some measurement errors in this experimental data. Therefore, a statistical analysis was conducted to quantify the correlation between residence time indicated by H/Q (except for $H/Q = 2, 4.7$ (mm.min/l)) and the particle separation efficiency at each particle size in the range of 10-100 nm.

Figure D-6 shows the correlation between particle residence time and the particle separation efficiency for particles in the range of 10-100 nm. Overall, the correlation is always positive, which quantitatively supports the conclusion above that the particle separation efficiency due to electrostatic forces increases with air flow residence time. The correlation factor is weak with an obvious fluctuation for particles between 10 nm and 20 nm. It means that the electrostatic force does not affect the particle removal efficiency in this range, and only the diffusion efficiency is dominant. Also, it is likely that other factors also affected the performance in this size range. The correlation factor is between +0.6 and +0.9 for particles in the size range of ~20-80 nm with an overall increase with the particle size.

Interestingly, results showed that the correlation factor decreases form about 0.7 to 0.5 (although still positive and relatively high) as the particle size increases from 80 nm to 100 nm. Thus, the results showed that the residence time may have more effects on particles in the rage of 20-80 nm rather than larger ones. These phenomena may be due to the effect of other mechanisms for particle removal efficiency such as interception which may be more dominant than electrostatic forces. More investigations are needed in order to better understand the reasons behind this phenomenon.

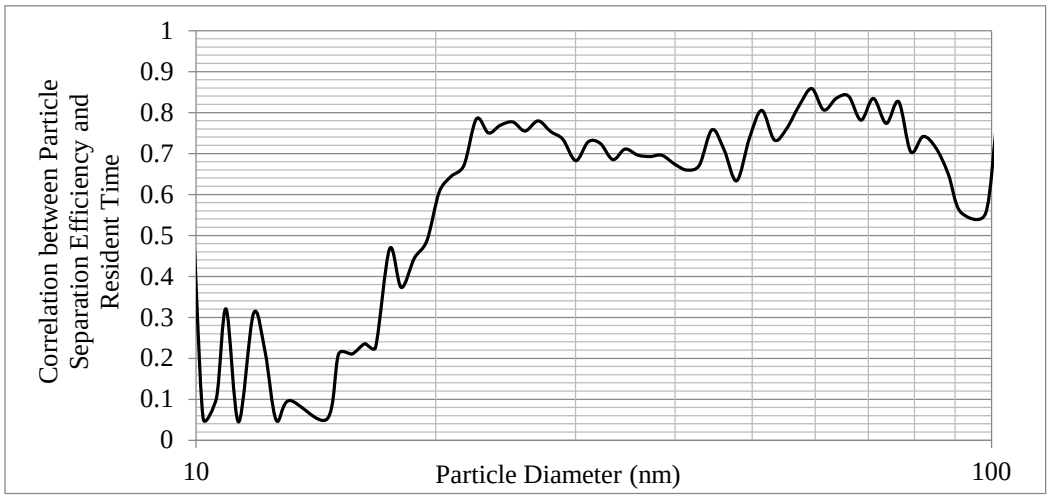

Figure D-6. Correlation between particle efficiency and residence time for particles in the range of 10-100 nm

D.6 Conclusion

The following conclusions can be drawn from the study in this paper. First of all, electrostatic force plays an important role in granular filtration using glass beads for nanoaerosol particles. Experimental data show that the electrostatic force has a positive effect on the filtration efficiency of nanosized particles. The efficiency due to electrostatic forces increased to a level of 30% when the particle sizes increased from 20 to 100 nm. Its effect on sub-20 nm particles was negligible, and sometimes negative, because these particles carry only single ion or negative ions.

In addition, there was a positive correlation between the separation efficiency due to electrostatic forces and the residence time of the air flow. The correlation is relatively strong (between 0.6 and 0.9) for particles in the range of 20-100 nm. However, it is weak for particles smaller than 20 nm.

Appendix E
Submicron Particle Sizing by Aerodynamic Focusing and Electrical Charge Measurement[1]

E.1 Summary

Principles of a novel submicron particle sizing technology are first introduced followed by experimental validation. The sizing was accomplished by coupling aerodynamic particle focusing and maximum ion measurement. Experimental results showed that the prototype could detect particle sizes down to 40 nm in diameter. Comparison between the prototype and a scanning mobility particle sizer using identical polydispersed particles showed that the measurements agreed well for the tested particles.

E.2 Introduction

The majority of airborne particles are smaller than 1 micrometer in diameter in various environments (Weimer et al. 2009; Whitby 1978; Yao et al. 2012; Zhang and Zhu 2012). Some of these particles are produced by both condensation and fuel combustion processes (Jung et al. 2006; Van Dijk et al. 2011; Wallace et al. 2004; Yin et al. 2012). Increasing amount of nanoparticles with recent rapid development of nanotechnology has also raised the concerns of potential negative impact on human health and the environment (Chow and Watson 2007; Ji et al. 2010; Lin et al. 2009; Mauderly and Chow 2008; Mengersen et al. 2011; Nazaroff 2004; Oberdörster et al. 2007; Torkmahalleh et al. 2012; Wang and Pui 2011). There are significant indications that submicron particles, especially nanosized ones, are more toxic than larger ones because of their small sizes and large surface areas (Oberdorster et al. 1995; Oberdörster et al. 2007; Roduner 2006; Shin et al. 2007).

Various technologies have been developed for the measurement of particle number concentration distribution (PSD); a comprehensive overview of micron and nanosized particle measurement methods

[1] A similar version of this chapter was published as:

Tan, Z., Givehchi, R., Saprykina, A (2015). Submicron Particle Sizing by Aerodynamic Focusing and Electrical Charge Measurement. *Particuology*, 18:105-111.

was given by Sabbagh-Kupelwieser, Maisser, and Szymanski (2011). Generally speaking, optical measuring methods work for aerosol particles larger than 100 nm; smaller ones are detected by electrical methods. An example of the latter is the well-known scanning mobility particle sizer (SMPS). It is able to measure particle number concentration distribution from 2 nm to a few microns with a high efficiency and high resolution with duration of between 3 and 5 min for a single measurement (Wang and Flagan 1990). SMPS consists of an electrostatic classifier with a differential mobility analyser (DMA) (Knutson and Whitby 1975) and a condensation particle counter (CPC). Particles of different sizes are classified based on their electrical mobility and they are counted by CPC using the light scattering technique (Kulkarni et al. 2011). Watson et al. (2011) compared four scanning mobility particle sizers in field and showed that they performed differently because of the differences in particle charging efficiency, CPC counting efficiency, diffusion losses, and non-ideal DMA transfer functions. In addition, SMPS usually costs more than other alternatives and it mainly aims at applications in a laboratory environment because of flammable and expendable liquid used in operation and a vibration-free environment.

There are also a few alternative technologies for submicron airborne particle measurement. SMPS+E substitutes CPC with a Faraday cup and an electrometer. It measures particle number concentrations in the size range of 0.8 nm to 1.1 μm. Electrical low pressure impactor (ELPI) employs aerosol corona charging and a cascade low pressure impactor to measure particle sizes in the range of 30 nm to 10 μm in real time (Keskinen et al. 1992; Marjamäki et al. 2000). However, ELPI showed poor size resolution for sub-30 nm particles, especially at high concentration (Ouf and Sillon 2009; Virtanen et al. 2001). Aerosol particle mass analyzer (APM) classifies particles according to their mass to charge ratio. APM consists of two rotating coaxial cylindrical electrodes which rotate at the same angular velocity (Ehara et al. 1996; Olfert and Collings 2005). It could detect particles down to about 50 nm. Fast integrated mobility spectrometer (FIMS) has been developed for measuring the particle number concentration distribution in the range of 15 to 170 nm for low particle number concentration, and there was good agreement with SMPS for particles larger than 20 nm in diameter (Kulkarni and Wang 2006; Olfert et al. 2008).

While it is tedious and challenging to list all existing technologies and devices for submicron particle sizing, it is safe to conclude that they can size the airborne submicron particles with different resolutions

and accuracies; their lower limits vary from a few nanometers to tens of nanometers. Each of them has advantages and disadvantages in terms of accuracy, resolution, responding time and cost as well as application environment. In general, none of the conventional technologies allow for the optimal combination of high efficiency, easy access, quick response and low cost (Friedlander and Pui 2004). Therefore, there is still a need to improve the performances of existing technologies or to develop alternative ones for the measurement of particle number concentration distribution (Sabbagh-Kupelwieser et al. 2011).

The work in this paper is inspired by that of Tan and Wexler (2007), who introduced another approach to sub-300 nm particle sizing by aerodynamic particle focusing coupled with diffusive charging. However, there was an error in the theoretical analysis part leading to wrong algorithm. The Coulomb constant was missing in Eq.(5) in that paper. More importantly, the instrument based on their algorithm relies on experimental calibration against another standard instrument (e.g., SMPS) to obtain two key coefficients for data processing. As such, the instrument could not perform particle sizing independently. This paper starts with an alternative theoretical analysis followed by an experimental evaluation of a prototype with state-of-the-art data collection systems. In addition, error sources are identified and taken into consideration in the performance evaluation of the prototype.

E.3 Theoretical

Considerable work has focused on aerodynamic particle focusing since it was first developed (Liu et al. 1995a; Liu et al. 1995b). In this type of device with multiple stages of focusing orifices, particles of decreasing diameter are focused along the axis with downstream the focusing orifice (Vidal-de-Miguel and de la Mora, Juan Fernandez 2012). Numerical works are also listed by Headrick et al. 2013.

In our approach, the sizes of particles are determined by aerodynamic particle focusing and the particle numbers by measuring maximum charge. In order to determine the maximum charge, these particles are passed through a charger where sufficient amount of ions are present. Aerodynamic particle focusing (APF) has been developed and employed for accurate particle characterization (Wexler and Johnston 2001). A well designed focusing orifice could isolate particles down to a few nanometers (Phares et al. 2002). Large particles cross the center line due to great inertia and small ones with low inertia do not cross the center line. The optimally focused particle size by a focusing orifice can be described as (Mallina et al. 2000)

$$\mathrm{d}_p^* = \frac{\left(\mathrm{d}_p^m\right)^2}{2\lambda C_c} \tag{E-1}$$

where λ is the mean free path of the carrier gas; Cunningham correction factor C_c can be calculated by

$$C_c = 1 + 1.66Kn \tag{E-2}$$

where Kn is the Knudsen number and the diameter of the optimum focused particle d_p^* is described as (Dahneke et al. 1982; Mallina et al. 2000; Middha and Wexler 2003)

$$\mathrm{d}_\mathrm{p}^* = \sqrt{(1.657\lambda)^2 + \left(\mathrm{d}_\mathrm{p}^\mathrm{m}\right)^2} - 1.657\lambda \tag{E-3}$$

The maximum size of the focused particles d_p^m is a function of critical Stokes number Stk^*,

$$d_p^m = \frac{18\mu d_f Stk^*}{\rho_{p.} v_f} \tag{E-4}$$

where ρ_p is the density of particle, μ is the viscosity of gas, d_f is the focusing orifice diameter and v_f is the average velocity in the focusing orifice exit plane. Gas velocity in the focusing orifice should reach sonic speed for enabling aerodynamic focusing of a certain-size particle. The critical Stokes number Stk^* is based on the gas properties at the orifice throat. The value of Stk^* has been numerically determined to be between 1 and 2 (Mallina et al. 2000) and experimentally determined to be around 2 (Phares et al. 2002). It does not depend on the pressure of the carrier gas.

The analysis above indicates that optimally focused particle size d_p^* depends on the mean free path of the carrier gas and the maximum focused diameterd_p^m. d_p^m varies with the focusing orifice diameter, the gas viscosity and the gas velocity through the orifice. From an engineering practice point of view, it is more challenging to alter the focusing orifice diameter or the gas velocity through the orifice than to control the size of the optimally focused particles by changing the gas mean free path, which can be done by adjusting the upstream gas pressure.

The mean free path of the carrier gas can be calculated following gas molecular dynamics (Bird, 1994):

$$\lambda = \frac{\mu}{P\sqrt{2M/\pi RT}} \tag{E-5}$$

where R is the universal gas constant, T is temperature, P is pressure, and M is the molecular weight of the carrier gas. This equation indicates that the mean free path λ of the carrier gas before the focusing orifice can be expressed in terms of its corresponding macro-scale parameters, temperature and pressure, which can be measured. Substituting Eqs. (E-4) and (E-5) into Eq.(E-3) gives

$$d_p^* = \sqrt{\left(\frac{1.657\mu}{P\sqrt{2M/\pi RT}}\right)^2 + \left(\frac{18\mu d_f Stk^*}{\rho_P v_f}\right)} - \frac{1.657\mu}{P\sqrt{2M/\pi RT}} \tag{E-6}$$

A particle can also be charged with ions and the maximum number of ions n_m that a particle can be charged is directly related to the particle size. Therefore, the particle size can be correlated with its maximum number of ions loaded. The maximum number of ions that a particle can be charged is described as (White 1951)

$$n_m = \frac{d_p^* kT}{2e^2 K_e} \ln\left(1 + \frac{d_p^*.K_e.v_i.\pi e^2.N_i.t}{2kT}\right) + \frac{E\left(d_p^*\right)^2}{4eK_e}\left(\frac{3\varepsilon_r}{2+\varepsilon_r}\right)\left(\frac{t}{t+\tau}\right) \tag{E-7}$$

where the first term on the right hand side (RHS) accounts for diffusion charging mechanism and the second term of RHS is for field charging mechanism. For submicron particles, diffusion charging mechanism is dominant and the last term in Eq.(E-7) can be ignored in most cases. Then the maximum number of ions charged onto a submicron particle can be described as

$$n_m = \frac{d_p^* kT}{2e^2 K_e} \ln\left(1 + \frac{d_p^* K_e v_i \pi e^2 N_i t}{2kT}\right) \tag{E-8}$$

where v_i is the mean thermal speed of ions (240 m/s at standard condition), k is Boltzmann constant (1.38×10^{-23} J/K), K_e is a Coulomb's constant of proportionality ($1/(4\pi\varepsilon_0) = 9\times10^9$ Nm^2/C^2), e is the elementary unit of charge (1.6×10^{-19} C), and N_i is ion concentrations and it is typically in the order of 5×10^{14} ions/m^3 (Tan and Wexler 2007).

In practice, it is nearly unlikely to count the actual number of ions charged on particles. This information is commonly determined by measuring the current of a stream of moving particles that carry these ions. The number of ions carried by the aerodynamically focused particles can be correlated

to the electrical current produced by these ions, which can be detected by a Faraday cup connected with an electrometer. The measured current is proportional to the number of particles that reach the cup and the maximum charge on the focused particle, $I = N_p^* Q n_m e$, and it gives

$$N_p^* = \frac{I}{Q n_m e} \tag{E-9}$$

where N_p^* is the particle number concentration $(\#/m^3)$ of the optimally focused particles by focusing orifice and Q (m^3/s) is the gas flow rate in the focusing orifice. This equation indicates that the number concentration of particles that were optimally focused can be determined by measuring the electrical current and the number of ions (calculated by Eq.(E-8)). Substituting Eq.(E-8) into Eq.(E-9) gives

$$N_p^* = \frac{I}{\frac{d_p^* kTQ}{2eK_e} \ln\left(1 + \frac{d_p^* K_e v_i \pi e^2 N_i t}{2K_b T}\right)} \tag{E-10}$$

Most of the parameters in this equation can be determined. The particle diameter is determined by aerodynamic particle focusing above Eq.(E-6). The others are constants or operating parameters. The ion number concentration and charging time depend on the specific particle charger. The device-specific information is introduced in the next section.

E.4 Experimental

E.4.1 Experimental setup

Figure E-1 shows the schematic diagram of the experimental setup for evaluating the performance of a laboratory prototype that was designed following the principles introduced above. Feed aerosol particles were generated using a constant output atomizer (TSI model 3076) with a concentration 0.1 g/L of NaCl in fresh distilled water. Diffusion dryer (TSI Model 3062) was used to remove the moisture from the produced aerosols. Feed aerosols were then neutralized by a neutralizer that employed a radioactive source ^{210}PO (NRD, Model P-2031) and the number concentration distribution of these feed particles were first characterized by a scanning mobility particle sizer (SMPS, Model 3936, TSI Inc.). Then these particles were charged by passing through a home-made corona charger before being directed into a low pressure channel through a pressure reducing orifice. Finally, they are passed through a focusing orifice where only particles with certain sizes are selectively focused to the aperture

of a Faraday cup, which was connected to an electrometer for electric current measurement. Other particles were pumped away by a vacuum pump. The size distribution was then calculated using the equations introduced in last section. Specifications of each component are elaborated in the sections that follow.

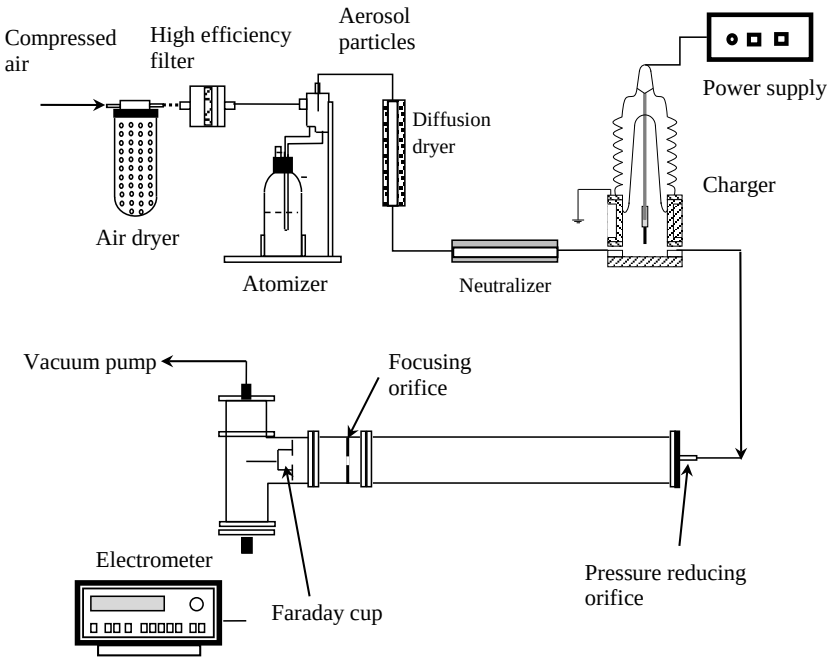

Figure E-1. Experimental setup for evaluation of the performance of the prototype

E.4.2 Corona charger

Figure E-2 shows the schematic diagram of the home-made needle-plate corona charger. The active electrode of the corona charger was a gold needle with a sharp cone-shaped tip. The top of the needle was connected to a stainless steel rod mounted into a ceramic isolator. The internal diameter of the bottom stainless steel plate (D_c) was 37.5 mm. The distance between the plate and the needle tip (δ) was 12.7 mm, allowing air to pass through the corona while ions were polarizing the surrounding air molecules. A high-voltage power supply (Glassman high voltage Model PS/EL30R01.5) was employed to supply an electric potential in the range of ±30 kV.

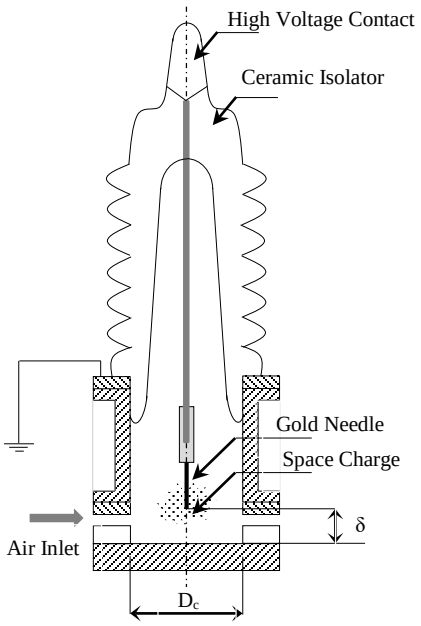

Figure E-2. Schematic diagram of the needle-plate corona charger

There have been various particle charging technologies and devices available. In this work the home-made corona charger was employed to show the feasibility of the principles introduced in theoretical section. However, it does not guarantee the best charging performance because optimum particle charging technology is not the main scope of this paper. Preliminary trials showed that positive charging was preferred in favor of the low particle loss effect in the corona charger (Saprykina 2009). The supplied voltage must reach a level that is high enough to ensure maximum charging with least error input and to avoid the electrical breakdown of the air. The corresponding charging time of this specific charger can be determined by

$$t = \frac{D_c}{V_g} = \frac{2\delta D_c^2}{Q_0} \tag{E-11}$$

where V_g is the air flow speed and δ is the distance between the plate and the needle tip. It has been speculated that the needle-plate corona charger like this could produce extra nanosized particles (Tan and Wexler 2007), and this may result in an error when it is employed to measure the sizes of nanosized particles. Therefore, particle generation in this charger was characterized to understand the errors resulted from the charger itself.

The experimental setup for the characterization of particle generation in the corona charger is different from that in Figure E-1. Air was first passed through a high-efficiency particulate air (HEPA) filter before entering the corona charger. The particle concentrations with and without power supply were measured using the same scanning mobility particle sizer (SMPS, Model 3936). The difference between the particle concentration measurements with and without power supply was considered as the level of particle generation, if any. In presentation of the result, the electric field at the tip of the needle is used instead of the voltage applied to the corona charger. It can be calculated as follows (Florkowska and Wlodek 1993).

$$(\zeta) = \frac{2U}{\ln(\frac{4\delta}{r_t})} \cdot \frac{1}{2\zeta + r_t - \frac{\zeta^2}{\delta}} \quad \text{(E-12)}$$

where ζ is the distance from the needle tip (ζ = 0 at the tip of the needle), U is the applied voltage, r_t is the radius of curvature of the corona needle (r_t = 0.25 mm for the setup herein).

Another potential error source is the loss of particles in the corona charger by electrostatic precipitation effect. To quantify the particle loss effect of the corona charger, if any, a correction coefficient (k) was experimentally determined to take this factor into account. This correction coefficient is defined as the ratio of number of particles entering and leaving the charger. To quantify this correction factor, polydispersed sodium chloride particles produced by the same aerosol generation system (see Figure E-1) were passed through the corona charger at a voltage of 0 kV and at the required voltages for maximum charging of the particles. The correction coefficient is used to relate the measured data by the new prototype to the actual particle number concentration independently without employing another device.

E.4.3 Aerodynamic particle focusing

A group of pressure reducing orifices (0.026, 0.022, 0.02, 0.018, 0.016, 0.014, 0.012, 0.01, 0.08, and 0.06 inches in diameter) were used to adjust the pressure of the carrier gas before the focusing orifice. Stainless steel tube was used as a low pressure region. Similar to what was done by Tan and Wexler (2007), the distance (L) between the pressure reducing orifice and the focusing one was 600 mm. This region is deemed long enough to obtain a well-mixed aerosol flow pattern.

The diameter of the focusing orifice was fixed at 3 mm and its thickness was 0.5 mm. Air flow reaches sonic speed if the downstream pressure reaches 52.8% of the upstream pressure (John and Keith 2006). The focal point of the optimum sized particles was at the aperture of the Faraday cup. Particles of different sizes from the selected optimum ones are pumped away by a vacuum pump. Therefore, theoretically only particles of the certain size are picked out from the suspending gas and focused into the Faraday cup.

F.4.4 Current measurement and maximum charging

Downstream the focusing orifice, the current coming to the Faraday cup was measured by an electrometer (Keithley Model 6430) connected via coaxial cable to Faraday cup to measure currents down to 10^{-17} A. The electrical current was generated by hitting the charged particles into the metal grid of the Faraday cup. The distance between the focusing orifice and the aperture of the Faraday cup was 14 mm. Trial tests showed that the focused particles were not observed when the distance was shorter than 14 mm, while for the distances larger than 14 mm there was significant loss of the focused particles.

Preliminary tests were also conducted to make sure that particles reached their maximum charging. Some basic experiment volt-ampere data was recorded to determine the required voltage for maximum particle charging. Results showed that the supplied voltage of approximately 4 kV in the corona charger was required to satisfy the maximum particle charging. Current measured did not increase any further with higher voltage, which means a greatest ion concentration. As a result, the particles exiting through the corona charger acquired the maximum charges for voltages greater than 4 kV. Since the particles reached maximum charging, Eq.(E-8) can be used to determine the number concentration of focused particles.

E.5 Results and Discussion

E.5.1 Checking nanoparticle generation in the corona charger

The numbers of particles generated by the corona charger by passing the filtered air were measured by SMPS at different applied voltages or electric filed. It was found that nanoparticles were generated by corona charging section when the supplied voltage was higher than a certain threshold value for the

corona charger. Figure E-3 shows the average size distribution of the nanoparticles generated in the corona charger operated at different voltages. The results indicate that the threshold voltage value for generating nanoparticles was about 7 kV corresponding to an electric field of 10,538 kV/m. The SMPS could not detect any particles when the supplied voltages were less than the mentioned threshold voltages.

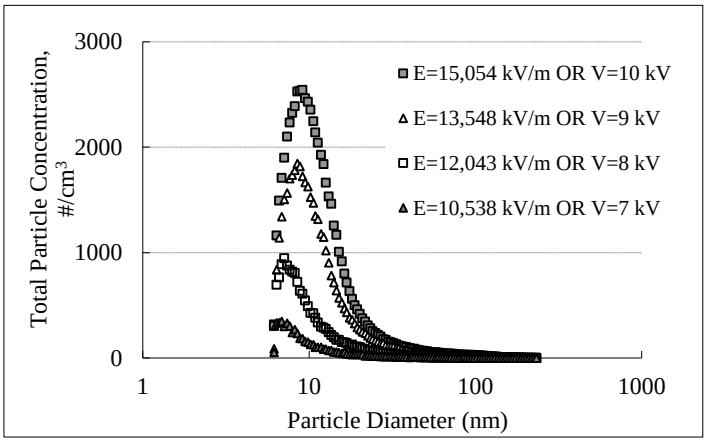

Figure E-3. Generation of particles in the filtered air with a volume flow rate of 1.4 lpm

A possible explanation of the generation of nanoparticles by the corona charger is that a corona charger has enough energy to initiate gas-phase chemical reactions in the charger region, such as the formation of ozone from oxygen, which may lead to particle generation (Romay et al. 1994). The sputtering of metal from the surface or the erosion of the electrodes could also cause particles to be generated (Liu et al. 1987; Romay et al. 1994). Unnecessarily high corona voltage intensifies the corona discharges, which facilitate the expansion of the active corona so that it occupies additional space between the needle and the plate (Chang et al. 1991). Therefore, the higher the voltage, the greater the erosion or chemical reactions, which increase the size and number of the particles generated around the peaks.

The positive corona produces nanoparticles with peak diameters of approximately similar sizes, which increase slightly with greater electric fields. The number of nanoparticles generated rises dramatically with an increased electric field. Hernandez-Sierra, Alguacil, and Alonso (2003) reported that the required voltages for a corona charger to generate ions are approximately 3.2 kV for a positive

corona charger. For greater voltages, the ion number concentration is approximately constant because of the greater electrical mobility and the electrostatic deposition loss (Hernandez-Sierra et al. 2003). Thus, in the present study, increasing the supplied voltages would not affect the concentration of ions generated; it changed only the concentration of nanoparticles generated.

Nanoparticles have special aggregation characteristics caused by the known van der Waals forces because of their small size. The attractive interactions between the nanoparticles are increasing when the particles are moving toward each other due to their natural tendency (Hakim et al. 2005). This also helps explain the uncertainty and less accuracy in the measurement of the size distribution in this range in the work of Tan and Wexler (2007). Nonetheless, the generation of particles was negligible when the operating voltage was below 7 kV.

E.5.2 Checking nanoparticle loss in the corona charger

Figure E-4 shows the size distribution of sodium chloride aerosol measured downstream of the corona charger at different charging voltages. The feeding size distribution of NaCl aerosol corresponds to the measurement at the applied voltage of zero in the corona charger. This concentration includes those NaCl particles passing through the charger as well as those generated in the corona charger. The measured particle number concentration decreased with the increase of supplied voltages because of the electrostatic deposition loss of nanoparticles (Hernandez-Sierra et al. 2003; Huang and Alonso 2011). As a result, although inconclusive, this experiment demonstrated for higher applied voltages, the corona charger tended to filter more particles and so decrease the number concentration of feed aerosol.

In this case, the needle discharge electrode was the constant supplied voltage, but the plate was grounded. The difference between the voltages of the needle and plates caused the electrical field in the corona charger to be intensified near the gold needle; however, its electrical intensity decreased by closing the plate. As a result, the corona charger acted as an electrostatic precipitator so that larger charged particles deposited electrostatically on the plate and lost. Increasing the voltage intensified the electrical field and the filtration effect that caused more particles to be lost in the corona charger.

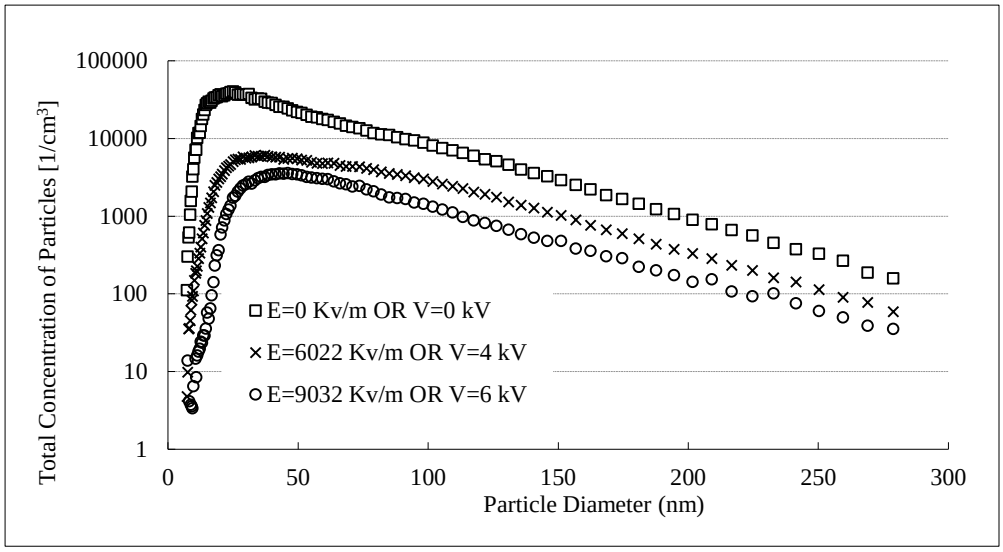

Figure E-4. Size distributions of the sodium chloride aerosols at different voltages applied to the corona charger

Considering the effect of aerosol generation above 7 kV, the maximum charge required at >4 kV and the particle loss effect above, the voltage supplied to the corona charger should not exceed 4 kV for the setup. Therefore, the experiments were run at 4 kV. The corresponding correction coefficient for particle loss was then determined for this voltage only as follows.

$$k = 1.99\left(d_p - 3.74\right)\left[\frac{\pi}{2} - \arctan\left(0.49d_p - 6.89\right)\right] - 1.57 \qquad \text{(E-13)}$$

This equation shows that, for the positive corona charger, there is no significant particles loss for the particles larger than 60 nm.

E.5.3 Size distribution comparison with SMPS

Figure E-5 shows the comparison between SMPS and the measurement using the new prototype, by considering different coefficients for the charging efficiency and particle loss. The concentration of particles correlates with the results of SMPS for particles down to 40 nm in diameter more efficiently than the study of Tan and Wexler (2007). The measured concentration for particles with diameter less than 70 nm is lower than the concentration in SMPS for particles of the same diameter. The error analysis was calculated in Figure E-5, based on the errors of the parameters included in the calculation

formula for focusing diameter, ion concentration, measured current, temperature and pressure before the focusing orifice and particle density.

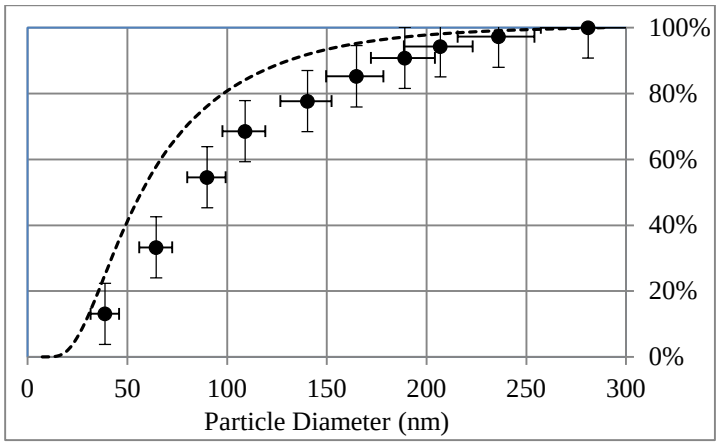

Figure E-5. Particle size cumulative distributions measured using the prototype (solid dots) and the SMPS (dashed line)

There are other error sources in the measurement of prototype to explain the difference between the SMPS and prototype. Smaller particles are charged less effectively than the larger ones because of their small cross section area (Flagan and Seinfeld 2012). Furthermore, a lot of particles can be pumped away due to the boundary layer within the orifice (Phares et al. 2002). In addition, some particles could be lost due to deposition on the surface of the pressure reducing section because of the high electrical mobility preventing them from having charges. Besides, there are some particles with the optimal size passing close to the edge of the focusing orifice that are not transmitted since they are not able to reach the same acceleration as those in the center of the flow (Middha and Wexler 2003).

E.6 Limitations and Recommendations

There are several significant limitations associated with this study. First of all, alternative particle charging should be considered in future prototypes. Although the current home-made corona charger served its purpose for proof-of-principle in this paper, it did complicate the calculation by requiring an extra correction factor to correct the particle loss in the charger. In addition, it was shown that corona charger generates nanoparticles at higher voltage. Although it did not affect the current result because the voltage was chosen to be 4 kV which was lower than the minimum voltage for nanosized particle generation, it may impact the operation of this device in the future work. Furthermore, this corona

charger has the very small active volume for ionization around the needle compared to the whole charge volume between the needle and plate (Yehia and Mizuno 2012). As a result, the corona charger was not helpful for maximum charging the nanoparticles especially the smaller ones and needs to be replaced by other alternative charging methods.

The prototype was not tested for particles smaller than 40 nm, and it is not safe to conclude whether the technology works for sub-40 nm particles. This is limited by the availability of pressure reducing orifice with a smaller size. In addition, the prototype worked by manual switching between different orifice nozzles. It took some time in the order of 10 seconds to complete a full measurement. In future product development, the more nozzles for finer resolution, the longer measurement time will be. An automatic scanning valve will greatly improve the measurement frequency. More work is needed to improve the lower limit of this device.

E.7 Conclusions

Theoretical analysis and experimental evaluation showed that it is feasible to measure the size distribution of airborne submicron particles by aerodynamic particle focusing and particle charge measurement. Despite the errors in the experimental parts, the prototype could measure particles in the range of 40 nm to 300 nm in a good agreement with SMPS. More research shall be done by alternative particle charging and improved lower size detection limit.

Appendix F

Facepiece Respiratory Mask Design and Evaluation

F.1 Summary

Filtering facepiece respirators are usually employed to protect against airborne particulate matter (PM). The performances of multiple respiratory masks were examined in this study and compared with the performance of a respiratory mask with nanofibrous filter media. Experiments were performed to determine how effective these respiratory masks were at micron-sized particulate matter filtration. Filtering facepiece respirators mounted on three different manikin heads were challenged with micron-sized dust particles. In order to distinguish the particle penetration through the filter media or leakage around the face, two sets of experiments, one including non-sealed respirators and the other respirators sealed to the face were done. The difference between the particle penetrations in these two cases showed the leakage around the respirators. The upstream and downstream particle concentrations were measured at a standard breathing rate simulated with a vacuum pump (30 lpm), using an aerodynamic particle sizer (APS TSI Model 3321).

Results showed that the penetration of challenged particles depends on both filter media and the fit of respiratory masks on different face shapes. Results of this study can help to determine efficient filtering facepiece respirators for PM removal.

F.2 Introduction

Filtering facepiece respirators (FFRs) are usually employed as a protection device against exposure to airborne particles. The performance of an FFR depends on four parameters: filtration efficiency, fitting, air resistance, and wearing time. The filter media inside the FFR must have a high filtration efficiency associated with a low resistance so that all unwanted particles are filtered without losing to the ease of breathability. The FFR must also fit comfortably and tightly enough to reduce passage of particles through the leakage between the FFR and face. Various parameters may affect the performance of FFR, such as facial hair, eyeglasses, facial deformities, and facial movement.

The main objective of this study is to evaluate the fitting and filtration performance of several commercial respiratory masks for particulate matter removal, and so determine the best respiratory mask. The following steps were taken to achieve this goal:

- Facial fitting tests to determine air leakage on the edges of the respiratory masks
- Measuring air resistance of the respiratory dust masks
- Determining how the facial structure of different test subjects (manikins) affects performance of the respiratory dust masks
- Comparing the filtration efficiency of the respiratory dust masks with that of a nanofibrous media

F.3 Materials and Methods

F.3.1 Tested respiratory masks

Six kinds of respiratory dust masks were tested in this study (Figure F-1).

Figure F-1. Respiratory dust masks used in this study from left to right: *a*, *b*, *c*, *d*, *e*, and *f*) replacing the filter of the commercial respiratory mask *e* with the fabricated nanofibrous filters

PVA nanofibrous filter media were fabricated by electrospinning at tip-to-collector distances of 10 cm and 15 cm, with deposition times of 5, 15, and 30 min. The applied voltage was 15 kV, and the PVA concentration was 10% w/w. The SEM image along with fiber size distributions are shown in Figure F-2.

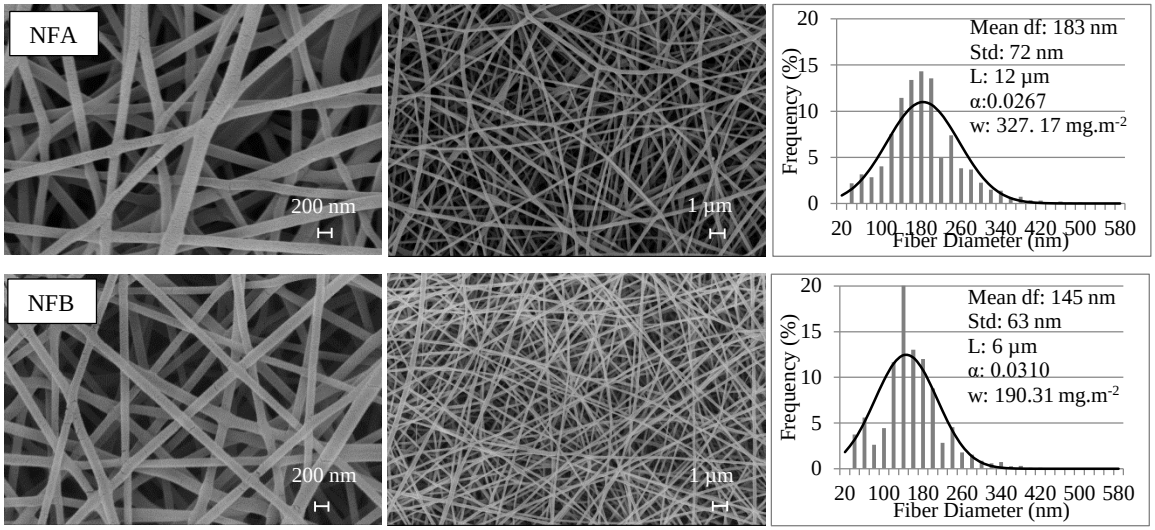

Figure F-2. SEM images and fiber diameter distributions of nanofibrous filters

F.3.2 Tested manikin heads

Figure F-3 shows the three manikin heads used in this study. The first two are standard form manikin heads provided for beauty salons and cannot represent the shape of an average individual's head. Thus, the National Institute for Occupational Safety and Health (NIOSH) provided a three dimensional (3D) scan of anthropologic data for the standard head used in respiratory-protection studies. In the current study, the standard head represents a medium-size Chinese male head.

Figure F-3. Three different manikin heads: a) Male manikin head (Head 1), b) LuckyFine male manikin head (Head 2), c) Chinese manikin head (Head 3)

F.3.3 Experimental design for filtration efficiency

The experiment for filtration efficiency had two steps. First, the filtration efficiencies of filter media were determined (Figure F-4). Generated particles were passed through the filter holder with a diameter

of 25 mm with and without the filter media inside. A thermal mass flowmeter (TSI Model 3063) along with a vacuum pump were connected downstream of the main stream to control the aerosol flow rate. Isokinetic sampling was employed downstream of the filter holder. Then, tests were performed for the corresponding masks mounted on a manikin head to determine the performance of the masks (Figure F-5). In both experimental setups, a fluidized bed aerosol generator (TSI, 3400A) was employed to generate dry powder in the size range of 0.5-5 µm, and an aerodynamic particle sizer spectrometer (APS, TSI 3321) was used for measuring the sizes and concentrations of particles.

Figure F-5 shows that aerosol particles were passed into the transparent box where a manikin head with the respiratory dust masks was mounted in place. The mask was pierced from inside near the nose and connected to the vacuum pump. Negative pressure was created by the vacuum pump to simulate inhalation. Thus, the pressure inside the mask was negative in comparison with that of the ambient air. The flow rate of 30 lpm was chosen as it represents the breathing flow rate for light work. The valve and the mass flow meter (TSI Model 3063) were used to adjust the flow rate.

A sample point for the respiratory dust mask was chosen in the center of the mask and between the nose and the mouth. Air was sampled from the inside of the respirator. A pressure gauge (Omegadyne, Model DPG409) was employed to measure the negative pressure inside, and used to quantify the air resistivity of the mask media.

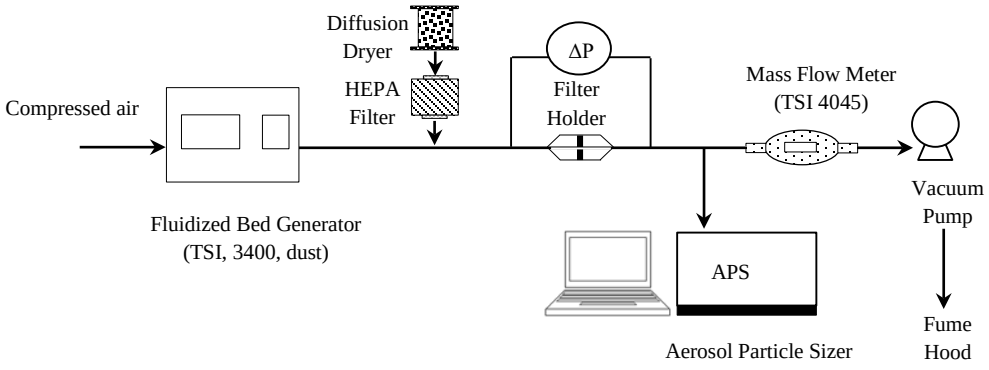

Figure F-4. Experimental setup for testing performance of filter

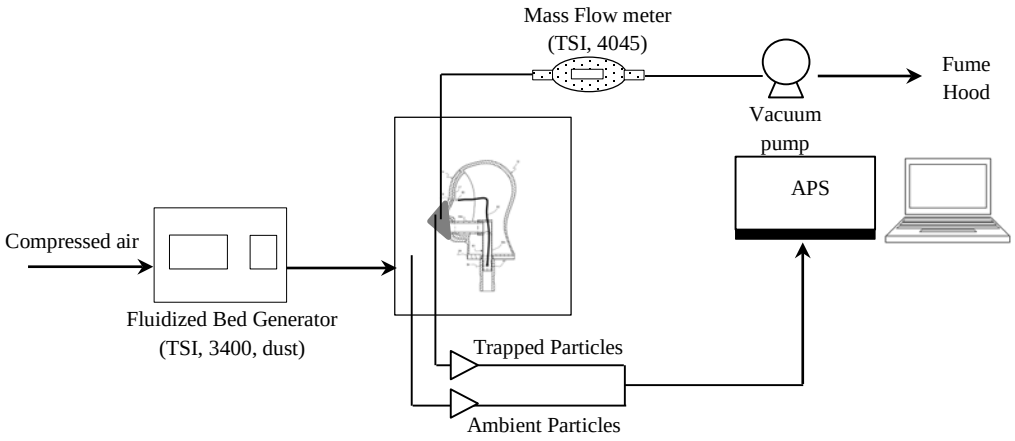

Figure F-5. Experimental setup for testing performance of respiratory dust mask mounted on manikin face

The filtration efficiency was then calculated based on the upstream and downstream particle concentrations.

$$\eta(\%) = \left(1 - \frac{C_{Down}}{C_{Up}}\right) * 100 \tag{F-1}$$

The filtration quality factor is defined as follows:

$$\mathrm{QF} = -\frac{\ln(1-\eta)}{\Delta P} \tag{F-2}$$

Quantitative respirator fit testing (QNFT) was conducted to quantify the leakage between the respirator and the face. The test involves a comparison of the particle concentrations inside and outside of the mask. The fitting factor is calculated as the ratio of the particle concentration outside of the respirator to the particle concentration that leaked inside the respiratory dust mask. It is important to know that most micron particles cannot pass through the filter media. As a result, particles in the microscopic range get into the respirator area through leakage and affect fitting performance. This test was performed at least 10 minutes after mounting the mask. Due to the changes in the ambient particle concentration, the ambient particle concentrations were measured before and after the respiratory dust mask sample. The fitting factor (FF) was calculated as follows (TSI manual 8030):

$$\mathrm{FF} = \frac{C_{A1} + C_{A2}}{2C_S} \tag{F-3}$$

where C_{A1}, C_{A2}, and C_S are particle concentrations in the ambient air before the tests, particle concentration in the ambient air after the tests, and that trapped between the mask and face, respectively. To avoid dividing by zero, the particle concentration in the respirator area changes to 1 if the initial value is zero. For each respiratory mask, the fitting factor is calculated for the three heads. The fitting factor has to be greater than or equal to the assigned protection factor (APF) multiplied by a safety factor. The assigned protection factor for the half-facepiece mask for a self-contained breathing apparatus (SCBA) is 10 (Lenhart and Campbell 1984).

One of the problems associated with the respirator leakage measurement is that it is not known exactly whether those particles trapped between the respiratory mask and face are due to the leakage of the respirators or due to particles passing through the respirators due to the low filtration efficiency. Thus, in this study, two sets of experiments were done. The first set is similar to that for filtration efficiency of masks explained above. The second set was achieved by repeating the experiments when the respiratory mask was mounted on the face and sealed by duct tape. The difference filtration efficiencies of these two sets of experiments shows the Facial Leakage (FL) of the filtering facepiece respirators.

$$\mathrm{FL} = \eta_{Sealed} - \eta_{Non-Sealed} \tag{F-4}$$

F.4 Results and Discussion

F.4.1 Performance of filter media in filtration efficiency

Figure F-6 shows the filtration efficiencies of fabricated nanofibrous filters for nanosized and micronized particles. Results show that the most penetration particle size occurs at a particle diameter of 84 nm. For smaller particles, the diffusion mechanism, and for larger particles, the interception mechanism, is more predominant. As the deposition time increases, the filtration efficiency increases due to the larger bed thickness. Comparing nanofibrous filter NFA and NFB for the same deposition time shows that although filter NFB has the smaller mean fiber diameter, it has lower filtration efficiency due to its smaller thickness.

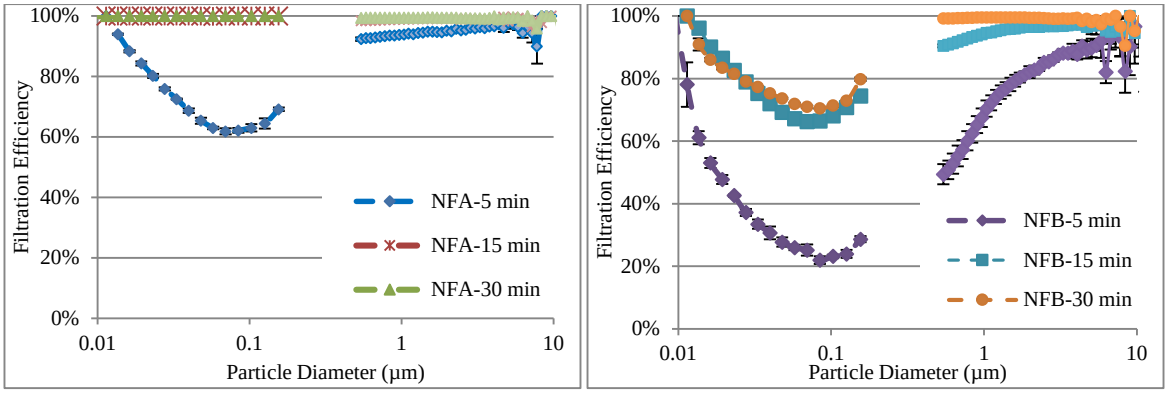

Figure F-6. Filtration efficiency of fabricated nanofibrous filter

Figure F-7 shows the filtration efficiency for micron particles of the filter media as a function of particle diameter at an air flow rate of 30 lpm. As expected, the filtration efficiency decreases as the particle size decreases. Apart from filter media *e* and *b*, the other filters, including nanofibrous filter, have a filtration efficiency of larger than 98% for particles larger than 1.5 µm. The filtration efficiency of filter media e is lower than that of other filter media. The filtration efficiency level of filter *e* is about 90% for particles in the range of 2.5 µm to 5 µm; however, it is decreases to about 60% for 0.54 µm particles. The differences among the filtration efficiencies of these filters are related to the filter's characteristics, including thickness, fiber diameter, solidity, and the number of layers.

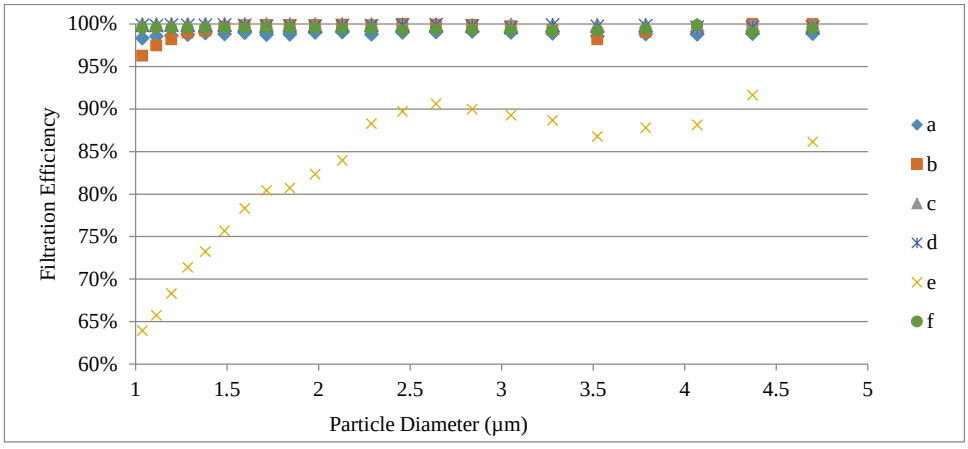

Figure F-7. Filtration efficiency of commercial filter media and nanofibrous filter at an aerosol flow rate of 30 lpm

F.4.2 Performance of facepiece respiratory masks

F.4.2.1 Filtration efficiency

As shown in Figure F-8, respiratory dust mask *a* has the highest filtration efficiency for all three tested heads, followed by respiratory mask *d*. For all three head shapes, employing a nanofibrous filter as the filter media has the lowest filtration efficiency. Thus, although the filter media for these respiratory dust masks are highly efficient, their employment in the respiratory dust mask do not have high filtration efficiency, which shows the importance of respiratory dust mask design and likely fitting.

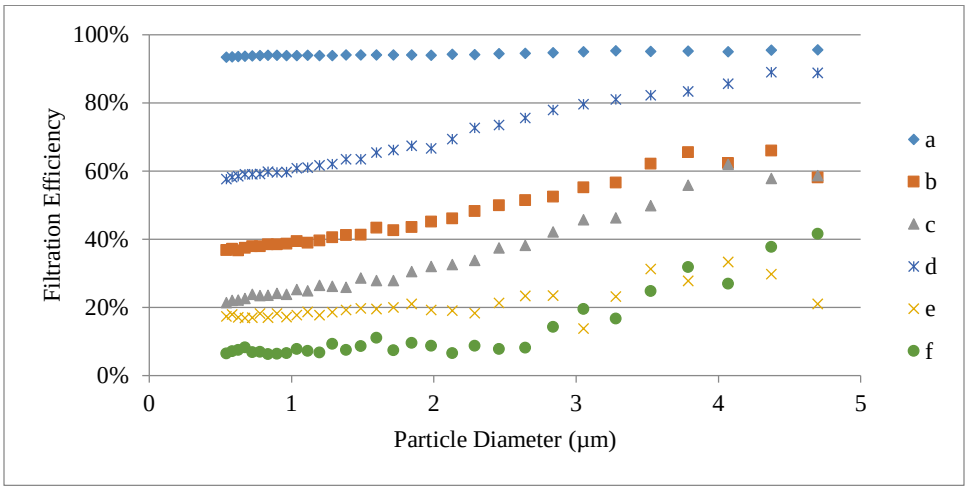

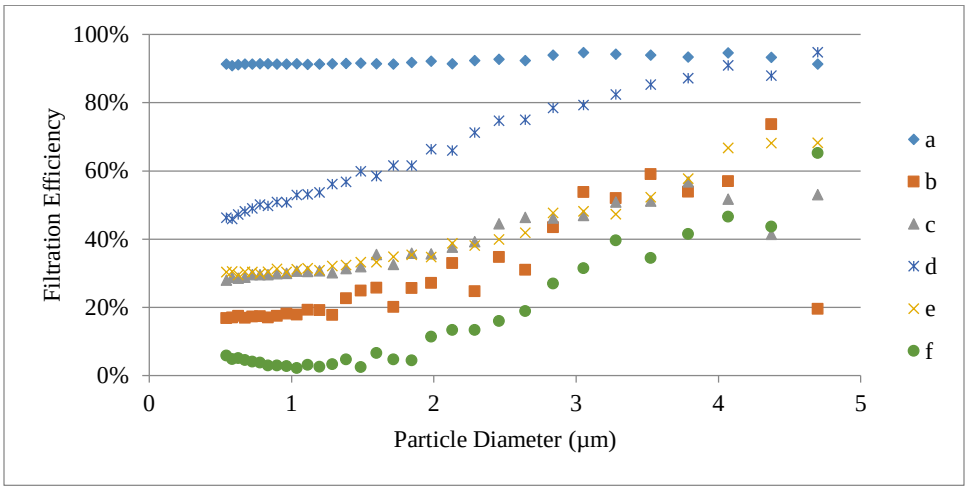

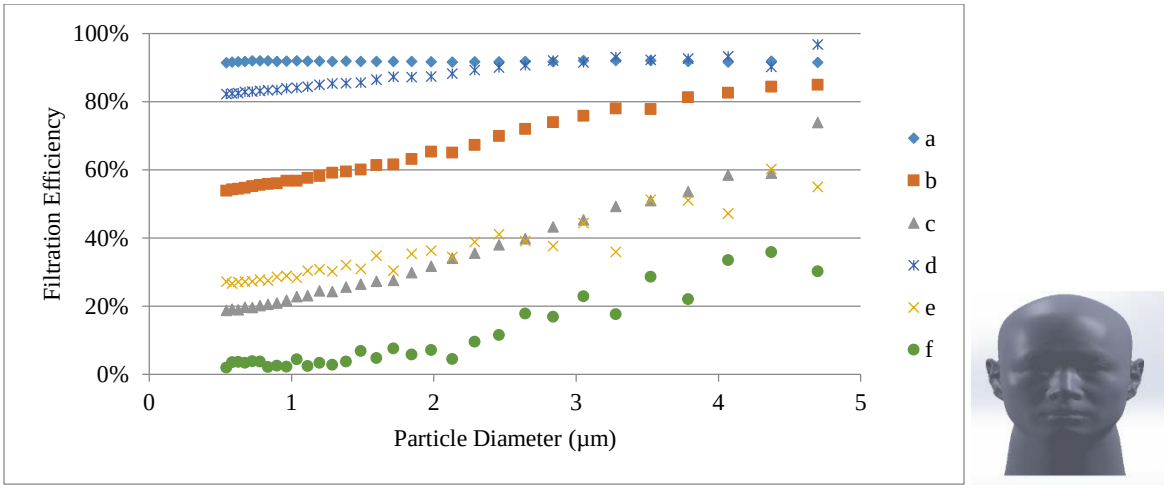

Figure F-8. Filtration efficiencies of tested masks at 30 lpm flow rate for three different head shapes

A two-way ANOVA test with replication on the effects of head shape and respiratory dust masks on filtration efficiency is summarized in Table F-1. The head shape has a strongly significant effect on the performance of FFR ($P<0.001$). Also, the filtration efficiencies of all of the FFRs significantly differ from one another.

Table F-1. Effects of head shape and filtering facepiece respirators on removal filtration efficiency (Two-way ANOVA with replication)

Source of Variation	SS	dF	MS	F	P-value	F critical
Heads	1.696682	2	0.848341	53.86647	1.42E-22	3.007827
FFR	42.59564	7	6.085091	386.3805	7.3E-243	2.021869
Interaction Head/FFR	2.099164	14	0.14994	9.520645	1.25E-19	1.705078

* SS: sum of squares; dF: degree of freedom; MS: mean square

Figure F-9 shows that respiratory dust masks *a*, *c*, *e* and *f* have the lowest standard deviations; however, the respirator *b* (Head 1,2,3) and *d* (Head 1,2) have the highest standard deviations for tested particles (around 20%). The difference between these standard deviations shows the importance of how the mask is mounted on the face at different times. The large standard deviation typically happens when the mask is difficult to mount. If the mask is not mounted in the same exact place as it was mounted last time, then there is a discrepancy in the data collected. Thus, training of users is necessary for mounting these respiratory masks, as different positions may lead to different performance of respiratory masks.

With different head shapes, the masks fit differently. As seen below, the results for Head 3 have the lowest standard deviation for all masks, meaning that all masks fit on Head 3 better than Heads 1 and 2. This may be due to the round facial features. With sharp facial features, it is difficult to properly mount the mask. With round facial features, the mask can smoothly follow the facial features for a better fit with less leakage.

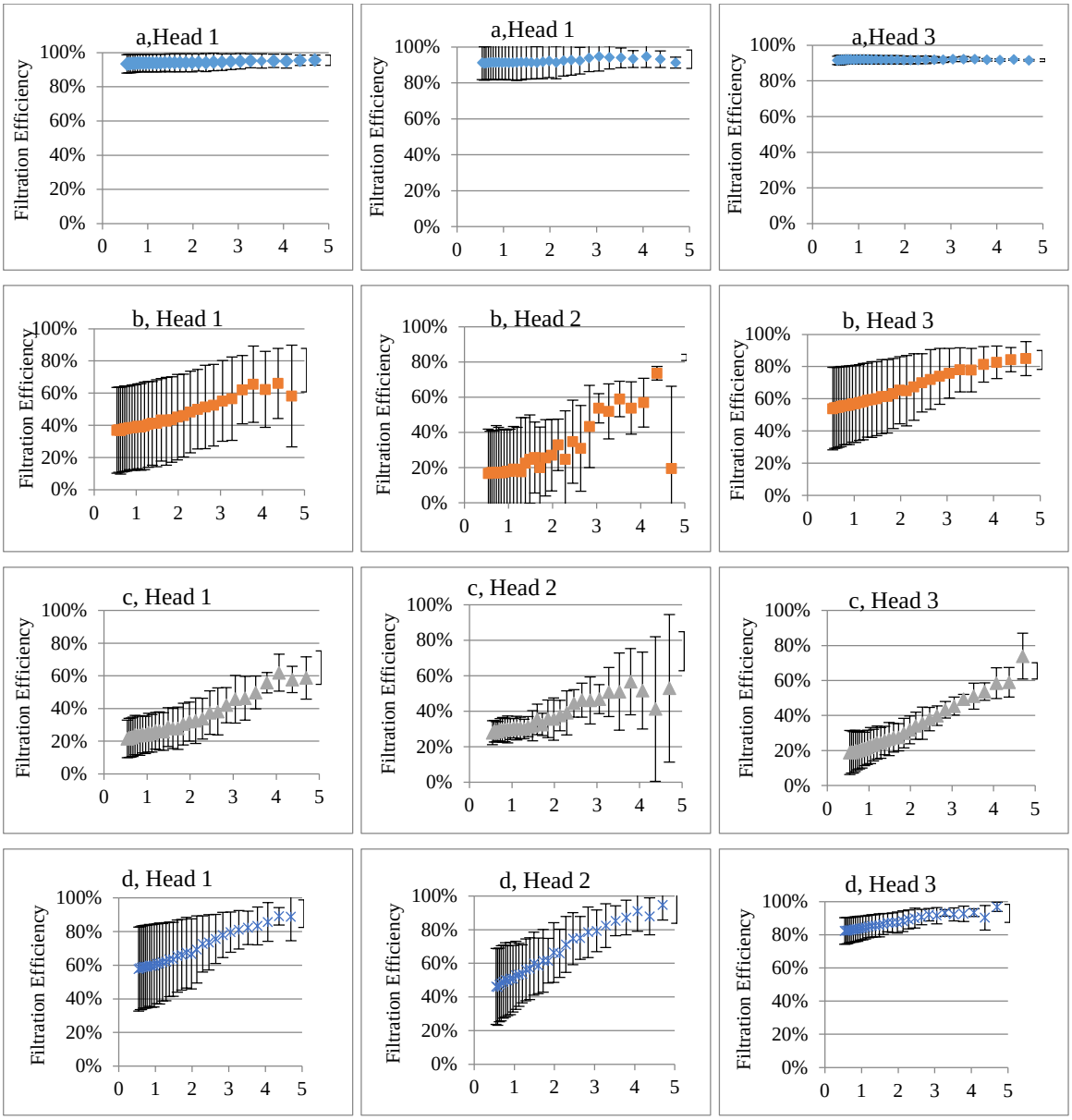

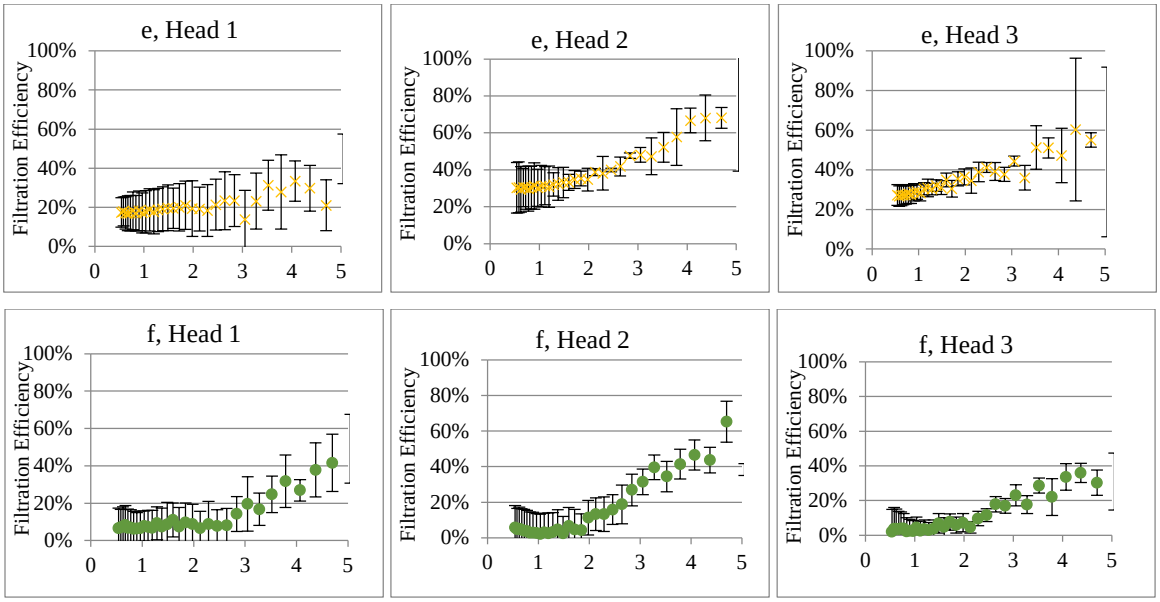

Figure F-9. Filtration efficiency of different respiratory dust masks for different heads versus particle diameter (µm)

Comparing each row in Figure F-9 highlights the importance of facial conformity of the masks. The efficiencies of the filter media can drastically change depending on the facial structure of the user. A small gap caused from any obstruction between the mask and face can be a detriment because of the small sizes of the particles being tested. With just a little gap between face and mask, it is easy for particles smaller than 5 µm in diameter to leak through.

The fitting factors for all of the respiratory dust masks for the three heads as a function of particle diameter are shown in Figure F-10. Results show that the fitting factors of all the respiratory masks except that for mask *a* are lower than the assigned fitting factor (AFF) of 10. Therefore, except respiratory dust mask *a*, none of these masks pass the safety factor for fitting tests herein.

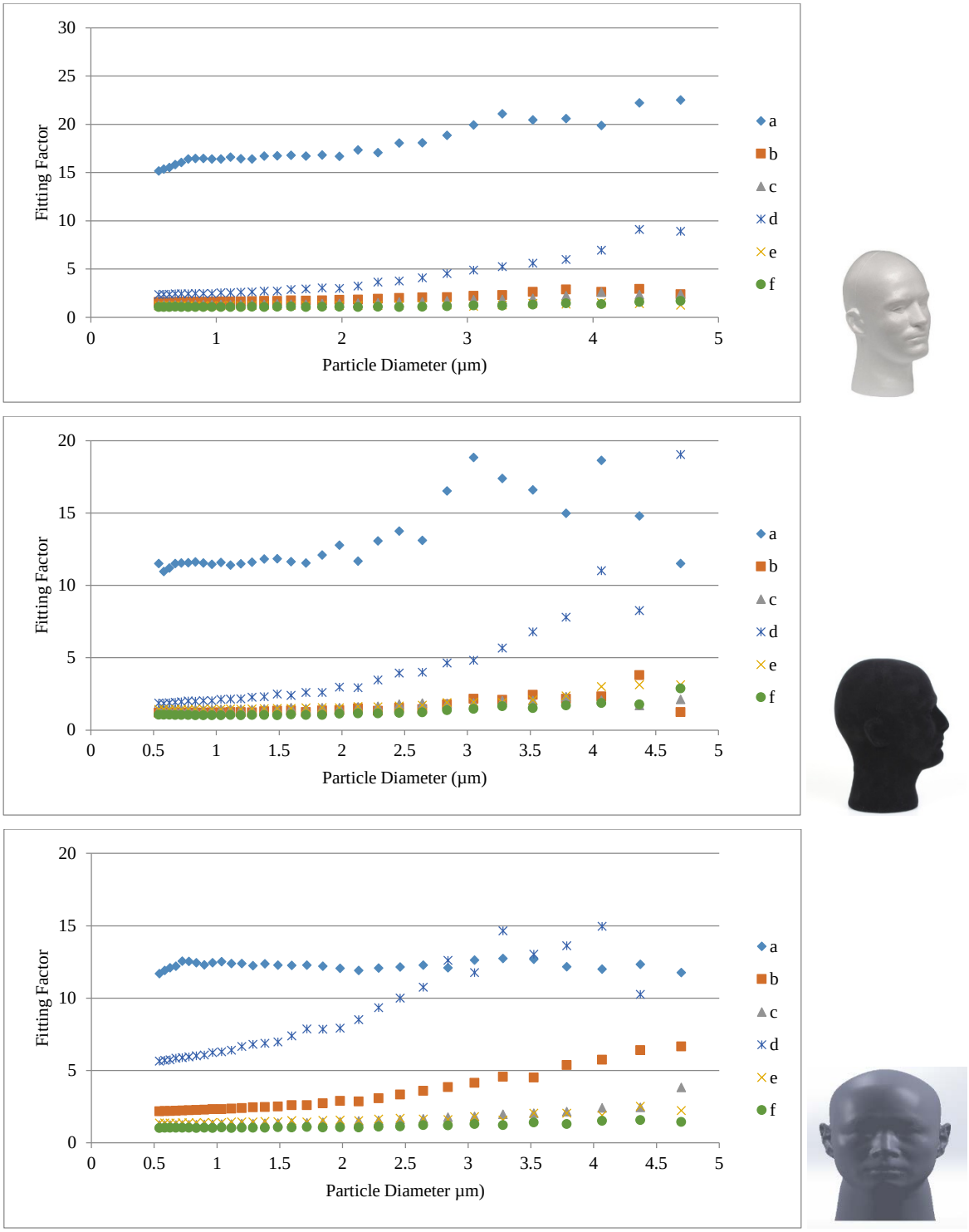

Figure F-10. Fitting factor of tested masks at 30 lpm flow rate for three different head shapes

F.4.2.2 Air leakage

Figure F-11 shows the Facial Leakage of different masks mounted on three different heads. As seen from the experimental results, no one mask perfectly fits all faces; therefore, users will often suffer from particle leakage. Results showed that the leakage of a mask strongly depends on the matching of face and mask. An overall trend was discovered with the leakage and particles diameter. As the particle diameter increased, the leakage decreased, because smaller particles have the greater probability to pass through any gap.

Overall, respirator *a* conforms better to various types of faces, with a leakage of less than 10% for the tested particles. This mask is slightly stiff, with a metal nosepiece for securing around the nose, which increases the fit around the nose. Respirator *b* fits well to Head 1 (max leakage of 15% for tested particles), and respirator *d* fits well to Head 3 (max leakage of 11% for tested particles). Respirator *e* fits well to Heads 2 and 3. This mask is a plastic covering with two removable disk filters on its sides. Its plastic construction makes it flexible enough to fit facial features, which may be the main cause for its relatively low leakage. However, the same respirator with a nanofibrous filter (*f*) has relatively high leakage. Respirator mask c is consistently the worst mask in terms of leakage, perhaps because of its loose straps that do not hold the mask tightly to the face.

F.4.2.3 Resistivity of filtering facepiece respirators

Figure F-12 shows the pressure drop across the masks, non-sealed and sealed with duct tape. In the case of sealed masks, air passes through the respirators, not through the gap between the mask and face. Thus, as expected, the pressure drop of a sealed respirator is higher than that for a non-sealed respirator. Also, results showed that in sealed conditions, employing nanofibrous filters led to a greater pressure drop for all three heads (0.5 inches of H_2O). The pressure drops for other masks were less than 0.2 inches of H_2O. Results show that the resistance of the respiratory dust masks slightly depends on head shape.

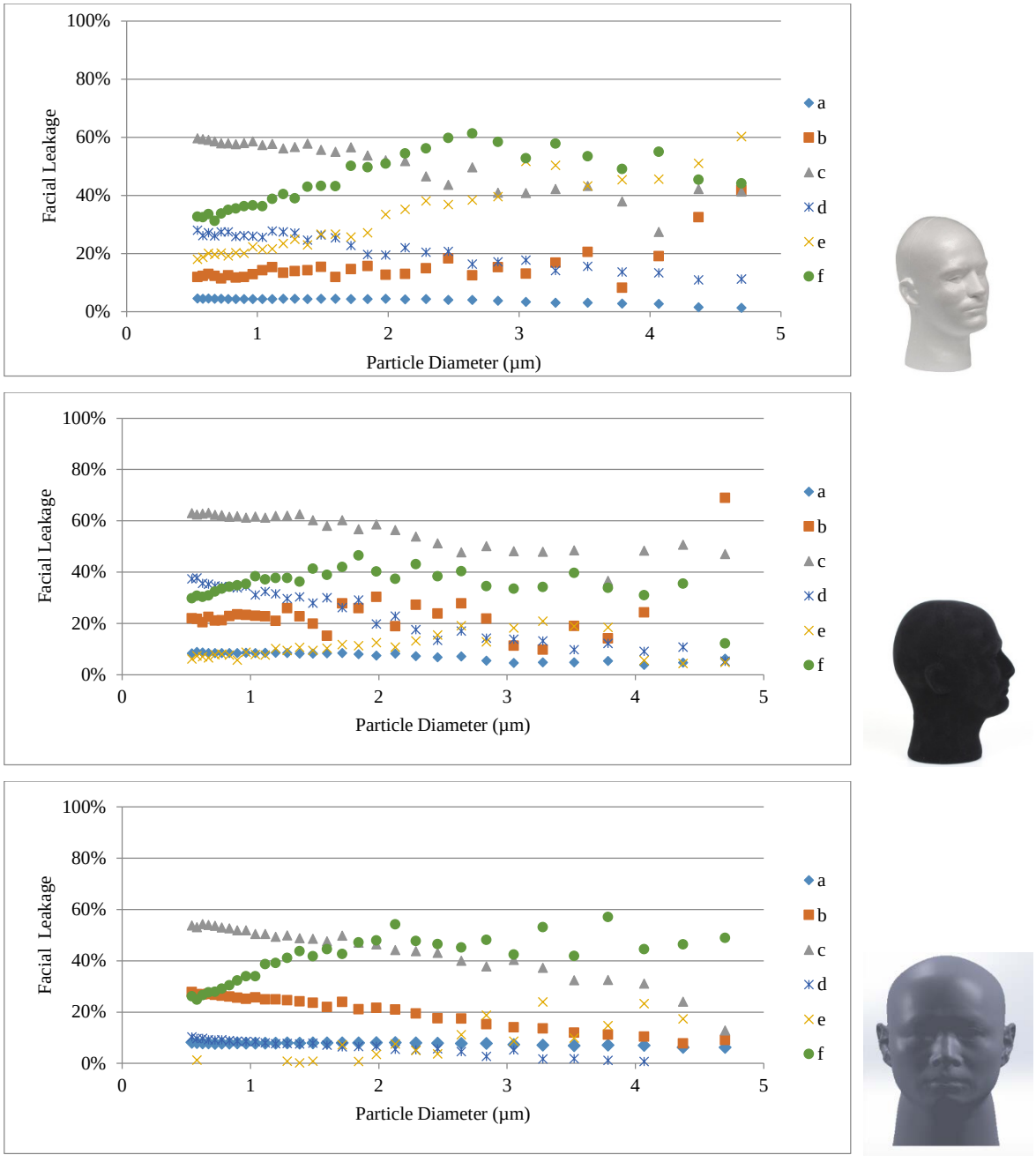

Figure F-11. Facial leakage of different respiratory dust masks mounted on three different head shapes

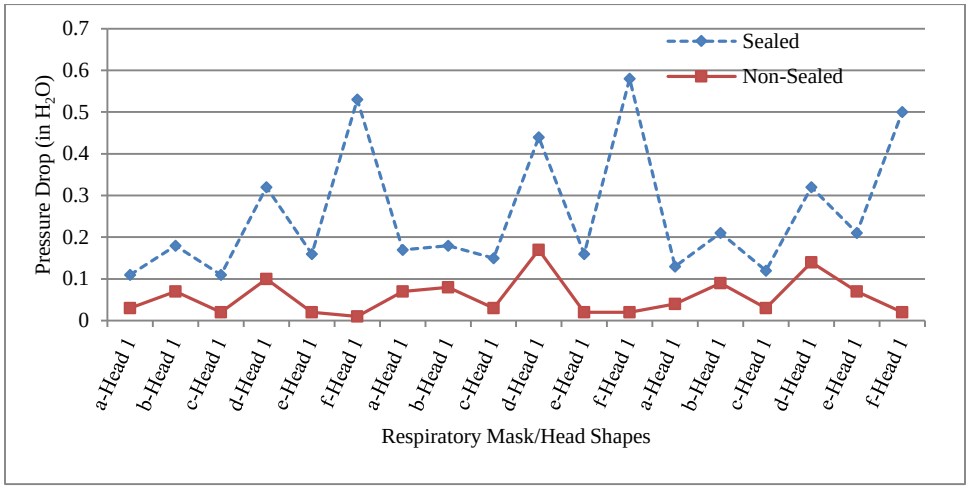

Figure F-12. Pressure drop across the respiratory masks

F.4.2.4. Performance of nanofibrous respirator masks

One of the questions arising here is why there is low efficiency for respiratory dust masks with a nanofibrous filter. Experiments were done to measure filtration efficiency and pressure drop in the case of sealed and non-sealed masks mounted in Head 1 for a commercial and a nanofibrous filters (Figure F-13). Results show that the pressure drops for non-sealed masks are exactly the same (±0.01 inches of H_2O), which shows that the leakage occurs at this place. However, in sealed situations, the pressure drop for the respiratory mask with commercial filter is 0.14 inches of H_2O, and that for the nanofibrous filter is 0.52 inches of H_2O.

In nonsealed conditions, the filtration efficiency of the respiratory mask with a commercial filter is higher than that with a nanofibrous filter; however, for sealed condition, the result is opposite. Thus, the leakage around the filter (gap between filtration efficiencies, sealed and nonsealed) for the nanofibrous filter is higher. Employing nanofibrous filters increase the pressure drop across the mask. Particulate matter tends to pass through areas of less resistance; thus, they most likely pass through the leakage instead of the filter, and decrease the performance of the respiratory mask. Thus, nanofibrous filters need special designs when employed for respiratory dust masks.

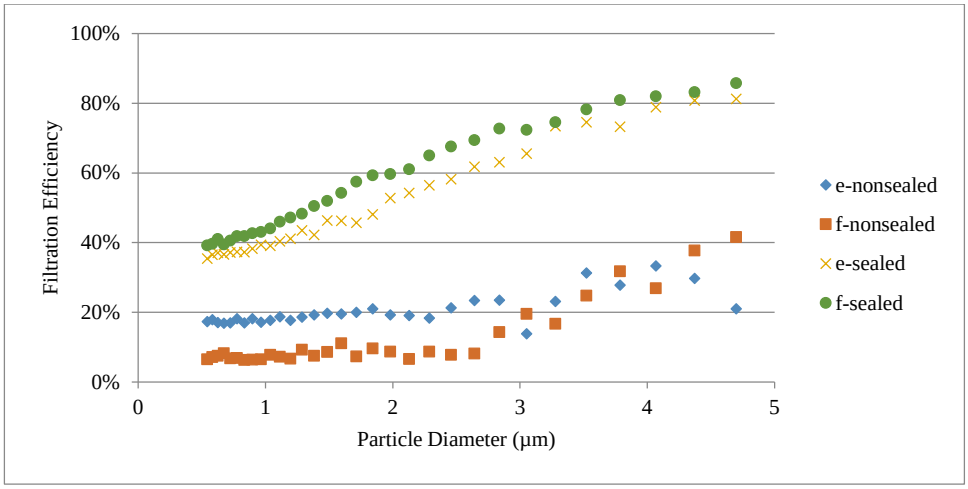

Figure F-13. Filtration efficiencies of respiratory masks employing commercial filter (*e*), and nanofibrous filter (*f*)

F.5 Conclusion

Although all of the filter media of the tested respirator masks have high filtration efficiencies for micron sized particles; this does not lead to high filtration efficiencies when they were in respiratory masks. The filtration efficiencies of respirator masks strongly depend on the fitting of the mask and face shape. Respiratory mask *a*, with its simple design and nose clip, has the highest filtration efficiency for all three heads. On the other hand, nanofibrous media mounted in respiratory mask *e* has the lowest filtration efficiency due to the small surface area of the media and high pressure drop. Employing nanofibrous filter media with larger surface areas in respiratory dust masks with lower leakages is recommended.

Appendix G

Copyright Permissions

Permissions for Chapter 5, Chapter 6, Appendix E and Appendix D:

Date	License No	Type Of Use	Fee	Publication	Title
5-Jan-2016	3783080993495	reuse in a thesis/dissertation	0.00 USD	Fuel	Quality factors of PVA nanofibrous filters for airborne particles in the size range of 10–125nm
16-Oct-2015	3731010662122	reuse in a thesis/dissertation	0.00 USD	Powder Technology	The effect of electrostatic forces on filtration efficiency of granular filters
16-Oct-2015	3731011034947	reuse in a thesis/dissertation	0.00 USD	Journal of Aerosol Science	The effect of capillary force on airborne nanoparticle filtration
16-Oct-2015	3734801501717	reuse in a thesis/dissertation	0.00 USD	Particuology	Submicron particle sizing by aerodynamic dynamic focusing and electrical charge measurement

Bibliography

Ahirwal, D., Hébraud, A., Kádár, R., Wilhelm, M., Schlatter, G. (2013). "From Self-Assembly of Electrospun Nanofibers to 3D Cm Thick Hierarchical Foams." *Soft Matter*, 9(11), 3164-3172.

Ahmadi, G., Guo, S., Zhang, X. (2007). "Particle Adhesion and Detachment in Turbulent Flows Including Capillary Forces." *Particulate Science and Technology*, 25(1), 59-76.

Ahn, Y., Park, S., Kim, G., Hwang, Y., Lee, C., Shin, H., Lee, J. (2006). "Development of High Efficiency Nanofilters made of Nanofibers." *Current Applied Physics*, 6(6), 1030-1035.

Alivisatos, P., Barbara, P. F., Castleman, A. W., Chang, J., Dixon, D. A., Klein, M. L., McLendon, G. L., Miller, J. S., Ratner, M. A., Rossky, P. J. (1998). "From Molecules to Materials: Current Trends and Future Directions." *Advanced Materials*, 10(16), 1297-1336.

Allen, M. D., and Raabe, O. G. (1985). "Slip Correction Measurements of Spherical Solid Aerosol Particles in an Improved Millikan Apparatus." *Aerosol Science and Technology*, 4(3), 269-286.

Allen, T. M., and Cullis, P. R. (2004). "Drug Delivery Systems: Entering the Mainstream." *Science*, 303(5665), 1818-1822.

Alofs, D. J., Lutrus, C. K., Hagen, D. E., Sem, G. J., Blesener, J. (1995). "Intercomparison between Commercial Condensation Nucleus Counters and an Alternating Temperature Gradient Cloud Chamber." *Aerosol Science and Technology*, 23(2), 239-249.

Alonso, M., Hernandez-Sierra, A., Alguacil, F. J. (2002). "Diffusion Charging of Aerosol Nanoparticles with an Excess of Bipoloar Ions." *Journal of Physics A: Mathematical and General*, 35(30), 6271-6280.

Alonso, M., Kousaka, Y., Hashimoto, T., Hashimoto, N. (1997). "Penetration of Nanometer-Sized Aerosol Particles through Wire Screen and Laminar Flow Tube." *Aerosol Science and Technology*, 27(4), 471-480.

Ankilov, A., Baklanov, A., Colhoun, M., Enderle, K. -., Gras, J., Julanov, Y., Kaller, D., Lindner, A., Lushnikov, A. A., Mavliev, R., McGovern, F., O'Connor, T. C., Podzimek, J., Preining, O., Reischl, G. P., Rudolf, R., Sem, G. J., Szymanski, W. W., Vrtala, A. E., Wagner, P. E., Winklmayr, W., Zagaynov, V. (2002). "Particle Size Dependent Response of Aerosol Counters." *Atmospheric Research*, 62(3-4), 209-237.

Arouca, F. O., Feitosa, N. R., Coury, J. R. (2010). "Effect of Sampling in the Evaluation of Particle Size Distribution in Nanoaerosols." *Powder technology*, 200(1-2), 52-59.

Asbach, C., Kaminski, H., Fissan, H., Monz, C., Dahmann, D., Mülhopt, S., Paur, H. R., Kiesling, H. J., Herrmann, F., Voetz, M., Kuhlbusch, T. A. J. (2009). "Comparison of Four Mobility Particle Sizers with Different Time Resolution for Stationary Exposure Measurements." *Journal of Nanoparticle Research,* 11(7), 1593-1609.

Austin, J., Brimblecombe, P., Sturges, W. (2002). *Air Pollution Science for the 21st Century,* Elsevier.

Awasthi, A., Hendy, S., Zoontjens, P., Brown, S. (2006). "Reentrant Adhesion Behavior in Nanocluster Deposition." *Physical Review Letters,* 97(18), 186103.

Awasthi, A., Hendy, S. C., Zoontjens, P., Brown, S. A., Natali, F. (2007). "Molecular Dynamics Simulations of Reflection and Adhesion Behavior in Lennard-Jones Cluster Deposition." *Physical Review B - Condensed Matter and Materials Physics,* 76(11).

Ayesh, A. I., Brown, S. A., Awasthi, A., Hendy, S. C., Convers, P. Y., Nichol, K. (2010). "Coefficient of Restitution for Bouncing Nanoparticles." *Physical Review B - Condensed Matter and Materials Physics,* 81(19).

Aylor, D. E., and Ferrandino, F. J. (1985). "Rebound of Pollen and Spores during Deposition on Cylinders by Inertial Impaction." *Atmospheric Environment - Part A General Topics,* 19(5), 803-806.

Bahk, Y. K., and Wang, J. (2014). "Filtration and Length Determination of Airborne Carbon Nanotubes in the Submicrometer Range using Nanofiber Filters." *Aerosol and Air Quality Research,* 14(5), 1352-1359.

Bałazy, A., and Podgórski, A. (2007). "Deposition Efficiency of Fractal-Like Aggregates in Fibrous Filters Calculated using Brownian Dynamics Method." *Journal of Colloid and Interface Science,* 311(2), 323-337.

Bałazy, A., Toivola, M., Adhikari, A., Sivasubramani, S. K., Reponen, T., Grinshpun, S. A. (2006). "Do N95 Respirators Provide 95% Protection Level Against Airborne Viruses, and how Adequate are Surgical Masks?" *American Journal of Infection Control,* 34(2), 51-57.

Balazy, A., Toivola, M., Reponen, T., Podgorski, A., Zimmer, A., Grinshpun, S. A. (2006). "Manikin-Based Performance Evaluation of N95 Filtering-Facepiece Respirators Challenged with Nanoparticles." *The Annals of Occupational Hygiene,* 50(3), 259-269.

Bałazy, A., Podgórski, A., Gradoń, L. (2004). "Filtration of Nanosized Aerosol Particles in Fibrous Filters. I - Experimental Results." *Journal of Aerosol Science,* 35(SUPPL. 2), S967-S968.

Barhate, R. S., and Ramakrishna, S. (2007). "Nanofibrous Filtering Media: Filtration Problems and Solutions from Tiny Materials." *Journal of Membrane Science,* 296(1–2), 1-8.

Barth, T., Lecrivain, G., Hampel, U. (2013). "Particle Deposition Study in a Horizontal Turbulent Duct Flow using Optical Microscopy and Particle Size Spectrometry." *Journal of Aerosol Science,* 60, 47-54.

Bateman, A. P., Belassein, H., Martin, S. T. (2014). "Impactor Apparatus for the Study of Particle Rebound: Relative Humidity and Capillary Forces." *Aerosol Science and Technology,* 48(1), 42-52.

Belyaev, S., and Levin, L. (1974). "Techniques for Collection of Representative Aerosol Samples." *Journal of Aerosol Science,* 5(4), 325-338.

Boor, B. E., Siegel, J. A., Novoselac, A. (2013). "Monolayer and Multilayer Particle Deposits on Hard Surfaces: Literature Review and Implications for Particle Resuspension in the Indoor Environment." *Aerosol Science and Technology,* 47(8), 831-847.

Boskovic, L., Agranovski, I. E., Altman, I. S., Braddock, R. D. (2008). "Filter Efficiency as a Function of Nanoparticle Velocity and Shape." *Journal of Aerosol Science,* 39(7), 635-644.

Boskovic, L., Altman, I. S., Agranovski, I. E., Braddock, R. D., Myojo, T., Choi, M. (2005). "Influence of Particle Shape on Filtration Processes." *Aerosol Science and Technology,* 39(12), 1184-1190.

Bradley, R. (1932). "The Cohesive Force between Solid Surfaces and the Surface Energy of Solids." *The London, Edinburgh, and Dublin Philosophical Magazine and Journal of Science,* 13(86), 853-862.

Brochot, C., Mouret, G., Michielsen, N., Chazelet, S., Thomas, D. (2011). "Penetration of Nanoparticles in 5 Nm to 400 Nm Size Range through Two Selected Fibrous Media." *Journal of Physics: Conference Series,* 304(1).

Broom, G. P. (1979). "Adhesion of Particles in Fibrous Filters." *Filtration & Separation,* 16(6), 661-662, 664.

Brown, R. C. (1993). *Air Filtration : An Integrated Approach to the Theory and Applications of Fibrous Filters,* Oxford : Pergamon Press, Oxford.

Buha, J., Fissan, H., Wang, J. (2013). "Filtration Behavior of Silver Nanoparticle Agglomerates and Effects of the Agglomerate Model in Data Analysis." *Journal of Nanoparticle Research,* 15(7), 1-11.

Buseck, P. R., and Adachi, K. (2008). "Nanoparticles in the Atmosphere." *Elements,* 4(6), 389-394.

Castellano, P., Ferrante, R., Curini, R., Canepari, S. (2009). "An Overview of the Characterization of Occupational Exposure to Nanoaerosols in Workplaces." *Journal of Physics: Conference Series,* 170.

Chang, J., Lawless, P. A., Yamamoto, T. (1991). "Corona Discharge Processes." *IEEE Transactions on Plasma Science*, 19(6), 1152-1166.

Chang, W., and Ling, F. F. (1991). "Normal impact model of rough surfaces." P*roceedings of American Society of Mechanical Engineers (Paper)*, 1-9.

Chen, S., and Soh, A. (2008). "The Capillary Force in Micro-and Nano-Indentation with Different Indenter Shapes." *International Journal of Solids and Structures*, 45(10), 3122-3137.

Chen, S. C., and Lin, J. F. (2008). "The capillary force between an AFM tip and a surface at different humidity." *Proc., 2008 Second International Conference on Integration and Commercialization of Micro and Nanosystems*, American Society of Mechanical Engineers, 341-344.

Chen, S., Tsai, C., Chen, H., Huang, C., Roam, G. (2011). "The Influence of Relative Humidity on Nanoparticle Concentration and Particle Mass Distribution Measurements by the MOUDI." *Aerosol Science and Technology*, 45(5), 596-603.

Chen, Y., Hsiau, S., Lai, S., Chyou, Y., Li, H., Hsu, C. (2009). "Filtration of Dust Particulates with a Moving Granular Bed Filter." *Journal of Hazardous Materials*, 171(1), 987-994.

Chen, C., and Huang, S. (1998). "The Effects of Particle Charge on the Performance of a Filtering Facepiece." *American Industrial Hygiene Association Journal*, 59(4), 227-233.

Chen, D., Pui, D. Y. H., Hummes, D., Fissan, H., Quant, F. R., Sem, G. J. (1998). "Design and Evaluation of a Nanometer Aerosol Differential Mobility Analyzer (Nano-DMA)." *Journal of Aerosol Science*, 29(5–6), 497-509.

Chen, S., Wang, J., Fissan, H., Pui, D. Y. H. (2013). "Use of Nuclepore Filters for Ambient and Workplace Nanoparticle Exposure assessment—Spherical Particles." *Atmospheric Environment*, 77(0), 385-393.

Cheng, Y., and Yeh, H. (1981). "Equilibrium Bipolar Charge Distribution of Aerosols Consisting of Chains of Uniform Spheres." *Journal of Colloid and Interface Science*, 84(2), 444-450.

Cheng, Y. S., and Yeh, H. C. (1980). "Theory of a Screen-Type Diffusion Battery." *Journal of Aerosol Science*, 11(3), 313-320.

Chow, J. C., and Watson, J. G. (2007). "Survey of Measurement and Composition of Ultrafine Particles." *Aerosol and Air Quality Research*, 7, 121-173.

Collins, D. R., Cocker, D. R., Flagan, R. C., Seinfeld, J. H. (2004). "The Scanning DMA Transfer Function." *Aerosol Science and Technology*, 38(8), 833-850.

Coquelin, L., Fischer, N., Motzkus, C., Mace, T., Gensdarmes, F., Le Brusquet, L., Fleury, G. (2013). "Aerosol Size Distribution Estimation and Associated Uncertainty for Measurement with a Scanning Mobility Particle Sizer (SMPS)." *Conference Series*, 429(1), 012018.

Coury, J. R., Thambimuthu, K. V., Clift, R. (1987). "Capture and Rebound of Dust in Granular Bed Gas Filters." *Powder technology*, 50(3), 253-265.

Crayford, A., Johnson, M., Marsh, R., Secvenco, Y., Walters, D., Williams, P., Petzold, A., Bowen, P., Wang, J., Lister, D. (2012). "SAMPLE III: Contribution to Aircraft Engine PM Certification Requirement and Standard." *Second Specific Contract, Final Report, European Aviatian Safety Agency, Cologne, Germany*, .

Cyrs, W. D., Boysen, D. A., Casuccio, G., Lersch, T., Peters, T. M. (2010). "Nanoparticle Collection Efficiency of Capillary Pore Membrane Filters." *Journal of Aerosol Science*, 41(7), 655-664.

Dahneke, B., Hoover, J., Cheng, Y. S. (1982). "Similarity Theory for Aerosol Beams." *Journal of Colloid and Interface Science*, 87(1), 167-179.

Dahneke, B. (1971). "The Capture of Aerosol Particles by Surfaces." *Journal of Colloid and Interface Science*, 37(2), 342-353.

Davies, C. (1952). "The Seperation of Airborne Dust and Mist Particles." *Proceedings of the Institution of Mechanical Engineers*, 185-198.

Davies, C. (1950). "The Separation of Airborne Dust and Particles." *Arhiv Za Higijenu Rada*, 1(4), 393-427.

DeCarlo, P. F., Slowik, J. G., Worsnop, D. R., Davidovits, P., Jimenez, J. L. (2004). "Particle Morphology and Density Characterization by Combined Mobility and Aerodynamic Diameter Measurements. Part 1: Theory." *Aerosol Science and Technology*, 38(12), 1185-1205.

Deitzel, J., Kleinmeyer, J., Harris, D., Beck Tan, N. (2001). "The Effect of Processing Variables on the Morphology of Electrospun Nanofibers and Textiles." *Polymer*, 42(1), 261-272.

Delrio, F. W., De Boer, M. P., Knapp, J. A., Reedy Jr., E. D., Clews, P. J., Dunn, M. L. (2005). "The Role of Van Der Waals Forces in Adhesion of Micromachined Surfaces." *Nature Materials*, 4(8), 629-634.

Demir, M. M., Yilgor, I., Yilgor, E., Erman, B. (2002). "Electrospinning of Polyurethane Fibers." *Polymer*, 43(11), 3303-3309.

Derjaguin, B., Muller, V., Toporov, Y. P. (1975). "Effect of Contact Deformations on the Adhesion of Particles." *Journal of Colloid and Interface Science*, 53(2), 314-326.

Donaldson, K., Tran, L., Jimenez, L. A., Duffin, R., Newby, D. E., Mills, N., MacNee, W., Stone, V. (2005). "Combustion-Derived Nanoparticles: A Review of their Toxicology Following Inhalation Exposure." *Particle and Fibre Toxicology*, 2.

Ehara, K., Hagwood, C., Coakley, K. J. (1996). "Novel Method to Classify Aerosol Particles According to their Mass-to-Charge Ratio - Aerosol Particle Mass Analyser." *Journal of Aerosol Science*, 27(2), 217-234.

Eichenlaub, S., Chan, C., Beaudoin, S. P. (2002). "Hamaker Constants in Integrated Circuit Metalization." *Journal of Colloid and Interface Science*, 248(2), 389-397.

El-Hedok, I. A., Whitmer, L., Brown, R. C. (2011). "The Influence of Granular Flow Rate on the Performance of a Moving Bed Granular Filter." *Powder technology*, 214(1), 69-76.

Elsaesser, A., and Howard, C. V. (2012). "Toxicology of Nanoparticles." *Advanced Drug Delivery Reviews*, 64(2), 129-137.

Eninger, R. M., Honda, T., Adhikari, A., Heinonen-Tanski, H., Reponen, T., Grinshpun, S. A. (2008). "Filter Performance of n99 and n95 Facepiece Respirators Against Viruses and Ultrafine Particles." *The Annals of Occupational Hygiene*, 52(5), 385-396.

Erickson, K., Singh, M., Osmondson, B. (2007). "Measuring Nanoparticle Size Distributions in Real-Time: Key Factors for Accuracy."

Esquivel-Sirvent, R., and Schatz, G. C. (2012). "Spatial Nonlocality in the Calculation of Hamaker Coefficients." *Journal of Physical Chemistry C*, 116(1), 420-424.

Fallahi, D., Rafizadeh, M., Mohammadi, N., Vahidi, B. (2010). "Effect of Applied Voltage on Surface and Volume Charge Density of the Jet in Electrospinning of Polyacrylonitrile Solutions." *Polymer Engineering & Science*, 50(7), 1372-1376.

Ferreira, A., Cemlyn-Jones, J., Robalo Cordeiro, C. (2013). "Nanoparticles, Nanotechnology and Pulmonary Nanotoxicology." *Revista Portuguesa De Pneumologia (English Edition)*, 19(1), 28-37.

Flagan, R. C., and Seinfeld, J. H. (2012). *Fundamentals of Air Pollution Engineering*, DoverPublications. com, .

Flagan, R. C. (1998). "History of Electrical Aerosol Measurements." *Aerosol Science and Technology*, 28(4), 301-380.

Florkowska, B., and Wlodek, R. (1993). "Pulse Height Analysis of Partial Discharge in Air." *IEEE Transactions on Electrical Insulation*, 28(6), 932-940.

Friedlander, S. K., and Pui, D. Y. H. (2004). "Emerging Issues in Nanoparticle Aerosol Science and Technology." *Journal of Nanoparticle Research,* 6(2-3), 313-320.

Fuchs, N. A. (1963). "On the Stationary Charge Distribution on Aerosol Particles in a Bipolar Ionic Atmosphere." *Geofisica Pura E Applicata,* 56(1), 185-193.

Furuuchi, M., Eryu, K., Nagura, M., Hata, M., Kato, T., Tajima, N., Sekiguchi, K., Ehara, K., Seto, T., Otani, Y. (2010). "Development and Performance Evaluation of Air Sampler with Inertial Filter for Nanoparticle Sampling." *Aerosol and Air Quality Research,* 10(2), 185-192.

Giechaskiel, B., Alessandrini, S., Forni, F., Carriero, M., Krasenbrink, A., Spielvogel, J., Gerhart, C., Wang, X., Horn, H., Southgate, J. (2008). "Calibration of PMP Condensation Particle Number Counters: Effect of Material on Linearity and Counting Efficiency." *EU Report,* 23495.

Giechaskiel, B., Wang, X., Horn, H. -., Spielvogel, J., Gerhart, C., Southgate, J., Jing, L., Kasper, M., Drossinos, Y., Krasenbrink, A. (2009). "Calibration of Condensation Particle Counters for Legislated Vehicle Number Emission Measurements." *Aerosol Science and Technology,* 43(12), 1164-1173.

Gilabert, F., Krivtsov, A., Castellanos, A. (2006). "A Molecular Dynamics Model for Single Adhesive Contact." *Meccanica,* 41(3), 341-349.

Givehchi, R., Tan, Z. (2014). "Thermal Rebound in Nanosized Particle Filtration." *Canadian Society for Mechanical Engineering International Congress*. June 1-4, 2014, Toronto, Canada.

Givehchi, R., Li, Q., Tan, Z. (2015). "The Effect of Electrostatic Forces on Filtration Efficiency of Granular Filters." *Powder technology*, 277, 135-140.

Givehchi, R., and Tan, Z. (2014). "An Overview of Airborne Nanoparticle Filtration and Thermal Rebound Theory." *Aerosol and Air Quality Research,* 14, 45-63.

Givehchi, R., and Tan, Z. (2015). "The Effect of Capillary Force on Airborne Nanoparticle Filtration." *Journal of Aerosol Science,* 83(0), 12-24.

Givehchi, R., Li, Q., Tan, Z. (2015). "Quality factors of PVA nanofibrous filters for airborne particles in the size range of 10–125 nm." *Fuel, In Press,* doi:10.1016/j.fuel.2015.12.010.

Golanski, L., Guiot, A., Tardif, F. (2010). "Experimental Evaluation of Individual Protection Devices Against Different Types of Nanoaerosols: Graphite, TiO2, and Pt." *Journal of Nanoparticle Research,* 12(1), 83-89.

Golanski, L., Guiot, A., Rouillon, F., Pocachard, J., Tardif, F. (2009). "Experimental Evaluation of Personal Protection Devices Against Graphite Nanoaerosols: Fibrous Filter Media, Masks, Protective Clothing, and Gloves." *Human and Experimental Toxicology,* 28(6-7), 353-359.

Golshahi, L., Abedi, J., Tan, Z. (2009). "Granular Filtration for Airborne Particles: Correlation between Experiments and Models." *The Canadian Journal of Chemical Engineering*, 87(5), 726-731.

Gómez, V., Huang, C. H., Alguacil, F. J., Alonso, M. (2012). "Deposition of Aerosol Particles Below 10 Nm on a Mixed Screen-Type Diffusion Battery." *Aerosol and Air Quality Research*, 12(3), 295-299.

Grafe, T. H., and Graham, K. M. (2003). "Nanofiber Webs from Electrospinning." *Nonwovens in Filtration - Fifth International Conference, Stuttgart, Germany*, , 1-5.

Graham, K., Ouyang, M., Raether, T., Grafe, T., McDonald, B., Knauf, P. (2002). "Polymeric Nanofibers in Air Filtration Applications." *Fifteenth Annual Technical Conference & Expo of the American Filtration & Separations Society*, , 9-12.

Greenwood, J. A. (1997). "Adhesion of Elastic Spheres." *Proceedings of the Royal Society A: Mathematical, Physical and Engineering Sciences*, 453(1961), 1277-1297.

GRIMM, A. T. (2012). Scanning Mobility Particle Sizer with Faraday Cup Electrometer (SMPS+E).

Gu, Q. F., Krauss, G., Steurer, W., Gramm, F., Cervellino, A. (2008). "Unexpected High Stiffness of Ag and Au Nanoparticles." *Physical Review Letters*, 100(4).

Guillory, J. L., Placer, F. M., Grace, D. S. (1981). "Electrostatic Enhancement of Moving-Bed Granular Filtration." *Environment International*, 6(1), 387-395.

Hakim, L. F., Portman, J. L., Casper, M. D., Weimer, A. W. (2005). "Aggregation Behavior of Nanoparticles in Fluidized Beds." *Powder technology*, 160(3), 149-160.

Hartland, G. V. (2004). "Measurements of the Material Properties of Metal Nanoparticles by Time-Resolved Spectroscopy." *Physical Chemistry Chemical Physics*, 6(23), 5263-5274.

Headrick, J. M., Schrader, P. E., Michelsen, H. A. (2013). "Radial-Profile and Divergence Measurements of Combustion-Generated Soot Focused by an Aerodynamic-Lens System." *Journal of Aerosol Science*, 58, 158-170.

Heim, M., Attoui, M., Kasper, G. (2010). "The Efficiency of Diffusional Particle Collection On to Wire Grids in the Mobility Equivalent Size Range of 1.2-8 Nm." *Journal of Aerosol Science*, 41(2), 207-222.

Heim, M., Mullins, B. J., Kasper, G. (2006). "Comment on: Penetration of Ultrafine Particles and Ion Clusters through Wire Screens by Ichitsubo Et Al." *Aerosol Science and Technology*, 40(2), 144-145.

Heim, M., Mullins, B. J., Wild, M., Meyer, J., Kasper, G. (2005). "Filtration Efficiency of Aerosol Particles Below 20 Nanometers." *Aerosol Science and Technology,* 39(8), 782-789.

Helsper, C., Horn, H., Schneider, F., Wehner, B., Wiedensohler, A. (2008). "Intercomparison of Five Mobility Size Spectrometers for Measuring Atmospheric Submicrometer Aerosol Particles." *Gefahrstoffe Reinhaltung Der Luft,* 68(11-12), 475-481.

Hernandez-Sierra, A., Alguacil, F. J., Alonso, M. (2003). "Unipolar Charging of Nanometer Aerosol Particles in a Corona Ionizer." *Journal of Aerosol Science,* 34(6), 733-745.

Hinds, W. C. (1999). *Aerosol Technology Properties, Behevior, and Measurment of Airborne Particles,* 2nd Ed., Wiley - Interscience, .

Hofmann, W., Morawska, L., Winkler-Heil, R., Moustafa, M. (2009). "Deposition of Combustion Aerosols in the Human Respiratory Tract: Comparison of Theoretical Predictions with Experimental Data Considering Nonspherical Shape." *Inhalation Toxicology,* 21(14), 1154-1164.

Hogan Jr., C. J., Li, L., Chen, D., Biswas, P. (2009). "Estimating Aerosol Particle Charging Parameters using a Bayesian Inversion Technique." *Journal of Aerosol Science,* 40(4), 295-306.

Hoppel, W. A., and Frick, G. M. (1986). "Ion-Aerosol Attachment Coefficients and the Steady-State Charge Distribution on Aerosols in a Bipolar Ion Environment." *Aerosol Science and Technology,* 5(1), 1-21.

Huang, C., Chen, S., Lai, C., Reneker, D. H., Qiu, H., Ye, Y., Hou, H. (2006). "Electrospun Polymer Nanofibres with Small Diameters." *Nanotechnology,* 17(6), 1558.

Huang, S. H., Chen, C. W., Kuo, Y. M., Lai, C. Y., McKay, R., Chen, C. C. (2013). "Factors Affecting Filter Penetration and Quality Factor of Particulate Respirators." *Aerosol and Air Quality Research,* 13, 162-171.

Huang, C., and Alonso, M. (2011). "Nanoparticle Electrostatic Loss within Corona Needle Charger during Particle-Charging Process." *Journal of Nanoparticle Research,* 13(1), 175-184.

Huang, S., Chen, C., Chang, C., Lai, C., Chen, C. -. (2007). "Penetration of 4.5 Nm to 10 M M Aerosol Particles through Fibrous Filters." *Journal of Aerosol Science,* 38(7), 719-727.

Hung, C., and Leung, W. W. (2011). "Filtration of Nano-Aerosol using Nanofiber Filter Under Low Peclet Number and Transitional Flow Regime." *Separation and Purification Technology,* 79(1), 34-42.

Hunter, S. C. (1957). "Energy Absorbed by Elastic Waves during Impact." *Journal of the Mechanics and Physics of Solids,* 5(3), 162-171.

Hutchings, I. (2001). "Energy Absorbed by Elastic Waves during Plastic Impact." *Journal of Physics D,* 12(11), 1819.

Ichitsubo, H., and Otani, Y. (2012). "Development of Variable Flow Rate Isokinetic Sampling System for 0.5–15-Mm Aerodynamic Diameter Particles." *Aerosol Science and Technology,* 46(12), 1286-1294.

Ichitsubo, H., Hashimoto, T., Alonso, M., Kousaka, Y. (1996). "Penetration of Ultrafine Particles and Ion Clusters through Wire Screens." *Aerosol Science and Technology,* 24(3), 119-127.

Ikeda, H., Qi, Y., Cagin, T., Samwer, K., Johnson, W. L., Goddard III, W. A. (1999). "Strain Rate Induced Amorphization in Metallic Nanowires." *Physical Review Letters,* 82(14), 2900.

Imhof, D., Weingartner, E., Prévôt, A., Ordónez, C., Kurtenbach, R., Wiesen, P., Rodler, J., Sturm, P., McCrae, I., Ekström, M. (2006). "Aerosol and NO X Emission Factors and Submicron Particle Number Size Distributions in Two Road Tunnels with Different Traffic Regimes." *Atmospheric Chemistry and Physics,* 6(8), 2215-2230.

Intra, P., and Tippayawong, N. (2011). "An Overview of Unipolar Charger Developments for Nanoparticle Charging." *Aerosol and Air Quality Research,* 11(2), 187-209.

Israelachvili, J. N. (1991). *Intermolecular and Surface Forces,* London ; Toronto : Academic Press, London ; Toronto; London.

Japuntich, D. A., Franklin, L. M., Pui, D. Y., Kuehn, T. H., Kim, S. C., Viner, A. S. (2007). "A Comparison of Two Nano-Sized Particle Air Filtration Tests in the Diameter Range of 10 to 400 Nanometers." *Journal of Nanoparticle Research,* 9(1), 93-107.

Jawahar, N., and Reddy, G. (2012). "Nanoparticles: A Novel Pulmonary Drug Delivery System for Tuberculosis." *Journal of Pharmaceutical Sciences and Research,* 4(8), 1901-1906.

Jaworek, A., Krupa, A., Czech, T. (2007). "Modern Electrostatic Devices and Methods for Exhaust Gas Cleaning: A Brief Review." *Journal of Electrostatics,* 65(3), 133-155.

Ji, X., Le Bihan, O., Ramalho, O., Mandin, C., D'Anna, B., Martinon, L., Nicolas, M., Bard, D., Pairon, J. (2010). "Characterization of Particles Emitted by Incense Burning in an Experimental House." *Indoor Air,* 20(2), 147-158.

John, J., and Keith, T. (2006). "Gas Dynamics ."

John, W. (1995). "Particle-Surface Interactions: Charge Transfer, Energy Loss, Resuspension, and Deagglomeration." *Aerosol Science and Technology,* 23(1), 2-24.

Johnson, K., Kendall, K., Roberts, A. (1971). "Surface Energy and the Contact of Elastic Solids." *Proceedings of the Royal Society of London.A.Mathematical and Physical Sciences,* 324(1558), 301-313.

Johnson, K. L. (1997). "Adhesion and Friction between a Smooth Elastic Spherical Asperity and a Plane Surface." *Proceedings of the Royal Society A: Mathematical, Physical and Engineering Sciences,* 453(1956), 163-179.

Johnson, K. L., and Greenwood, J. A. (1997). "An Adhesion Map for the Contact of Elastic Spheres." *Journal of Colloid and Interface Science,* 192(2), 326-333.

Joshi, M., Sapra, B. K., Khan, A., Tripathi, S. N., Shamjad, P. M., Gupta, T., Mayya, Y. S. (2012). "Harmonisation of Nanoparticle Concentration Measurements using GRIMM and TSI Scanning Mobility Particle Sizers." *Journal of Nanoparticle Research,* 14(12).

Jung, J. H., Cheol Oh, H., Soo Noh, H., Ji, J. H., Soo Kim, S. (2006). "Metal Nanoparticle Generation using a Small Ceramic Heater with a Local Heating Area." *Journal of Aerosol Science,* 37(12), 1662-1670.

Jung, S., Suh, D., Yoon, W. (2010). "Molecular Dynamics Simulation on the Energy Exchanges and Adhesion Probability of a Nano-Sized Particle Colliding with a Weakly Attractive Static Surface." *Journal of Aerosol Science,* 41(8), 745-759.

Kang, M. (2011). "Assessment of NIOSH-Approved N95 Filter Performance Against Varying Conditions."

Keck, L., Spielvogel, J., Grimm, H. (2009). "From Nanoparticles to Large Aerosols: Ultrafast Measurement Methods for Size and Concentration." *Nanosafe 2008: International Conference on Safe Production and use of Nanomaterials,* 170(1).

Keskinen, J., Pietarinen, K., Lehtimäki, M. (1992). "Electrical Low Pressure Impactor." *Journal of Aerosol Science,* 23(4), 353-360.

Kim, C. S., Bao, L., Okuyama, K., Shimada, M., Niinuma, H. (2006). "Filtration Efficiency of a Fibrous Filter for Nanoparticles." *Journal of Nanoparticle Research,* 8(2), 215-221.

Kim, S. C., Harrington, M. S., Pui, D. Y. H. (2007). "Experimental Study of Nanoparticles Penetration through Commercial Filter Media." *Journal of Nanoparticle Research,* 9(1), 117-125.

Kirsch, A. A., and Fuchs, N. A. (1968). "Studies on Fibrous Aerosol Filters-III Diffusional Deposition of Aerosols in Fibrous Filters." *The Annals of Occupational Hygiene,* 11(4), 299-304.

Knutson, E. O., and Whitby, K. T. (1975). "Aerosol Classification by Electric Mobility: Apparatus, Theory, and Applications." *Journal of Aerosol Science,* 6(6), 443-451.

Kousaka, Y., Okuyama, K., Shimada, M., Takii, Y. (1990). "Development of a Method for Testing very High-Efficiency Membrane Filters for Ultrafine Aerosol Particles." *Journal of Chemical Engineering of Japan*, 23(5), 568-574.

Krämer, M., and Afchine, A. (2004). "Sampling Characteristics of Inlets Operated at Low U/U_0 Ratios: New Insights from Computational Fluid Dynamics (CFX) Modeling." *Journal of Aerosol Science*, 35(6), 683-694.

Kreyling, W. G., Semmler-Behnke, M., Möller, W. (2006a). "Ultrafine Particle-Lung Interactions: Does Size Matter?" *Journal of Aerosol Medicine*, 19(1), 74-83.

Kreyling, W. G., Semmler-Behnke, M., Möller, W. (2006b). "Health Implications of Nanoparticles." *Journal of Nanoparticle Research*, 8(5), 543-562.

Krish, A. A., and Stechkina, I. B. (1978). *The Theory of Aerosol Filtration with Fibrous Filters*, Wiley Ed., Fundamentals of Aerosol Science, New York.

Krupp, H. (1967). "Particle Adhesion Theory and Experiment." *Advances in Colloid and Interface Science*, 1(2), 111-239.

Kulkarni, P., Baron, P. A., Willeke, K. (2011). *Aerosol Measurement: Principles, Techniques, and Applications*, John Wiley & Sons, .

Kulkarni, P., and Wang, J. (2006). "New Fast Integrated Mobility Spectrometer for Real-Time Measurement of Aerosol Size Distribution-I: Concept and Theory." *Journal of Aerosol Science*, 37(10), 1303-1325.

Lasher, S. W. (1999). "Ultra-Fine Soot Investigation in Flames." *Diss. Massachusetts Institute of Technology*.

Lee, K. H., Kim, H. Y., La, Y. M., Lee, D. R., Sung, N. H. (2002a). "Influence of a Mixing Solvent with Tetrahydrofuran and N, N-dimethylformamide on Electrospun Poly (Vinyl Chloride) Nonwoven Mats." *Journal of Polymer Science Part B: Polymer Physics*, 40(19), 2259-2268.

Lee, K., and Liu, B. (1982a). "Theoretical Study of Aerosol Filtration by Fibrous Filters." *Aerosol Science and Technology*, 1(2), 147-161.

Lee, M., Otani, Y., Namiki, N., Emi, H. (2002b). "Prediction of Collection Efficiency of High-Performance Electret Filters." *Journal of Chemical Engineering of Japan*, 35(1), 57-62.

Lee, K. W., and Liu, B. Y. H. (1982b). "Theoretical Study of Aerosol Filtration by Fibrous Filters." *Aerosol Science and Technology*, 1(C), 147-161.

Lee, K. W., and Gieseke, J. A. (1980). "Note on the Approximation of Interceptional Collection Efficiencies." *Journal of Aerosol Science*, 11(4), 335-341.

Lenhart, S. W., and Campbell, D. L. (1984). "Assigned Protection Factors for Two Respirator Types Based upon Workplace Performance Testing." *The Annals of Occupational Hygiene*, 28(2), 173-182.

Leob, L. B. (1961). *The Kinetic Theory of Gases*, Dover, New York.

Leung, W. W., Hung, C., Yuen, P. (2010). "Effect of Face Velocity, Nanofiber Packing Density and Thickness on Filtration Performance of Filters with Nanofibers Coated on a Substrate." *Separation and Purification Technology*, 71(1), 30-37.

Li, D., and Xia, Y. (2004). "Electrospinning of Nanofibers: Reinventing the Wheel?" *Advanced Materials*, 16(14), 1151-1170.

Li, L., Zuo, Z., Japuntich, D. A., Pui, D. Y. H. (2012). "Evaluation of Filter Media for Particle Number, Surface Area and Mass Penetrations." *The Annals of Occupational Hygiene*, 56(5), 581-594.

Lim, J., Lim, C., Liya, E. Y. (2009). "Composition and Size Distribution of Metals in Diesel Exhaust Particulates." *Journal of Environmental Monitoring*, 11(9), 1614-1621.

Lim, J., Yu, L. E., Kostetski, Y. Y., Lim, C., Ryu, J., Kim, J. (2008). "Effects of Driving Conditions on Diesel Exhaust Particulates." *Journal of the Air and Waste Management Association*, 58(8), 1077-1085.

Lin, L., Lin, C., Lin, Y., Chuang, K. (2009). "The Effects of Indoor Particles on Blood Pressure and Heart Rate among Young Adults in Taipei, Taiwan." *Indoor Air*, 19(6), 482-488.

Liu, B. Y., and Pui, D. Y. (1974). "A Submicron Aerosol Standard and the Primary, Absolute Calibration of the Condensation Nuclei Counter." *Journal of Colloid and Interface Science*, 47(1), 155-171.

Liu, B., and Rubow, K. (1990). "Efficiency, pressure drop and figure of merit of high efficiency fibrous and membrane filter media." *Proceedings of the Fifth World Filtration Congress, NICE*.

Liu, C., Chien, C., Lo, C., Lin, G., Chen, S., Tsai, C. (2011). "Drag Coefficient of a Spherical Particle Attached on the Flat Surface." *Aerosol and Air Quality Research*, 11(5), 482-486.

Liu, B. Y. H., Pui, D. Y. H., Kinstley, W. O., Fisher, W. G. (1987). "Aerosol Charging and Neutralization and Electrostatic Discharge in Clean Rooms." *Journal of Environmental Sciences*, 30(2), 42-46.

Liu, P., Ziemann, P. J., Kittelson, D. B., McMurry, P. H. (1995a). "Generating Particle Beams of Controlled Dimensions and Divergence: I. Theory of Particle Motion in Aerodynamic Lenses and Nozzle Expansions." *Aerosol Science and Technology,* 22(3), 293-313.

Liu, P., Ziemann, P. J., Kittelson, D. B., McMurry, P. H. (1995b). "Generating Particle Beams of Controlled Dimensions and Divergence: II. Experimental Evaluation of Particle Motion in Aerodynamic Lenses and Nozzle Expansions." *Aerosol Science and Technology,* 22(3), 314-324.

Lore, M. B., Sambol, A. R., Japuntich, D. A., Franklin, L. M., Hinrichs, S. H. (2011). "Inter-Laboratory Performance between Two Nanoparticle Air Filtration Systems using Scanning Mobility Particle Analyzers." *Journal of Nanoparticle Research,* 13(4), 1581-1591.

Lundgren, D. A., and Whitby, K. (1965). "Effect of Particle Electrostatic Charge on Filtration by Fibrous Filters." *Industrial & Engineering Chemistry Process Design and Development,* 4(4), 345-349.

Mädler, L., and Friedlander, S. K. (2007). "Transport of Nanoparticles in Gases: Overview and Recent Advances." *Aerosol and Air Quality Research,* 7, 304-342.

Mallina, R. V., Wexler, A. S., Rhoads, K. P., Johnston, M. V. (2000). "High Speed Particle Beam Generation: A Dynamic Focusing Mechanism for Selecting Ultrafine Particles." *Aerosol Science and Technology,* 33(1-2), 87-104.

Mandl, F. (1988). *Statistical Physics,* Chichester, West Sussex ; Toronto : Wiley, Chichester, West Sussex ; Toronto; Chichester England.

Marjamäki, M., Keskinen, J., Chen, D. -., Pui, D. Y. H. (2000). "Performance Evaluation of the Electrical Low-Pressure Impactor (ELPI)." *Journal of Aerosol Science,* 31(2), 249-261.

Marlow, W., and Brock, J. (1975). "Calculations of Bipolar Charging of Aerosols." *Journal of Colloid and Interface Science,* 51(1), 23-31.

Marra, J., Voetz, M., Kiesling, H. (2010). "Monitor for Detecting and Assessing Exposure to Airborne Nanoparticles." *Journal of Nanoparticle Research,* 12(1), 21-37.

Martin Jr, S. B., and Moyer, E. S. (2000). "Electrostatic Respirator Filter Media: Filter Efficiency and most Penetrating Particle Size Effects." *Applied Occupational and Environmental Hygiene,* 15(8), 609-617.

Martin, S. T. (2000). "Phase Transitions of Aqueous Atmospheric Particles." *Chemical Reviews,* 100(9), 3403-3454.

Mauderly, J. L., and Chow, J. C. (2008). "Health Effects of Organic Aerosols." *Inhalation Toxicology,* 20(3), 257-288.

Maugis, D., and Pollock, H. M. (1984). "Surface Forces, Deformation and Adherence at Metal Microcontacts." *Acta Metallurgica,* 32(9), 1323-1334.

Maugis, D. D. (2000). *Contact, Adhesion and Rupture of Elastic Solids*, Berlin ; New York : Springer, Berlin ; New York.

Maw, N., Barber, J. R., Fawcett, J. N. (1981). "Role of Elastic Tangential Compliance in Oblique Impact." *Journal of Lubrication Technology,* 103(1), 74-80.

Maw, N., Barber, J. R., Fawcett, J. N. (1976). "The Oblique Impact of Elastic Spheres." *Wear,* 38(1), 101-114.

McKenna, J. D., Turner, J. H., McKenna, J. P. (2008). *Fine Particle (2.5 Microns) Emissions : Regulation, Measurement, and Control*, Hoboken, N.J. : Wiley, .

McMurry, P. H., and Woo, K. S. (2002). "Size Distributions of 3-100-Nm Urban Atlanta Aerosols: Measurement and Observations." *Journal of Aerosol Medicine,* 15(2), 169-178.

Megelski, S., Stephens, J. S., Chase, D. B., Rabolt, J. F. (2002). "Micro-and Nanostructured Surface Morphology on Electrospun Polymer Fibers." *Macromolecules,* 35(22), 8456-8466.

Mei, Y., Wang, Z., Li, X. (2013). "Improving Filtration Performance of Electrospun Nanofiber Mats by a Bimodal Method." *Journal of Applied Polymer Science,* 128(2), 1089-1094.

Mengersen, K., Morawska, L., Wang, H., Murphy, N., Tayphasavanh, F., Darasavong, K., Holmes, N. S. (2011). "Association between Indoor Air Pollution Measurements and Respiratory Health in Women and Children in Lao PDR." *Indoor Air*, 21(1), 25-35.

Middha, P., and Wexler, A. S. (2003). "Particle Focusing Characteristics of Sonic Jets." *Aerosol Science and Technology,* 37(11), 907-915.

Miguel, A. F. (2003). "Effect of Air Humidity on the Evolution of Permeability and Performance of a Fibrous Filter during Loading with Hygroscopic and Non-Hygroscopic Particles." *Journal of Aerosol Science*, 34(6), 783-799.

Mit-uppatham, C., Nithitanakul, M., Supaphol, P. (2004). "Ultrafine Electrospun Polyamide-6 Fibers: Effect of Solution Conditions on Morphology and Average Fiber Diameter." *Macromolecular Chemistry and Physics,* 205(17), 2327-2338.

Montgomery, J. F., Green, S. I., Rogak, S. N. (2015). "Impact of Relative Humidity on HVAC Filters Loaded with Hygroscopic and Non-Hygroscopic Particles." *Aerosol Science and Technology*, 49(5), 322-331.

Morton, W. J. (1902). "Method of Dispersing Fluids." *US Patent 705691*.

Motzkus, C., Chivas-Joly, C., Guillaume, E., Ducourtieux, S., Saragoza, L., Lesenechal, D., MacÉ, T., Lopez-Cuesta, J., Longuet, C. (2012). "Aerosols Emitted by the Combustion of Polymers Containing Nanoparticles." *Journal of Nanoparticle Research,* 14(3).

Mouret, G., Chazelet, S., Thomas, D., Bemer, D. (2011). "Discussion about the Thermal Rebound of Nanoparticles." *Separation and Purification Technology*, 78(2), 125-131.

Mulheran, P. A. (1994). "Surface Free-Energy Calculations and the Equilibrium Shape of NaCl Crystals." *Modelling and Simulation in Materials Science and Engineering*, 2(6), 1123-1129.

Muller, V., Yushchenko, V., Derjaguin, B. V. (1980). "On the Influence of Molecular Forces on the Deformation of an Elastic Sphere and its Sticking to a Rigid Plane." *Journal of Colloid and Interface Science*, 77(1), 91-101.

Mullins, B. J., Agranovski, I. E., Braddock, R. D. (2003). "Particle Bounce during Filtration of Particles on Wet and Dry Filters." *Aerosol Science and Technology*, 37(7), 587-600.

Namasivayam, C., Muniasamy, N., Gayatri, K., Rani, M., Ranganathan, K. (1996). "Removal of Dyes from Aqueous Solutions by Cellulosic Waste Orange Peel." *Bioresource Technology*, 57(1), 37-43.

Nazarboland, M., Chen, X., Hearle, J., Lydon, R., Moss, M. (2007). "Effect of Different Particle Shapes on the Modelling of Woven Fabric Filtration." *Journal of Information and Computing Science*, 2(2), 111-118.

Nazaroff, W. W. (2004). "Indoor Particle Dynamics." *Indoor Air, Supplement*, 14(SUPPL. 7), 175-183.

Nedjari, S., Schlatter, G., Hébraud, A. (2015). "Thick Electrospun Honeycomb Scaffolds with Controlled Pore Size." *Materials Letters*, 142, 180-183.

Nieh, S., and Nguyen, T. (1988). "Effects of Humidity, Conveying Velocity, and Particle Size on Electrostatic Charges of Glass Beads in a Gaseous Suspension Flow." *Journal of Electrostatics*, 21(1), 99-114.

Oberdorster, G., Gelein, R. M., Ferin, J., Weiss, B. (1995). "Association of Particulate Air Pollution and Acute Mortality: Involvement of Ultrafine Particles?" *Inhalation Toxicology*, 7(1), 111-124.

Oberdörster, G., Stone, V., Donaldson, K. (2007). "Toxicology of Nanoparticles: A Historical Perspective." *Nanotoxicology*, 1(1), 2-25.

Oberdörster, G., Oberdörster, E., Oberdörster, J. (2005). "Nanotoxicology: An Emerging Discipline Evolving from Studies of Ultrafine Particles." *Environmental Health Perspectives,* 113(7), 823-839.

Olfert, J. S., Kulkarni, P., Wang, J. (2008). "Measuring Aerosol Size Distributions with the Fast Integrated Mobility Spectrometer." *Journal of Aerosol Science,* 39(11), 940-956.

Olfert, J. S., and Collings, N. (2005). "New Method for Particle Mass Classification - the Couette Centrifugal Particle Mass Analyzer." *Journal of Aerosol Science,* 36(11), 1338-1352.

Orr, F. M., Scriven, L. E., Rivas, A. P. (1975). "Pendular Rings between Solids: Meniscus Properties and Capillary Force." *Journal of Fluid Mechanics,* 67(pt 4), 723-742.

Otani, Y., Eryu, K., Furuuchi, M., Tajima, N., Tekasakul, P. (2007). "Inertial Classification of Nanoparticles with Fibrous Filters." *Aerosol and Air Quality Research,* 7, 343-352.

Otani, Y., Emi, H., Cho, S. J., Namiki, N. (1995). "Generation of Nanometer Size Particles and their Removal from Air." *Advanced Powder Technology,* 6(4), 271-281.

Ouf, F., and Sillon, P. (2009). "Charging Efficiency of the Electrical Low Pressure Impactor's Corona Charger: Influence of the Fractal Morphology of Nanoparticle Aggregates and Uncertainty Analysis of Experimental Results." *Aerosol Science and Technology,* 43(7), 6-698.

Paik, S., and Vincent, J. H. (2002). "Aspiration Efficiency for Thin-Walled Nozzles Facing the Wind and for very High Velocity Ratios." *Journal of Aerosol Science,* 33(5), 705-720.

Pakarinen, O. H., Foster, A. S., Paajanen, M., Kalinainen, T., Katainen, J., Makkonen, I., Lahtinen, J., Nieminen, R. M. (2005b). "Towards an Accurate Description of the Capillary Force in Nanoparticle-Surface Interactions." *Modelling and Simulation in Materials Science and Engineering,* 13(7), 1175-1186.

Paur, H., Cassee, F. R., Teeguarden, J., Fissan, H., Diabate, S., Aufderheide, M., Kreyling, W. G., Hänninen, O., Kasper, G., Riediker, M., Rothen-Rutishauser, B., Schmid, O. (2011). "In-Vitro Cell Exposure Studies for the Assessment of Nanoparticle Toxicity in the Lung-A Dialog between Aerosol Science and Biology." *Journal of Aerosol Science,* 42(10), 668-692.

Paw U, K. T. (1983). "The Rebound of Particles from Natural Surfaces." *Journal of Colloid and Interface Science,* 93(2), 442-452.

Payet, S., Boulaud, D., Madelaine, G., Renoux, A. (1992). "Penetration and Pressure Drop of a HEPA Filter during Loading with Submicron Liquid Particles." *Journal of Aerosol Science,* 23(7), 723-735.

Peineke, C., and Schmidt-Ott, A. (2008). "Explanation of Charged Nanoparticle Production from Hot Surfaces." *Journal of Aerosol Science,* 39(3), 244-252.

Peukert, W., and Wadenpohl, C. (2001). "Industrial Separation of Fine Particles with Difficult Dust Properties." *Powder technology,* 118(1), 136-148.

Peukert, W., and Löffler, F. (1991). "Influence of Temperature on Particle Separation in Granular Bed Filters." *Powder technology,* 68(3), 263-270.

Phares, D. J., Rhoads, K. P., Wexler, A. S. (2002). "Performance of a Single Ultrafine Particle Mass Spectrometer." *Aerosol Science and Technology,* 36(5), 583-592.

Pich, J. (1966a). "The Effectiveness of the Barrier Effect in Fiber Filters at Small Knudsen Numbers." *Staub Reinhalt,* 26, 1-4.

Pich, J. (1966b). "Pressure Drop of Fibrous Filters at Small Knudsen Numbers." *The Annals of Occupational Hygiene,* 9(1), 23-27.

Pich, J. (1965). "The Filtration Theory of Highly Dispersed Aerosols." *Staub Reinhalt,* 5, 16-23.

Pinchuk, A. O. (2012). "Size-Dependent Hamaker Constant for Silver Nanoparticles." *Journal of Physical Chemistry C,* 116(37), 20099-20120.

Podgórski, A., Bałazy, A., Gradoń, L. (2006). "Application of Nanofibers to Improve the Filtration Efficiency of the most Penetrating Aerosol Particles in Fibrous Filters." *Chemical Engineering Science,* 61(20), 6804-6815.

Przekop, R., and Gradoń, L. (2008). "Deposition and Filtration of Nanoparticles in the Composites of Nano and Microsized Fibers." *Aerosol Science and Technology,* 42(6), 483-493.

Pushnov, A. (2006). "Calculation of Average Bed Porosity." *Chemical and Petroleum Engineering,* 42(1-2), 14-17.

Qin, X., and Wang, S. -. (2006). "Filtration Properties of Electrospinning Nanofibers." *Journal of Applied Polymer Science,* 102(2), 1285-1290.

Rahmat, M., Ghiasi, H., Hubert, P. (2012). "An Interaction Stress Analysis of Nanoscale Elastic Asperity Contacts." *Nanoscale,* 4(1), 157-166.

Ramakrishna, S., Fujihara, K., Teo, W., Yong, T., Ma, Z., Ramaseshan, R. (2006). "Electrospun Nanofibers: Solving Global Issues." *Materials Today,* 9(3), 40-50.

Reneker, D. H., and Chun, I. (1996). "Nanometre Diameter Fibres of Polymer, Produced by Electrospinning." *Nanotechnology*, 7(3), 216.

Rengasamy, S., Eimer, B. C., Shaffer, R. E. (2009). "Comparison of Nanoparticle Filtration Performance of NIOSH-Approved and CE-Marked Particulate Filtering Facepiece Respirators." *The Annals of Occupational Hygiene*, 53(2), 117-128.

Rengasamy, S., King, W. P., Eimer, B. C., Shaffer, R. E. (2008). "Filtration Performance of NIOSH-Approved N95 and P100 Filtering Facepiece Respirators Against 4 to 30 Nanometer-Size Nanoparticles." *Journal of Occupational and Environmental Hygiene*, 5(9), 556-564.

Rennecke, S., and Weber, A. P. (2013a). "On the Pressure Dependence of Thermal Rebound." *Journal of Aerosol Science*, 58, 129-134.

Rennecke, S., and Weber, A. P. (2013b). "The Critical Velocity for Nanoparticle Rebound Measured in a Low Pressure Impactor." *Journal of Aerosol Science*, 58, 135-147.

Richter, G., Hillerich, K., Gianola, D. S., Mönig, R., Kraft, O., Volkert, C. A. (2009). "Ultrahigh Strength Single Crystalline Nanowhiskers Grown by Physical Vapor Deposition." *Nano Letters*, 9(8), 3048-3052.

Rim, D., Wallace, L., Persily, A. (2010). "Infiltration of outdoor ultrafine particles into a test house." *Environmental science & technology*, 44, 5908-5913.

Roduner, E. (2006). "Size Matters: Why Nanomaterials are Different." *Chemical Society Reviews*, 35(7), 583-592.

Romay, F. J., Liu, B. Y. H., Pui, D. Y. H. (1994). "A Sonic Jet Corona Ionizer for Electrostatic Discharge and Aerosol Neutralization." *Aerosol Science and Technology*, 20(1), 31-41.

Sabbagh-Kupelwieser, N., Maisser, A., Szymanski, W. W. (2011). "From Micro- to Nanosized Particles: Selected Characterization Methods and Measurable Parameters." *Particuology*, 9(3), 193-203.

Saprykina, A. (2009). "Airborne Nanoparticle Sizing by Aerodynamic Particle Focusing and Corona Charging."

Sato, S., Chen, D. R., Pui, D. Y. H. (2007). "Molecular Dynamics Study of Nanoparticle Collision with a Surface–Implication to Nanoparticle Filtration." *Aerosol and Air Quality Research*, 7(3), 278-303.

Savkoor, A. R., and Briggs, G. A. D. (1977). "The Effect of Tangential Force on the Contact of Elastic Solids in Adhesion." *Proc R Soc London Ser A*, 356(1684), 103-114.

Saxena, S., Henry, R., Podolski, W. (1985). "Particulate Removal from High-Temperature, High-Pressure Combustion Gases." *Progress in Energy and Combustion Science*, 11(3), 193-251.

Scheibel, H. G., and Porstendörfer, J. (1984). "Penetration Measurements for Tube and Screen-Type Diffusion Batteries in the Ultrafine Particle Size Range." *Journal of Aerosol Science,* 15(6), 673-682.

Sem, G. J. (2002). "Design and Performance Characteristics of Three Continuous-Flow Condensation Particle Counters: A Summary." *Atmospheric Research,* 62(3), 267-294.

Sener, A., Altay, A. S., Altay, F. (2011). "Effect of voltage on morphology of electrospun nanofibers." *Proc., Electrical and Electronics Engineering (ELECO), 2011 7th International Conference On,* IEEE, , I-324-I-328.

Seville, J., Chuah, T. G., Sibanda, V., Knight, P. (2003). "Gas Cleaning at High Temperatures using Rigid Ceramic Filters." *Advanced Powder Technology*, 14(6), 657-672.

Shaffer, R. E., and Rengasamy, S. (2009). "Respiratory Protection Against Airborne Nanoparticles: A Review." *Journal of Nanoparticle Research,* 11(7), 1661-1672.

Shapiro, M., Laufer, G., Gutfinger, C. (1983). "Electric Forces in Aerosol Filtration in Fibrous and Granular Filters—a Parametric Study." *Atmospheric Environment (1967),* 17(3), 477-484.

Shapiro, M., Laufer, G., Gutfinger, C. (1986). "Electrostatically Enhanced Granular Bed Filters." *Aerosol Science and Technology*, 5(1), 39-54.

Shi, B., and Ekberg, L. (2015). "Ionizer Assisted Air Filtration for Collection of Submicron and Ultrafine Particles—Evaluation of Long-Term Performance and Influencing Factors." *Environmental Science & Technology*, 49 (11), 6891–6898.

Shin, E. H., Cho, K. S., Seo, M. H., Kim, H. (2008a). "Determination of Electrospun Fiber Diameter Distributions using Image Analysis Processing." *Macromolecular Research,* 16(4), 314-319.

Shin, W. G., Mulholland, G. W., Kim, S. C., Pui, D. Y. H. (2008b). "Experimental Study of Filtration Efficiency of Nanoparticles Below 20 Nm at Elevated Temperatures." *Journal of Aerosol Science,* 39(6), 488-499.

Shin, W. G., Pui, D. Y. H., Fissan, H., Neumann, S., Trampe, A. (2007). "Calibration and Numerical Simulation of Nanoparticle Surface Area Monitor (TSI Model 3550 NSAM)." *Journal of Nanoparticle Research*, 9(1), 61-69.

Skaptsov, A. S., Baklanov, A. M., Dubtsov, S. N., Laulainen, N. S., Sem, G., Kaufman, S. (1996). "An Experimental Study of the Thermal Rebound Effect of Nanometer Aerosol Particles." *Journal of Aerosol Science*, 27(SUPPL.1), S145-S146.

Soltani, M., and Ahmadi, G. (1995). "Direct Numerical Simulation of Particle Entrainment in Turbulent Channel Flow." *Phys. Fluids,* 7(3), 647-657.

Song, K., Wu, Q., Zhang, Z., Ren, S., Lei, T., Dooley, K. M., Liu, D., Janes, M. E. (2015). "Fabricating Electrospun Nanofibers with Antimicrobial Capability: A Facile Route to Recycle Biomass Tar." *Fuel,* 150, 123-130.

Stechkina, I., and Fuchs, N. (1966). "Studies on Fibrous Aerosol filters—I. Calculation of Diffusional Deposition of Aerosols in Fibrous Filters." *The Annals of Occupational Hygiene,* 9(2), 59-64.

Stechkina, I. B. (1966). "Diffusion Precipitation of Aerosols in Fiber Filters." *Doklady Akademii Nauk SSSR,* 167(6), 1327-1330.

Stechkina, I. B., Kirsch, A. A., Fuchs, N. A. (1969). "Studies on Fibrous Aerosol Filters. IV. Calculation of Aerosol Deposition in Model Filters in the Range of Maximum Penetration." *The Annals of Occupational Hygiene,* 12(1), 1-8.

Steffens, J., and Coury, J. R. (2007a). "Collection Efficiency of Fiber Filters Operating on the Removal of Nano-Sized Aerosol Particles: I-Homogeneous Fibers." *Separation and Purification Technology,* 58(1), 99-105.

Steffens, J., and Coury, J. R. (2007b). "Collection Efficiency of Fiber Filters Operating on the Removal of Nano-Sized Aerosol Particles. II. Heterogeneous Fibers." *Separation and Purification Technology,* 58(1), 106-112.

Stein, S. W., Turpin, B. J., Cai, X., Huang, P., Mcmurry, P. H. (1994). "Measurements of Relative Humidity-Dependent Bounce and Density for Atmospheric Particles using the DMA-Impactor Technique." *Atmospheric Environment,* 28(10), 1739-1746.

Stephens, B., and Siegel, J. (2013). "Ultrafine Particle Removal by Residential Heating, Ventilating, and Air-conditioning Filters." *Indoor Air,* 23(6), 488-497.

Stevens, A. B., and Hrenya, C. M. (2005). "Comparison of Soft-Sphere Models to Measurements of Collision Properties during Normal Impacts." *Powder technology,* 154(2-3), 99-109.

Stolzenburg, M. R., and McMurry, P. H. (2008). "Equations Governing Single and Tandem DMA Configurations and a New Lognormal Approximation to the Transfer Function." *Aerosol Science and Technology,* 42(6), 421-432.

Stolzenburg, M. R., McMurry, P. H., Sakurai, H., Smith, J. N., Mauldin, R. L., Eisele, F. L., Clement, C. F. (2005). "Growth Rates of Freshly Nucleated Atmospheric Particles in Atlanta." *Journal of Geophysical Research: Atmospheres (1984–2012),* 110(D22).

Stolzenburg, M. R. (1988). *An Ultrafine Aerosol Size Distribution Measuring System,* na, .

Sun, B., Jiang, X., Zhang, S., Zhang, J., Li, Y., You, Q., Long, Y. (2015). "Electrospun Anisotropic Architectures and Porous Structures for Tissue Engineering." *Journal of Materials Chemistry B,* .

Suthar, A., and Chase, G. (2001). "Nanofibres in Filter Media." *Chemical Engineering,* (726), 26-28.

Tabakoff, W., and Malak, M. F. (1987). "Laser Measurements of Fly Ash Rebound Parameters for use in Trajectory Calculations." *Journal of Turbomachinery,* 109(4), 535-540.

Tabor, D. (1977). "Surface Forces and Surface Interactions." *Journal of Colloid and Interface Science,* 58(1), 2-13.

Tabor, D. (1948). "A Simple Theory of Static and Dynamic Hardness." *Proceedings of the Royal Society of London,* 192, 247-274.

Tan, Z., Givehchi, R., Saprykina, A. (2015). "Submicron Particle Sizing by Aerodynamic Dynamic Focusing and Electrical Charge Measurement." *Particuology,* 18, 105-111.

Tan, Z. (2014). *Air Pollution and Greenhouse Gases: From Basic Concepts to Engineering Applications for Air Emission Control,* Springer.

Tan, Z. C., and Wexler, A. S. (2007). "Fine Particle Counting with Aerodynamic Particle Focusing and Corona Charging." *Atmospheric Environment,* 41(25), 5271-5279.

Teodorescu, M., and Rahnejat, H. (2007). "Dry and Wet Nano-Scale Impact Dynamics of Rough Surfaces with Or without a Self-Assembled Monolayer." *Proceedings of the Institution of Mechanical Engineers, Part N: Journal of Nanoengineering and Nanosystems,* 221(2), 49-58.

Thomas, D., Mouret, G., Cadavid-Rodriguez, M. C., Chazelet, S., Bémer, D. (2013). "An Improved Model for the Penetration of Charged and Neutral Aerosols in the 4 to 80nm Range through Stainless Steel and Dielectric Meshes." *Journal of Aerosol Science,* 57, 32-44.

Tien, C. (1989). *Granular Filtration of Aerosols and Hydrosols,* Boston ; Toronto : Butterworths, Boston ; Toronto.

Tiwari, G., Tiwari, R., Sriwastawa, B., Bhati, L., Pandey, S., Pandey, P., Bannerjee, S. K. (2012). "Drug Delivery Systems: An Updated Review." *International Journal of Pharmaceutical Investigation,* 2(1), 2.

Tomba, E., Facco, P., Roso, M., Modesti, M., Bezzo, F., Barolo, M. (2010). "Artificial Vision System for the Automatic Measurement of Interfiber Pore Characteristics and Fiber Diameter Distribution in Nanofiber Assemblies." *Industrial & Engineering Chemistry Research,* 49(6), 2957-2968.

Torkmahalleh, M. A., Goldasteh, I., Zhao, Y., Udochu, N. M., Rossner, A., Hopke, P. K., Ferro, A. R. (2012). "PM 2.5 and Ultrafine Particles Emitted during Heating of Commercial Cooking Oils." *Indoor Air*, 22(6), 483-491.

Tsai, C., Pui, D. Y. H., Liu, B. Y. H. (1991). "Elastic Flattening and Particle Adhesion." *Aerosol Science and Technology*, 15(4), 239-255.

Tsai, C. S., White, D., Rodriguez, H., Munoz, C. E., Huang, C., Tsai, C., Barry, C., Ellenbecker, M. J. (2012). "Exposure Assessment and Engineering Control Strategies for Airborne Nanoparticles: An Application to Emissions from Nanocomposite Compounding Processes." *Journal of Nanoparticle Research*, 14(7).

Tsai, S., Ashter, A., Ada, E., Mead, J. L., Barry, C. F., Ellenbecker, M. J. (2008). "Airborne Nanoparticle Release Associated with the Compounding of Nanocomposites using Nanoalumina as Fillers." *Aerosol and Air Quality Research*, 8(2), 160-177.

Tufenkji, N., and Elimelech, M. (2004). "Correlation Equation for Predicting Single-Collector Efficiency in Physicochemical Filtration in Saturated Porous Media." *Environmental Science & Technology*, 38(2), 529-536.

Van Dijk, W. D., Gopal, S., Scheepers, P. T. J. (2011). "Nanoparticles in Cigarette Smoke; Real-Time Undiluted Measurements by a Scanning Mobility Particle Sizer." *Analytical and Bioanalytical Chemistry*, 399(10), 3573-3578.

Van Gulijk, C., Bal, E., Schmidt-Ott, A. (2009). "Experimental Evidence of Reduced Sticking of Nanoparticles on a Metal Grid." *Journal of Aerosol Science*, 40(4), 362-369.

Van Osdell, D. W., Liu, B. Y. H., Rubow, K. L., Pui, D. Y. H. (1990). "Experimental Study of Sub-Micrometer and Ultrafine Particle Penetration and Pressure Drop for High Efficiency Filters." *Aerosol Science and Technology*, 12, 911-925.

Vasiliou, J. G., Sorensen, D., McMurry, P. H. (1999). "Sampling at Controlled Relative Humidity with a Cascade Impactor." *Atmospheric Environment*, 33(7), 1049-1056.

Vial, J., and Carré, A. (1991). "Calculation of Hamaker Constant and Surface Energy of Polymers by a Simple Group Contribution Method." *International Journal of Adhesion and Adhesives*, 11(3), 140-143.

Vidal-de-Miguel, G., and de la Mora, Juan Fernandez. (2012). "Continuously Converging Multistage Focusing Lenses to Concentrate Aerosols at High Reynolds Numbers." *Aerosol Science and Technology*, 46(3), 287-296.

Virtanen, A., Marjamäki, M., Ristimäki, J., Keskinen, J. (2001). "Fine Particle Losses in Electrical Low-Pressure Impactor." *Journal of Aerosol Science*, 32(3), 389-401.

Wall, S., John, W., Wang, H. (1990). "Measurements of Kinetic Energy Loss for Particles Impacting Surfaces." *Aerosol Science and Technology*, 12(4), 926-946.

Wallace, L. A., Emmerich, S. J., Howard-Reed, C. (2004). "Source Strengths of Ultrafine and Fine Particles due to Cooking with a Gas Stove." *Environmental Science and Technology*, 38(8), 2304-2311.

Wang, H., Yang, Z. Y., Liu, J. Y., Zheng, G. F., Liu, Y. P. (2011a). "Research on the Advantages of Nanofibrous Air Filtration Membrane." *Key Engineering Materials*, 474, 2016-2019.

Wang, H., Zheng, G., Sun, D. (2007a). "Electrospun nanofibrous membrane for air filtration." *Proc., Nanotechnology, 2007. IEEE-NANO 2007. 7th IEEE Conference On*, IEEE, , 1244-1247.

Wang, J., and Tronville, P. (2014). "Toward Standardized Test Methods to Determine the Effectiveness of Filtration Media Against Airborne Nanoparticles." *Journal of Nanoparticle Research*, 16(6), 1-33.

Wang, C., and Otani, Y. (2013). "Removal of Nanoparticles from Gas Streams by Fibrous Filters: A Review." *Industrial and Engineering Chemistry Research*, 52(1), 5-17.

Wang, H., and Kasper, G. (1991). "Filtration Efficiency of Nanometer-Size Aerosol Particles." *Journal of Aerosol Science*, 22(1), 31-41.

Wang, J., and Pui, D. Y. H. (2011). "Characterization, Exposure Measurement and Control for Nanoscale Particles in Workplaces and on the Road." *Journal of Physics: Conference Series*, 304(1).

Wang, J., Kim, S. C., Pui, D. Y. H. (2008). "Investigation of the Figure of Merit for Filters with a Single Nanofiber Layer on a Substrate." *Journal of Aerosol Science*, 39(4), 323-334.

Wang, J., Chen, D. R., Pui, D. Y. H. (2007b). "Modeling of Filtration Efficiency of Nanoparticles in Standard Filter Media." *Journal of Nanoparticle Research*, 9(1), 109-115.

Wang, S. C., and Flagan, R. C. (1990). "Scanning Electrical Mobility Spectrometer." *Aerosol Science and Technology*, 13(2), 230-240.

Wang, Z., Wagner, J., Wall, S. (2011b). "Characterization of Laser Printer Nanoparticle and VOC Emissions, Formation Mechanisms, and Strategies to Reduce Airborne Exposures." *Aerosol Science and Technology*, 45(9), 1060-1068.

Ward, G. (2005). "Nanofibres: Media at the Nanoscale." *Filtration Separation*, 42(7), 22-24.

Watson, J. G., Chow, J. C., Sodeman, D. A., Lowenthal, D. H., Chang, M. O., Park, K., Wang, X. (2011). "Comparison of Four Scanning Mobility Particle Sizers at the Fresno Supersite." *Particuology,* 9(3), 204-209.

Watson, J. G., Chow, J. C., Lowenthal, D. H., Stolzenburg, M. R., Kreisberg, N. M., Hering, S. V. (2002). "Particle Size Relationships at the Fresno Supersite." *Journal of the Air & Waste Management Association,* 52(7), 822-827.

Weimer, S., Mohr, C., Richter, R., Keller, J., Mohr, M., Prévôt, A. S. H., Baltensperger, U. (2009). "Mobile Measurements of Aerosol Number and Volume Size Distributions in an Alpine Valley: Influence of Traffic versus Wood Burning." *Atmospheric Environment,* 43(3), 624-630.

Weir, G., and McGavin, P. (2008). "The Coefficient of Restitution for the Idealized Impact of a Spherical, Nano-Scale Particle on a Rigid Plane." *Proceedings of the Royal Society A: Mathematical, Physical and Engineering Sciences,* 464(2093), 1295-1307.

Wenzel, B. M., Porciúncula, C. B., Marcilio, N. R., Menegolla, H. B., Dornemann, G. M., Godinho, M., Martins, C. B. (2014). "Filtration of Dust in an Intermittent Moving Granular Bed Filter: Performance and Modeling." *Separation and Purification Technology,* 133(0), 108-119.

Werner, R. M., and Clarenburg, L. A. (1965). "Aerosol Filters: Pressure Drop Across Single-Component Glass Fiber Filters." *IandEC Process Design and Development,* 4(3), 288-293.

Wexler, A. S., and Johnston, M. V. (2001). "Real-Time Single-Particle Analysis." *Aerosol Measurment: Principles, Techniques and Applications,* New York, 365-385.

Whitby, K. T. (1978). "The Physical Characteristics of Sulfate Aerosols." *Atmospheric Environment,* 12, 135-159.

White, H. J. (1951). "Particle Charging in Electrostatic Precipitation." *American Institute of Electrical Engineers,* 70(2), 1186-1191.

Wiedensohler, A., Birmili, W., Nowak, A., Sonntag, A., Weinhold, K., Merkel, M., Wehner, B., Tuch, T., Pfeifer, S., Fiebig, M. (2012). "Mobility Particle Size Spectrometers: Harmonization of Technical Standards and Data Structure to Facilitate High Quality Long-Term Observations of Atmospheric Particle Number Size Distributions." *Atmospheric Measurement Techniques,* 5, 657-685.

Willeke, K., and Baron, P. A. (1993). *Aerosol Measurement : Principles, Techniques, and Applications,* New York : Van Nostrand Reinhold, New York.

Wimmer, D., Attoui, M., Steiner, G. W., Sipila, M., Reischl, G. P. (2008). "Performance of Different Faraday Cup Electrometers with High Resolution Electro Mobility Spectrometers." *Poster at the EAC.*

Wimmer, D., Lehtipalo, K., Franchin, A., Kangasluoma, J., Kreissl, F., Kürten, A., Kupc, A., Metzger, A., Mikkilä, J., Petäjä, T. (2013). "Performance of Diethylene Glycol-Based Particle Counters in the Sub-3 Nm Size Range." *Atmospheric Measurement Techniques*, 6(7), 1793-1804.

Winkler, P. M., Steiner, G., Reischl, G., Vrtala, A., Wagner, P. E., Kulmala, M. (2007). "The Effect of Seed Particle Charge on Heterogeneous Nucleation." *Nucleation and Atmospheric Aerosols*, Springer, 358-362.

Winklmayr, W., Reischl, G., Lindner, A., Berner, A. (1991). "A New Electromobility Spectrometer for the Measurement of Aerosol Size Distributions in the Size Range from 1 to 1000 Nm." *Journal of Aerosol Science*, 22(3), 289-296.

Wise, M. E., Semeniuk, T. A., Bruintjes, R., Martin, S. T., Russell, L. M., Buseck, P. R. (2007). "Hygroscopic Behavior of NaCl-bearing Natural Aerosol Particles using Environmental Transmission Electron Microscopy." *Journal of Geophysical Research: Atmospheres (1984–2012)*, 112(D10).

Wittmer, C. R., Hébraud, A., Nedjari, S., Schlatter, G. (2014). "Well-Organized 3D Nanofibrous Composite Constructs using Cooperative Effects between Electrospinning and Electrospraying." *Polymer*, 55(22), 5781-5787.

Wu, C., Thornton, C., Li, L. (2008). "Rebound Behaviour of Spheres during Elastic-Plastic Oblique Impacts." *International Journal of Modern Physics B*, 22(9-11), 1095-1102.

Wu, C., Li, L., Thornton, C. (2003). "Rebound Behaviour of Spheres for Plastic Impacts." *International Journal of Impact Engineering*, 28(9), 929-946.

Xia, Y., Yang, P., Sun, Y., Wu, Y., Mayers, B., Gates, B., Yin, Y., Kim, F., Yan, H. (2003). "One-dimensional Nanostructures: Synthesis, Characterization, and Applications." *Advanced Materials*, 15(5), 353-389.

Xiao, G., Wang, X., Zhang, J., Ni, M., Gao, X., Luo, Z., Cen, K. (2013). "Granular Bed Filter: A Promising Technology for Hot Gas Clean-Up." *Powder technology*, 244, 93-99.

Xu, B., Wu, Y., Lin, Z., Chen, Z. (2014). "Investigation of Air Humidity Affecting Filtration Efficiency and Pressure Drop of Vehicle Cabin Air Filters." *Aerosol and Air Quality Research*, 14(3), 1066-1073.

Xu, M., and Willeke, K. (1993). "Right-Angle Impaction and Rebound of Particles." *Journal of Aerosol Science*, 24(1), 19-30.

Xu, M., Willeke, K., Biswas, P., Pratsinis, S. E. (1993). "Impaction and Rebound of Particles at Acute Incident Angles." *Aerosol Science and Technology*, 18(2), 143-155.

Yamada, S., Seto, T., Otani, Y. (2011). "Influence of Filter Inhomogeneity on Air Filtration of Nanoparticles." *Aerosol and Air Quality Research,* 11(2), 155-160.

Yang, S., and Lee, G. W. M. (2005). "Filtration Characteristics of a Fibrous Filter Pretreated with Anionic Surfactants for Monodisperse Solid Aerosols." *Journal of Aerosol Science,* 36(4), 419-437.

Yao, J., Bastiaansen, C. W., Peijs, T. (2014). "High Strength and High Modulus Electrospun Nanofibers." *Fibers,* 2(2), 158-186.

Yao, J., Liu, W., Chen, W., Wang, G., Zeng, Y., Huang, Y., Lin, J. (2012). "Effect of Atmospheric Parameters on Fine Particulate Concentration in Suburban Shanghai." *Particuology,* 11(1), 48-54

Yeh, H., and Liu, B. Y. H. (1974). "Aerosol Filtration by Fibrous Filters-I. Theoretical." *Journal of Aerosol Science,* 5(2), 191-204.

Yehia, A., and Mizuno, A. (2012). "Expectation of Ozone Generation in Alternating Current Corona Discharges." *Physics of Plasmas,* 19(3).

Yin, Z., Lin, J., Qian, L. (2012). "An Experimental Study on the Characteristics of Nanoparticles Emission from a Vehicle." *Advanced Materials Research,* 508, 180-183.

Yoon, K., Hsiao, B. S., Chu, B. (2008). "Functional Nanofibers for Environmental Applications." *Journal of Materials Chemistry,* 18(44), 5326-5334.

Yuan, X., Zhang, Y., Dong, C., Sheng, J. (2004). "Morphology of Ultrafine Polysulfone Fibers Prepared by Electrospinning." *Polym. Int.,* 53(11), 1704-1710.

Yun, K. M., Hogan Jr., C. J., Matsubayashi, Y., Kawabe, M., Iskandar, F., Okuyama, K. (2007). "Nanoparticle Filtration by Electrospun Polymer Fibers." *Chemical Engineering Science,* 62(17), 4751-4759.

Zaatari, M., Novoselac, A., Siegel, J. (2014). "The relationship between filter pressure drop, indoor air quality, and energy consumption in rooftop HVAC units." *Building and Environment,* 73, 151-161.

Zenker, P. (1971). "Investigation into the Problem of Sampling from a Partial Flow with Different Flow Velocities for the Determination of the Dust Content in Flowing Gases." *Staub-Reinhalt.Luft,* 31, 30-36.

Zhang, C., Yuan, X., Wu, L., Han, Y., Sheng, J. (2005). "Study on Morphology of Electrospun Poly (Vinyl Alcohol) Mats." *European Polymer Journal,* 41(3), 423-432.

Zhang, Q., Welch, J., Park, H., Wu, C., Sigmund, W., Marijnissen, J. (2010). "Improvement in Nanofiber Filtration by Multiple Thin Layers of Nanofiber Mats." *Journal of Aerosol Science*, 41(2), 230-236.

Zhang, Q., and Zhu, Y. (2012). "Characterizing Ultrafine Particles and Other Air Pollutants at Five Schools in South Texas." *Indoor Air*, 22(1), 33-42.

Zhang, X., and Ahmadi, G. (2007). "Effects of Capillary Force and Surface Deformation on Particle Removal in Turbulent Flows." *Journal of Adhesion Science and Technology*, 21(16), 1589-1611.

Zhou, H., Green, T. B., Joo, Y. L. (2006). "The Thermal Effects on Electrospinning of Polylactic Acid Melts." *Polymer*, 47(21), 7497-7505.

Zong, X., Kim, K., Fang, D., Ran, S., Hsiao, B. S., Chu, B. (2002). "Structure and Process Relationship of Electrospun Bioabsorbable Nanofiber Membranes." *Polymer*, 43(16), 4403-4412.